
THE UNIVERSITY *of* EDINBURGH

# Adsorption for desalination, cooling and generation of electricity from low-grade heat

Christopher Jan Olkis


THE UNIVERSITY
*of* EDINBURGH

**Thesis submitted for the degree of**
**Doctor of Philosophy**

**The University of Edinburgh**
**School of Engineering**

**Year of Submission 2019**

# Declaration

I hereby certify that this thesis has been composed solely by myself and that it has not been submitted, either in whole or in part, in any previous application for a degree. Except where otherwise acknowledged, the work presented is entirely my own. In addition, the work has not been previously submitted for any other degree.

Christopher Olkis

# Abstract

Two thirds of all primary energy are converted into waste heat causing thermal pollution and economic loss. The heat is emitted at different temperatures, but most of it is 100 °C and below, where it is more difficult for another process to use it. This work concerns the utilisation of waste heat $< 100$ °C for desalination and the generation of electricity in the Reverse Electrodialysis Heat-to-Power process. The process combines a Reverse Electrodialysis membrane stack *RED* with a thermal desalination system in a closed loop. Two salt solutions at different concentrations circulate between them; the RED unit generates electricity, while the thermal desalination unit restores the salt concentration difference between the two solutions.

The thermodynamics of salt solutions are fundamental to the process and were experimentally assessed using a Barker's cell to determine saturation pressures and temperatures. Novel salt solutions for K, Li and Cs acetate salts are measured and the results have been presented in a joint publication with the Università degli Studi di Palermo, Italy. The results were fitted to the Pitzer model for further process modelling of both RED and desalination. The salt measurements were conducted for T = 10-90 °C in increments of 10 °C and concentrations 2-8 mol/kg resulting in boiling point elevations up to 12 °C.

Different common desalination methods were identified and have been modelled in Matlab and UniSim to compare their performance. The Matlab models used the Pitzer parameters from either the literature or the previous investigation on the novel salt solutions. UniSim was used in combination with the OLI electrolytes package allowing UniSim to access precise salt properties for established salts.
Multi-effect distillation is the best performing, benchmarking desalination method as the Specific Thermal Consumption increases with the number of effects ranging from 25 kWh/m$^3$ for large systems (27 effects) to 150 kWh/m$^3$ for compact systems (5 effects). Absorption vapour compression desalination was identified as another promising desalination method with a simpler process design than multi-effect distillation. A UniSim model has shown that the performance of the system is constant at 250 kWh/m$^3$ and almost independent of the salt concentration.

The focus of this work is adsorption desalination as it has the simplest process scheme of all desalination methods with a minimum of moving parts and pumps. Experimental systems in the literature have proven the feasibility of the process, but all systems are very large in size with the best performing system using 144 kg of silica gel. The large size makes it difficult to test novel adsorption materials and system components, which is necessary to advance the technology. Thus, an experimental adsorption desalinator was designed and build with 0.025 - 0.4 kg adsorption material capacity. In addition, the system can also be used as an adsorption chiller. The first set of experiments was conducted using silica gel showing that the small size is not detrimental to the system performance. A maximum Specific Daily Water Production *SDWP* of 10.9 $kg_w/(kg_{sg}d)$ was experimentally obtained at 80 °C, which is one of the best results ever reported for silica gel. A full characterisation of the test rig using silica gel was presented in two publications highlighting the novelty of the small scale, novel analysis methods (e.g. cycle analysis, thermal response) and regeneration temperatures as low as 40 °C. In addition, an ionogel adsorption material was analysed in a water adsorption process for the first time. The novel material is composed of a silica gel support structure impregnated with an ionic liquid. The ionic liquid was chosen based on an equilibrium data screening that identified 1-Ethyl-3-methylimidazolium acetate as best for the application. Experiments in the test rig showed that the ionogel can be regenerated using a waste heat source of 25 °C achieving SDWP = 6.7 $kg_w/(kg_{sg}d)$. An increase of the regeneration temperature to 45 °C improves the SDWP to 17.5 $kg_w/(kg_{sg}d)$. The material appears stable in terms of performance and even improved by 30 % due to thermal swings in the test rig, but minor leakages of the ionic liquid from the support structure were observed.

The results of the experiments on the test rig provided a better understanding of the process and led to the development of Adsorption Reverse Electrodialysis process (ADRED). The ADRED process integrates adsorption desalination into the closed-loop of the RED Heat-to-Power process. A thermodynamic analysis assesses different adsorption materials and salts to identify the best combination having the highest efficiency. In addition, the results show that the energy consumption of adsorption desalination is independent of the salt concentration. Thus, ADRED is not limited by the salt concentration on the regeneration side.
A dynamic ADRED model was developed and validated. The AD side is validated on the results of the experimental test rig for regeneration temperatures 40-60 °C, while a validated RED model was adapted from literature. A case study was performed for a system powered by 700 MW of waste heat emitted by a power plant at 40 °C. The simulations show a net electricity output of 2.3 MW with a net exergy efficiency of 7.1 % and net energy efficiency of 0.33 %.

# Lay Summary

Industry, power plants and transportation emit vast amounts of excess heat into the environment causing thermal pollution and economic losses. This thesis aims at utilising this low grade heat to produce electricity, cooling or drinking water using thermal desalination technologies with a special focus on adsorption desalination within the framework of the European funded RED Heat-to-Power project.

The RED concept is based on a reverse electrodialysis membrane that generates electricity by controlled mixing of two salt solutions with different salinities, which releases energy. The mixture is regenerated into the two initial solutions using thermal desalination driven by low temperature waste heat 40-100 °C. Hence, the RED Heat-to-Power process converts low temperature heat into electricity.

The first part of the thesis experimentally assesses the thermodynamic properties of novel acetate salt solutions, which release a high amount of energy when mixed. In addition, the results were required for later modelling and were not available in the literature.

The second part applies these thermodynamic properties as well as literature data to different thermal desalination methods. Multi effect distillation represents the most efficient thermal desalination technology and showed the highest efficiency in large systems with a large number of evaporation effects. Small, compact systems are up to six times less efficient than large versions leading to similar efficiencies as competing systems like absorption vapour compression, which was identified as a very promising thermal desalination technology. However, all established thermal desalination systems require high driving temperatures of more than 50-70 °C, while lower temperatures cannot be used. Adsorption desalination is a novel desalination method that evolved from adsorption chillers and can be powered by heat sources as low as 25 °C as it is shown in the third part of the thesis.

The third part presents an experimental adsorption desalinator featuring the smallest design presented in the literature. The system was designed, built and commissioned as part of this thesis. A thorough experimental characterisation was conducted using

silica gel as benchmarking material. Silica gel is an inexpensive, commercially available adsorbent with good water adsorption properties. Silica gel requires at least 40-50 °C for regeneration, but much higher performances can be achieved at 80 °C. The results show that the small scale is not detrimental as it achieves the same performance as the best system presented in the literature. In addition to silica gel, a novel ionogel adsorption material was tested reaching twice the performance of silica gel, but at only 45 °C instead of 80 °C. The results also show that the ionogel process can still be driven by a heat source of 25 °C achieving similar results as silica gel. The low regeneration temperature is a unique characteristic of Ionogel and it enables adsorption desalination to utilise any waste heat source.

The final part integrates adsorption desalination into the RED Heat-to-Power framework by combining it with reverse electrodialysis in a thermodynamic as well as a dynamic model. The thermodynamic model screens a large number of salts and adsorption materials to identify the best combination for the highest system efficiency. The dynamic model is validated against experimental data obtained from the small-scale adsorption test rig and silica gel on the adsorption side, while a validated model from the literature was adapted for the reverse electrodialysis side. In a case study, the system is powered by waste heat from a large steam power plant condenser highlighting the potential of the technology.

# Publications

## Published

- Olkis C, Santori G, Brandani S. An Adsorption Reverse Electrodialysis system for the generation of electricity from low-grade heat. Applied Energy. 2018 Dec 1;231:222-34.
  DOI: https://doi.org/10.1016/j.apenergy.2018.09.112
  *Contribution: The entire analysis. Support and advice was provided by the co-authors.*

- Giacalone F, Olkis C, Santori G, Cipollina A, Brandani S, Micale G. Novel solutions for closed-loop reverse electrodialysis: Thermodynamic characterisation and perspective analysis. Energy. 2019 Jan 1;166:674-89.
  DOI: https://doi.org/10.1016/j.energy.2018.10.049
  *Contribution: Experimental analysis of saturation temperatures and pressures of novel acetate salts.*

- Olkis C, Brandani S, Santori G. A small-scale adsorption desalinator. Energy Procedia. 2019 Feb 1;158:1425-30.
  DOI: https://doi.org/10.1016/j.egypro.2019.01.345
  *Contribution: The entire analysis. Support and advice was provided by the co-authors.*

- Olkis C, Brandani S, Santori G. Design and experimental study of a small scale adsorption desalinator. Applied Energy. 2019 Nov 1;253:113584.
  DOI: https://doi.org/10.1016/j.apenergy.2019.113584
  *Contribution: The entire analysis. Support and advice was provided by the co-authors.*

- Olkis C, Brandani S, Santori G. Cycle and performance analysis of a small-scale adsorption heat transformer for desalination and cooling applications. Chemical Engineering Journal. 2019 Dec 15;378:122104.
  DOI: https://doi.org/10.1016/j.cej.2019.122104
  *Contribution: The entire analysis. Support and advice was provided by the co-authors.*

- Askalany A, Olkis C, Calabrese L, Proverbio E, Bramanti E, Freni A, Santori G. Silica-supported ionic liquids for heat powered desalination. Accepted manuscript Applied Materials and Interfaces
  DOI: `https://doi.org/10.1021/acsami.9b07602`
  *Contribution: Experimental testing of the Ionogel in adsorption rig.*

- Olkis C, Dong H, Brandani S, Santori G. Ionogels at the water energy nexus for desalination powered by ultra low grade heat. Accepted manuscript. Environmental Science & Technology
  *Contribution: The entire analysis with the exception of the preparation of the Ionogel. Support and advice was provided by the senior co-authors.*

## In preparation

- Olkis C, Brandani S, Santori G. Increased efficiency of steam power plants through waste heat recovery.
  *Contribution: The entire analysis. Support and advice was provided by the co-authors.*

# Acknowledgements

I would like to acknowledge the funding for this work from the European Union for the RED-Heat-to-Power project (Conversion of Low-grade Heat to Power through closed loop Reverse Electro-Dialysis) - Horizon 2020 programme, Project Number: 640667.

I would like to express my gratitude to my two supervisors Prof. Stefano Brandani and Dr. Giulio Santori, who supported me with their in-depth knowledge, encouragement and advice. Officially, Giulio was only my second supervisor, but he provided enormous support.

The Institute of Materials and Processes was a fantastic place to carry out my research and I would like to thank the technical staff and all members for their support. In particular, Paul Aitken, Steven Gourlay and Douglas Carmichael.

I would also like to thank my friends and family for their support and encouragements throughout the time.

# Contents

# List of Figures

# List of Tables

# Nomenclature

**Greek**

| | |
|---|---|
| $\alpha$ | Thermal expansion coefficient (1/K) |
| $\alpha_x$ | Pitzer model constant |
| $\alpha_{CEM/AME}$ | Permselectivity (-) |
| $\beta_{MX}^{(0)}$ | Virial coefficient |
| $\beta_{MX}^{(1)}$ | Virial coefficient |
| $\Delta h_{ads}$ | Heat of adsorption (kJ/kg$_w$) |
| $\Delta q$ | Working capacity [g/g]) |
| $\Delta T$ | Temperature difference [K]) |
| $\delta$ | Membrane thickness (m) |
| $\eta_{en}$ | Energy efficiency (%) |
| $\eta_{ex}$ | Exergy efficiency (%) |
| $\gamma$ | Activity coefficient |
| $\Lambda$ | Equivalent conductivity (S m$^2$/mol) |
| $\omega$ | Modelling parameter (-) |
| $\Phi$ | Osmotic coefficient |
| $\rho$ | Density (kg/m$^3$) |
| $\tau$ | Modelling parameter (-) |
| $\Theta$ | Normalised adsorption uptake |
| $\varepsilon_{sp}$ | Spacer porosity |
| $\xi$ | Modelling parameter |

**Roman**

| | |
|---|---|
| $\tilde{M}$ | Molar mass (g/mol) |
| $A$ | Heat exchanger area (m$^2$) |
| $A_\Lambda$ | Parameter Jones and Dole equation |
| $a_s$ | Activity of the solution |
| $a_w$ | Activity of water |
| $A_\Phi$ | Debye Hückel coefficient |
| $b$ | Pitzer model constant |
| $B_\Lambda$ | Parameter Jones and Dole equation |
| $C$ | Salt concentration (mol/kg) |
| $C_\Lambda$ | Parameter Jones and Dole equation |
| $c_p$ | Specific heat (kJ/(kg K)) |
| $C_{MX}^\Phi$ | Virial coefficient |
| $c_{sol}$ | Experimental molality (mol/kg) |
| $D$ | Dielectric constant |
| $D_{S0}$ | Kinetic constant for the silica gel water system (m$^2$/s) |
| $E$ | DA parameter (kJ/kg) |
| $e$ | Electron charge (C) |
| $E_t$ | Electricity production (kJ) |
| $E_a$ | Activation energy (kJ/kg) |
| $E_{cell}$ | Cell voltage (V) |
| $F$ | Faraday constant (s A/mol) |
| $F_i$ | Flow rate in ADRED scheme (kg/s) |
| $I$ | Ionic strength (mol/kg) |
| $j$ | Electrical current density (A/m$^2$) |
| $J_{salt}$ | Salt flux (mol/(m$^2$s)) |
| $k$ | Boltzmann constant (m$^2$kgK/s$^2$) |
| $L$ | Latent heat (kJ/kg) |
| $M$ | Mass (kg) |
| $m$ | Molality (mol/kg) |
| $N$ | Number of MED effects (-) |
| $n$ | DA exponent (-) |
| $n$ | Number of MED effects (-) |
| $N_0$ | Avogadro constant (1/mol) |
| $N_d$ | Number of cycles per day |
| $N_{cell}$ | Number of cell pairs (-) |
| $P$ | pressure (kPa) |
| $P_d$ | Power per cell pair area (W/m$^2$) |

| | |
|---|---|
| $P_{d,s}$ | Flow rate specific power density of membrane (W s/kg) |
| $P_{el}$ | Electric power (MW) |
| $Q$ | Heat (kJ) |
| $q$ | Water vapour uptake on the silica gel (kg/kg) |
| $q_0$ | Saturation uptake (kg/kg) |
| $R$ | Real gas constant (J/(mol K)) |
| $r$ | Discount rate () |
| $R_p$ | Diameter of silica gel beads (mm) |
| $R_{low/high/cell}$ | Electrical resistances ($\Omega m^2$) |
| $s_f$ | Spacer shadow factor (-) |
| $T$ | Temperature (K) |
| $t$ | Time (s) |
| $T'$ | Temperature at flashing [K] |
| $T_\Delta$ | Temperature drop between two MED effects (K) |
| $T_{red}$ | Reduced temperature (-) |
| $U$ | Heat transfer coefficient ($W/(m^2K)$) |
| $U_i$ | Dielectric constant parameters |
| $v_M$ | Number of ions (-) |
| $v_X$ | Number of ions (-) |
| $w$ | Mass fraction (kg/kg) |
| $X$ | Conversion factor for ADRED (-) |
| $Y$ | Indicates use of MED effect |
| $z$ | Charge of ion |
| $\dot{m}$ | Water flow rate (kg/s) |
| $\dot{Q}$ | Heat flow (kJ/s) |
| $\dot{V}$ | Volumetric flow rate ($m^3/s$) |

**Subscripts**

| | |
|---|---|
| $ad$ | Adsorption material |
| $ads$ | Adsorber |
| $amb$ | Ambient |
| $b$ | Brine |
| $bf$ | Vapour from flash evaporation |
| $c$ | Condenser |
| $cond$ | Condenser |
| $cw$ | Cooling water |
| $cycle$ | Adsorption cycle |
| $d$ | Distillate |
| $des$ | Desorber |
| $dil$ | Dilute |
| $dm$ | Distillate in the MED mixers |
| $eff$ | Effect |
| $el$ | Electricity |
| $evap$ | Evaporator |
| $exp$ | Experimental |
| $f$ | Feed |
| $gb$ | Vapour from boiling |
| $gf$ | Vapour from flash evaporation |
| $high$ | High salinity |
| $hx$ | Heat exchanger |
| $ig$ | Ionogel |
| $il$ | Ionic liquid |
| $in$ | Inlet |
| $int$ | Internal circulation |
| $low$ | Low salinity |
| $N$ | Number of MED effects |
| $out$ | Outlet |
| $ph$ | Pre-heater |
| $s$ | Steam |
| $sat$ | Saturation conditions |
| $sg$ | Silica gel |
| $sim$ | Simulation |
| $sol$ | Salt solution |
| $sw$ | Seawater |
| $th$ | Thermal energy |
| $v$ | Vapour |
| $vap$ | Vapour |
| $vh$ | Vapour condensed by preheater |
| $w$ | Water |

**Acronyms**

| | |
|---|---|
| $ABVC$ | Absorption vapour compression |
| $AC$ | Activated carbon |
| $Ac$ | Acetate |
| $AD$ | Adsorption desalination |
| $ADVC$ | Adsorption vapour compression |

$AEM$ Anion exchange membrane

$AQSOA-Z01$ Commercial zeolite

$AQSOA-Z02$ Commercial zeolite

$BMIM$ 1-Butyl-3-methylimidazolium

$BPE$ Boiling point elevation (°C)

$c-e\ int.$ Heat integration between AD condenser and evaporator

$CapEx$ Capital expenses (€)

$CE$ Cascade evaporation

$CEM$ Cation exchange membrane

$COP$ Coefficient of performance (-)

$ED$ Electrodialysis

$EDS$ Energy dispersive X-ray spectroscopy

$EMIM$ 1-Ethyl-3-methylimidazolium

$FIB$ Focus ion beam

$IEM$ Ion exchange membrane

$IL$ Ionic liquid

$LCOE$ Levelized cost of electricity (€/kWh)

$MD$ Membrane distillation

$MED$ Multi effect distillation

$MSF$ Multi Stage Flash

$NF$ Nanofiltration

$NIST$ National Institute of Standards and Technology

$OCV$ Open circuit voltage (V)

$OLI$ Software extension package for UniSim Process Simulator

$OpEx$ Operational expenses (€)

$ORC$ Organic Rankine cylce

$PR$ Performance Ratio

$PRO$ Pressure retarded osmosis

$PT$ Pressure transducer

$RED$ Reverse Electrodialysis

$Ref.$ Reference

$REFPROP$ Reference Fluid Thermodynamic and Transport Properties Database

$RH$ Relative humidity (%)

$RO$ Reverse osmosis

$RR$ Recovery Ratio (%)

$SCC$ Specific cooling capacity ($W/kg_{ad}$)

$SDWP$ Specific Daily Water Production ($kg_w/(kg_{sg}d)$)

$SEC$ Specific energy consumption ($kJ/kg_w$)

$SEM$ Scanning electron microscope

$Siogel$ Siogel silica gel (Oker Chemie)

$STC$ Specific Thermal Consumption ($kWh/m^3$)

$TBT$ Top brine temperature (°C)

$TC$ Thermocouple

$UniSim$ Process modelling software

# Chapter 1

# Introduction

Global warming, water scarcity and energy security are some of the world's major issues. It is widely recognized that a key role in solving these issues is a sustainable and efficient use of the planet's limited resources. However, energy is not used efficiently, with estimates showing that 72 % of the global primary energy produced is converted to waste heat (Fig. 1.1a) [1, 2]. Low-grade heat available from numerous sources such as industrial sites, power plants, geothermal areas or solar collectors [3, 4].

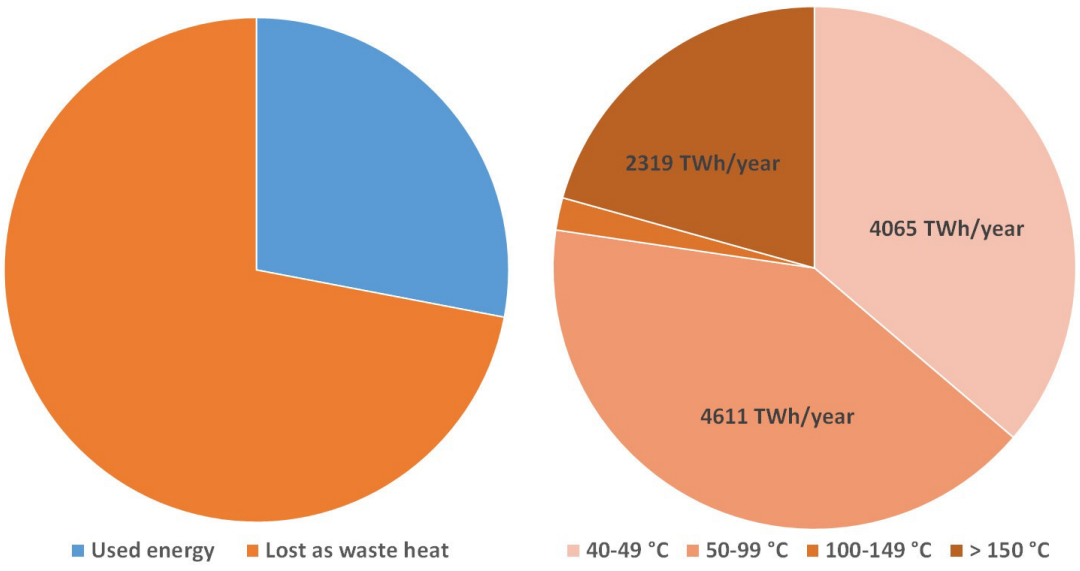


(a) (b)

Figure 1.1: (a) Global primary energy conversion (data from [1]).
(b) Waste heat is emitted at different temperatures (data for United States from [5]).

Papapetrou et al. analysed the availability of industrial waste heat in the EU and estimated the availability at 300 TWh per year excluding power plants and transportation [6]. They categorised waste heat at different temperature levels between ambient temperature up to 1000 °C, where the highest waste heat potential lies below 200 °C representing one third of the emitted waste heat. Rattner and Garimella eval-

uated the waste heat potential in the USA in a comprehensive study including power plants, transportation and manufacturing [5]. They found that 4000 TWh of waste heat are annually available from condensers of power plants in the temperature range from 40-49 °C. Another 4500 TWh per year are emitted at temperature levels between 50-99 °C. Both temperature ranges amount to a total of 78 % of the entire waste heat available below 100 °C (Fig. 1.1b).

Recently, the utilisation of low-grade heat has attracted much attention, but only few of the proposed systems are able to operate at temperatures below 100 °C. Lower waste heat temperatures increase the difficulty to use the heat for subsequent processes. Moreover, the cost of such systems increases with decreasing source temperatures, because they require larger heat exchanger surface areas due to a lower temperature difference available, often need to operate under vacuum or use toxic organic fluids like Organic Rankine Cycles.

Waste heat recovery systems for temperatures below 100 °C have been proposed for electricity generation (e.g. Organic Rankine Cycles [7] or heat engines [8, 9]), refrigeration (e.g. absorption [10], adsorption [11]) or thermal desalination [12] to mention a few of them. All of the above are commercially available, but with limited success as it is usually cheaper to use electricity for each application. For example, vapour compression refrigeration features performances more than six times higher than the thermally driven alternative [13]. In desalination, reverse osmosis processes (RO) are usually chosen, as they only require energy to overcome the osmotic pressure [14] instead of the latent heat of water for evaporation. Thus, electrically driven systems are usually considered advantageous compared to their thermally driven counterparts that are less energy efficient and more expensive at a first glance. However, electric systems require the conversion of additional primary energy into electricity, which emits $CO_2$ and contributes to global warming. Elimelech and Phillip report in a review that RO emits about 1.8 kg($CO_2$)/$m^3$(water) [15], e.g. a relatively small country like Spain has a projected desalination requirement of 1 billion $m^3$/year [15], which leads to $CO_2$ emissions of 1.8 million tons per year. Spain is a small country and by far not one of the driest [16].

Mekonnen and Hoekstra report that half a billion people around the world face water scarcity all year and four billion for at least one month each year, which is two-thirds the world population [16]. Providing two-thirds of the world population with RO-water would require vast amounts of electricity and emit hundreds of millions of tons of additional $CO_2$ each year with devastating consequences for global warming.

Ng et al. argue that waste heat from industrial processes is free of charge, because it would usually be disposed into the environment. Thus, the energy consumption of thermal desalination system can be reduced to their electricity consumption (e.g. pumps) and the thermal consumption can be neglected [17]. Brückner et al. share the opinion that waste heat is free of charge and compare absorption heat transformers to electrical heat transformers under this premise [18]. The assumption that waste heat is free of charge makes both systems more comparable to each other and they find that the thermally driven process can even be more economically attractive to certain users [18]. Ng et al. come to the same conclusion comparing different thermal desalination systems to reverse osmosis [17]. They report that in most cases thermally driven systems have a comparable or lower electricity consumption than RO [17]: RO ≈ 3-5 kWh/m$^3$, multi effect distillation ≈ 2 kWh/m$^3$, multi stage flash ≈ 2.5 kWh/m$^3$ and adsorption desalination ≈ 1.4 kWh/m$^3$ [17]. Thus, adsorption desalination *AD* has the lowest electricity consumption, because the system uses a minimum of pumps and moving parts [17]. On the other hand, AD has one of the highest thermal consumptions of approximately 850 kWh$_{th}$/m$^3$ and while this utility may be free of charge, a reduction would still lead to an increase of water output per waste heat source.

More research is needed on the improvement of the AD process to reduce the energy consumption and improve the adsorption material efficiency through novel concepts of heat integration and novel adsorption materials. All experimental adsorption desalinators are large in size > 10 kg$_{sg}$, where the best performing system uses 144 kg$_{sg}$ and was developed by the group of Prof. Ng [17]. The large size has the consequence that only commercial materials could be tested with silica gel as the predominant choice. Non-commercial materials are developed by chemistry labs, which can usually provide quantities at milligram scale. Hence, there is a need for smaller experimental systems to advance the process on the material side.
The integration of adsorption desalination into other processes is largely unexplored. Most notably, the group of Prof Ng proposed to integrate multi effect distillation and adsorption desalination [19]. By contrast, the combination of thermal desalination with membrane processes to generate electricity from waste heat has never been investigated for AD.

This work is carried out as part of the European Horizon 2020 funded RED Heat-to-Power project in collaboration with partners across Europe: Università degli Studi di Palermo (Italy), Universitat Politècnica de Catalunya (Spain), Plataforma Solar de Almería (Spain), REDstack BV (Netherlands), Fujifilm Manufacturing Europe BV (Netherlands), and WIP GmbH (Germany). The project aims to generate electricity from waste heat 40-100 °C using artificial saline solutions in a closed loop. The closed-loop connects a reverse electrodialysis membrane and a thermal separation step. The salt gradient is converted into electricity and restored in the thermal regeneration step.

This work contributes to the project by investigating adsorption desalination as one possible thermal separation system for the project. The analysis combines both modelling and experimental work arranged as follows:

- **Chapter 2**: Introducing the main topics in a literature review reporting important findings and providing background information for the development of the following research.

- **Chapter 3**: The thermodynamics of salts are important for all modelling activities within the project and were assessed within this work through experiments using a Barker's cell. The Barker's cell can measure saturation temperatures and pressures of aqueous salt solutions that can be used to fit the Pitzer model. The results of three novel acetate salts are presented here and are correlated with the Pitzer model to be used for desalination modelling.

- **Chapter 4**: Several desalination methods were investigated in simulations. Multi-effect distillation *MED* is the most efficient and one of the most established thermal desalination methods. A model was created in UniSim design software to study the process. Ng et al. proposed the combination of MED with AD to enhance the performance of MED. A thermodynamic, steady state model was implemented in Matlab to investigate the proposed system and the possibility for its application in the closed-loop. Moreover, absorption vapour compression *ABVC* was identified as another promising desalination possibility for the closed-loop. ABVC combines an adsorption chiller with an evaporation stage and thermally integrates the two. The system reuses the latent heat of evaporation multiple times within the system using a minimum of vessels and heat exchangers compared to MED. The performance of ABVC was evaluated in a UniSim model for different salts and concentrations.

- **Chapter 5**: An experimental adsorption desalination system was designed, built and tested as main part of this work. The design is a novelty as the system is downscaled by two orders of magnitude compared to systems in the literature. The system is characterised using silica gel through established performance indicators. In addition, a novel thermal response method and a novel cycle analysis gave deeper insight into the performance and process characteristics. An advantage of the small design is the possibility to test novel, non-commercial adsorption materials, which are not available in large quantities. Ionogels are a novel class of adsorption materials and an Ionogel was comprehensively tested in the test rig for the first time.

- **Chapter 6**: Combines the findings of the previous chapters to investigate AD and RED in a closed loop for the first time. The entire analysis of chapter 6 is novel,

because the adsorption reverse electrodialysis concept has not been proposed before. A thermodynamic model of the integrated system assesses energy and exergy efficiencies using different aqueous solutions of different salt types, salt concentrations, adsorption materials and regeneration temperatures. The thermodynamic investigation is extended to non-aqueous solutions. Ammonia features very high solubilities for certain salts, while having a latent heat of evaporation lower than water making it a promising non-aqueous candidate. ADRED using salt dissolved in liquid ammonia was investigated with the thermodynamic model. Moreover, a dynamic, lumped-parameter dynamic model was implemented and validated using experimental data from chapter 5 for regeneration temperatures 40-60 °C. The validated, dynamic AD model was linked to a validated RED model from the literature to calculate exergy and energy efficiencies . The results are scaled up in a case study for a large scale application of 700 MW waste heat input at 40 °C from a steam power plant. Finally, the Levelised Cost of Electricity are estimated for ADRED.

# Chapter 2

# Background

## 2.1 Adsorption

Porous solids of large internal surface areas can adsorb considerable volumes of vapour and gases [20]. The accumulation on the interface between solid and gas phase can take place through physical forces (physisorption) or through chemical bonds (chemisorption). Physisorption can be reversed by regeneration, whereas chemisorption is generally irreversible [21]. Adsorption processes are used for gas purification, e.g. air separation as an alternative to cryogenic processes. In addition, adsorption processes can also be applied to energy storage, desalination, air conditioning and refrigeration. The most important families of adsorption materials are activated carbons, molecular sieve zeolites, silica gel and activated alumina. All these adsorbents have pore sizes in the order of a few nanometer with varying pore size distributions. By contrast, zeolitic adsorbents have sharp pore size distribution as the micropores are determined by the crystal structure of the material [20]. A suitable adsorption material for a process is selected by stability, capacity and selectivity towards the adsorbate [20], where knowledge of sorption equilibrium is required first [21].

### 2.1.1 Materials and their suitability for water adsorption

#### Activated Carbons

Activated carbons are decomposed carbonaceous material thermally activated at 700-1100 °C by steam or supercritical carbon dioxide [20]. The pore size distribution depends on the conditions during the pyrolysis and activation processes [20]. Activated carbons are typically not suitable for water adsorption as the surfaces are essentially non-polar, but a slight polarity can be caused by surface oxidation [20].

#### Zeolites

Zeolites are porous, crystalline frameworks of $SiO_4$ and $AlO_4$ tetrahedra forming an open lattice into which molecules can penetrate [20]. Each aluminium atom adds a

negative charge to the framework, which is balanced by an exchangeable cation, which can be altered by ion exchange to adjust the adsorption properties [20]. In addition, the Si/Al ratio is always greater than 1.0 and has an impact on the water adsorption properties [20]. Aluminium rich zeolites have high water affinities that decrease with the Si content. The transition between hydrophilic to hydrophobic occurs at a Si/Al ≈ 8-10. Two commercial zeolites of particular interest for desalination are Mitsubishi AQSOA Z01 and Z02. AQSOA Z01 is an iron aluminophosphate zeolite with a pore diameter of 7.4 Å and AQSOA Z02 [22] is a silico aluminophosphate zeolite with a pore diameter of 3.7 Å [22]. Both materials exhibit S-shaped isotherms which can be classified as Type IV/V [23, 24]. Kayel et al. [23] found that AQSOA Z01 is particularly suitable for the application in water adsorption chillers operating at regeneration temperatures below 65 °C achieving a working capacity of about 0.2 g/g [22]. AQSOA Z02 features a higher working capacity than Z01 of about 0.3 g/g, but requires 80 °C for regeneration [22].

### Silica gels

The chemical composition of silica gel is $SiO_2 \cdot nH_2O$, a partially dehydrated form of polymeric colloidal silicic acid [20]. The water content of silica gel is usually around 5 wt.-% in the form of chemically bound hydroxyl groups [20]. The hydroxyl groups give the molecule a degree of polarity and the ability to form hydrogen bonds. This effect is why water, alcohols or amines adsorb to the surface in preference to non-polar molecules like saturated hydrocarbons [20]. The uptake curves for silica gel usually show a steady increase with increasing pressure, because of the wide pore size distribution [20].

### Metal Organic Frameworks

Metal organic frameworks *MOFs* are three dimensional networks of metal clusters linked with organic ligands [25]. MOFs are an emerging, recent class of adsorption materials attracting research interest [26] due to their high water adsorption capacities [27]. MOF materials feature ultra high porosities up to 6000 $m^2/g$, have tuneable pore sizes and surface properties [28]. The surfaces can be either hydrophilic or hydrophobic, where the frameworks are not always stable towards water as water molecules can displace ligand in the framework breaking the metal-ligand bond [26]. However, this can be prevented by using high valence metal ions like $Fe^{3+}$, $Cr^{3+}$ or $Zr^{4+}$ creating a rigid structure, which makes the metal sites less exposed to water intrusion [26]. For example, MIL-101(Cr) and MIL-101(Fe) can sustain water providing chemical stability for months and are suitable for water adsorption [26]. $NH_2$-MIL-125 is another promising material for adsorption heat transformation and heat storage using water as working fluid [29]. $NH_2$-MIL-125 features good hydrothermal stability and high system performances [27].

### Ionogels

Ionogels represent a novel class of hybrid materials, where a solid support structure is impregnated with ionic liquids *IL* while retaining the unique properties of the IL [30]. By definition, ionic liquids are organic salts with melting points below 100 °C featuring high ionic conductivity, negligible vapour pressure, thermal stability and non-flammability [30]. 1-Alkyl-3-methylimidazolium ionic liquids are reported as some of the most important and most investigated ionic liquids [31]. Seddon et al. showed that the solubility of water for Imidazolium salts depends on the anion, where the sorption capacity was best for the acetate anion [32]: $Ac^-$> $Cl^-$> $Br^-$>$NO_3^-$>$BF_4^-$>$PF_4^-$ [31, 32]. The cation type is reported to play a minor role with water solubility decreasing with the length of the alkyl group of the cation [31, 32]. Cuadrado-Prado et al. measured the sorption equilibria and kinetic data of several Imidazolium salts showing that long alkyl chains reduce the affinity to water [33]. Cao et al. discussed various sorption mechanisms that differentiate between the surface and volume [32]. They reported fast kinetics at the initial phase of water sorption slowing down at larger uptakes [32]. The precise mechanism remains unclear, but they proposed a scheme where fast surface sorption occurs first followed by slow diffusion into the bulk [32].
Silica supported ionic liquids maintain the water sorption properties of the pure ionic liquid at high loadings [34]. Askalany et al. measured the isotherms for different degrees of impregnations from 1.8 wt% to 60 wt% of 1-ethyl-3-methylimidazolium methanesulfonate in Syloid AL-1FP [34]. The sorption isotherm properties of the pure ionic liquid are maintained down to 17 wt%, while doubling the saturation uptake of the silica gel support structure. The highest impregnation of 60 wt% has the best adsorption properties exceeding the uptake of pure silica gel from RH > 50 %. The 60 wt% impregnation achieves about 60 % of the uptake of the pure ionic liquid, which is why it is important to reduce the amount of support material as much as possible. Horowitz and Panzer reported loadings of 80 wt% 1-ethyl-3-methylimidazolium bis(trifluoromethylsulfonyl)imide (EMIM TFSI) on a poly(dimethylsiloxane) functualised polymer structure (PDMS) forming a flexible, bendable rubber-like material [35]. They tested the stress resistance and ionic conductivity, but not water sorption properties [35]. The samples showed no IL leakage despite the open pore structure of PDMS and were stable when exposed to water [35].

### 2.1.2 Temperature swing regeneration

Adsorption processes can be categorised as cyclic batch processes and continuous countercurrent systems [20]. Countercurrent systems move the adsorbent between an adsorber and regenerator, while cyclic batch systems have a static adsorption bed, which is alternately adsorbing and regenerating [20]. The present work focuses on thermal swing cyclic batch processes, whereas cyclic batch adsorbers can also be regenerated using pressure swing, purge gas stripping or displacement desorption [20].

An example for a thermal swing system is an adsorption chiller as shown in Fig. 2.1. Similar systems employing silica gels in the adsorber have been around for almost 100 years [36]. The system consists of an evaporator, condenser and at least one adsorber. Each vessel is equipped with a heat exchanger, where the adsorber heat exchanger is packed with an adsorbent. The system is powered by alternatingly cooling the adsorber bed for adsorption and heating the bed for desorption. The evaporating water adsorbs on the adsorbent, where the evaporator provides cooling, which can be used for refrigeration or air conditioning. After adsorption, the bed is heated, water desorbs and condenses. The condensed water is recirculated to the evaporator, which enables unrestricted run times. A cyclic batch process as shown in Fig. 2.1 is intermittent, because the adsorption bed only adsorb or desorb. Two or more adsorbers are required for semi-continuous operation, where the evaporator provides constant cooling.

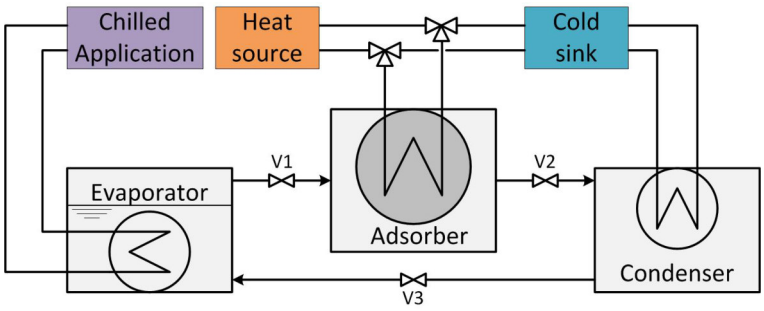


Figure 2.1: Scheme of a single bed adsorption chiller

The adsorber bed is powered by cyclic heating followed by cooling as shown on real experimental data in Fig. 2.2a, which corresponds to the adsorption cycle in the P,T-diagram in Fig. 2.2b.

During the desorption step, the cold, saturated bed is heated moving from points 1→2 in Fig. 2.2. At the same time, the bed is disconnected from the evaporator and condenser (isosteric heating) by closing V1 and V2 in Fig. 2.1. The pressure of the bed increases until it reaches the condenser pressure. The bed is then connected to the condenser by opening V2, while heating continues to move from 2→3. Water vapour desorbs from the silica gel and condenses on the cold surface of the condenser heat exchanger. Once the bed is regenerated (point 3), valves V1 and V2 are closed, while the bed is cooled to decrease the pressure again (isosteric cooling) to moves from 3→4. When the pressures of the adsorber bed and evaporator are equal (point 4), valve V1 between the two vessels is opened. As a result, the silica gel bed adsorbs water vapour from the evaporator 4→1, which is partially filled with water. A semi-continuous mode of the test rig is ensured by regenerating one bed, while the other bed adsorbs. Valve 3 is used to recirculate water from the condenser to the evaporator.

In Fig. 2.2b, the diagonal lines 1→2 and 3→4 represent the isosteres where the water uptake of the material remains constant. The distance between the rich isostere $q_{high}$ 1→2 and lean isostere $q_{low}$ 3→4 depicts the working capacity $\Delta$q of the material. The

working capacity can be maximised when shifted $q_{high}$ towards the saturation curve by increasing $P_{evap}$.

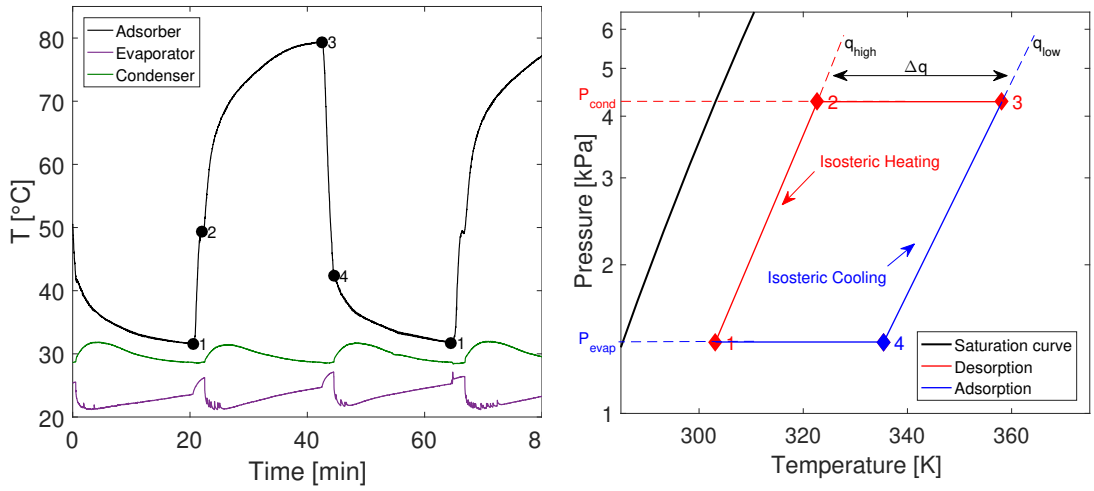


(a) (b)

Figure 2.2: Cyclic heating and cooling powers the adsorption process. (a) Experimental temperature curves from this study using silica gel to explain the thermodynamic adsorption cycle in (b): 1→2 isosteric heating, 2→3 adsorption with continued heating, 3→4 isosteric cooling, 4→1 desorption with continued heating.

While silica-gel/water is one of the most commonly used, non-toxic working pairs, there are many other possibilities where the choice of material and fluid enables different process designs as well [37]:

- *Activated carbon - methanol/ethanol [38]:* Methanol has a lower freezing point than water. Hence, the evaporator operates at lower temperatures compared to water. The vapour pressures are higher than water $P_{sat}(20\ °C) = 13$ kPa, but the system still operates under vacuum [39]. Temperatures $> 60$ °C are usually needed to regenerate this working pair and uptake capacities are up to 0.5 g/g [38]. Ethanol is less toxic than methanol and can replace it as experimentally proven by Frazzica et al. [40].

- *Activated carbon - ammonia [41]*: Ammonia can also provide cooling at lower temperatures than water. The system is pressurised as $P_{sat}(20\ °C) = 857$ kPa [39], but systems need to be regenerated at more than 100 °C for optimal performance [42].

- *Zeolite - water:* Zeolites feature high adsorption uptakes and tuneable properties, but conventional zeolites have a high affinity towards water resulting in high desorption temperatures $> 200$ °C [43]. In order to overcome this issue, AlPO and SAPO zeolites were developed. Bauer et al. investigated AlPO zeolite - water as working pair, where $[AlO_4]^-$ and $[PO_4]^+$ tetrahedrons are altered [43].

Introducing silicon atoms into the AlPO framework forms SAPO materials [43]. Both types of zeolites have S-shaped water isotherms, which are favourable for refrigeration applications, because they allow large uptakes even at lower relative humidity with regeneration temperature for both zeolites below 100 °C [43].

## 2.2 Adsorption desalination

### 2.2.1 Performance Analysis

Performance indicators are a useful tool to compare systems between each other at a glance. Each desalination method has its own performance indicators, but some can be applied universally like the Performance Ratio. The following performance indicators are most commonly used to describe and characterise adsorption desalination systems.

#### Reduced Temperature

The performance indicators depend on the three inlet temperatures to evaporator, condenser and adsorber/desorber. Experimental analyses usually keep two inlet temperatures constant and change the third. However, this complicates the analysis as different results cannot easily be compared. Nuñez et al. addressed this issue by introducing the reduced temperature $T_{red}$ [-], which takes the different temperatures into account in a single parameter [44].

$$T_{red} = \frac{T_{cond} - T_{evap}}{T_{hot} - T_{cond}} \tag{2.1}$$

$T_{evap}$, $T_{cond}$ and $T_{hot}$ are the inlet temperatures [K] to the heat exchangers of the vessels from the chilled application, cold sink and heat source.
The inlet temperatures from the three thermostatic baths have a significant impact on the system performance and there are hundreds of possible combinations. $T_{red}$ is a function of all three inlet temperatures and represents the ratio of the temperature lift to the driving force [44]. $T_{red}$ simplifies the comparison of different inlet temperatures since many performance indicators collapse on one single curve if plotted against $T_{red}$. This occurrence makes $T_{red}$ a useful tool in the prediction of results and the system characterisation.
A single-purpose desalinator is operated at $T_{red} = 0$, where no temperature lift for cooling is desired. Whereas, $T_{red}$ increases depending on the cooling application [45], i.e. in air-conditioning $T_{red} < 0.3$ or in refrigeration $T_{red} > 0.3$.

### Performance indicators for adsorption desalination and cooling

The main performance indicators for adsorption desalination are the Performance Ratio *PR* [-] and Specific Daily Water Production *SDWP* [$kg_w/(kg_w d)$]:

$$PR = \int_0^{t_{cycle}} \frac{\dot{m}_{water} \cdot L_w}{\dot{Q}_{des}} dt \tag{2.2}$$

$$SDWP = N_d \int_0^{t_{cycle}} \frac{\dot{Q}_{cond}}{L \cdot M_{sg}} dt \tag{2.3}$$

Where L is the latent heat [kJ/kg], $M_{sg}$ is the mass of silica gel in each bed [kg], $N_d$ is the number of cycles per day, t is the time [s] and $\dot{Q}$ are the heat flows [kJ/s] provided to desorber $\dot{Q}_{des}$, evaporator $\dot{Q}_{evap}$ and condenser $\dot{Q}_{cond}$.
The PR stands for the energy efficiency of the process and can be used in adsorption desalination as well as other thermal desalination methods. The specific daily water production SDWP examines the performance within one day including many cycles N [-], while not providing any information on the energy input into the adsorbers. The SDWP depicts a trade-off between the cycle time and the number of cycles within one day. Longer cycles lead to a larger working capacity of the material, but at the same time, the number of cycles per day is reduced. The SDWP peaks at medium cycle times. Whereas, the PR increases with the cycle time. Hence, the combination of all indicators leads to a more comprehensive picture of the system performance.
Adsorption chilling is characterised by the Coefficient of Performance *COP* [-] and the specific cooling capacity *SCC* [$W/kg_{sg}$]:

$$COP = \int_0^{t_{cycle}} \frac{\dot{Q}_{evap}}{\dot{Q}_{des}} dt \tag{2.4}$$

$$SCC = \int_0^{t_{cycle}} \frac{\dot{Q}_{evap}}{M_{sg}} dt \tag{2.5}$$

### 2.2.2 Materials and performances on a system level

Table 2.1 provides an overview of the performances for different materials in adsorption desalination.

Thu et al. (2017) represent the latest investigation from a large number of experimental work conducted with the same four-bed adsorption desalinator, which is the largest and best performing system in the literature [17, 46–52]. The four-bed adsorption prototype contains 36 kg of silica gel in each bed [52] and was improved and modified over the time. Wang et al. (2005) presented the addition of a heat recovery system between the adsorber beds increasing the energy efficiency of the four-bed system by 25 % [50]. Thu et al. (2011) reported further heat integration between evaporator and condenser

of the system leading to an SDWP = 13.5 $m^3_w/(ton_{sg}d)$ at 85 °C and PR = 0.75 [51]. In the same study they also reported SDWP = 14.2 $m^3_w/(ton_{sg}d)$ at 85 °C [51], which is the highest value reported for silica gel today. Ng et al. (2013) provided a comprehensive summary of adsorption desalination in general and of all results accomplished with their four-bed system until then [17].

In the latest study, Thu et al. (2017) present an updated analysis for the four-bed system with an internal heat integration scheme first presented in Thu et al. (2011) [51, 52]. Each of the four beds is filled with 36 kg of mesoporous silica gel type A++ [52]. The study investigates low temperature regeneration 50 - 70 °C with a full cycle time between 720 s and 1920 s at $T_{cond,in}$ = 27.6 °C. The PR increases with the cycle time from 0.54 to 0.79 [52]. The SDWP at the lowest regeneration temperature 50 °C is reduced to SDWP = 5.5 $m^3_w/(ton_{ad}d)$.

Table 2.1: Recent studies on adsorption materials for adsorption desalination. Simulations are reported if no experimental data is available for the material

| **Author** | **Year** | **Material** | **Product** | **Type** | **SDWP** $[m^3/(t{\cdot}d)]$ | **Ref.** |
|---|---|---|---|---|---|---|
| Thu et al. | 2017 | Silica gel | Type A++ | Exp. | 14.2 | [52] |
| Mitra et al. | 2017 | Silica gel | RD | Exp. | 0.9 | [53] |
| Wu et al. | 2014 | Silica gel | RD | Sim.(+Exp) | 1.1 | [54] |
| Alsaman et al. | 2017 | Silica gel | blue | Exp. | 4.2 | [55] |
| Youssef et al. | 2017 | MOF | CPO27-Ni | Exp. | 12 | [56] |
| Elsayed et al. | 2017 | MOF | MIL-101Cr & Al-Fumarate | Sim. | 6 & 10 | [57] |
| Youssef et al. | 2015 | Zeolite | SAPO-34 | Sim. | 7 | [58] |
| Ali et al. | 2018 | Salt | $CuSO_4$ | Sim. | 8.2 | [59] |

Mitra et al. built a two stage adsorption desalinator using four adsorption beds combining desalination and cooling [60]. The two stage system is based on an adsorption chiller of Saha et al. [61]. Each of the two stages comprises two adsorbers and the two stages are connected to each other in series [53]. The system operates the following: Water evaporates, adsorbs on the first adsober stage, desorbs from the first adsorber stage, adsorbs on the second adsorber stage, desorbs from the second adsorber stage and condenses in the condenser [53]. The authors report that the second stage allows improved working capacities for chillers using low temperature heat sources in combination with air-cooled condensers that have high condenser and cooling water temperatures [61].

The adsorber beds are in a shell and tube design filled with Fuji Silisya silica gel type RD on the tube side. A stainless steel mesh housing is wrapped around the silica gel to ascertain a 5 mm gap between adsorption material and shell wall. The first stage contains 5.6 kg of adsorption material each, whereas the second stage contains 3.2 kg each as it is reported to operate at larger working capacities than the first. The condenser is

air-cooled and the evaporator heat exchanger is connected to a constant temperature bath. The temperature levels inside the system are $T_{evap}$= 11-24 °C, $T_{cond}$ = 36 °C and $T_{hot}$ = 65-80 °C. The system was tested for full cycle times of 1200 s to 7200 s achieving SDWP < 1 $m^3_w/(ton_{ad}d)$ [53]. The SDWP remains relatively constant over the entire time of 7200 s indicating that the adsorption material is not saturated with water after 7200 s [53]. The reason appears to be the shell tube heat exchanger design leading to heat transfer limitations throughout the bed.

Wu et al. presented a one-bed experimental adsorption desalinator [62] and validated the results against a dynamic model taking radial heat and mass transfer gradients along the bed into account [54]. Usually adsorption systems are modelled with a lumped parameter dynamic model assuming a uniform temperature and water distribution within the bed. The cylindrical adsorption bed features an empty middle tube through the entire bed connecting it to evaporator and condenser. Like Mitra et al. [53], the bed is filled as bulk between the thermal jacket on the outside and vapour tube in the centre of the bed [54]. The adsorption bed contains 2.14 kg of Fuji silica gel type RD and is tested for cycle times from 4000 s to 100,000 s, which is less than one cycle per day and by far the longest cycle time tested. The experiments as well as the simulations to optimise the cycle time are performed at $T_{evap}$ = $T_{cond}$ = 20 °C and $T_{hot}$ = 80 °C. The study reports the optimal cycle time at 22,000 seconds achieving a maximum SDWP = 1.1 $m^3_w/(ton_{ad}d)$.

Both bulk adsorption bed systems of Mitra et al. [60] and Wu et al. [54] show poor performances SDWP ≈ 1 $m^3_w/(ton_{ad}d)$, whereas finned tube heat exchanger can increase the performance by one order of magnitude.

Alsaman et al. introduced a two-bed adsorption desalinator powered by a solar collector where they used 13.5 kg of a low-cost silica gel split between the two beds [55]. The solar collector provides hot water at 85 °C to the adsorption beds. The evaporator is designed as a shell and helical coil, the condenser as a tube in tube heat exchanger, and the adsorber bed consists of a fin tube heat exchanger inserted into a cylindrical casing [55]. The adsorber heat exchanger has a metal mass of 3.7 kg holding 6.75 kg of silica gel leading to a metal to adsorbent ratio of 0.55. The system was tested for a full cycle time of 1300 s, while $T_{cond,in}$ = $T_{evap,in}$ = 30 °C and $T_{hot,in}$ = 76-92 °C for all experiments. These parameters let to a maximum SDWP = 4.15 $m^3_w/(ton_{ad}d)$ at $T_{hot,in}$ = 92 °C and PR = 0.45.
The low SDWP is caused by a low evaporator temperature and heat transfer limitations in the evaporator. The evaporator pressure is below 2 kPa suggesting $T_{evap,vap}$ ≈ 15 °C despite $T_{evap,in}$ = 30 °C. The condenser pressure ranges 4-5 kPa, which is close to the saturation pressure of water at $T_{cond,in}$ = 30 °C with $P_{sat,w}$(30 °C) = 4.2 kPa [39]. The reduced evaporator pressure leads to a reduced working capacity of the silica gel. In

addition, the solar collector area of 4.5 $m^2$ is insufficient to power the process as the hot water inlet temperature decreases over time.

Youssef et al. presented a one-bed adsorption desalinator and tested 0.67 kg of CPO-27Ni metal organic framework. The material is placed on a heat exchanger of 29.3 kg leading to a very high metal to adsorbent weight ratio of 44. The heat exchangers are in a rectangular finned tube design combining copper tubes with aluminium fins having a 1 mm fin pitch [56]. The MOF material is packed between the fins and secured with a fine stainless steel mesh. They tested the material for full cycle times between 960 s to 2160 s [56]. A heat source temperature of 95 °C was used for all experiments, while the adsorber bed was cooled to 15 °C using cooling water from the mains water line for all experiments [56]. In addition, the evaporator and condenser temperature were varied 10-40 °C and 5-30 °C respectively [56]. Thus, the system is operated using four temperature levels. The low adsorption temperature increases the temperature difference between adsorption and desorption, which maximises the adsorption uptake. The combination of evaporator temperatures up to 40 °C and the adsorber bed temperature of 15 °C can lead to condensation of water on the aluminium fins of the adsorber bed. Thus, the reported maximum SDWP of up to 23 $m^3_w/(ton_{ad}d)$ needs to be treated with caution, because they may be caused by vacuum distillation rather than adsorption. A more practical temperature combination of $T_{evap}$ = 20 °C, $T_{cond} \approx T_{ads}$ = 15 °C and $T_{hot}$ = 95 °C leads to a maximum SDWP between 10 and 12 $m^3_w/(ton_{ad}d)$ [56]. The PR was not reported, but can be assumed to be very low due to the high metal to adsorbent weight ratio.

Elsayed et al. extended the metal organic frameworks for adsorption desalination analysis from CPO-27Ni to aluminium fumarate, another commercially available MOF, and MIL-101Cr, which can currently only be synthesised in laboratories [57]. The adsorption isotherms were measured using a dynamic vapour sorption gravimetric balance showing that the two commercially available materials have improved water saturation uptakes compared to silica. Aluminium fumarate can adsorb 0.53 $g_w/g_{ads}$ and CPO-27Ni saturates at 0.47 $g_w/g_{ads}$. The non-commercially available MIL-101Cr material has a saturation uptake of 1.47 $g_w/g_{ads}$. In addition, the study provides isotherm fitting data based on a set of polynomial equations and estimated linear driving force parameters. The isotherm data was used to predict the SDWP in a lumped parameter dynamic model for a cooling+desalination application and a sole desalination application. The results show that all three materials are not suitable for cooling+desalination with $T_{evap}$ = 5 °C and $T_{cond}$ = 25 °C as SDWP(70-150 °C) = 2.5 $m^3_w/(ton_{ad}d)$ for aluminium fumarate. For the same evaporator and condenser conditions, CPO-27Ni requires $T_{hot}$ > 90 °C with 1.5 < SDWP(90-150 °C) < 4.5 $m^3_w/(ton_{ad}d)$. Thus, both results are similar to silica gel, while silica gel can be regenerated at $T_{hot}$ = 80 °C [57]. In addition, they tested desalination conditions with $T_{evap}$ = 20 °C and $T_{cond}$ = 25 °C.

Aluminium fumarate shows a constant SDWP(70-150 °C) = 6 $m^3_w/(ton_{ad}d)$. For the same conditions, the results of CPO-27Ni are SDWP < 4.5 $m^3_w/(ton_{ad}d)$, which is 6 times less than the experimental results reported by Youssef et al. for the same material [56]. Youssef et al. used a very unconventional set of temperature combinations with a low adsorber temperature (15 °C) and high evaporator temperature (up to 40 °C), whereas Elsayed et al. applied realistic temperatures to the model. The large deviation between Elsayed et al. and Youssef et al. is another indication for condensation on the adsorber heat exchanger in Youssef et al. [56]. The results of the novel, non-commercial MIL-101Cr for $T_{evap}$ = 20 °C and $T_{cond}$ = 25 °C are SDWP(70 °C) = 4.5 $m^3_w/(ton_{ad}d)$ and increase until they reach SDWP(150 °C) = 11 $m^3_w/(ton_{ad}d)$ [57]. Hence, MIL-101Cr is the most promising MOF material, but requires high regeneration temperatures $T_{hot}$ > 110 °C for high performance.

Youssef et al. simulated the performance of AQSOA Z02, which is also known as SAPO-34 [58]. They validated their model for silica gel against experimental data obtained by Thu et al. [63]. They measured isotherms and kinetic data of SAPO-34 both in a Dynamic vapour sorption *DVS* device and applied them to their model. The SDWP results of SAPO-34 for $T_{hot}$ = 65 °C and $T_{hot}$ = 75 °C are 1 and 3 $m^3_w/(ton_{ad}d)$ respectively, but at $T_{hot}$ = 85 °C the performance increased to SDWP = 7 $m^3_w/(ton_{ad}d)$ [58]. The SDWP was calculated for each $T_{hot}$ step and different $T_{evap}$ and compared to silica gel. SAPO-34 achieves a constant SDWP for each $T_{hot}$ regardless of $T_{evap}$, whereas the SDWP of silica gel increases with $T_{evap}$. Therefore, SAPO-34 appears to be an excellent material for cooling in combination with desalination. By contrast, silica gel should not be used for combined cooling and desalination as the SDWP decreases with $T_{evap}$. The combined application of cooling and desalination was suggested in many publications, but mostly with silica gel [17, 52, 55, 60].

Ali et al. proposed anhydrous copper sulfate as an adsorbent in adsorption desalination. They measured the adsorption isotherms and kinetics in a self-designed volumetric system consisting of a dosing tank, an adsorption chamber and an evaporator. The system measures pressures and temperatures for each vessel and an unspecified sample mass [59]. Water uptake data is provided for 25, 35, 45, and 55 °C, which is fitted to the DA-isotherm equation and LDF constants are provided. The saturation uptake of $CuSO_4$ is reported at 0.51 $g_w/g_{ad}$. The lumped parameter dynamic model fitted to silica gel results in their previous study [55] was used to determine the performance of copper sulfate in a simulation. The SDWP was simulated for different cycle times and regeneration temperatures $T_{hot,in}$ = 55-95 °C at constant $T_{evap}$ = $T_{cond}$ = 25 °C. The results show that $T_{hot}$ > 70 °C to achieve the maximum performance of SDWP = 8 $m^3_w/(ton_{ad}d)$ [59]. Moreover, the simulation proposes short half cycle times of 400 s for SDWP = 8 $m^3_w/(ton_{ad}d)$ indicating that the actual working capacity is well below 0.51 $g_w/g_{ad}$.

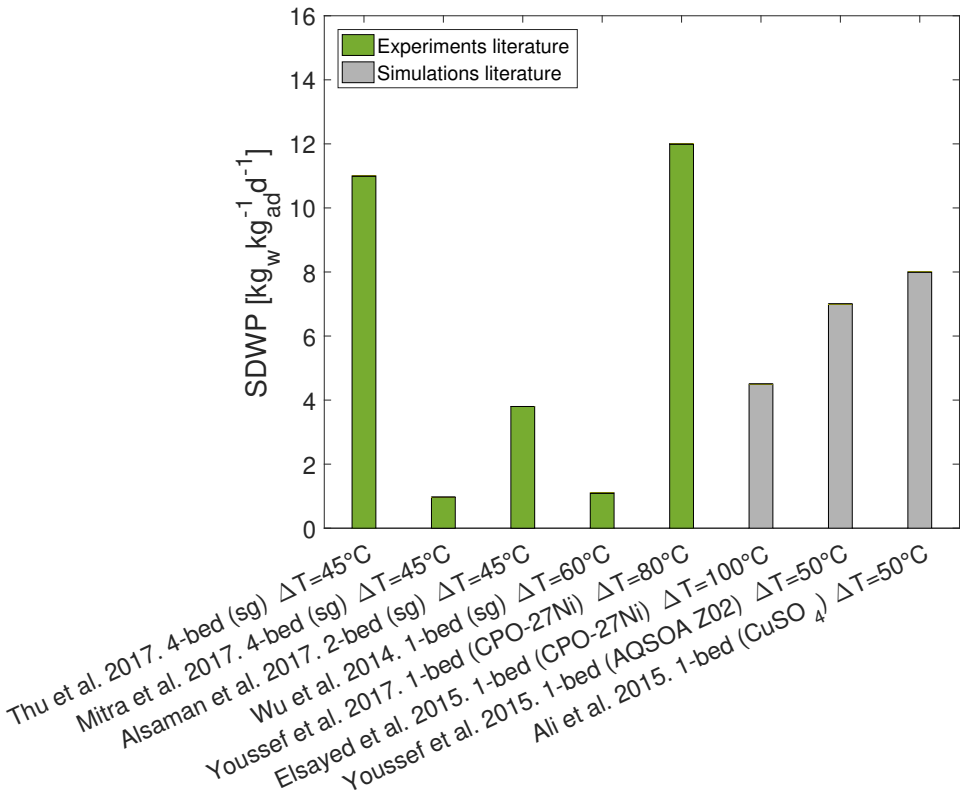


Figure 2.3: Comparison of different SDWP of experimental studies and simulations across the literature [52–55, 57–59]. $\Delta T = T_{hot} - T_{cond}$. $T_{red} = 0$ for all cases. sg = silica gel

## 2.3 Other thermal desalination methods

Desalination technologies can be distinguished between thermal and membrane processes. Currently, the market is dominated by membrane processes like reverse osmosis (RO) as shown in Fig 2.4. Jones et al. report that early desalination plants were dominated by thermal systems built in the Middle East, but membrane improvements past the 1980s let to an exponential increase of reverse osmosis systems. In 2000, thermally driven systems were still dominating the market with MSF providing 54 % of the total capacity [64]. Today, the proportions have shifted significantly towards membrane-based processes. By number of plants, RO has a share of 85 %, while its share is reduced to 69 % by fresh water production capacity [65]. By contrast, Fig. 2.4 shows that multi stage flash (MSF) has only 2 % share in terms of numbers, but 18 % in terms of capacity making MSF the most important thermally driven process.

Thermal desalination systems require a phase change of water, whereas reverse osmosis needs to overcome the osmotic pressure, which is significantly lower than the latent heat of water. Reverse osmosis is driven by electric energy, whereas thermal systems

require predominantly thermal energy usually from waste heat, but less electricity than membrane processes. The energy consumptions of commercial desalination systems is listed in table 2.2.

Table 2.2: Thermal and electric energy consumptions of commercial desalination technologies.

| System | Heat source [°C] | Thermal energy [$kWh_{th}/m^3$] | Electricity [$kWh_{el}/m^3$] | Ref. |
|---|---|---|---|---|
| MED | 70 | 40-65 | 2-2.5 | [66] |
| MSF | 90-110 | 53-70 | 2.5-5 | [66] |
| MD | 60-90 | 100-1600 | 2.2-24 | [66–68] |
| RO | Ambient | - | 2-6 | [15, 66, 69] |

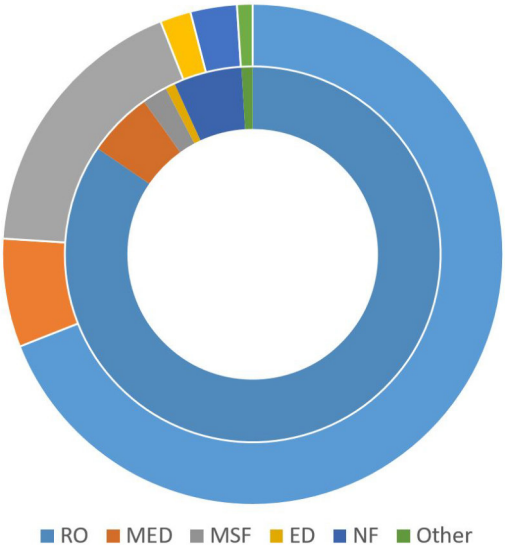


Figure 2.4: The market share of commercial desalination systems by capacity (outer chart) and number of systems (inner chart) reported by Jones et al. (2018) [65]. RO: Reverse osmosis. MED: Multi effect distillation. ED: Electrodialysis. MSF: Multi stage flash. NF: Nanofiltration.

### 2.3.1 Multi Effect Distillation

Multi effect distillation (MED) represents one of the oldest processes in desalination with patents existing since 1840 [70]. MED plants have a lower commercial market share than multi-stage flash (MSF) desalination plants or reverse osmosis (RO) plants. MED plants consist of a number of evaporator effects and a final condenser as shown in Fig. 2.5. The condenser helps to preheat the feed water while it condenses the vapour coming from the last effect. Each effect features a heat exchanger, called preheater. The feed passes through each one of the preheaters in a countercurrent to the distillate, brine and vapour in each effect. The feed is heated in each preheater until it reaches the first effect, which has the highest temperature of the effects. In addition to the

preheater each effect consists of another heat exchanger (tube bundle), spray nozzles, a demister and a flash box.

### First Effect

The preheated feed is sprayed through the spray nozzles onto the tube bundle. Inside the tube bundle, saturated steam transfers its latent heat into the system and leaves the tube bundle as saturated liquid. The first effect is the only effect in the MED plant, which is powered by an external heat source.
A fraction of the feed water evaporates on the tube bundle while the rest of the feed remains as a liquid brine on the bottom of the effect. The brine and the vapour are in vapour-liquid equilibrium at the same temperature and pressure. The water vapour goes through the demister and past the preheater to the next effect. Part of it condenses on the preheater, where the latent heat of the condensed vapour is used to increase the temperature of the feed by a few degrees. The condensate is collected and brought to the flash box of the effect. The rest of the vapour flows into the tube bundle of the second effect to be condensed. [71]

### Effects n-1

The brine from the first effect is sprayed over the tube bundle of the second effect. The first effect operates at a higher temperature and higher pressure than the second effect. Hence, a pressure drop occurs when the feed enters the second effect and a portion of the brine forms vapour in a flash evaporation. The tube bundle is fed with the saturated vapour from the first effect. The saturated vapour transfers its latent heat onto the outside of the tube bundle and the stream leaves the tube bundle as saturated liquid distillate and flows to the flash box.
Again, a part of the brine evaporates on the surface of the tube bundle. The vapour originating from the boiling and flash evaporation goes through a demister again and transfers a fraction of its latent heat to the feed in the preheater before it enters the tube bundle of the third effect.
This principle continues in the subsequent effects. The vapour from the previous effect is used or "recycled" to evaporate more brine in each effect generating more distillate with the same energy input in the first effect. This is possible, because each effect operates at a lower pressure and temperature than the previous effect.
Each additional effect increases the performance ratio of the MED plant, which is why a large number of effects is desirable for the thermal energy performance of the process. The system is limited by the ambient temperature, because the vapour from the last effect has to be condensed with a cooling source at ambient temperature. More limitations are the increasing salt concentration and the boiling point elevation.

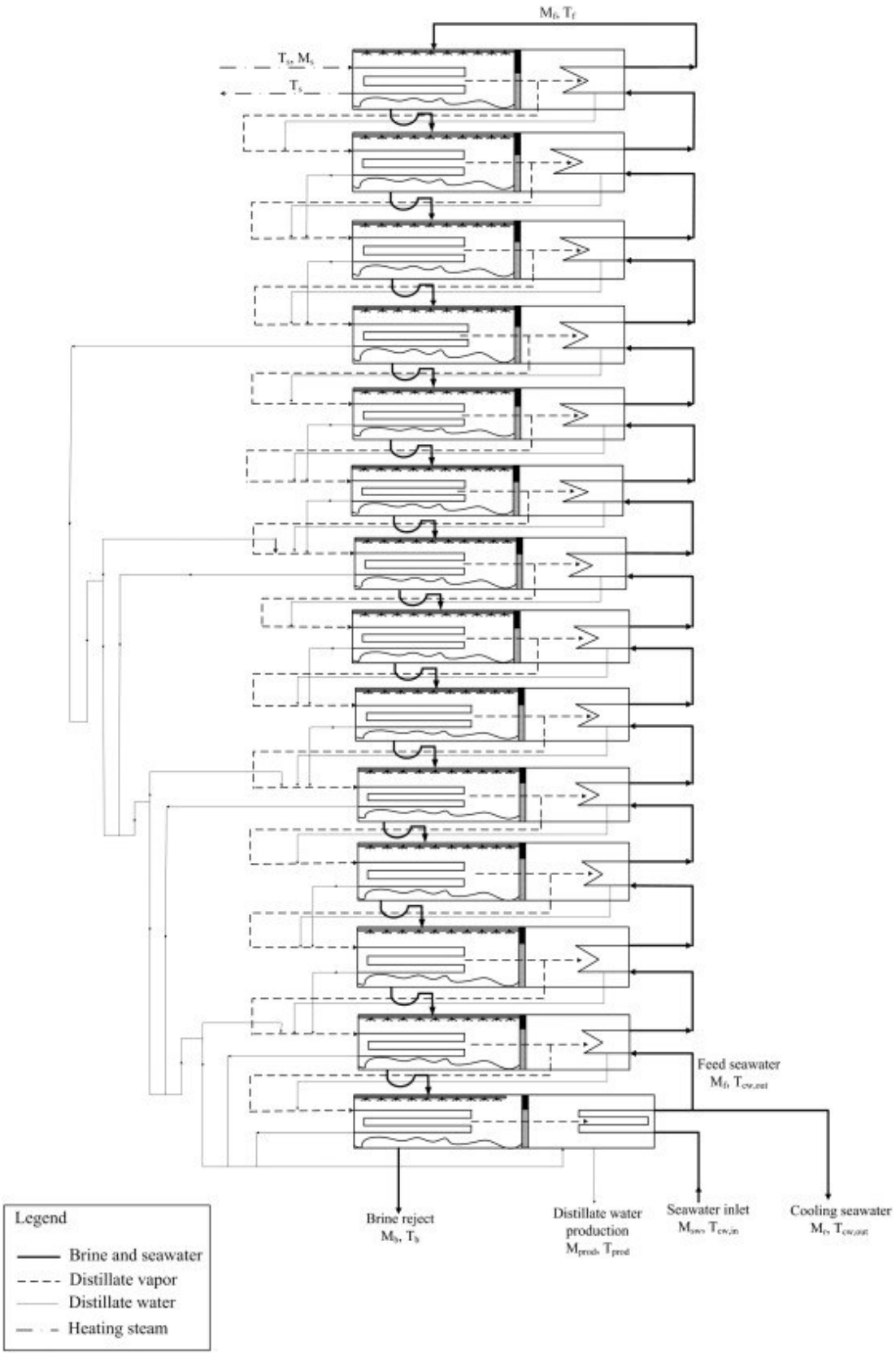


Figure 2.5: Multi effect distillation system at Centro de Investigaciones Energéticas, Medioambientales y Tecnológicas - Plataforma Solar de Almería (CIEMAT-PSA) with 14 effects ([72] with permission)

### 2.3.2 Multi Effect Distillation and Adsorption

Multi effect distillation can be coupled with adsorption desalination to increase the distillate output [73]. Multi effect distillation operates between the heat source temperature and ambient temperature. By contrast, the addition of an adsorption heat pump enables the last MED stage to operate as low the freezing temperature of water as it was suggested by Ng et al. [74] and is shown in Fig. 2.6. The larger temperature window allows the increase of the number of effects. Ng et al. reported a doubled distillate production based on their modelling and experimental work [74], while Shazhad et al. documented a threefold increase of the distillate production [19].

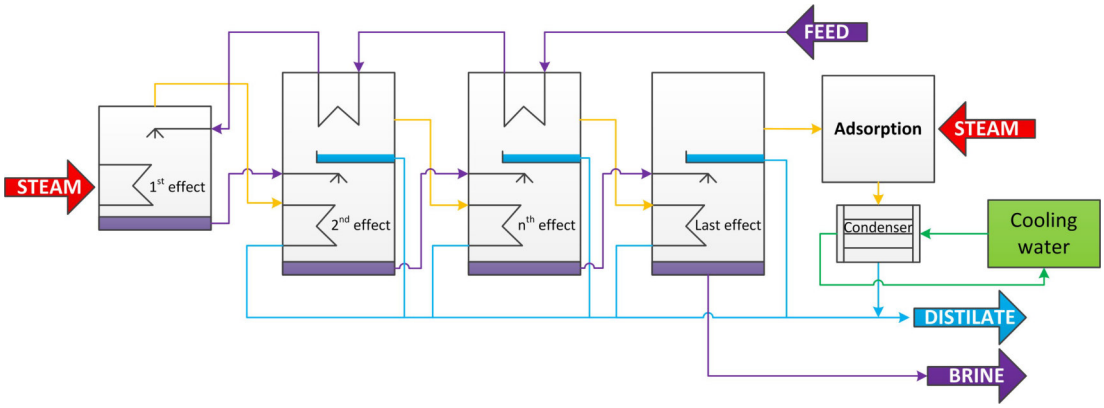


Figure 2.6: MED enhanced with adsorption desalination as suggested by Ng et al. [74]

### 2.3.3 Multi stage flash

Multi stage flash *MSF* is similar to MED, but does not feature tube bundles for evaporation in the effects [64]. Instead, water is flash evaporated within the liquid phase of each effect [64]. The vapour is used to preheat the feed stream by transferring all the latent heat, while condensing on the preheater surface. The advantage of MSF over MED is its reduced scaling due to the lack of evaporating tubes and spray nozzles [64]. Salt scale on the tube surface has a reduced thermal conductivity resulting in a reduced overall performance and frequent maintenance [64].

### 2.3.4 Membrane distillation

Membrane distillation *MD* uses hydrophobic membranes that represent a barrier to the liquid phase, while water vapour can pass through the pores. The separation is driven by a temperature difference causing a pressure gradient through the membrane. Thus, a phase change occurs here as opposed to other membrane separation processes where a static pressure forces a part of the feed to permeate through the membrane [75]. The membranes have a thickness of 30 to 200 µm and pore diameters of 100 nm to 1 µm [75]. The drawbacks of MD are a sensitivity of the permeate flux to the feed salt concentration and temperature, which cause polarisation on the membrane limiting

mass transfer [75]. Multi stage membrane distillation systems help to overcome the polarisation issue allowing the membrane to operate at higher salinities [76].
Dow et al. powered a MD pilot system using waste heat from a power plant at 33 °C, where their experimental apparatus achieved a permeate flux of 2.7 L/($m^2$h). Higher heat source temperatures of 59 °C increase the permeate flux to 11 L/($m^2$h) with STEC ≈ 1500 kWh/$m^3$ [68]. The tested feed water salinity was between 1.7 - 4 g/L, which is one order of magnitude below seawater at 35 g/L [77].

## 2.4 Electricity generation from low grade heat

More than two thirds of all primary energy are converted into waste heat with 63 % of this waste heat stream arising below 100 °C [1]. These vast quantities of waste heat are leading to economic loss as someone paid for the lost energy. In addition, all the waste heat is emitted into the environment, into rivers, oceans and the atmosphere causing thermal pollution.

A challenge of all low-grade heat processes is the low exergy content. Exergy describes the useful content of energy between ambient temperature and the heat source temperature. The same energy flow at a lower temperature provides less exergy for the process making it more difficult to utilise. The Carnot factor $\eta_c$ [-] describes the theoretically highest possible efficiency that can be achieved at a given ambient and hot temperature ($T_{amb}$ and $T_{hot}$ [K]) [78]:

$$\eta_c = 1 - \frac{T_{amb}}{T_{hot}} \tag{2.6}$$

The maximum energy efficiency a system can achieve at $T_{amb}$ = 20 °C and $T_{hot}$ = 25 °C is 3 %. An increase of the hot temperature to 100 °C increases the maximum energy efficiency to 21 %. Thus, the energy efficiencies of all low grade heat processes cannot be very high. The energy efficiency divided by the Carnot factor provides the exergy efficiency, which is a useful indicator for low grade heat processes as it tells how much of the available exergy is used.
Different processes have been developed to convert heat to power and some of the most common processes are listed 2.3. The processes can convert heat at different temperatures into waste heat. Most processes in table 2.3 convert heat above 300 °C, but cannot be applied to low grade heat sources. The following sections will present low grade heat conversion processes applicable to source temperatures below 100 °C.

Table 2.3: Common heat to electric power conversion processes

| **Process** | **T [°C]** | $\eta_{el}$ [%] | **Description** | **Ref.** |
|---|---|---|---|---|
| Steam Rankine Cycle | 300-550 | 42 | Water as working fluid is superheated in a boiler and expanded in a turbine to generate electricity | [79–81] |
| Organic Rankine Cycle | 80-300 | 24 | Same process as the steam rankine cycle, but water is replaced by an organic working fluid with lower boiling temperature enabling heat sources with lower temperatures | [7, 81] |
| Stirling Engine | 120-900 | 25 | Cyclic expansion and compression of a working fluid (helium) driven by a temperature gradient | [8, 82, 83] |
| Thermoelectric Generation | >350 | 5 | A junction of two materials with different conductivities converts heat directly into electricity | [84–86] |
| Osmotic Heat Engine | 50-100 | 2.5 | Water is transported from fresh water to brine through a membrane, which increases the brine pressure first, which is converted into electricity by a turbine. The salt gradient is restored by thermal desalination. | [87, 88] |
| Reverse Electrodialysis Heat Engine | 50-100 | 2.5 | Ion exchange membranes enable the controlled mixing of two saline solutions to convert the concentration gradient directly into electricity | [8, 89] |

### 2.4.1 Organic Rankine Cycle

Organic Rankine Cycle *ORC* systems resemble the steam Rankine cycle replacing water with an organic fluid that has a lower boiling point [90]. ORC are a common, established way to convert low grade waste heat into electricity using an organic fluid with a lower boiling point than water in the traditional Rankine cycle. Most systems are driven by heat source temperatures 100-350 °C [91], but Kang reported an experimental system powered by waste heat source temperatures around 80 °C and ambient temperature of 20 °C achieving energy efficiencies of 8 % [90] corresponding to an exergy efficiency of 47 %.

A scheme of an ORC system is given in Fig. 2.7, where a pump pressurises the organic working fluid. The evaporator uses waste heat to transform the working fluid into a saturated or superheated vapour, which is then expanded to produce mechanical energy for a generator producing electricity [91]. The saturated vapour from the expander is condensed and returned to the pump [91].

Many ORC systems are commercially available with system sizes from 50 kW at $T_{hot}$ ≥ 93 °C up to 70 MW at $T_{hot}$ ≤ 300 °C, where most systems require a heat source temperature of at least 120 °C [81]. System pressures in ORC cycles usually do not exceed 30 bar and the organic fluid can be chosen for $P_{sat}(T_{amb}) > 1$ bar, which allows the condenser and with it the entire system to operate above ambient pressure [81]. However, the organic fluid is often harmful to the environment and climate [81]. The efficiency of high temperature ORC is usually below 24 %, while steam Rankine cycles feature thermal efficiencies > 30 % [81].

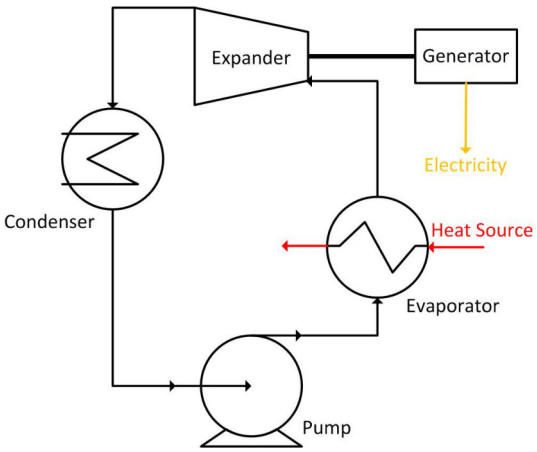


Figure 2.7: Basic Organic Rankine Cycle scheme

### 2.4.2 Reverse Electrodialysis Heat Engine

Logan and Elimelech reported a membrane-based process for power generation from saline solutions [92]. The systems can either harvest energy from naturally occurring salt gradients between fresh water and sea water, which is a large untapped energy source of 980 GW globally [92]. A United States patent for a reverse electrodialysis

heat engine was issued to Loeb in 1979 [93] applying the concept shown in Fig. 2.8. Reverse electrodialysis membranes generate electricity through the salt gradient between a concentrated and diluted feed solution. Early research focused on their application between seawater and river water [94]. However, seawater has a limited salinity of about 35 $g_{salt}/kg_w$ [95] and both river and seawater can be polluted, which requires pretreatment of the feed streams. Artificial feed solutions do not require pretreatment and allow tuning salt type and salinity gradient.

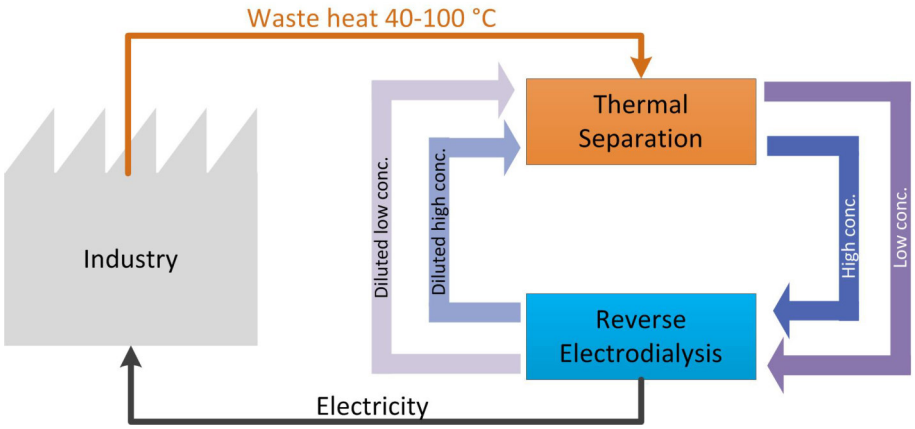


Figure 2.8: Heat engine scheme using Reverse Electrodialysis in a closes loop

Reverse electrodialysis consists of anion and cation exchange membranes (AEM and CEM), which are arranged in cells of one each with a salt water and fresh water compartment between the membranes [94]. Multiple cells together build a RED stack as shown in Fig. 2.9.

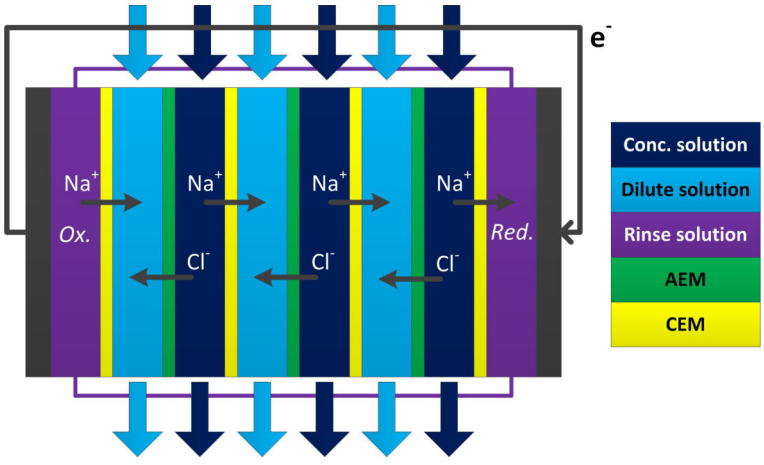


Figure 2.9: The schematic of a RED stack with 3 cells [8, 96]

Positive ions from the salt water diffuse through the CEM to the fresh water compartment on its right in Fig. 2.9, which creates a positive potential [94]. The negative ions of the seawater diffuse through the AEM to the fresh water compartment on it left in Fig. 2.9 creating a negative potential in the cell. The electrical potential $E_{cell}$ between

seawater and river water is 140-160 mV per cell [94] as calculated through the Nernst equation [8]:

$$E_{cell} = (\alpha_{AEM} + \alpha_{CEM}) \frac{R\,T}{F} ln\left(\frac{\gamma_{conc} m_{conc}}{\gamma_{dil} m_{dil}}\right) \tag{2.7}$$

where α[-] is the permselectivity for the respective membrane, R is the ideal gas constant [J/molK], F is the Faraday constant [J/mol], γ is the activity coefficient and m the molality.

The respective ion transport through the membrane causes a net ionic current through the membrane stack [8]. Redox reactions on the electrodes at each end of the stack generate an electric current. Electric power can be extracted from the system by connecting an external circuit between the end electrodes. Parasitic currents reduce the power output, which are caused by co-ion transport through the membranes due to restricted selectivity and ionic shortcut currents, which occur through the rinse solution and the feed/drain channels within the membrane.

### 2.4.3 Osmotic Heat Engine compared to Reverse Electrodialysis

Pressure Retarded Osmosis *PRO* [97] is another membrane process that represents an alternative to RED membranes [98]. Section 2.4.2 shows in Fig. 2.9 that RED membranes are permeable to salt ions, while the water molecules are retained within the compartment. By contrast, PRO membranes are salt rejecting and only permeable for water, which moves from the fresh water compartment to the brine compartment due to the chemical potential difference between the two [98]. The water transport increases the pressure, which can be used to generate electricity in a turbine as shown in in Fig. 2.10. Hence, PRO membranes convert the salt gradient into a pressure gradient first before it can be converted into electricity, whereas RED membranes directly convert the salt gradient into electricity.

Yip and Elimelech compared RED and PRO membranes in terms of power density and energy efficiency in rough simulations using literature properties of high performance membranes [99]. They reported that PRO membranes are advantageous at higher concentrations. Examples of different concentration differences are given comparing the share of the Gibbs free energy of mixing converted into electricity between each other. The Gibbs free energy of mixing $\Delta G_{mix}$ represents a theoretical maximum value of the energy released due to the mixing of two solutions in a reversible process. At low concentration gradients as present in river-seawater, PRO is reported to convert 54 % and RED 38 % of $\Delta G_{mix}$ into electricity. Hence, the two are similar at low concentrations, but PRO maintains a constant conversion rate even at mixing 4 M with 17 mM of NaCL, whereas RED converts 18.1 % of $\Delta G_{mix}$ at this concentration [99]. At these concentrations, the power densities of PRO are estimated at 40 W/m$^2$ and 1.8 W/m$^2$ for RED.

In a study prior to Yip and Elimelech [99], Post et al. conduct the same comparison

between RED and PRO membranes and review other literature comparisons critically [98]. They conclude that efficiency losses due to the turbine in the PRO process are usually neglected, whereas RED electrode reactions are usually taken into account [98]. The analysis of Yip and Elimelech assesses the power density $P_d$ of PRO through $P_{d,PRO} = J_w \cdot \Delta P$ using the water flux $J_w$ and the hydrostatic pressure difference $\Delta P$, while not mentioning turbine losses [99]. Post et al. reported a modelled comparison on equal terms showing that PRO is better at higher salt gradients, whereas RED is more efficient for the power generation using river-seawater [98].

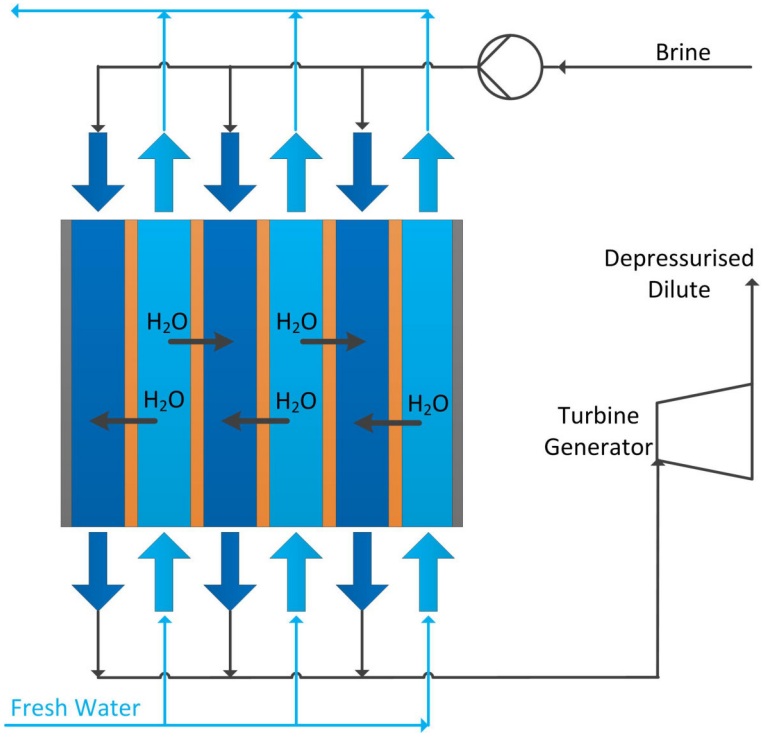


Figure 2.10: The schematics of a PRO process [98, 100]

Micari et al. presented a modelling analysis combining validated models of RED and MD [88]. The study reports the maximum exergy efficiency of the processes at 2 % using current technology and a waste heat source of 80 °C [88]. Future improvements of the system are projected to enhance the exergy efficiency to 16.5 % at 80 °C as future membrane distillation units are reported to have a lower Specific Thermal Consumption *STC* [88]. Future membrane distillation systems are projected to operate at higher concentrations up to 5 M, higher fluxes, feature heat recovery improvements and innovative module designs to reach STC $<$ 100 kWh/m$^3$ [88]. In addition, Micari et al. assumed that future RED membranes will achieve permselectivities of 98 % [88] as an improvement to 65-90 % permselectivity of current membranes [8]. By contrast, Dow et al. reported experimental STC $\approx$ 1500 kWh/m$^3$ for all experiments and temperatures using MD for water purification [68].

Hickenbottom et al. investigated the techno economic cost of a 4.9 MW PRO-MD system in a closed loop simulation using a heat source of 80 °C. They reported pumping losses of the MD plant of 1.1 MW and PRO losses of 0.6 MW reducing the system size to a net electrical output of 2.5 MW [89]. Hickenbottom et al. assumed high efficiencies of all components, e.g. 90 % turbine efficiency, 95 % generator efficiency and 95 % pressure exchanger efficiency [89]. The exergy efficiency of the system is predicted at 3-17 % with a power density of the membrane of 45 $W/m^2$ [89], which is one order of magnitude higher than the current power density reported for RED [88].

## 2.5 Summary

Adsorption desalination is a thermal desalination technology that evolved from adsorption chillers. Adsorption desalination and adsorption chillers are temperature swing adsorption processes driven by cyclic heating and cooling of the beds. Several experimental adsorption desalinators have been been built and tested usually using silica gel as adsorption material. The group of Prof. Ng has presented the most efficient adsorption chiller with silica gel and 4 adsorption beds of 36 $kg_{sg}$ each achieving a maximum SDWP of 14.2 $kg_w/(kg_{sg}d)$. Other systems and materials have been presented and tested by different groups with lower performances or requiring regeneration temperatures above 100 °C. Adsorption desalination as well as other thermal desalination technologies like multi effect distillation or membrane distillation can be coupled with a membrane processes in a closed loop to generate electricity from low grade heat. Pressure retarded osmosis membranes and reverse electrodialysis membranes have both been proposed for this closed loop application. Most investigations have been focusing on modelling activities predicting exergy efficiencies up to 16 % for both technologies.

# Chapter 3

# Vapour liquid equilibria of novel salt solutions

## 3.1 Background

The Barker's cell experiments aimed at getting a better understanding for the thermodynamics of salt solutions as they are essential to desalination processes. Moreover, acetate salts were identified as promising salts for the RED process, but have not been experimentally investigated for a large number of temperature and concentration combinations yet. Thus, the results for the acetate salts presented in this chapter are a novelty, because they extend the available data in the literature and their application to the RED process has been published in Energy [101].

### 3.1.1 Barker's cell experiments and apparatus

A Barker's cell is designed to measure the saturation pressure and temperature of aqueous salt solutions under vacuum. The saturation pressures and temperatures obtained with the Barker's cell can be used to calculate the boiling point elevation caused by the presence of the salt. The boiling point elevation is important for modelling desalination systems as it impairs the performance. In addition, osmotic coefficients can be derived from the pressure and temperature measurements. The osmotic coefficients can be used to fit the Pitzer model virial coefficients, which in return can be used to calculate the activity coefficients and thereby several other thermodynamic properties. Therefore, the aim of the measurements is to determine the boiling point elevation and to fit the Pitzer virial coefficients from the osmotic coefficients derived from the experimental data.

The set-up of the system can be seen in Fig. 3.1a. The cell itself is made of glass and consists of a vacuum cell within a thermal jacket (Fig. 3.1b). A glass capillary leads inside the vacuum cell to insert a T-type thermocouple (RS Pro T Type Thermocouple Copper probe 0.2 mm Nr. 8140153), which measures the temperature of the salt

solution. In addition, the vacuum cell is equipped with a pressure transducer (General Electric UNIK 5000, premium accuracy ±0.04% FS).

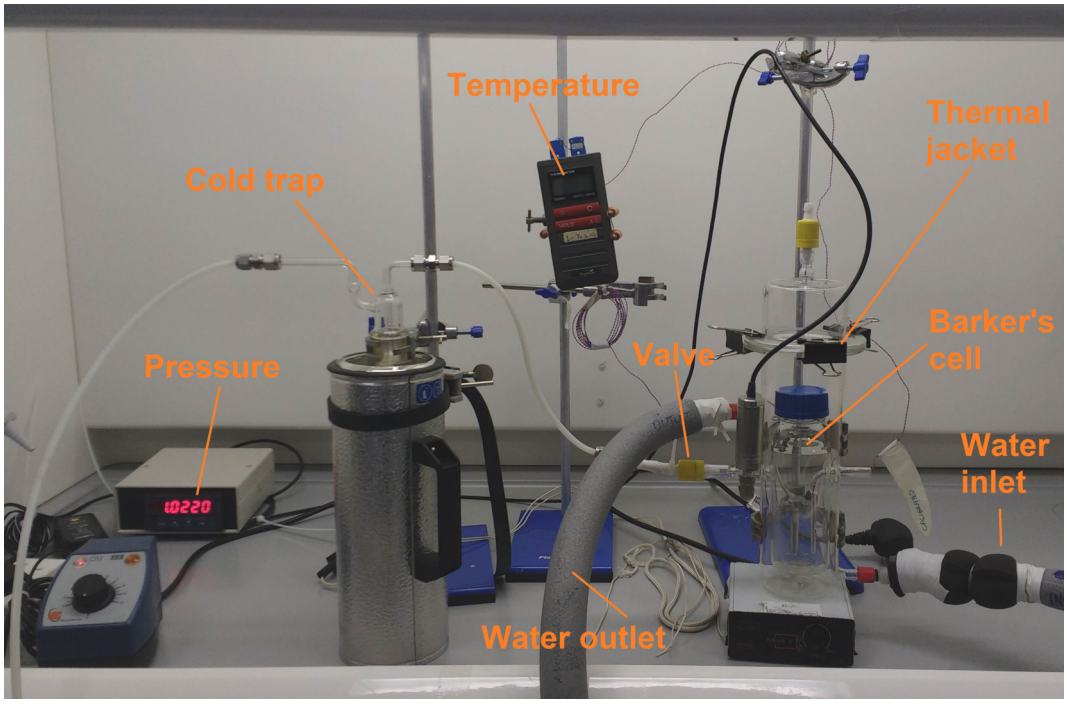


(a)

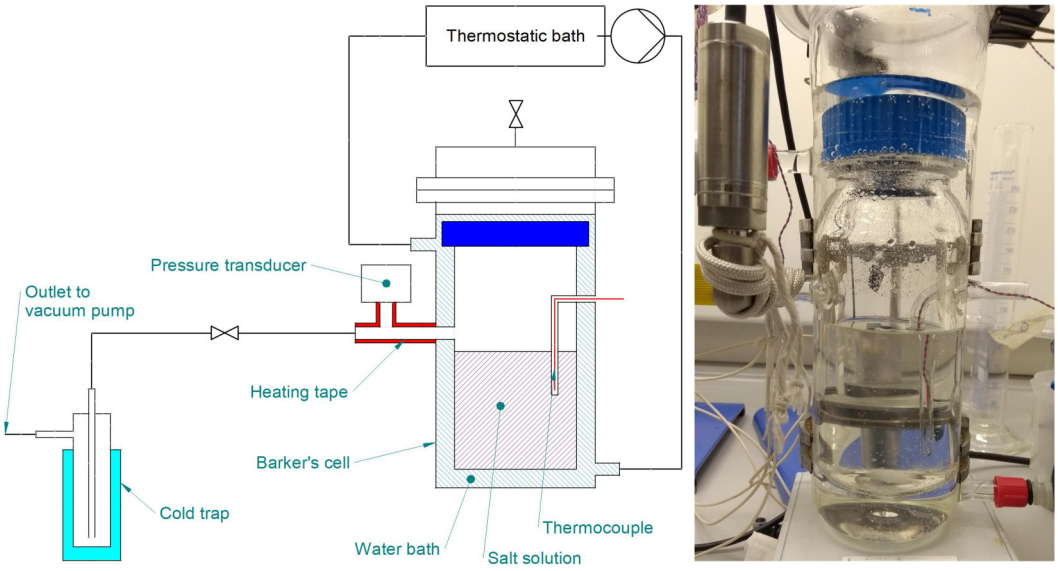


(b)

Figure 3.1: (a) Photograph of the Barker's cell system. (b) Schematic of the experimental set up and photo of Barker's cell.

The Barker's cell operates at pressures between ambient and 0.5 kPa (Fig. 3.1b). The vacuum cell is connected to a cold trap through a glass arm and a valve. The pressure transducer is placed on a branch of this glass arm, which needs to be heated by a heating tape to prevent condensation affecting the pressure measurement. The thermal jacket

is connected to a thermostatic bath, which supplies it with heating or cooling water flowing around the vacuum cell. Furthermore, the thermostatic bath is used to set a target temperature for the salt solution.
The solutions were made by anhydrous salts of at least 99 % purity (listed in appendix table A.1) and deionised water. Salt and water were weighed on a high accuracy balance (Mettler Toledo XS205 dual range, UK) (±1 mg) to formulate the molality of the solution with the following equation:

$$m_{salt} = \frac{c_{sol}\ \tilde{M}_{salt}\ m_{water}}{1000} \tag{3.1}$$

where $m_{salt}$ and $m_{water}$ are the mass of salt and water [g], $\tilde{M}_{salt}$ is the molar mass of the salt [g/mol] and $c_{sol}$ is the molality of the solution [mol/kg]. After the solution is prepared, it needs to be degassed. Firstly, it is placed in an ultrasonic bath for 30 minutes. Secondly, the solution is filled into the vacuum cell and a vacuum is pulled. Afterwards, it is cooled to 10 °C, heated to 40 °C and cooled back to 10 °C, while the cell is connected to the vacuum pump again at each one of the temperature steps. This procedure ensures that the solution is air-free at the start of the experiment. The experiment begins with a first temperature and pressure measurement at a temperature of 10 °C and continues in steps of 10 °C until the final temperature of 90 °C is reached. Between each one of the temperature steps, at least 30-40 minutes have to elapse to ensure that an equilibrium is reached. Before and after an experiment, the Barker's cell is thoroughly cleaned and rinsed with deionised water for several times to remove all salt residues from the previous experiment.

### 3.1.2 Pure water validation

Before measuring the salt solutions, the Barker's cell was calibrated with pure, deionised water. The Barker's cell measures saturation pressures and temperatures. Ideally, the experimental saturation pressure $P_{exp}$ should match the calculated saturation pressure at the measured temperature $P_{sat}(T_{exp})$, which can be obtained through the Antoine equation eq. (3.6) [102] or NIST refprop [103]. The comparison between the ideal match and the experimental result is shown in Fig. 3.2. At low pressures, the experimental pressure matches the saturation pressure derived through the thermocouple. However, at higher pressures there is a significant deviation of about 0.05 bar. Therefore, a temperature fitting curve is needed to adjust the readings of the thermocouple to match them with the pressure readings, which have a higher accuracy. A second-degree polynomial was fitted to correct the temperatures from $T_{exp}$ to $T_{actual}$:

$$T_{actual} = -6.72 \cdot 10^{-4}\ T_{exp}^2 + 1.026\ T_{exp} + 0.453; \tag{3.2}$$

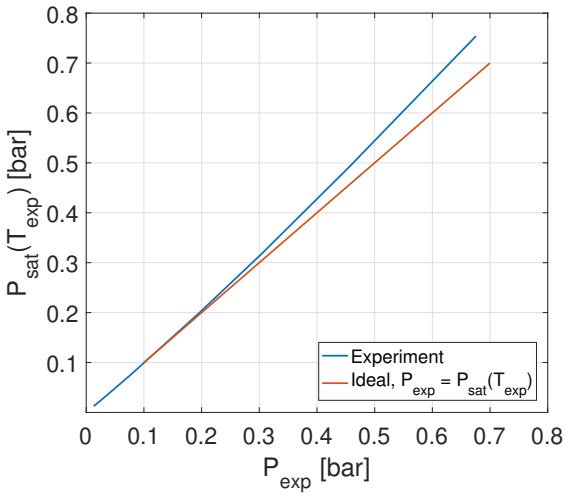


Figure 3.2: Calibration for deionised water. Comparison of the pressure transducer reading $P_{exp}$ and the saturation pressure $P_{sat}(T_{exp})$ based on the temperature reading of the T-type thermocouple.

### 3.1.3 Fundamental equations: The Pitzer model

The experimental results (P, T) can be used to assess the boiling point elevation BPE and osmotic coefficient $\Phi$. The boiling point elevation is a parameter needed for the design and modelling of closed-loop RED systems. The osmotic coefficient can be used to fit the model of Pitzer and Mayorga, which also allows the calculation of activity coefficients $\gamma$. The BPE is defined as:

$$BPE = T_{sat,solution,exp} - T_{sat,water}(P_{sat,solution,exp}) \tag{3.3}$$

The dimensionless osmotic coefficient $\Phi$ is given by:

$$\Phi = -\left(\frac{1000}{(v_M + v_X)c_{sol}M_w}\right) ln(a_s) \tag{3.4}$$

Where $v_M$ and $v_X$ are the number of ions [-], while $z_M$ and $z_X$ are the charges of the ions [-]. The molality of the solution is given by $c_{sol}$ [mol/kg] from eq. (3.20), the molar mass of water $\tilde{M}_w$ [g/mol] and the activity $a_s$ of the solution can be expressed by the saturation pressures at low pressures.

$$a_s = \frac{P_{sat,sol}}{P_{sat,H_2O}} \tag{3.5}$$

The saturation pressures $P_{sat,H_2O}$ [bar] of pure water for a given temperature T between 256-373 K can be calculated using the Antoine equation [102]:

$$log_{10}(P_{sat,H_2O}) = 4.6543 - \frac{1435.264}{T - 64.848} \tag{3.6}$$

The osmotic coefficient is also defined by the Pitzer model [104]:

$$\Phi - 1 = |z_M z_X| f^{\Phi} + m \left( \frac{2 v_X v_M}{v_X + v_M} \right) B^{\Phi}_{MX} + m^2 \left( \frac{2 (v_M v_X)^{3/2}}{v_X + v_M} \right) C^{\Phi}_{MX} \tag{3.7}$$

The other coefficients are as follows:

$$f^{\Phi} = -A_{\Phi} \left( \frac{I^{1/2}}{1 + b I^{1/2}} \right) \tag{3.8}$$

$$B^{\Phi}_{MX} = \beta^{(0)}_{MX} + \beta^{(1)}_{MX} \, e^{-\alpha I^{1/2}} \tag{3.9}$$

$$I = \frac{1}{2} \sum m_i z_i^2 \tag{3.10}$$

The coefficients $b$ and $\alpha$ are constants with the values of 1.2 and 2 for all solutes [104]. The ionic strength is represented by $I$ [mol/kg] in the equations above. For each salt, the virial coefficients ${\beta_{MX}}^{(0)}$, ${\beta_{MX}}^{(1)}$ and ${C_{MX}}^{\Phi}$ are given by Pitzer and Mayorga [104] for a large number of salts and differing ranges of concentrations. The Debye Hückel coefficient $A_{\Phi}$ for water is given in [104, 105]:

$$A_{\Phi} = \frac{1}{3} \left( \frac{2 \pi N_0 \rho_w}{1000} \right)^{1/2} \left( \frac{e^2}{DkT} \right)^{3/2} \tag{3.11}$$

In eq. (3.11) $N_0$ represents the Avogadro constant [$mol^{-1}$], $k$ is the Boltzmann constant [$m^2 kg\ s^{-2} K$], $e$ is the electron charge [C] and $D$ the dielectric constant [-] [106]:

$$D = D_{1000} + C ln \left( \frac{B + P}{B + 1000} \right) \tag{3.12}$$

where $P$ is the saturation pressure of water at the corresponding temperature T [K]. The coefficients $U_{1\text{-}9}$ are shown in table 3.1.

$$D_{1000} = U_1 exp(U_2 T + U_3 T^2) \tag{3.13}$$

$$C = U_4 + \frac{U_5}{U_6 + T} \tag{3.14}$$

$$B = U_7 + \frac{U_8}{T} + U_9 T \tag{3.15}$$

Table 3.1: Parameters to calculate the dielectric constant of water [106]

| | | | | | |
|---|---|---|---|---|---|
| $U_1$ | 342.8 | $U_4$ | -2.05 | $U_7$ | -8032.5 |
| $U_2$ | $-5.09 \cdot 10^{-3}$ | $U_5$ | 3115.9 | $U_8$ | $4.21 \cdot 10^{6}$ |
| $U_3$ | $9.47 \cdot 10^{-7}$ | $U_6$ | -182.9 | $U_9$ | 2.14 |

### 3.1.4 Error analysis

The uncertainty of the boiling point elevation is caused by errors of the temperature measurements $\Delta T_{sat,sol}$ and error of the measured pressure inserted into the Antoine equation eq. 3.6 [107]:

$$\Delta BPE \approx \Delta T_{sat,sol} + T_{sat,w}(P_{\Delta exp}) \tag{3.16}$$

The osmotic coefficient $\Phi$ from eq. (3.4) is a delicate parameter to assess from the results of the Barker's cell and many factors contribute to the uncertainty [107]:

$$\Delta\Phi = \sqrt{\left(\frac{\partial\Phi}{\partial P}\Delta P\right)^2 + \left(\frac{\partial\Phi}{\partial P_{sat}(T_{sat})}\Delta P_{sat}(T_{sat})\right)^2 + \left(\frac{\partial\Phi}{\partial m_{salt}}\Delta m_{salt}\right)^2 + \left(\frac{\partial\Phi}{\partial m_{water}}\Delta m_{water}\right)^2} \tag{3.17}$$

The uncertainties of each one of the independent variables are shown in table 3.2. The uncertainty of the pressure transducer is given by the manufacturer. Since the thermocouple was calibrated with the pressure transducer, the accuracy of the pressure transducer applies to the thermocouple as well as the average deviation of the calibration polynomial of 0.03 %. The salt and water are both measured on the same scale. However, their uncertainties are different, because a small amount of water evaporates while the solution is inside the ultrasonic bath to degas. Weighing the solution before and after degassing aimed at minimising the uncertainty.

Table 3.2: Uncertainties of independent variables needed to assess the osmotic coefficient

| Variable | Unit | Error |
|---|---|---|
| $\Delta$P | bar | 0.04% FS (FS=0-1.5 bar) |
| $P_{sat}(\Delta T_{sat,\ solution})$ | bar | 0.04% + 0.03% |
| $\Delta m_{salt}$ | g | 0.1 % |
| $\Delta m_{water}$ | g | 0.2 % |
| $\Delta$T | °C | 0.1 |

## 3.2 Results: VLE of aqueous salt solutions

### 3.2.1 Lithium Acetate

Lithium acetate has a lower solubility at room temperature than the other acetate salts [77]. The solubility curve of LiAc is shown in Fig. 3.3a. The first two concentrations of interest at 2 m and 4 m are not affected by the solubility, but the two higher concentrations are not soluble at room temperature. Thus, the saturations pressures of LiAc at 6 m were only measured from 30-90 °C and at 8 m they were only measured from 40-90 °C (Fig. 3.3b).
The first result of the saturation pressure and temperature measurements at a concentration of 2.004 m is shown in Fig. 3.3b to compare it to literature data,. Pitzer and Mayorga [104] fitted their model with experimental data up to 4 m and this model was used for the comparison. Fig. 3.3b demonstrates that the experiments are in good agreement with the literature.

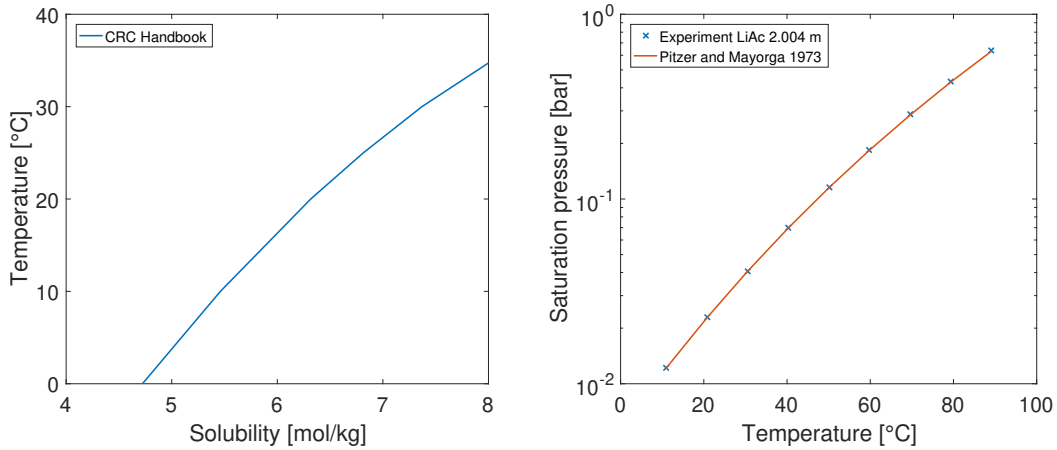


(a) (b)

Figure 3.3: (a) The solubility of LiAc in water is temperature dependent [77].
(b) The measured results match the Pitzer model using parameters from Pitzer and Mayorga [104].

Table B.5 in the appendix presents the results of all the saturation pressure and temperature measurements for LiAc. It can be seen that the temperature dependent solubility was taken into account. The BPE and Φ of the LiAc solutions were calculated from the results and are given in table B.5 as well as Fig. 3.4. The BPE is increased by almost 8 °C at the highest concentration and temperature under investigation. At molalities of 2 m and 4 m the BPE of LiAc is very similar to NaCl, which is also between 1-2 °C for 2 m in the temperature range between 10-90 °C and between 2-4 °C at 4 m for 10-90 °C.

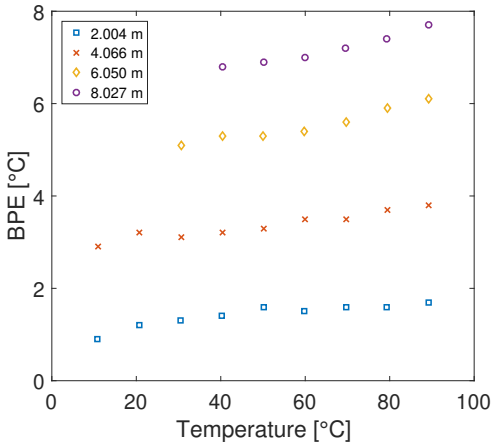


Figure 3.4: The boiling point elevation of LiAc at different temperatures and molalities

The osmotic coefficients assessed through the experiments are displayed in Fig. 3.5.

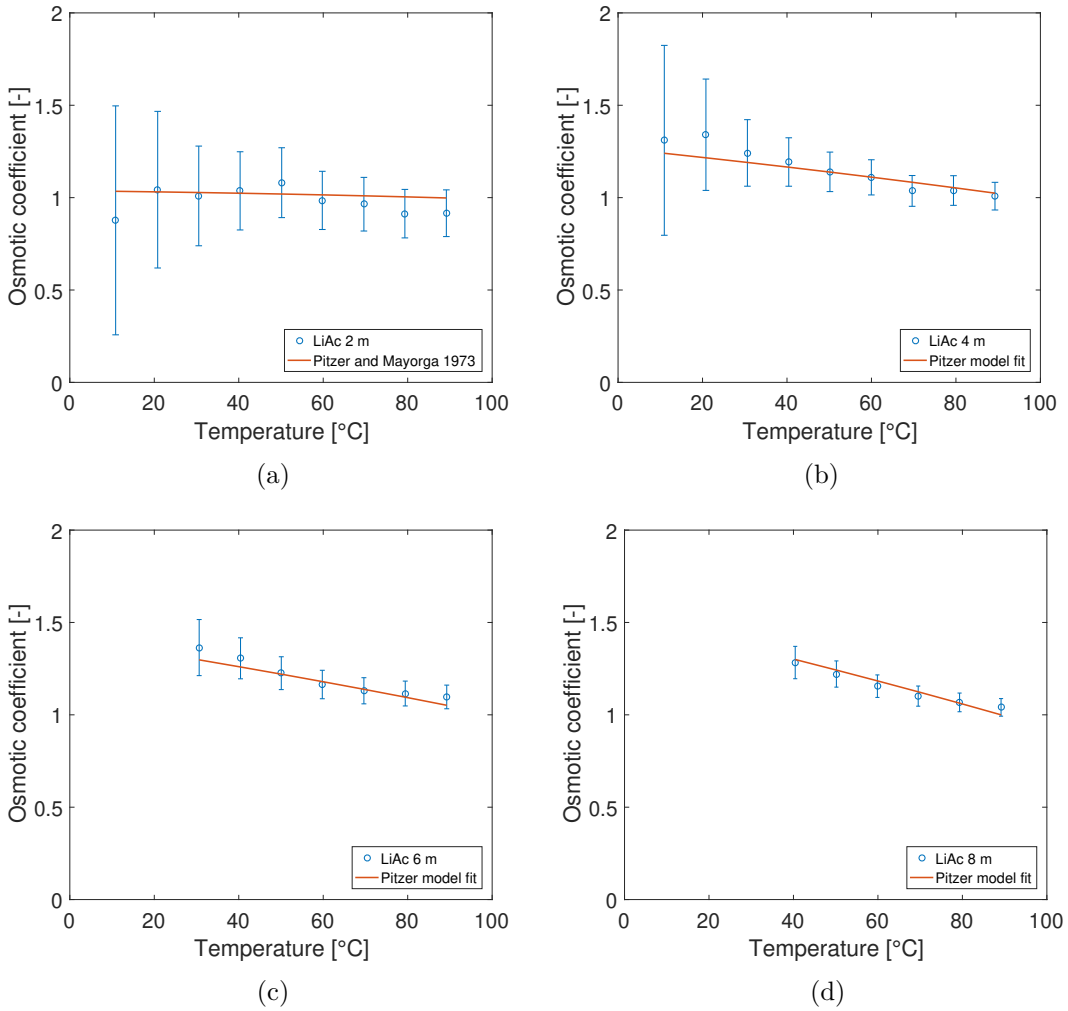


Figure 3.5: Osmotic coefficients calculated from experiments and model fit of LiAc at 4 different concentrations and temperatures up to 90 °C

The error of the osmotic coefficient is quite high at temperatures below 30 °C and low concentrations, because of the low vapour pressures, which lead to an increased error of the pressure transducer.

The osmotic coefficients were used to fit the virial coefficients of the Pitzer model. Firstly, they were fitted to the model using the three virial coefficients of Pitzer and Mayorga: $\beta^{(0)} = 0.1273$, $\beta^{(1)} = 0.0905$ and $c^{\Phi} = -0.0092$. However, the osmotic coefficients show a temperature dependency in Fig. 3.5 with deviation up to 25 % from the experimental data as shown in Fig. 3.6a. Thus, each one of the parameters was changed to a linear function of the temperature [K] with two fitting parameters each:

$$\beta^{(0)} = a_1\ T + a_2 \tag{3.18}$$

$$\beta^{(1)} = a_3\ T + a_4 \tag{3.19}$$

$$c^{\Phi} = a_5\ T + a_6 \tag{3.20}$$

The parameters $a_1$ - $a_6$ were fitted to the data and are given in table 3.3:

Table 3.3: The coefficients of the fitted Pitzer model for LiAc up to 8 m and 10-90 °C

| | | | | | |
|---|---|---|---|---|---|
| $a_1$ | $-1.80 \cdot 10^{-4}$ | $a_3$ | $-7.19 \cdot 10^{-3}$ | $a_5$ | $-5.49 \cdot 10^{-5}$ |
| $a_2$ | 0.184 | $a_4$ | 2.239 | $a_6$ | $9.81 \cdot 10^{-3}$ |

Fig. 3.6 justifies this decision since the original three-parameter model leads to deviations between 10 % and -25 %. The introduction of temperature dependent Pitzer parameters reduces the deviation to 5 %.

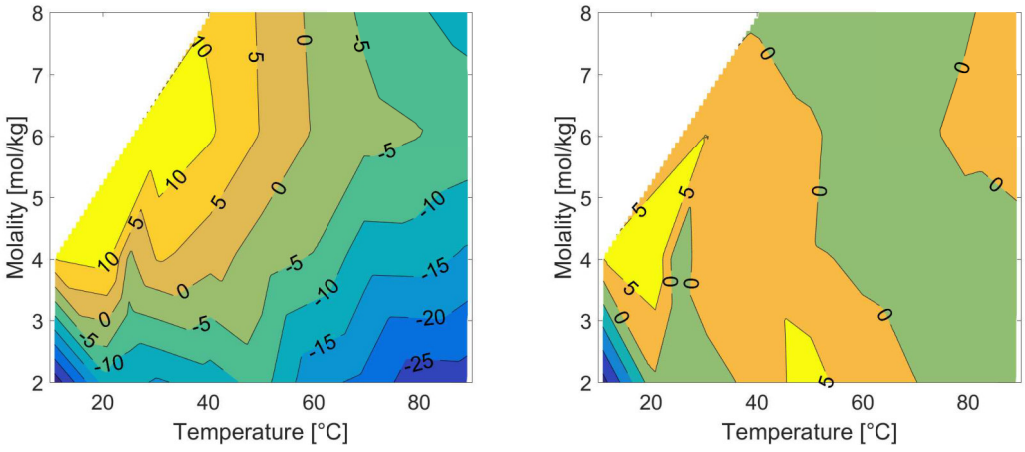


(a) (b)

Figure 3.6: The deviation [%] of the experimentally obtained osmotic coefficient and the fitted Pitzer model: (a) The classic Pitzer model with only three fitting parameters. (b) The extended Pitzer model with temperature dependent fitting parameters

### 3.2.2 Caesium Acetate

Caesium acetate has a very high solubility in water. The solubility shows a temperature dependency as well as it does for lithium acetate, but at a much lower level. At 0 °C the solubility is 49 m and at 90 °C the solubility increases to 70 mol/kg [108]. Therefore, the saturation pressures of the chosen solutions of 2, 4. 6 and 8 m could be measured for the entire temperature range of interest from 10-90 °C. Fig. 3.7a presents the measured saturations pressures and temperatures of the 2 m solution, which is still in the range of the Pitzer model parameters fitted up to 3.5 m [104]. In addition, the saturation pressure curve of the model using literature parameters is also shown in Fig. 3.7a. The experimental results are in good agreement with the model using literature virial coefficients [104] as the deviation is less than 0.77 %.

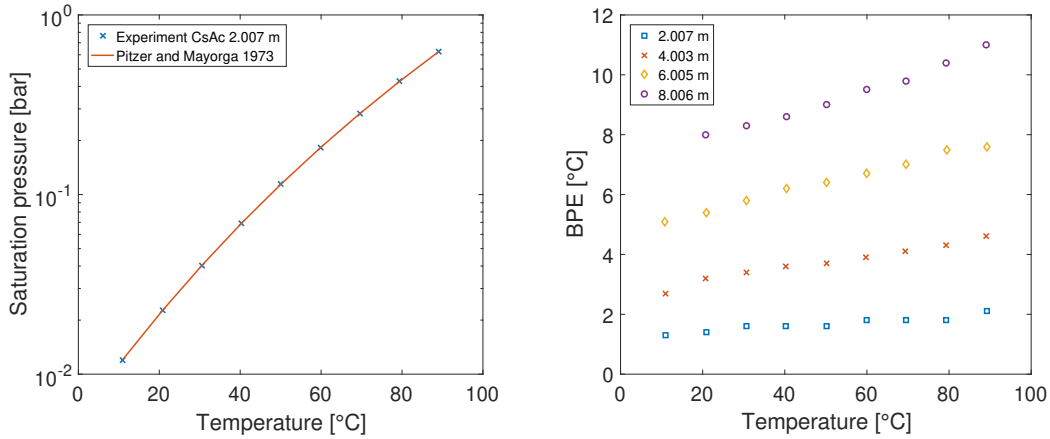


(a) (b)

Figure 3.7: (a) The experimental saturation pressure and temperature curves of CsAc solutions at 2 m in comparison to literature data.
(b) The BPE calculated for CsAc for different temperatures and concentrations.

The measured saturation pressures and temperatures for four concentrations are given in table B.6 in the appendix including the calculated BPE and Φ. The BPE of the CsAc solutions are also shown in Fig. 3.7b. At low concentrations of 2 and 4 m the BPE of CsAc is similar to the BPE of LiAc. However, at higher concentrations the BPE of the CsAc solutions is up to 3 °C higher than LiAc. Therefore, the interactions of the CsAc ions and the water molecules in the solution seem to be stronger than the interactions within the LiAc solution, which causes a higher BPE and higher osmotic coefficients. The osmotic coefficients obtained of CsAc from the experimental results of the pressure and temperature measurements are shown in Fig. 3.8. The trends are less temperature dependent than the results of LiAc. Thus, a fit with the regular Pitzer model was undertaken. The use of single, non-temperature dependent parameters is preferable for consistency and comparability with Pitzer's work.

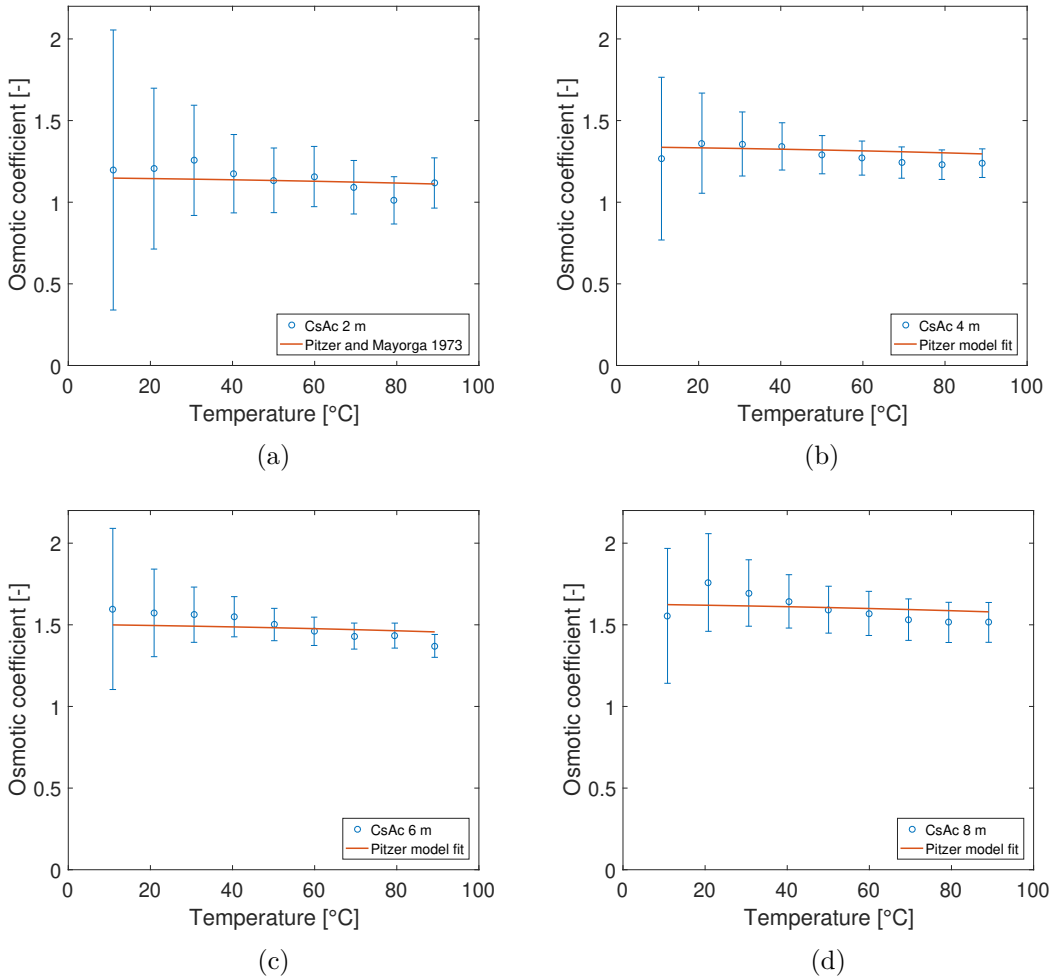


Figure 3.8: The osmotic coefficient calculated from experiments and the model fit of CsAc at 4 different concentrations and temperatures up to 90 °C

The Pitzer model parameters were fitted based on the osmotic coefficients derived from the experimental results. In addition, the experimental results were supplemented with the osmotic coefficients published by Robinson and Stokes [109]. Robinson and Stokes published osmotic coefficients at 25 °C and 18 different molalities between 0.1 - 3.5 m of CsAc. The experimental results extended the data available in the literature to a wide temperature range and to concentrations up to 8 m. However, the data of Robinson and Stokes was included to improve the quality of the fit at low concentrations down to 0.1 m. The fitting was implemented in Matlab by using the *nlinfit* solver, which used the original Pitzer parameters [104] as initial guesses. The result is shown in table 3.4 for CsAc solutions between 0.1 - 8 m and temperatures from 10 °C and 90 °C.

Table 3.4: Coefficients of the fitted Pitzer model for CsAc up to 8 m and 10-90 °C

| | |
|---|---|
| $\beta^0$ | 0.1557 |
| $\beta^1$ | 0.4681 |
| $c^\Phi$ | -0.0061 |

The fitted Pitzer model and the osmotic coefficients derived from the experimental results are in good agreement as it can be seen in Fig. 3.9a. Fig. 3.9a illustrates the deviation [%] between the experimental osmotic coefficients and the fitted Pitzer model. At low temperatures the model under predicts the osmotic coefficients slightly by up to 6 %, while at high concentrations the model over predicts the values by up to -8 %. However, the deviation between the model and the experimentally derived osmotic coefficients is still within the experimental error as it can also be seen in Fig. 3.8. Therefore, it is not necessary to alter the Pitzer model to temperature dependant coefficients in the case of CsAc.

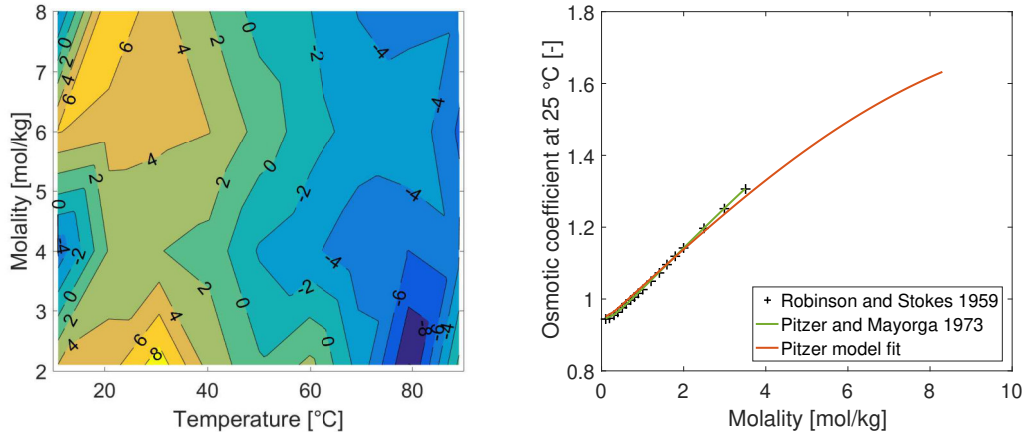


(a) (b)

Figure 3.9: (a) The deviation [%] of the experimentally obtained osmotic coefficient and the fitted Pitzer model.
(b) The osmotic coefficients of CsAc at 25 °C reported by Robinson and Stokes [109] in comparison to the Pitzer model results using the original virial coefficients [104] and the extended virial coefficients fitted here.

The original Pitzer parameters [104] based on data provided by Robinson and Stokes [109] are fitted at 25 °C from 0.1 - 3.5 m. Both, the model fitted by Pitzer-Mayorga and the data of Robinson-Stokes, are plotted in Fig. 3.9b. For comparison, the fitted model of this work is also shown in Fig. 3.9b. The virial coefficient fitted within this work are in good agreement with the original virial coefficients [104] and the literature data [109]. Fig. 3.9b highlights the novelty of the data as it extends the molality from 4 to 8 m

### 3.2.3 Potassium Acetate

The saturation pressures and temperatures of potassium acetate were measured in the Barker's cell and are listed in table B.4 in the appendix. The deviation between the experimental saturation pressures at 2.006 mol/kg of KAc and the saturation pressures of KAc predicted by the Pitzer model based on the parameters of Pitzer and Mayorga [104] is less than 0.5 % as it can be seen in figure 3.10a.
The experimental saturation pressures and temperatures in table B.4 in the appendix were used to calculate the BPE of KAc (Fig. 3.10b. KAc has high BPE of up to 12 °C at 9 mol/kg and 90 °C. In addition, the BPE is increasingly temperature dependent at higher salinities.

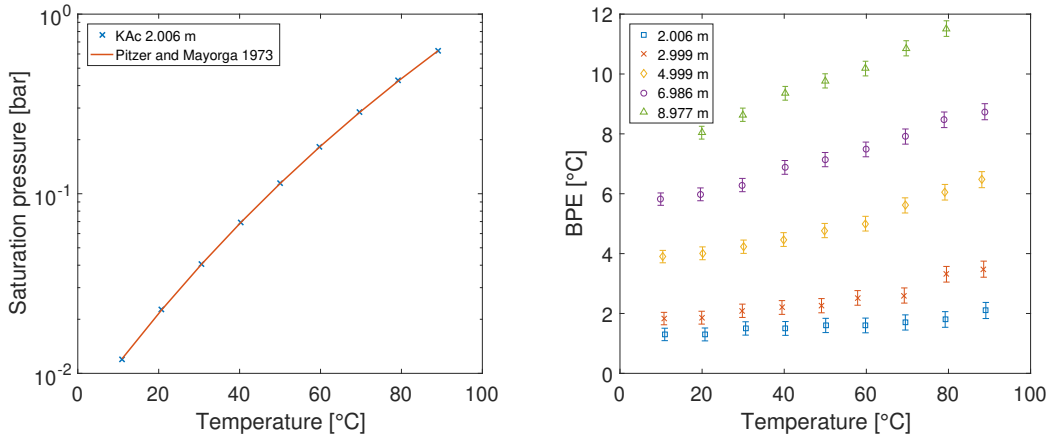


(a) (b)

Figure 3.10: (a) The experimental saturation pressure and temperature curves of KAc solutions at different concentrations and the curve of pure water for comparison, which is also experimentally obtained.
(b) The BPE of KAc solutions for different temperatures and concentrations.

The saturation pressures and temperatures in table B.4 from the appendix are also used to assess the osmotic coefficients for each temperature and concentration in Fig. 3.11. Again, the experimental error at 10 °C is very large due to the error of the pressure transducer and the low pressure of the solution. The osmotic coefficients of KAc are lower than LiAc. The fitting parameters for the experimental results are given in Fig. 3.11 as well as table B.4.

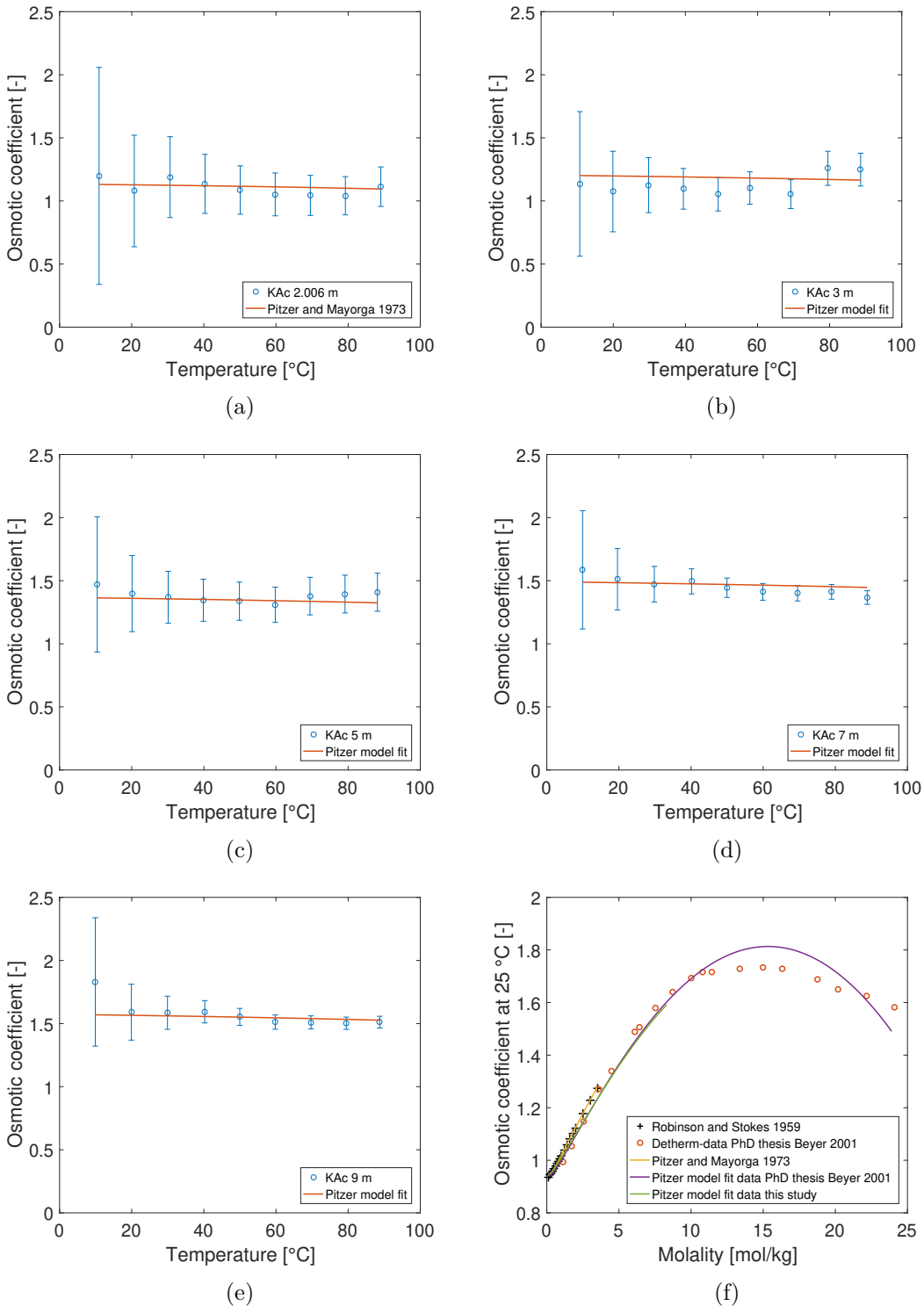


Figure 3.11: (a-e) The osmotic coefficient calculated from experiments and the model fit of KAc at 5 different concentrations and temperatures up to 90 °C.
(f) Comparison between the Pitzer fit in table 3.5 with literature data [109, 110] and a second Pitzer fit performed on the literature data from [110]

The vapour liquid equilibrium of KAc has been investigated in several publications for concentrations up to 3.5 m [110] and up to 25 m [109], both at 25 °C. The literature results are compared to the Pitzer fit to the experimental results from table 3.5.

Table 3.5: The coefficients of the fitted Pitzer model for 0-9 m of KAc and saturation temperatures of 10-90 °C.

| | |
|---|---|
| $\beta^0$ | 0.1363 |
| $\beta^1$ | 0.3958 |
| $c^\Phi$ | -0.0043 |

In addition, the Osmotic coefficients of [110] were used to obtain a second Pitzer fit for concentrations up to 25 m: $\beta^0 = 0.1388$; $\beta^1 = 0.3958$; $c^\Phi = -0.0045$.
The second set of Pitzer parameters only differs from table 3.5 in the last digit. In Fig. 3.11f the two Pitzer model fits do not vary up to 9 m and match the literature well [110]. Beyond 10 m the literature data for $\Phi$ flattens, which the Pitzer model takes into account, but the model does not fit the data exactly with a deviation of less than 7 %.
Fig. 3.11f shows that the osmotic coefficient of KAc flattens and decreases above 10 m. To investigate the reliability of this trend, Fig 3.12 compares the osmotic coefficients of KAc to the osmotic coefficients of two other salts with high solubilities: Sodium acetate and lithium chloride. All three salts show a similar behaviour that the osmotic coefficient reaches a plateau at high concentrations and even decreases slightly in the cases of the two acetate salts.

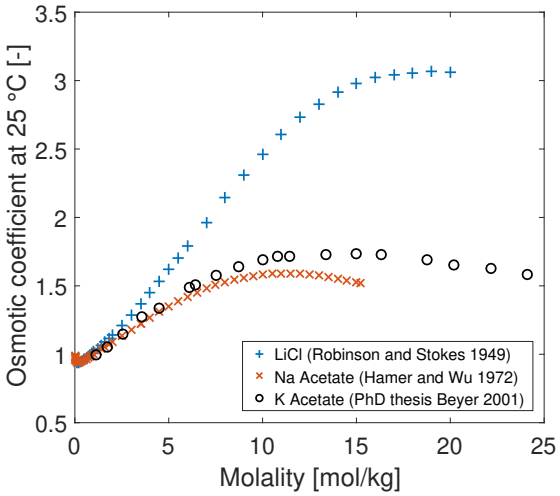


Figure 3.12: The osmotic coefficients of KAc [110], LiCl [111] and NaAc [112] reach a plateau at high concentrations.

### 3.2.4 Salt mixture of LiCl and NaCl

Salt mixtures were investigated as a possible improvement to the RED process. The aim of the investigation was to check if aqueous solutions of two salts reduce the BPE through salt-salt interactions. Robinson et al. reported osmotic coefficients for LiCl and NaCl mixtures at varying concentrations at 25 °C [113]. This investigation extended the temperatures to 10-90 °C for a concentration not covered by Robinson et al. [113]. The temperature and pressure results of the Barker's cell are shown in Fig. 3.13a as well as predictions obtained from OLI electrolytes within Honeywell UniSim Design R443. UniSim Design is a process simulation software that obtains physical properties from thermodynamic packages. The OLI electrolyte package (OLI Systems Inc., USA) is a third-party software that is integrated into UniSim Design. OLI electrolytes includes different databases and models to provide properties of electrolytes systems. OLI is very accurate for known systems like NaCl and also incorporates predictive models for electrolyte systems where little or no experimental data is available.

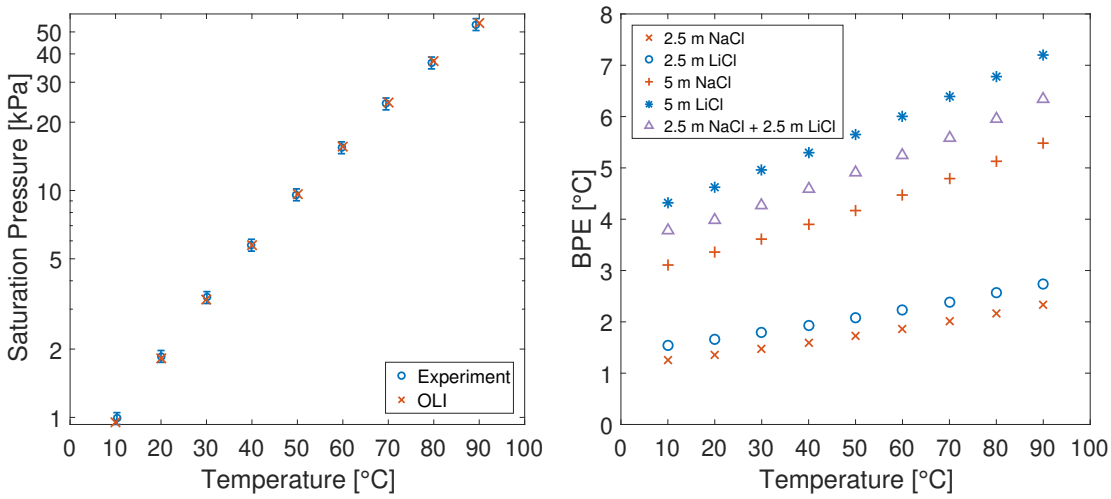


(a) (b)

Figure 3.13: (a) The saturation pressures of an aqueous solution of 2.5 m of LiCl mixed with 2.5 mol/kg of NaCl. The pressures have been measured in the Barker's cell and are compared to OLI electrolytes in UniSim.
(b) The BPE of the mixed salt solution compared to the BPE of the pure salts at 2.5 m and 5 m. The saturation pressures to calculate the BPE were obtained in UniSim through the OLI electrolytes package.

The results in Fig. 3.13a also show that the OLI electrolytes package in Honeywell UniSim can predict the vapour pressures of this specific salt mixture very well. Thus, the rest of the investigation can be carried out by using OLI electrolytes in UniSim instead of measuring the vapour pressures experimentally.
Fig. 3.13b shows the boiling point elevation derived from vapour pressures obtained through OLI electrolytes. The BPE of NaCl and LiCl in single salt mixtures at 2.5 m

are very similar to each other. However, the BPE of the two salts deviates by more than 1 °C at doubled molality. The BPE of the mixed salt solution is exactly in the middle between the two single salt solutions comparing 5 m NaCl, 5 m LiCl, and 2.5+2.5 m NaCl+LiCl. Therefore, it is not beneficial to use mixed salt solutions, because it does not reduce the BPE. Table B.7 in the appendix presents the experimental results and the properties that can be derived from the measurements.

## 3.3 Conclusions

A Barker's cell was used to measure saturation pressures and temperatures of aqueous salt solutions up to 9 m and temperatures 10-90 °C. Three novel acetate salts were investigated, significantly extending the available literature data [104]. Acetate salts have very high salt solubilities, which is interesting for RED heat engines as large salt gradients increase the electricity production. The pressure and temperature measurements were used to calculate boiling point elevations and osmotic coefficients. The boiling point elevations of the salts are very similar and up to 12 °C at the highest measured concentration 8-9 m. High salt concentrations are not favourable for MED systems, because the BPE limits the number of effects and the performance. The osmotic coefficients were used to fit the virial coefficients of the Pitzer model, which are necessary for desalination modelling in the following chapter and to calculate activity coefficients.

The behaviour of salt mixtures was assessed to analyse if salt mixtures have reduced BPE compared to aqueous solutions of single salts. An aqueous solution using a salt mixture of 2.5 m LiCl and 2.5 m NaCl was tested for temperatures 10-90 °C. The results showed that the use of LiCl/NaCl mixtures does not offer any advantages compared to single salt solutions.

# Chapter 4

# Desalination modelling

In this chapter, three promising desalination technologies are investigated in terms of their thermal performance. All three systems can also be applied to the closed loop in combination with Reverse Electrodialysis to generate electricity from low-grade heat. Seawater always has a comparably low salinity with a BPE of less than 1 °C. However, the closed-loop application can operate at high salinities and allows the application of different types of salts. The previous chapter presented an experimental assessment of the salt thermodynamics, which have a direct impact on the performance of the regeneration systems presented here. The first section 4.1 presents a model of multi effect distillation in UniSim, where the pressure drop between a given number of effects is calculated in a preliminary analysis using the Pitzer model presented in the previous chapter. The second section 4.2 implements a steady state model for multi effect distillation and combines it with an adsorption desalination model in Matlab. Several publications (e.g. [74]) have proposed this type of system as advantageous over MED alone. Adsorption desalination cools the last effect of MED below ambient temperature allowing additional MED effects operated below ambient temperature, which increases the distillate output. In the third section 4.3, a completely different regeneration system is presented for the first time in a UniSim simulation. This system, Absorption Vapour Compression, combines a single evaporator with an absorption heat pump. Thermal integration between the two components boosts the performance of the simpler process design compared to MED.

## 4.1 Multi effect distillation

### 4.1.1 The pressure drop between effects

The Unisim model allows setting a pressure drop between each effect, where a minimum pressure drop leads to the maximum number of effects. Each additional effect recycles the latent heat of the generated vapour back into the process leading to a higher performance. A pressure drop is concurrent with a temperature drop and the minimum temperature drop between two effects is the boiling point elevation. However, the BPE

increases with every MED effect as the brine concentration increases as well. Thus, a preliminary analysis in Matlab established the pressure drop between the effects for a given number of stages $N$, top brine temperature $TBT$ [°C], ambient temperature $T_{amb}$ [°C], feed concentration $C_f$ [m] of LiCl/NaCl/KAc, recovery ratio $RR$ and distillate production $\dot{m}_d$ [kg/s]. The procedure is outlined in Fig. 4.1.

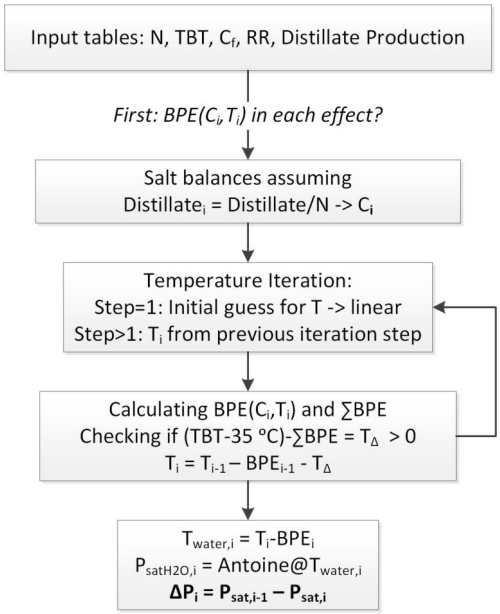


Figure 4.1: The iteration method to determine the pressure drops between the effects as input for UniSim

In the preliminary analysis (Fig. 4.1), the BPE is assessed through the Pitzer model in the sequence shown in Fig. 4.1. In the main model, the UniSim OLI package uses a conjunction of different models to assess the BPE and activity coefficients of salt solutions [114]: Debye Hückel, Bromley, Pitzer, Helgeson, Chen and Meissner. Notably, the Meissner model is reported as a highly predictive and extrapolative method to calculate the activity coefficient when experimental data is lacking and can be used in combination with other models [114]. By contrast, the Pitzer model is highly accurate when experimental data is available, but not predictive. The VLE for different temperatures and concentrations of NaCl and LiCl are well established and Pitzer model data is available [104]

The salt concentration of the last effect $C_N$ can be derived through the recovery ratio:

$$C_N = \frac{C_f}{1 - RR} \tag{4.1}$$

The feed flow rate $\dot{m}_f$ is determined through a salt balance:

$$\dot{m}_f = \frac{\dot{m}_d \, C_N}{C_N - C_f} \tag{4.2}$$

The vapour production of each stage $\dot{m}_{vap,i} = \dot{m}_{d,i} = \dot{m}_d/N$ is calculated under the assumption that every stage produces the same amount of vapour. A real MED plant has a decreasing vapour production for each stage as Planezuela et al. reported a decrease of 30 % between the 1st and 14th stage of their pilot plant [72]. However, the preliminary step only determines the pressure drops between the effects. By contrast, the main analysis in UniSim calculates the vapour production for each individual effect.

The salt concentration of each effect is calculated through the brine flow rate for the first effect $\dot{m}_{b,1} = \dot{m}_f - \dot{m}_{d,1}$ and for each subsequent effect $\dot{m}_{b,i} = \dot{m}_{b,i-1} - \dot{m}_{d,i}$:

$$C_i = \frac{\dot{m}_{b,i-1} C_{i-1}}{\dot{m}_{b,i}} \tag{4.3}$$

The BPE is a function of temperature and salt concentration. In a first iteration step, a linear temperature profile was assumed: $T_{i-1} - T_i = (TBT - T_{amb})/N$. A linear temperature profile is sufficient for smaller numbers of effect where $\Sigma(BPE_i) << (TBT - T_{amb})$. However, for large numbers of effects and $\Sigma(BPE_i) \approx (TBT - T_{amb})$ the temperature drop cannot be constant and needs to be adjusted to the BPE. Thus, the first iteration step assumes the linear temperature profile, assess the BPE and then calculates a new temperature profile based on the BPE:

$$T_i = T_{i-1} - BPE_{i-1} - T_\Delta \tag{4.4}$$

where $T_\Delta \geq 0$ assures that the system utilises the full temperature window between $TBT$ and $T_{amb}$:

$$T_\Delta = \frac{TBT - T_{amb} - \Sigma(BPE_i)}{N - 1} \tag{4.5}$$

The next iteration step calculates the BPE based on the new temperature profile from eq. (4.4). This continues until the temperature profile does not change from one iteration step to the next. Once the individual temperature drops between the effects are established together with the salt concentrations from eq. (4.3), the pressure drops can be calculated through the Pitzer model for the respective salt. An example result for $BPE_i$ and the pressure drop for each effect $\Delta P_i$ [kPa] is shown in Fig. 4.2 for potassium acetate. The BPE slightly decreases for the first half of effects, before it increases again. This behaviour has two causes as the growing brine concentration increases the BPE from the first to the last effect, while the decreasing temperature reduces the BPE. Both causes compensate for each other leading to the curve in Fig. 4.2.

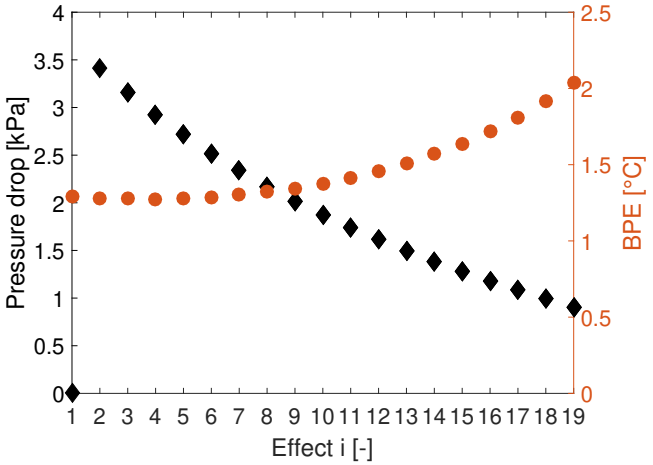


Figure 4.2: An example result for the predicted pressure drops ($P_{i-1} - P_i$) and BPE in each effect for N = 19, TBT = 80 °C, $C_f$ = 1.5 m, Salt = Potassium acetate, RR = 0.5 and $\dot{m}_d$ = 100 tons/day

The number of effects is an input value to the procedure above, which can be changed to find the maximum number of effects automatically. A while-loop adds effects until $T_{vap,i} \geq T_{amb}$ is reached with $T_{vap,i} = T_{vap,i-1} - (BPE_{i-1} + \Delta T_{hx})$. Fig. 4.3 shows that the temperature difference of the heat exchanger $\Delta T_{hx}$ [°C] between the inside and the outside is crucial to the number of effects in seawater desalination. Seawater does not have a high salinity (≈ 0.7 m) and therefore a low BPE (≈ 0.3 °C). Therefore, 114 effects are theoretically possible at $\Delta T_{hx}$ = 0.1 °C. However, this number is reduced to 32 effects at $\Delta T_{hx}$ = 1 °C and 12 effects at $\Delta T_{hx}$ = 3 °C for $TBT$ = 70 °C and $T_{amb}$ = 30 °C. This emphasises that the heat exchanger design and heat exchanger area are the true limitation for the number of effects in seawater desalination and not the BPE.

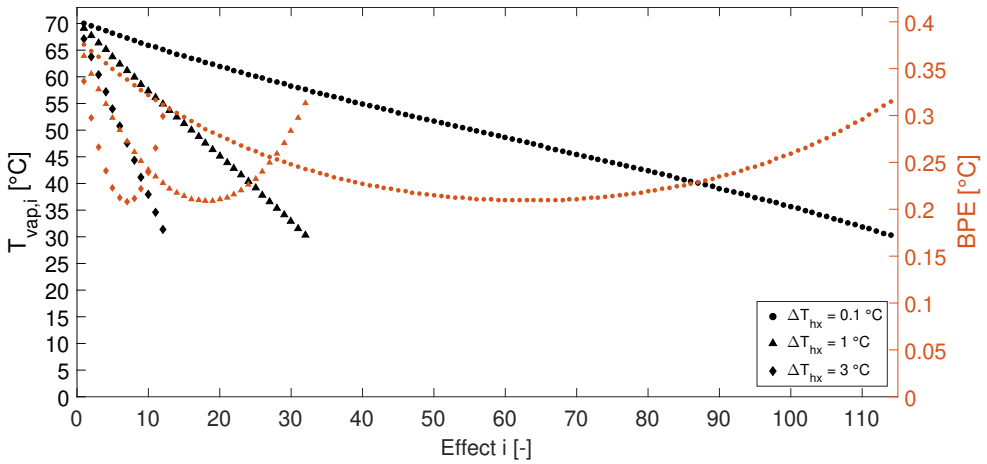


Figure 4.3: The predicted, maximum number of effects if \$$T_{vap,i} = T_{vap,i-1} - (BPE_{i-1} + \Delta T_{hx})$. TBT = 70 °C, $T_{vap,N}$ = 30 °C, $C_f$ = 0.7 m, Salt = NaCl (seawater), RR = 0.1 and $\dot{m}_d$ = 100 tons/day

High salinity solutions of NaCl change this result as the BPE increases from 0.4 °C to 5 °C, when the feed concentration is increased from 0.7 m to 5 m. This would be the case for a Reverse Electrodialysis heat engine with MED as regeneration where a high salinity maximises the electricity output of the RED membrane [8]. Here, the number of effects is reduced to 10 effects even at the lowest $\Delta T_{hx}$ = 0.1 °C in Fig. 4.4. At the larger temperature gradient of 3 °C only 6 effects are possible, which is half compared to the seawater desalination (Fig. 4.3). Therefore, the energy efficiency of MED is limited at large feed concentrations, because of the BPE limiting the maximum number of effects. For seawater, better heat exchanger designs would allow very big, energy efficient systems.

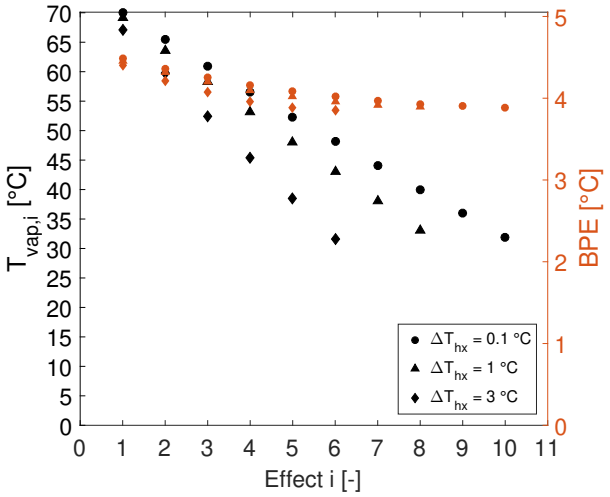


Figure 4.4: The predicted, maximum number of effects if $\Delta T_{effect}$ = BPE. TBT = 70 °C, $T_{vap,N}$ = 30 °C, $C_f$ = 5 m, Salt = NaCl, RR = 0.1 and $\dot{m}_d$ = 100 tons/day

### 4.1.2 UniSim modelling

MED systems of different sizes up to 27 effects were considered for the performance analysis with the model implemented in Honeywell UniSim R443 with the OLI electrolytes package. UniSim is a process modelling software that can accurately calculate physical properties using thermodynamic packages like OLI.

The investigation is similar to the publications of Palenzuela et al. [115] and Giacalone et al. [101], but independent of them although within the RED Heat-to-Power project. The investigation of Giacalone et al. [101] is comparable to the preliminary model analysing the pressure drops between the effects. Palenzuela et al. [115] combined the RED model of Tedesco et al. [116] with the steady-state model presented by Ortega-Delgado et al. [117]. The MED-RED model of Palenzuela et al. [115] is split between gPROMS for RED and Engineering Equations Solver for MED.

The MED model here was implemented in UniSim with the OLI electrolytes package. The OLI electrolytes package allows a straightforward change of different salts as

UniSim can obtain all thermodynamic properties of salt solutions from it. The properties of well established salts like NaCl are predicted accurately by UniSim as shown in Fig. 4.5. However, potassium acetate is a novel salt solution and OLI underpredicts it for high concentrations as shown in Fig. 4.5 for KAc 9 m, where the experimental BPE is 2-3 times higher than OLI. For smaller concentrations the deviation between OLI and the experiments is 25 % to 35 % in Fig. 4.5. Thus, the MED model in UniSim can be used for low, but not for high concentrations.

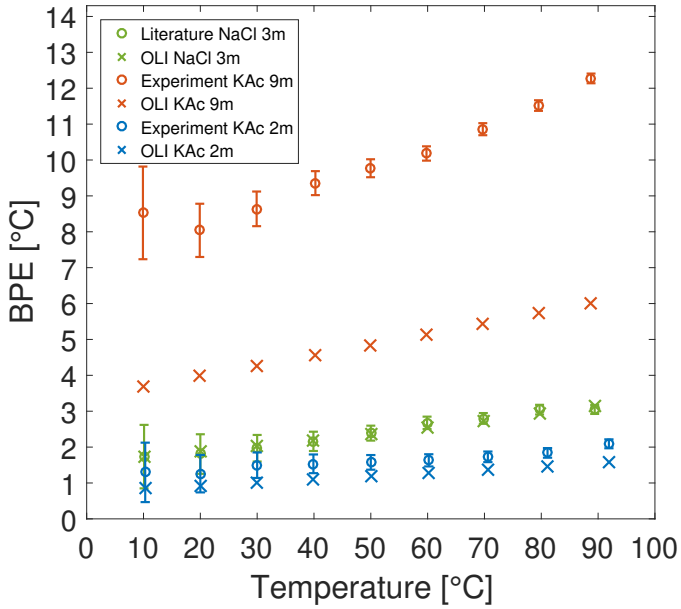


Figure 4.5: Comparison of the BPE calculated from VLE data from the Barker's cell test rig with OLI electrolytes. The vapour pressure of NaCl 3 m is taken from [101], whereas the data for KAc was measured as part of section 3.2.3.

Palenzuela et al. reported the scheme of a single MED effect [72] as shown in Fig. 4.6. The same scheme was implemented in UniSim as given in Fig. 4.6. Each process step of the MED effect was assigned a separate unit in UniSim. The flash vessel in Fig. 4.6 as well as the flash box use the respective pressure drop from the preliminary analysis as input value. The tube bundle condenses all the vapour from the previous effect to heat up the brine from the flash vessel (input: vapour fraction = 0). The main vessel is used to separate vapour from brine as it occurs around at the demister of the MED effect. The vapour from the main vessel is then partially condensed in the pre-heater before it is passed on to the next effect, while the brine from the main vessel is also passed on to the next effect.

The effect is inserted into the overall MED flow scheme as seen in Fig. 4.6. Four different MED schemes of 5, 15, 19 and 27 effects were implemented in UniSim to investigate different scenarios. Large numbers of effects have some practical disadvantages, as they are expensive to build, have a complex process design and require high top brine tem-

peratures. Hammond et al. estimated the investment cost of a 341,000 $m^3$/day MED desalination plant with 30 effects at USD 187 million in 1994 [118], which would be USD 370 million today at an average inflation of 2.8 %, but was never built. Moreover, TBT > 75 °C leads to significant scaling and corrosion within the process [70]. Thus, the large systems of 19 and 27 effects have only theoretical interest as they represent the maximum number of effects for the maximum energy efficiency.

A 3 stage MED system is presented in Fig. 4.7, where the first effect, the middle effect and the last effect can be seen in detail. The middle effect is the same unit as shown in the Fig. 4.6. Example results for each one of the streams in Fig. 4.7 are listed in Appendix C in detail. The example analysis investigated the system performance for seawater and a TBT of 80 °C, where PR = 2.4 and the STC amounts to 265 kWh/$m^3$.

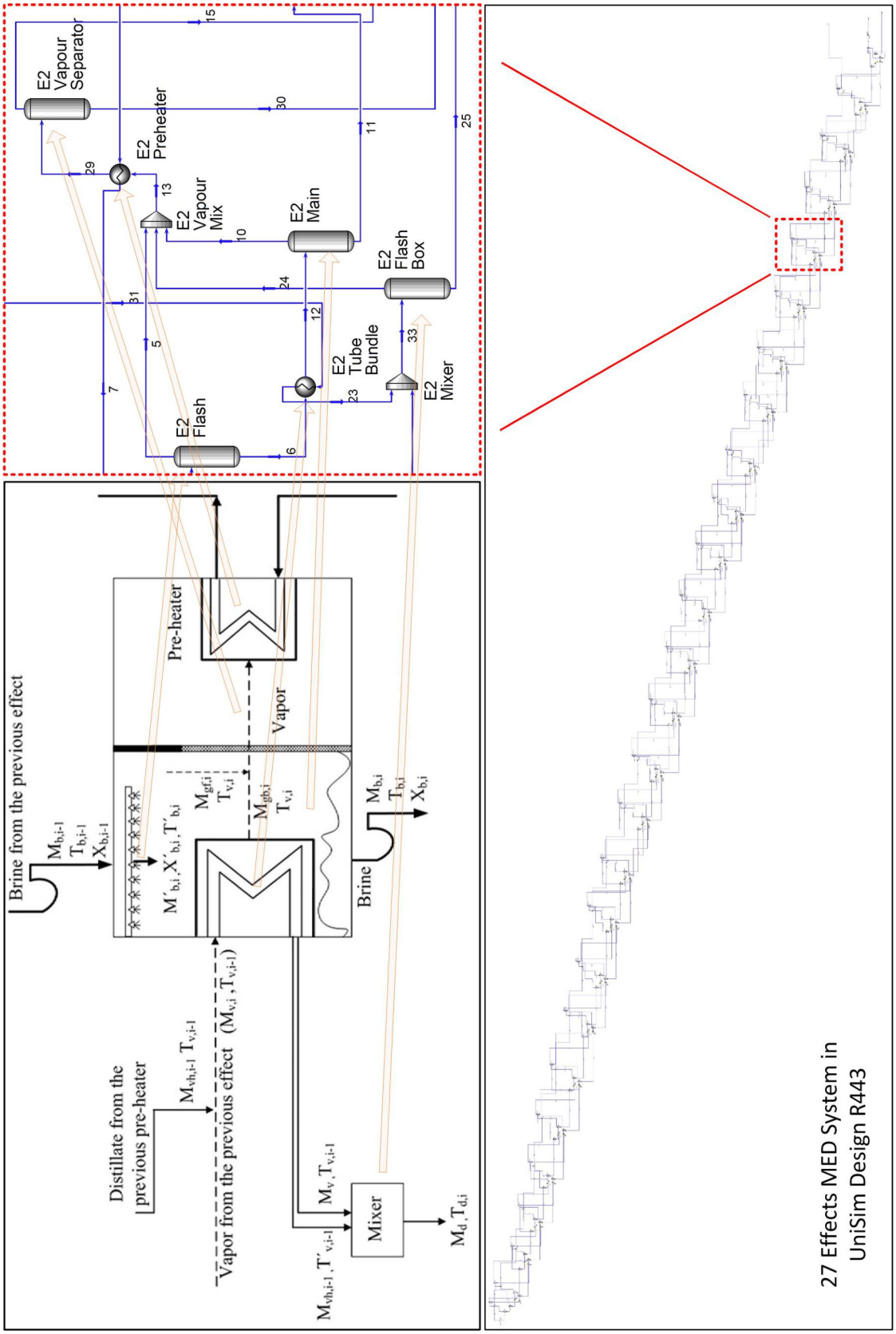


Figure 4.6: MED effect (from [72] with permission) implemented in UniSim and inserted into an exemplary 27 effects MED system

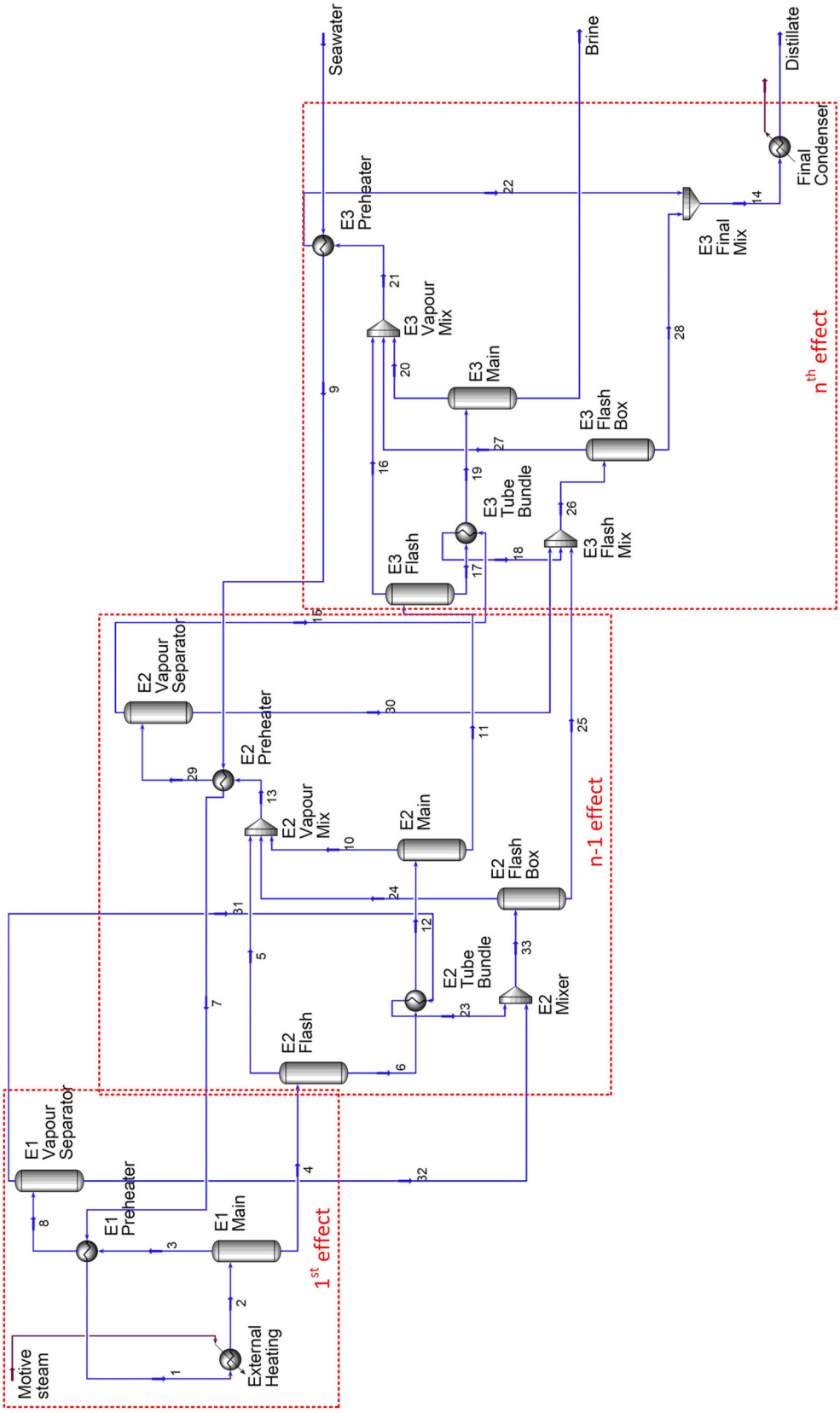


Figure 4.7: A detailed view of the MED UniSim model. The model can be extended by repetition of the middle effect (n-1).

### 4.1.3 Results

The analysis was conducted for LiCl and KAc as salts, because they were identified as best performing salts for the RED membrane [8, 119]. The inlet concentration of KAc was limited to 2 mol(KAc)/L on the basis of Fig. 4.5. The input values of the salt, N, $T_s$ and RR, as well as the results of the simulation are listed in table 4.1. The key performance indicators are presented in Fig. 4.8.

Table 4.1: Input (Salt, N, $T_s$ and RR) and results for 10 different cases and 2 different salts. The distillate production is 100 tons/day in all cases (≈ 4167 kg/s)

| # | Salt | N | $T_s$ | RR | Brine | Feed | $C_f$ | $C_b$ | Steam | STC |
|---|---|---|---|---|---|---|---|---|---|---|
| - | - | - | [°C] | - | [kg/s] | [kg/s] | [mol/L] | [mol/L] | [kg/s] | [kWh/m$^3$] |
| 1 | LiCl | 5 | 70 | 0.2 | 16667 | 20833 | 4.00 | 4.70 | 902.2 | 140.3 |
| 2 | LiCl | 5 | 70 | 0.1 | 37500 | 41667 | 4.00 | 4.09 | 950.0 | 147.8 |
| 3 | LiCl | 15 | 90 | 0.2 | 16667 | 20833 | 2.00 | 2.47 | 325.0 | 50.0 |
| 4 | KAc | 15 | 80 | 0.5 | 4167 | 8333 | 2.00 | 3.86 | 311.5 | 47.9 |
| 5 | KAc | 19 | 80 | 0.6 | 2778 | 6944 | 1.00 | 2.48 | 239.3 | 36.8 |
| 6 | KAc | 19 | 80 | 0.5 | 4167 | 8333 | 1.50 | 2.94 | 241.4 | 37.1 |
| 7 | LiCl | 19 | 80 | 0.5 | 4167 | 8333 | 1.00 | 2.01 | 259.1 | 39.9 |
| 8 | LiCl | 19 | 90 | 0.2 | 16667 | 20833 | 1.50 | 1.88 | 276.5 | 42.1 |
| 9 | KAc | 27 | 100 | 0.3 | 9722 | 13889 | 0.50 | 0.73 | 189.1 | 29.4 |
| 10 | LiCl | 27 | 100 | 0.7 | 1786 | 5952 | 0.50 | 1.65 | 179.8 | 28.0 |

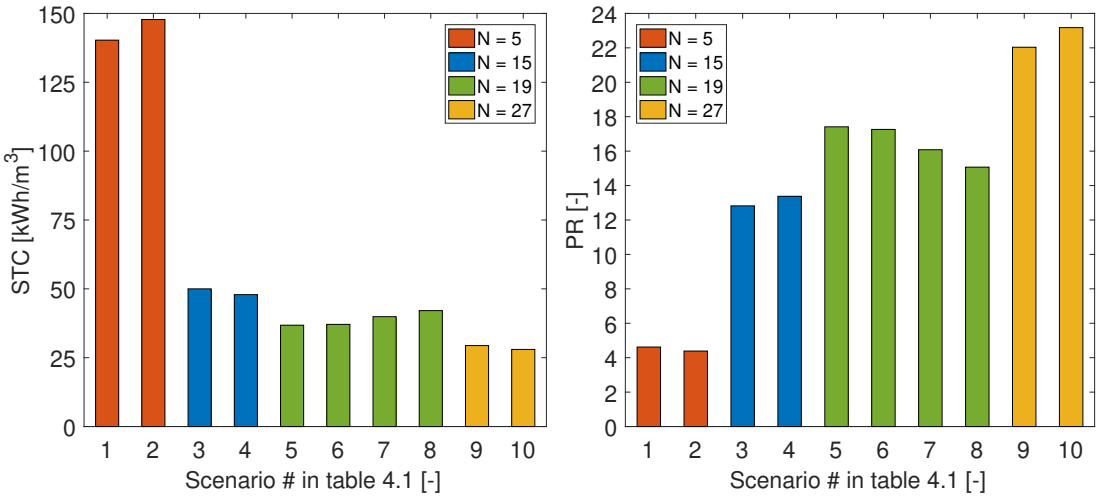


(a) (b)

Figure 4.8: (a) Modelled specific thermal consumption from table 4.1 of the MED system in UniSim grouped by the number of effects $N$.
(b) Modelled performance ratio of the system $PR \approx \dot{m}_d/\dot{m}_s$ from table 4.7.

From Fig. 4.8 it is evident that the STC is least dependent on the salt type: Between scenarios 9 and 10, the PR is slightly lower for KAc, but in scenario 6 the PR is higher than LiCl in scenario 7 (Fig. 4.8b). The comparison between 6 and 7 is more accurate

as both cases have the same TBT and RR. The most important factor for the STC is the number of effects. Each effect recycles the latent heat one more time, which is why the value of the PR is similar to the number of stages. For each N in Fig. 4.8, PR and STC remain almost constant. Moreover, the STC decreases proportionally with the number of effects e.g. $STC_{\#9} \approx N_{\#2} \cdot STC_{\#2}/N_{\#9}$. The recovery ratio affects the STC as well as the STC decreases by 5 % from #8 to #7 where the RR is changed from 0.2 to 0.5. A higher recovery ratio decreases the feed water at constant distillate production. At high RR, less feed water needs to be preheated from ambient to TBT which conserves energy. However, high RR also leads to higher brine concentrations and as a consequence thereof high BPE limiting N and higher risk of corrosion in a real MED plant.

The results are in line with the results of the validated model reported by Palenzuela et al. [115] in Fig. 4.9, where all input parameters are the same between the models, except the salt, where Palenzuela et al. used NaCl instead of LiCl/KAc here (table 4.1). The comparison with the validated model emphasises the high accuracy of the UniSim model. In addition, UniSim allows easy switching to different salts because of the OLI electrolytes packages. The EES model requires the manual implementation of thermodynamic salt properties, which is not necessary with UniSim.

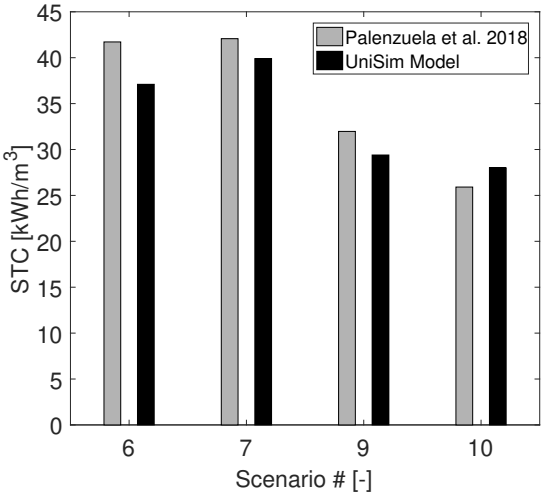


Figure 4.9: Comparison of the UniSim model presented here with Palenzuela et al. 2018 [115]. Both models use the same RR, N, TBT, $C_f$ from table 4.1 for each scenario respectively, but the salts differ. The salts used in the UniSim model are listed in table 4.1, while Palenzuela et al. use NaCl.

## 4.2 Multi effect distillation adsorption

Multi effect distillation can be coupled with adsorption desalination in order to increase the temperature range. Multi effect distillation operates between the heat source temperature and ambient temperature. By contrast, the addition of an adsorption heat pump enables the last MED stage to operate as low the freezing temperature of water as it was suggested by Ng et al. [74] and is shown in Fig. 2.6. The larger temperature window allows the increase of the number of effects. Ng et al. reported a doubled distillate production based on their modelling and experimental work [74], while Shazhad et al. documented a threefold increase of the distillate production [19]. Based on Ng and Shazhad et al. the combination of MED with AD was identified as a promising regeneration method for the RED Heat-to-Power cycle as well. Thus, the energy efficiency of MED-AD was investigated in a thermodynamic model combining the MED model of Palenzuela et al. [72] with the adsorption cycle analysis of Wu et al. [120].

### 4.2.1 Steady state multi effect distillation model

#### Input correlations

A linear temperature profile was implemented with the constraint of $\Delta T \geq BPE_i$. For most simulations a temperature difference of $\Delta T = 5$ K was set throughout all effects. This was used to find the vapour temperature $T_{v,i}$ [K] for each effect $i$ as model input values [121]:

$$T_{v,i} = T_{v,1} - (i-1) \cdot \Delta T_{stages} \tag{4.6}$$

Preheater temperatures:

$$T_{ph,i} = T_{feed,out} - (i-1) \cdot \Delta T_{ph} \tag{4.7}$$

#### Preheater

Some vapour $\dot{m}_{vh,i}$ [kg/s] is used to preheat the feed stream $\dot{m}_f$ [kg/s] within the effect. The feed enters the last effect at ambient temperature and needs to be heated up to 10 K below the heat source temperature, when it exits the preheater of the first effect and is then sprayed over the tube bundle of the first effect:

$$\dot{m}_{vh,i} \cdot L_{vh,i} = \dot{m}_f \cdot c_p \cdot (T_{ph,i+1} - T_{ph,i}) \tag{4.8}$$

where $T_{ph,i}$ [°C] is the inlet temperature to the preheater and $T_{ph,i+1}$ [°C] is the outlet temperature from the preheater. The heat transfer area necessary for the preheater is determined with the following heat transfer equation using the log mean temperature difference method [72]:

$$\dot{m}_f \cdot c_p \cdot (T_{ph,i+1} - T_{ph,i}) = A_{ph,i} \cdot U_{ph,i} \cdot LTMD_{ph,i} \tag{4.9}$$

$$LTMD_{ph,i} = \frac{(T_{v,i} - T_{ph,i+1}) - (T_{v,i} - T_{ph,i})}{ln\left(\frac{T_{v,i} - T_{ph,i+1}}{T_{v,i} - T_{ph,i}}\right)} \tag{4.10}$$

The overall heat transfer coefficient for the preheater is given by El-Dessouky and Ettourney [64]:

$$U_{ph,i} = 1.7194 + 3.2063 \cdot 10^{-3} \cdot T_{v,i} + 1.5971 \cdot 10^{-5} \cdot T_{v,i}^2 - 1.9918 \cdot 10^{-7} \cdot T_{v,i}^3 \tag{4.11}$$

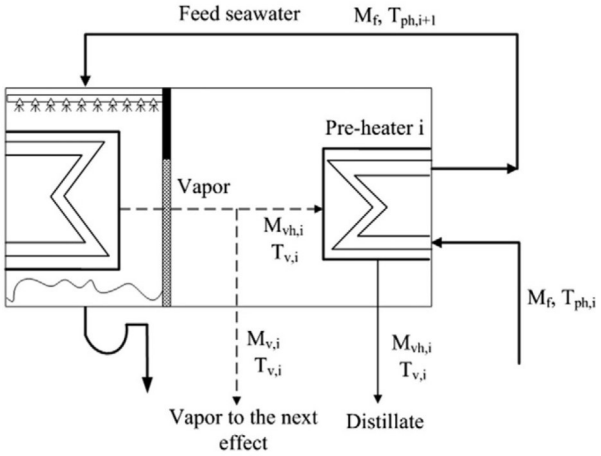


Figure 4.10: Preheater scheme applicable to all preheaters ([72] with permission)

**First Effect (with no flashing, but steam heating)**

The first effect is powered by the motive steam $\dot{m}_s$ [kg/s] coming from the low grade heat source. The feed temperature from the preheater is 10 °C below the top brine temperature or heat source temperature. Therefore, no flash evaporation occurs in the first effect leading to the following mass balance:

$$\dot{m}_f = \dot{m}_{gb,1} + \dot{m}_{b,1} \tag{4.12}$$

where $\dot{m}_{gb,1}$ is the vapour produced in the first effect and $\dot{m}_{b,1}$ is the brine from the first effect. The salinity of the brine $C_{b,1}$ [kg/kg] is assessed through the salt balance:

$$\dot{m}_f \cdot C_f = \dot{m}_{b,1} \cdot C_{b,1} \tag{4.13}$$

The following energy balance determines the amount of vapour produced in the first effect $\dot{m}_{gb,1}$ [kg/s]:

$$\dot{m}_{gb,1} \cdot L_{gb,1} = \dot{m}_s \cdot L_s + \dot{m}_f \cdot c_p \cdot (T_{b,1} - T_f) \tag{4.14}$$

The heat transfer equation to calculate the surface area of the heat exchanger:

$$\dot{m}_s \cdot L_s = U_{eff,1} \cdot A_{eff,1} \cdot (T_s - T_{b,1}) \tag{4.15}$$

$$U_{eff,i} = 1.9695 + 1.2057 \cdot 10^{-2} \cdot T_{b,i} - 8.5989 \cdot 10^{-5} \cdot T_{b,i}^2 + 2.5651 \cdot 10^{-7} \cdot T_{b,i}^3 \tag{4.16}$$

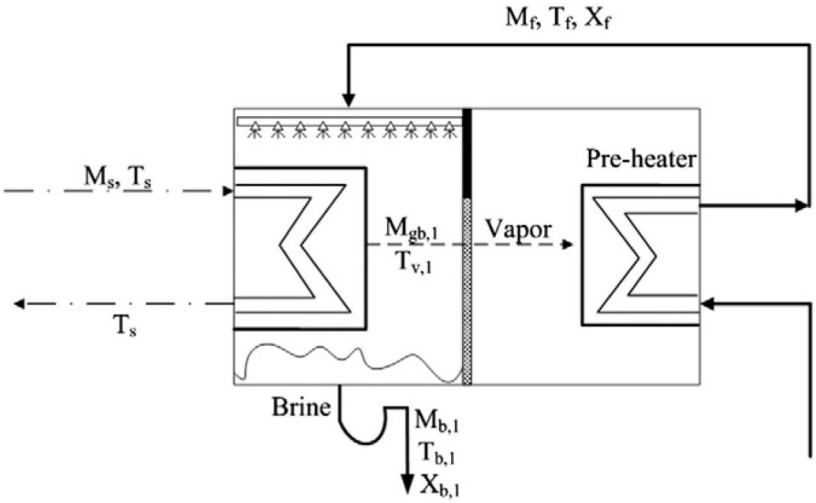


Figure 4.11: The first effect ([72] with permission)

## Subsequent effects

### General equations

The following energy and mass balances are applicable to all subsequent effects. The distillate production through flash evaporation $\dot{m}_{gf,i}$ [kg/s] is given by:

$$\dot{m}_{gf,i} = \frac{(\dot{m}_{b,i-1} \cdot c_{p,bi-1} \cdot (T_{b,i-1} - T_{bf}))}{L_{gf}} \tag{4.17}$$

where the temperature of the flash evaporated vapour is equal to the brine temperature and the vapour temperature from the tube bundle $T_{bf,i} = T_{b,i} = T_{v,i}$. The mass flow of the vapour from the previous effect $\dot{m}_{v,i}$ [kg/s]:

$$\dot{m}_{v,i} = \dot{m}_{gb,i} + \dot{m}_{gf,i} - \dot{m}_{vh} \tag{4.18}$$

The salt balance to determine the change of the brine concentration $C_{b,i}$ due to the evaporation within the effect is:

$$\dot{m}_{b,i-1} \cdot C_{b,i-1} = \dot{m}_{b,i} \cdot C_{b,i} \tag{4.19}$$

The heat transfer coefficient for the effect is taken from El-Dessouky and Ettouney [64]

$$U_{eff,i} = 1.9695 + 1.2057 \cdot 10^{-2} \cdot T_{b,i} - 8.5989 \cdot 10^{-5} \cdot T_{b,i}^2 + 2.5651 \cdot 10^{-7} \cdot T_{b,i}^3 \qquad (4.20)$$

Table 4.2: Effect type I, II and III assigned to effect number of a 16-effect MEDAD system

| | 1 | 2 | 3 | 4 | 5 | 6 | 7 | 8 | 9 | 10 | 11 | 12 | 13 | 14 | 15 | 16 |
|---|---|---|---|---|---|---|---|---|---|---|---|---|---|---|---|---|
| Type I | | Y | | | Y | | | Y | | | Y | | | Y | | |
| Type II | | | Y | Y | | Y | | | Y | | | Y | | | Y | |
| Type III | | | | | | | Y | | | Y | | | Y | | | Y |

**Effects of type I**

Fig. 4.12 shows an effect of the first type. The mass balance accounting for the distillate produced in the effect $\dot{m}_{d,i}$ [kg/s] in the tube bundle from vapour from the previous effect $i-1$:

$$\dot{m}_{d,i} = \dot{m}_{v,i-1} + \dot{m}_{vh,i-1} \qquad (4.21)$$

while the temperature of the distillate leaving the mixer $T_{d,i}$ [K] is obtained from the following energy balance:

$$\dot{m}_{d,i} \cdot c_p \cdot T_{d,i} = \dot{m}_{v,i-1} \cdot c_p \cdot T_{v,i-1} + \dot{m}_{vh,i-1} \cdot c_p \cdot T'_{v,i-1} \qquad (4.22)$$

The vapour generated through boiling $\dot{m}_{gb,i}$ [kg/s] is:

$$\dot{m}_{gb,i} = \frac{\dot{m}_{v,i-1} \cdot L_{v,i-1} + \dot{m}_{bf} \cdot c_{p,bf} \cdot (T_{bf} - T_{b,i}) + \dot{m}_{vh,i-1} \cdot c_{p,vi-1} \cdot (T_{v,i-1} - T'_{v,i-1})}{L_{gb,i}} \qquad (4.23)$$

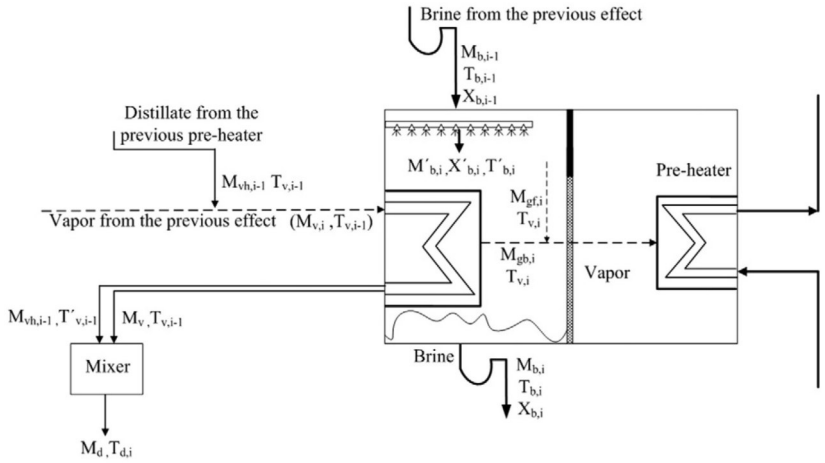


Figure 4.12: Scheme of a type I effect ([72] with permission)

### Effects of type II

The vapour generated through boiling $\dot{m}_{gb,i}$ [kg/s] in the second type of effect, which has a heat integration of a higher degree and reuses the sensible heat of the distillate from the previous effect $\dot{m}_{d,i-1}$ again:

$$\dot{m}_{gb,i} = \frac{\dot{m}_{v,i-1}L_{v,i-1} + \dot{m}_{bf}c_p(T_{bf} - T_{bi}) + \dot{m}_{vh,i-1}c_p(T_{v,i-1} - T'_{v,i-1}) + \dot{m}_{d,i-1}c_p(T_{d,i-1} - T'_{d,i-1})}{L_{gb,i}} \tag{4.24}$$

The produced distillate in this effect $\dot{m}_{d,i}$ [kg/s] is the sum of the three feed streams to the tube bundle as shown in Fig. 4.13:

$$\dot{m}_{d,i} = \dot{m}_{v,i} + \dot{m}_{vh,i-1} + \dot{m}_{d,i-1} \tag{4.25}$$

The energy balance around the mixer is used to calculate the distillate temperature $T_{d,i}$ [K]:

$$T_{d,i} = \frac{\dot{m}_{v,i}c_pT_{v,i-1} + \dot{m}_{vh,i-1}c_pT'_{v,i-1} + \dot{m}_{d,i-1}c_pT'_{d,i-1}}{\dot{m}_{d,i}c_p} \tag{4.26}$$

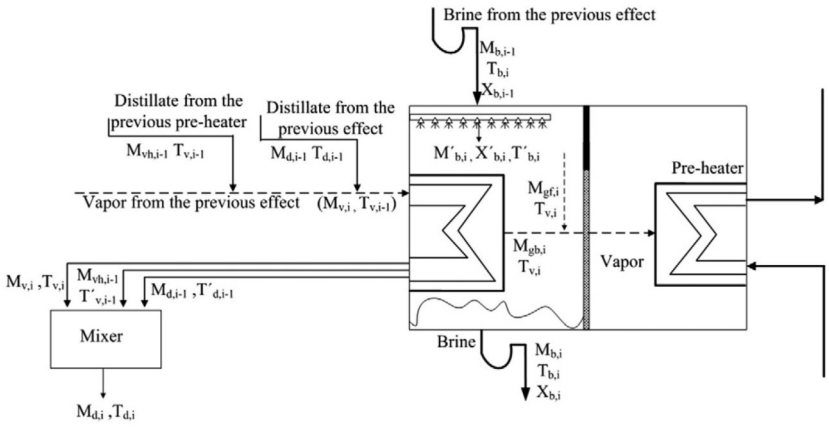


Figure 4.13: Scheme of a type II effect ([72] with permission)

### Effects of type III

The third type of effects has an even higher heat integration than type two as seen in Fig. 4.14. Type III reuses the remaining sensible heat of the distillate from the distribution line collecting the distillate of the previous three effects $\dot{m}_{da,i}$ with temperature $T_{dm,i-3}$:

$$\begin{aligned}\dot{m}_{gb,i}L_{gb,i} = \dot{m}_{v,i-1}L_{v,i-1} + \dot{m}_{bf}c_p(T_{bf} - T_{bi}) + \dot{m}_{vh,i-1}c_p(T_{v,i-1} - T'_{v,i-1}) + \\ \dot{m}_{d,i-1}c_p(T_{d,i-1} - T'_{d,i-1}) + \dot{m}_{da,i}c_p(T_{dm,i-3} - T'_{dm,i-3})\end{aligned} \tag{4.27}$$

The mass balance to determine the distillate from the tube bundle as the sum of the the vapour from the previous effect $\dot{m}_{v,i-1}$ [kg/s], the saturated liquid distillate from the previous preheater $\dot{m}_{vh,i-1}$ [kg/s], the distillate from the previous effect $\dot{m}_{di-1}$ [kg/s]

and the distillate from the distribution line:

$$\dot{m}_{d,i} = \dot{m}_{v,i-1} + \dot{m}_{vh,i-1} + \dot{m}_{d,i-1} + \dot{m}_{da,i} \tag{4.28}$$

The energy balance around the mixer is used to calculate the distillate temperature $T_{d,i}$ [K]:

$$T_{d,i} = \frac{\dot{m}_{v,i} c_p T_{v,i-1} + \dot{m}_{vh,i-1} c_p T'_{v,i-1} + \dot{m}_{d,i-1} c_p T'_{d,i-1} + \dot{m}_{da,i} c_p T'_{dm,i-3}}{\dot{m}_{d,i} c_p} \tag{4.29}$$

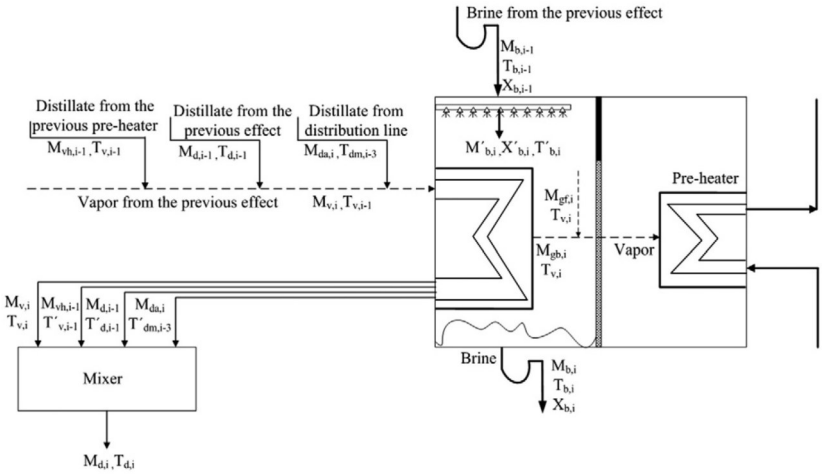


Figure 4.14: Scheme of a type III effect ([72] with permission)

### 4.2.2 Thermodynamic adsorption model

The main objective of the thermodynamic adsorption analysis is determining the specific energy consumption per kilogram of water produced, which is derived from the adsorption cycle. Required are the evaporator temperature $T_{ev}$ [K], which is the temperature of the last MED effect, the condenser temperature $T_1$ [K] of the adsorption system and the heat source temperature $T_3$ [K] which is equal to the TBT.
The Antoine equation with the parameters for water [102] is used to determine the pressures $P$ [bar] in the adsorption system and is valid for 255.9 - 373.0 K:

$$P_{sat} = 10^{4.6543 - \left(\frac{1435.264}{(T - BPE) - 64.848}\right)}; \tag{4.30}$$

where T is the current temperature [K], while the uptake of the adsorption material $q$ [$g_w/g_{sg}$] is calculated with the Dubinin Astakhov isotherm $DA$ equation [122], which is commonly used in adsorption desalination:

$$A = R \cdot T \cdot log\left(\frac{P_{sat}}{P}\right) \tag{4.31}$$

$$q = q_0 \; exp\left(-\left(\frac{A}{E}\right)^n\right) \tag{4.32}$$

where the DA fitting parameters E, n and the saturation uptake $q_0$ are given in table 4.3:

Table 4.3: Dubinin Astakhov paramters

| | $q_0$ [kg/kg] | E [J/mol] | n [-] | Ref. |
|---|---|---|---|---|
| Siogel | 0.38 | 3960 | 1.1 | [123] |
| AQSOA Z01 | 0.21 | 4000 | 5 | [23] |

The isosteric heat of adsorption $\Delta$h is [124]:

$$\Delta h = L + E \; ln\left(\frac{q_0}{q}\right)^{1/n} + \frac{E\alpha T}{n}\left(\frac{q_0}{q}\right)^{-(n-1)/n} \tag{4.33}$$

The Specific Energy Consumption $SEC$ [$kJ/kg_w$] determines the amount of energy required to produce 1 kg of distillate:

$$SEC = \frac{(q_1 C_{p,w} + C_{p,sg})(T_2 - T_1) + \left[C_{p,sg} + \frac{q_2+q_3}{2} C_{p,w}\right](T_3 - T_2) + (q_2 - q_3)\Delta h}{q_2 - q_3} \tag{4.34}$$

The energy consumption of the adsorption system $Q_{AD}$ [kJ/s] is calculated by:

$$Q_{AD} = (\dot{m}_{gb,n} + \dot{m}_{gf,n}) \cdot SEC \tag{4.35}$$

Where $\dot{m}_{gb,n}$ and $\dot{m}_{gf,n}$ add up to the vapour generated by the $n^{th}$ effect of the MED system, which is adsorbed by the silica gel of the adsorption system.
The STC [$kWh/m^3$] of the overall system is determined by:

$$STC = \frac{\dot{m}_s \cdot L + Q_{AD}}{3600 \cdot \dot{m}_d \cdot \rho} \tag{4.36}$$

In their early publications Ng et al. neglected the heat input to the adsorption side of the system as the system is utilising waste heat, which does not need to be accounted for [74]. This analysis takes all heat input into account as Shazhad and Ng did in a recent publication [125]. The analysis had the objective to determine the STC for each scenario by varying RR, N, $C_{feed}$ and $T_{feed}$

### 4.2.3 Results

Using the last MED effect as evaporator of adsorption desalination enables the operation of the adsorption system below ambient temperature. For all results, the feed inlet temperature to the preheater of the last effect was 30 °C, the temperature of the last MED effect 35 °C and the temperature of the last effect for the MEDAD process at 5 °C. A temperature of 5 °C prevents freezing, but also maximises the temperature

window of operation for the MED system, but it has some negative implications on the performance of the adsorption material.

The isotherms in Fig. 4.15 show the impact of the evaporation temperature on the working capacity of Siogel silica gel (Fig. 4.15a) and AQSOA ZO1 zeolite (Fig. 4.15b). The last MED effect functions as evaporator of the adsorption desalination part of MEDAD. In MEDAD, the last effect operates at 5 °C [74], whereas in adsorption desalination the evaporator operates at ambient temperature [17] (≈ 30 °C). The low temperature of the last MEDAD effect reduces the working capacity $\Delta q$ due to the low relative humidity $RH = P_{evap}/P_{sat,ads}$ during adsorption. A low relative humidity decreases the adsorption uptake. The relative humidity of MEDAD during adsorption is approximately 25 %, whereas it is approximately 90 % for adsorption desalination. Therefore, operating MEDAD as proposed by Ng et al. [74] with evaporation at 5 °C leads to a reduced working capacity of the adsorbent. Hence, very large adsorption beds would be required to link a MED plant to an adsorption desalination system.

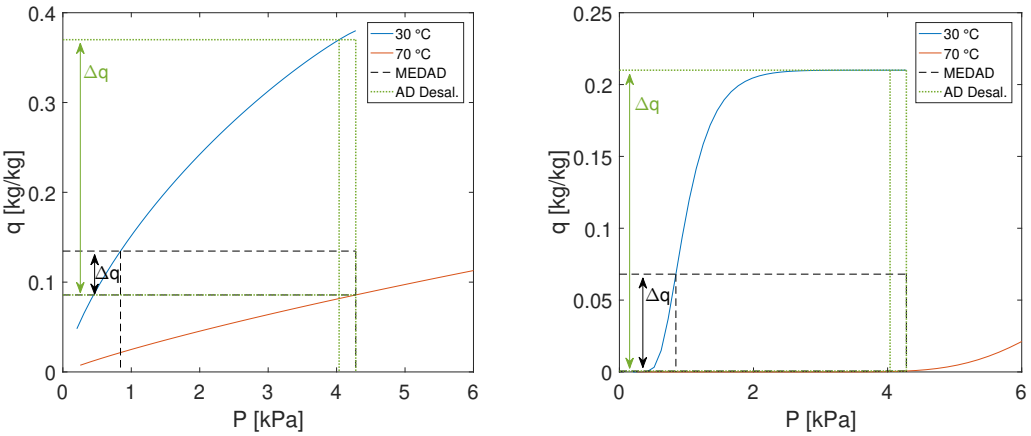


Figure 4.15: Cooling to 5 °C in a MEDAD plant reduces the working capacity of (a) Siogel silica gel and (b) Mitsubishi AQSOA Z01 zeolite.

The model assessed 59 different input scenarios as shown in appendix C.4 and C.5 or in an excerpt in table 4.4. Each one of the 59 scenarios was applied to the steady state MED model as well as the MEDAD model. The analysis determines the performance of MED first and then for the case of MEDAD adds additional effects to the MED below ambient temperature. Thus, the effects above ambient temperature are exactly the same for both cases MED and MEDAD. This way of comparison is in line with Thu et al. [126], who suggested that MEDAD could rejuvenate existing MED plants by increasing their distillate output by simple modification and adding additional effects. The recovery ratio varies between the two models, while the feed flow rate and the heat input to the first effect is the same for MED and MEDAD. The adsorption system requires additional heat input, which MED alone does not need. The larger temperature

difference between TBT and the last effects combined with the constant temperature drop of 5 °C allows an additional 6 effects for MEDAD (table 4.4).

Table 4.4: Excerpt from results tables C.4 and C.5 in the appendix, which are shown in Fig. 4.16. The salt is NaCl and Siogel as adsorption material.

| | | | **MED** | | | **MEDAD** | | |
|---|---|---|---|---|---|---|---|---|
| **Scenario Number** | **$C_f$ [mol/kg]** | **$T_s$ [°C]** | **RR** | **N** | **STC [kWh/m³]** | **RR** | **N** | **STC [kWh/m³]** |
| 1 | 0.5 | 60 | 0.1 | 5 | 220 | 0.4 | 11 | 185 |
| 2 | 0.5 | 60 | 0.3 | 5 | 167 | 0.8 | 11 | 153 |
| 3 | 0.5 | 70 | 0.1 | 7 | 193 | 0.3 | 13 | 184 |
| 4 | 0.5 | 70 | 0.3 | 7 | 134 | 0.6 | 13 | 144 |
| 5 | 0.5 | 70 | 0.5 | 7 | 122 | 1.0 | 13 | 130 |
| 6 | 0.5 | 80 | 0.1 | 9 | 180 | 0.3 | 15 | 185 |
| 7 | 0.5 | 80 | 0.3 | 9 | 117 | 0.6 | 15 | 138 |
| 8 | 0.5 | 80 | 0.5 | 9 | 106 | 0.8 | 15 | 123 |
| 9 | 0.5 | 90 | 0.3 | 11 | 109 | 0.5 | 17 | 136 |
| 10 | 0.5 | 90 | 0.5 | 11 | 95 | 0.8 | 17 | 117 |
| 11 | 0.5 | 90 | 0.7 | 11 | 90 | 1.0 | 17 | 107 |
| 12 | 0.5 | 100 | 0.3 | 13 | 103 | 0.5 | 19 | 134 |
| 13 | 0.5 | 100 | 0.5 | 13 | 90 | 0.7 | 19 | 113 |
| 14 | 0.5 | 100 | 0.7 | 13 | 85 | 0.9 | 19 | 102 |
| | | | | | | | | |
| 29 | 1.5 | 60 | 0.1 | 5 | 215 | 0.4 | 11 | 183 |
| 30 | 1.5 | 60 | 0.3 | 5 | 161 | 0.8 | 11 | 151 |
| 31 | 1.5 | 70 | 0.1 | 7 | 192 | 0.3 | 13 | 185 |
| 32 | 1.5 | 70 | 0.3 | 7 | 131 | 0.7 | 13 | 144 |
| 33 | 1.5 | 70 | 0.5 | 7 | 118 | 1.0 | 13 | 129 |
| 34 | 1.5 | 80 | 0.1 | 9 | 177 | 0.3 | 15 | 185 |
| 35 | 1.5 | 80 | 0.3 | 9 | 116 | 0.6 | 15 | 139 |
| 36 | 1.5 | 80 | 0.5 | 9 | 102 | 0.8 | 15 | 121 |
| 37 | 1.5 | 90 | 0.3 | 11 | 106 | 0.5 | 17 | 136 |
| 38 | 1.5 | 90 | 0.5 | 11 | 93 | 0.7 | 17 | 117 |
| 39 | 1.5 | 90 | 0.7 | 11 | 88 | 1.0 | 17 | 118 |
| 40 | 1.5 | 100 | 0.3 | 13 | 102 | 0.5 | 19 | 135 |
| 41 | 1.5 | 100 | 0.5 | 13 | 89 | 0.7 | 19 | 113 |
| 42 | 1.5 | 100 | 0.7 | 13 | 84 | 0.9 | 19 | 102 |

The STC for MED and MEDAD in each scenario of table 4.4 are shown in Fig. 4.16. The comparison between Fig. 4.16a and 4.16b shows that the salt concentration does not have an influence on the results. It can be seen that the STC of both systems are very similar, but in most scenarios MED has a slightly lower energy consumption to produce one cubic meter of distillate. MEDAD is only advantageous at low heat source temperatures $T_s < 70$ °C (Fig. 4.16c). Even in the best cases (scenario 1 and 29 in table 4.4), the STC is only 15 % lower for MEDAD than MED alone, while the MEDAD system is more than twice as big. Here, the first five effects are identical

between MED and MEDAD, but then MEDAD has six additional effects. The additional effects of the MEDAD system double the distillate output, but the energy input is also doubled. All the vapour of the last effects needs to be adsorbed by the silica gel beds, which in return needs to be desorbed by the low grade heat source. Shahzad et al. distinguished between payable and non-payable energy, where the heat input to the adsorption material is non-payable energy such as waste heat and does not need to be considered for the system efficiency [19]. For this reason, Shazhad et al. report extraordinary performances for MEDAD compared to MED alone.

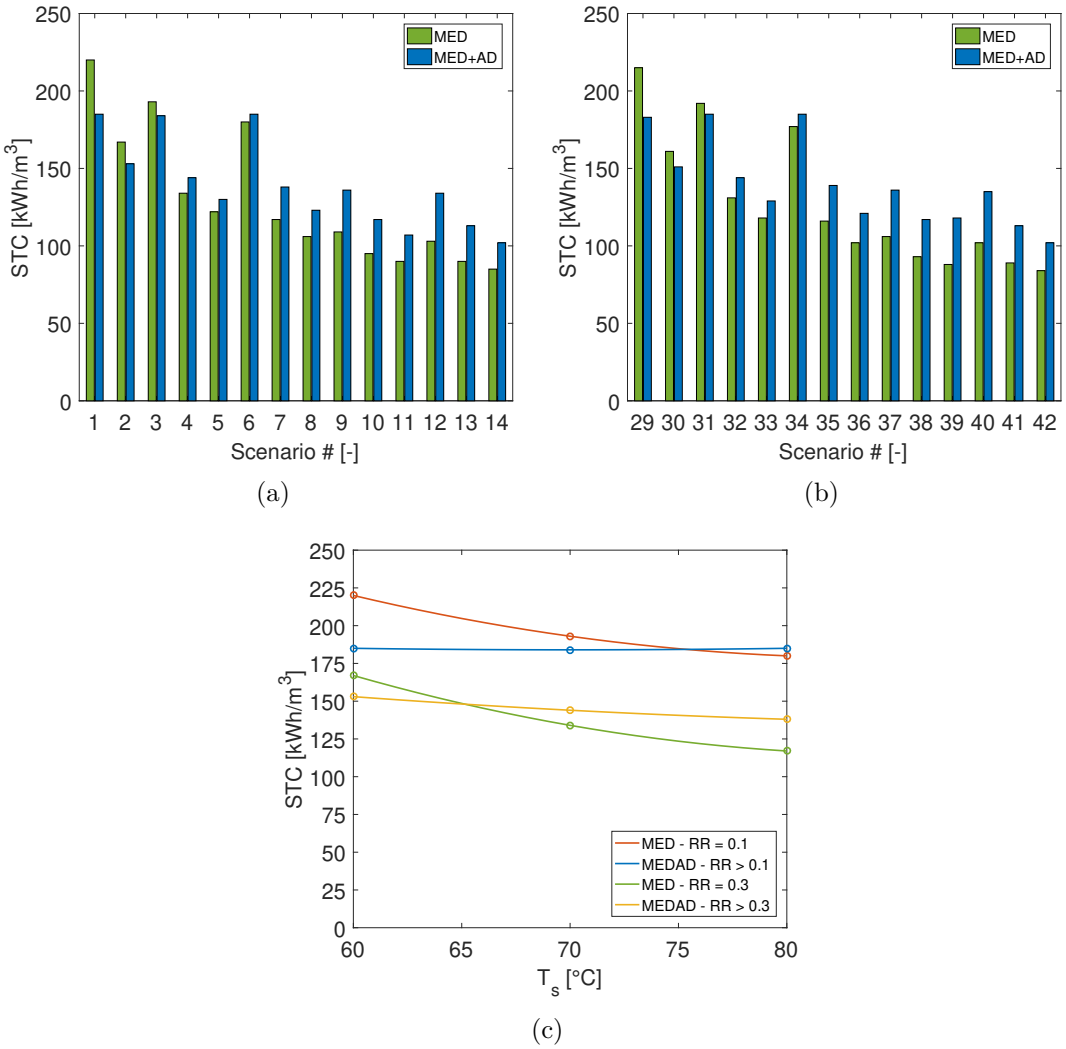


Figure 4.16: STC compared for MED and MEDAD as shown in table 4.4.
(a) The inlet concentration is constant for all cases at 0.5 mol/kg NaCl
(b) Inlet concentration of 1.5 mol/kg NaCl
(c) Comparison of MED and MEDAD at different heat source temperatures for an inlet concentration of 0.5 mol/kg. N and RR varies between the data points. Scenarios # 1, 3 and 6 for RR = 0.1 and Scenarios # 2, 4 and 7 for RR = 0.3 in table 4.4

When the energy to the first MED effect and the AD system are both considered the

benefits of the increased temperature gap falls behind the additional energy requirements of the MEDAD system. In addition, the benefit of the bigger temperature gap is debatable as well. The analysis in Fig. 4.3 shows that the BPE for seawater desalination is comparably low at about 0.4 °C, where the BPE is the minimum temperature difference between two effects. The additional temperature difference facilitates the heat transfer from one effect to the next. Thus, well-designed heat exchangers could allow as many MED effects as MEDAD would allow from an economical point of view. Hammond et al. presented the design of MED with 30 effects vertically arranged in a 160 m high tower and TBT = 110 °C [118]. Al-Shammiri and Safar reviewed MED plants and reported systems between 4 and 55 effects [70]. Thus, the temperature gap for MED alone is already big enough to build very large systems. However, MEDAD can be an option to increase the distillate output of an existing MED plant by adding additional effects without increasing the STC as it was also suggested by Thu et al. [126].

## 4.3 Absorption Vapour Compression

Absorption heat pumps can be combined with multi effect distillation similar to MED-AD to increase the temperature frame of the MED system below ambient temperatures and with it the number of stages. Another application for absorption systems is Single effect Absorption Vapour Compression *ABVC* as described by El-Dessouky and Ettouney [64]. El-Dessouky and Ettouney reported that the system can utilise heat sources between 50 °C to 100 °C, where it achieves performance ratios 2.5 to 3. The simplicity of the system combined with the high performance ratio make ABVC an interesting option for the RED Heat-to-Power process.

### 4.3.1 UniSim modelling

The ABVC system consists of a single stage absorption heat pump and an evaporator effect. The evaporator effect is thermally integrated with the absorption heat pump, while having to separate salt solutions. The absorption cycle utilises a 27 wt-% LiBr solution, which is separate from the seawater feed to the evaporator effect. The heat integration allows the exchange of heat between the two: the heat of absorption is used to preheat the feed stream, the hot vapour from the absorption generator is used to heat the tube bundle inside the evaporator effect by transferring its sensible and latent heat into the seawater. On the other hand, the LiBr-solution absorbs colder vapour extracted from the evaporator effect. The motive steam is heating the absorption generator at 90 °C in Fig. 4.17 and no external heat is supplied to the seawater evaporator.

UniSim offers the advantage of using the OLI electrolytes package to precisely assess all the properties of the two salt solutions. NaCl and LiBr are common salts reported in numerous publications and OLI can be very accurate in this case. In addition, the ABVC system solely consists of standard components present in UniSim, which allows a straightforward implementation of the system to test the performance. The system has been reported in the literature [64], but the performance analysis of El-Dessouky and Ettouney is rather basic and not as accurate in the thermodynamics as UniSim. Thus, this study aimed at replicating the flow-scheme reported by El-Dessouky and Ettouney and to assess the STC of the system in one single waste heat source case of 90 °C. The model of El-Dessouky and Ettouney already showed a temperature independence of ABVC on the PR between 50 and 100 °C for seawater [64]. Here, the impact of the salt type and concentration are investigated for LiCl and NaCl. The lowest molality of 1 mol/kg is similar to the concentration of seawater, whereas the higher concentrations are of interest for the RED Heat-to-Power process, where a higher salinity leads to a higher Gibbs free energy of mixing, which can be converted into electricity by Reverse Electrodialysis.

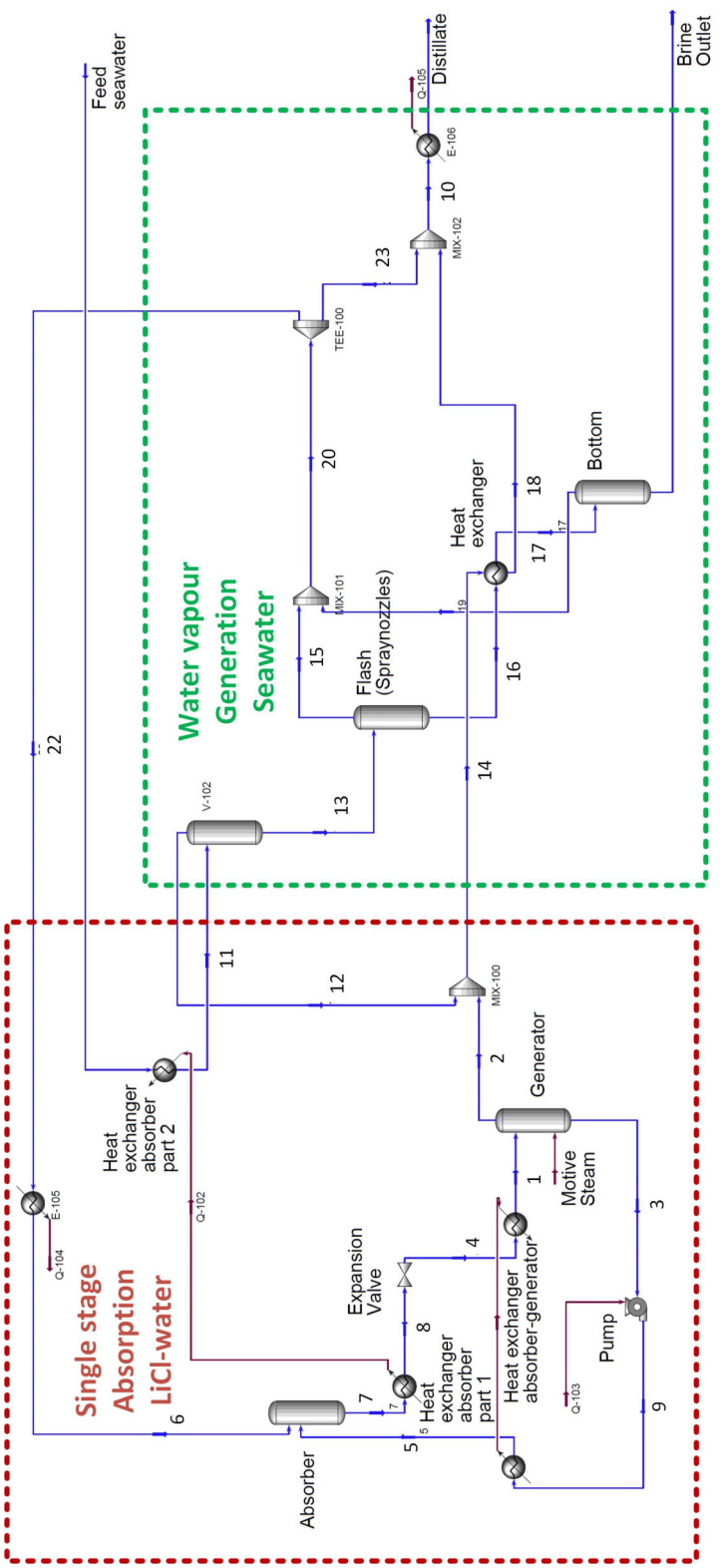


| Stream | | Feed | Brine | Distillate | 1 | 2 | 3 | 4 | 5 | 6 | 7 | 8 | 9 | 10 |
|---|---|---|---|---|---|---|---|---|---|---|---|---|---|---|
| Vapour Fraction | - | 0.00 | 0.00 | 0.00 | 0.00 | 0.00 | 0.00 | 0.00 | 0.00 | 1.00 | 0.19 | 0.00 | 0.00 | 0.36 |
| Temperature | kPa | 25.00 | 36.00 | 31.95 | 70.00 | 87.67 | 87.67 | 60.00 | 74.45 | 40.00 | 90.70 | 59.88 | 87.86 | 31.95 |
| Mass Flow | kg/h | 10.00 | 6.21 | 3.79 | 10.00 | 1.19 | 8.81 | 10.00 | 8.81 | 1.19 | 10.00 | 10.00 | 8.81 | 3.79 |
| Heat flow | kJ/h | -1.45E+05 | -8.50E+04 | -6.00E+04 | -9.00E+04 | -1.58E+04 | -7.26E+04 | -9.21E+04 | -7.28E+04 | -1.59E+04 | -8.87E+04 | -9.21E+04 | -7.26E+04 | -5.67E+04 |

| Stream | | 11 | 12 | 13 | 14 | 15 | 16 | 17 | 18 | 19 | 20 | 22 | 23 | |
|---|---|---|---|---|---|---|---|---|---|---|---|---|---|---|
| Vapour Fraction | - | 0.14 | 1.00 | 0.00 | 1.00 | 1.00 | 0.00 | 0.32 | 0.00 | 1.00 | 1.00 | 1.00 | 1.00 | |
| Temperature | kPa | 37.83 | 37.83 | 37.83 | 62.10 | 34.36 | 34.36 | 36.02 | 35.37 | 36.02 | 35.99 | 35.99 | 35.99 | |
| Mass Flow | kg/h | 10.00 | 1.27 | 8.74 | 2.45 | 0.04 | 8.69 | 8.69 | 2.45 | 2.48 | 2.52 | 1.19 | 1.34 | |
| Heat flow | kJ/h | -1.42E+05 | -1.70E+04 | -1.25E+05 | -3.27E+04 | -5.62E+02 | -1.25E+05 | -1.19E+05 | -3.88E+04 | -3.32E+04 | -3.38E+04 | -1.59E+04 | -1.79E+04 | |

Figure 4.17: The absorption vapour compression scheme of El-Dessouky [64] implemented in UniSim using the OLI electrolytes package.

### 4.3.2 Results

The ABVC system's performance for two different salts and feed salinities are shown in Fig. 4.18. In case of NaCl, the performance is independent of the salinity. In case of LiCl, the performance decreases by 5 % from 1 m to 5 m and decreases by 20 % compared between 1 m and 10 m. LiCl has a higher BPE than NaCl leading to a larger concentration dependency of the energy consumption. The water vapour from a salt solution is superheated by the BPE. Thus, a higher BPE leads to a lower condensation temperature of the vapour, which reduces the energy efficiency. However, compared to other desalination systems like MED the 20 % performance decrease is small, because the high BPE limits the number of effects and the MED performance significantly.

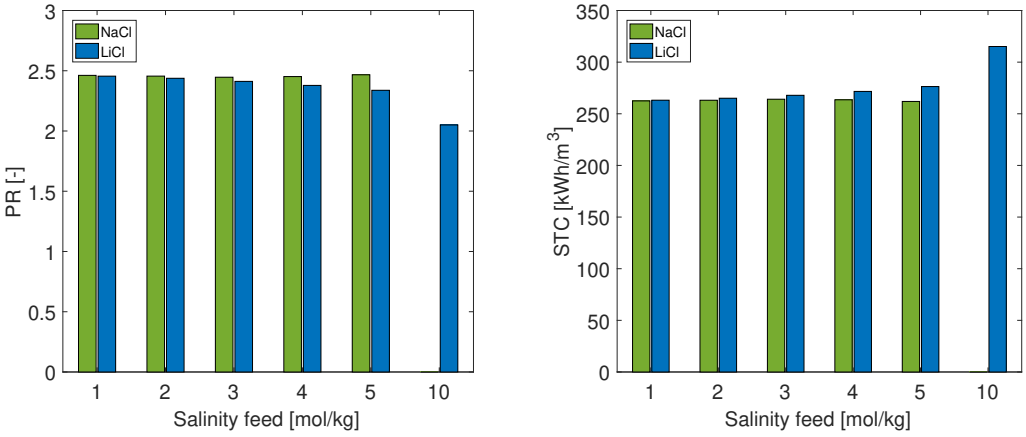


(a) (b)

Figure 4.18: The influence of the feed salinity on the system performance. $T_{feed,in}$ = 25 °C and $T_s$ = 90 °C
(a) Performance Ratio. (b) Specific Thermal Consumption.

Fig. 4.19a assesses the number of effects a MED plant can have for LiCl at feed salinity of 10 m. The BPE in Fig. 4.19a was assessed through the water activities $a_w$ of LiCl [127] and $P_{sat,LiCl} = P_{sat,w} \cdot a_w$, where the saturation pressure of pure water $P_{sat,w}$ can be calculated with NIST REFPROP [103]. LiCl at 10 m has a BPE of 17-23 °C. The high BPE limits the number of MED effects to 3 (Fig. 4.19a), because superheated steam evaporates in each effect at $T_{v,i}$, which can only be condensed at $T_{v,i} - BPE_i$ in the next effect resulting in a maximum number of 3 effects despite $T_s$ = 90 °C.
A three effect MED system is shown in UniSim in Fig. 4.7, where the feed concentration was adjusted to 10 m, the salt to LiCl and the heat source temperature to 90 °C for the purpose of the comparison in Fig. 4.19b. In Fig. 4.19b, the two systems achieve similar PR at a feed concentration of 10 m. Fig. 4.19b shows that ABVC has the same PR ≈ 2 and STC ≈ 300 kWh/m$^3$ as MED has under the same conditions. Both systems require 3 main vessels, but ABVC has only 4 heat exchangers, whereas three MED effects need 7 heat exchangers in total. This in combination with the comparable

performance make ABVC a striking alternative to MED for high salt concentrations. However, ABVC has never been investigated experimentally [64] and there remains a strong need to prove the concept experimentally.

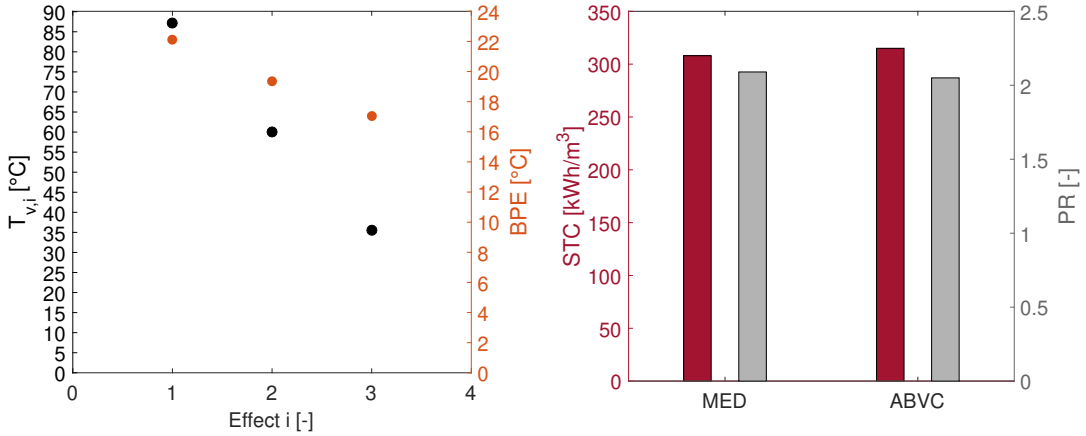


(a) (b)

Figure 4.19: The influence of the feed salinity on the system performance. $T_{feed,in}$ = 25 °C and $T_s$ = 90 °C
(a) A MED system with an aqueous LiCl feed at 10 m and $T_s$ = 90 °C can only have 3 effects, while the BPE is 17-23 °C.
(b) The 3-effect MED system compared to ABVC with an aqueous LiCl feed at 10 m and $T_s$ = 90 °C for both systems

## 4.4 Conclusions

Three different desalination technologies have been investigated in terms of their Specific Thermal Consumption assessing the thermal energy required to produce a cubic meter of water. Multi effect distillation is known as one of the most energy efficient ways to produce distilled water at a large scale. The first part of the investigation shows the importance of the number of effects on the MED system performance and how it is determined. The minimum temperature difference between two effects is the boiling point elevation of the brine solution. However, the heat exchangers within the effect require a certain temperature difference between the inside and the outside as well. Improving the heat exchangers and minimising the required temperature difference allows maximising the number of effects and with it the energy efficiency. For example, the investigation in UniSim showed that a MED system of 5 effects has STC ≈ 145 kWh/m$^3$, while a system of 27 effects has STC ≈ 30 kWh/m$^3$. Moreover, the investigation demonstrated that the main factor determining the thermal efficiency is the number of effects. One aspect determining the number of effects is the heat source temperature, because a larger temperature window between heat source and ambient temperatures allows more effects to operate in between. Factors like salt type and concentration affect the STC by up to 15 % at the same number of effects based on the scenarios investigated,

which is much less than the number of effects. However, salt type and concentration limit the maximum number of effects. A 10 mol/kg feed solution of LiCl allows only 3 MED effects at a high heat source temperature $T_s = 90$ °C. In this case, MED is less advantageous compared to other desalination system like Absorption Vapour Compression, where both systems achieve STC $\approx 300$ kWh/m$^3$. Absorption Vapour Compression features a simpler process design and the STC is almost independent of the salt concentration as the STC increases by 20 % when the LiCl feed salinity is increased from 1 to 10 mol/kg.

Some authors have suggested combining MED with Adsorption Desalination forming a MEDAD system. MEDAD increases the maximum number of effects compared to MED alone as the adsorption desalinator works like a heat pump cooling the last effect down to 5 °C instead of ambient temperature. Additional effects can be added to MED below ambient temperature increasing the distillate output. However, the adsorption beds require additional energy input, which needs to be added to the STC. Therefore, the simulations in a thermodynamic model in Matlab showed that MED and MEDAD have almost the same performance. Only at very low heat sources below 60 °C MEDAD has a slightly better performance than MED alone. In addition, an isotherm analysis showed that adsorption materials utilise less than a third of their saturation capacity, when the last effect is operated at 5 °C. Hence, the silica gel adsorption beds of a MEDAD system would be large when the working capacity is about 0.05 $g_w/g_{sg}$. Therefore, MEDAD was discarded for further study and the focus was laid upon adsorption desalination alone for further investigations.

# Chapter 5

# Experimental adsorption test rig

Adsorption desalinators evolved from adsorption chillers, have a similar design, but are operated differently as cooling is sacrificed for a large working capacity. Several adsorption desalinators have been presented and tested in the literature, but their design is large (> 10 kg). The best performing system in the literature is also the largest with 144 kg of silica gel split between four beds [17].
The currently world's smallest, reported system was designed, built and tested here. It can be operated with as little as 0.025 kg of adsorption material. The small scale enables testing of non-commercial adsorption materials, which cannot be obtained in large quantities yet. In addition, the system is designed in a modular way to easily change components (e.g. heat exchanger, vessels). The design has been presented at the International Conference on Applied Energy, Hong Kong 2018 [128] and in a publication [129].
Silica gel was first tested comprehensively as benchmarking material to show the system performance in comparison to larger systems in the literature. The results have been presented in [130].
Afterwards the investigation moved to an Ionogel material, which has never been tested in adsorption desalination before. First experimental results have been shown in [131].

## 5.1 Design

### 5.1.1 An overview of the adsorption test rig

The adsorption test rig is designed to utilise low-grade heat up to 90 °C. An image of the entire set-up can be seen in Fig. 5.1.
The four adsorber vessels are secured on an aluminium frame. The vessels are connected to the pipework of the heating and cooling cycle, which features rotameters to determine the flow rates and three thermostatic baths. The thermostatic baths provide water at three temperature levels: desorption < 100 °C, adsorption/condensation 20-35 °C and evaporation 5-35 °C. The system is controlled by a Labview code on a PC through a DAQ board and Modbus communication protocol. The copper line in the back of

the photo shown in figure 5.1 supplies compressed air to the electro pneumatic valves interconnecting the vessels. All the main items used to build the rig are listed in the appendix A.2 with the exception of a detailed list of the fittings and other minor components.

### 5.1.2 Computer-aided design and assembly

The test rig was designed in a computer-aided design *CAD* software (Siemens Solid Edge ST9) in a 3D model. The 3D design aimed to help the workshop in building the real test rig. Having the test rig in a 3D computer model helped to make sure that all the vessels are compatible to each other during the assembly. The drawings of each vessel are shown in detail in appendix chapter D.1. Fig. 5.2a presents a 2D drawing of the four vessels and Fig. 5.2b shows the four vessels during construction of the test rig in the technical workshop of the School of Engineering at the University of Edinburgh. The vessels are made of 316L stainless steel sheets with a thickness of 3 mm. The sheets were machined to size by the technical workshop and welded together. ISO-KF vacuum flanges in 316L steel were acquired in DN10, DN16, DN25 and DN40 (Pfeiffer, Germany). A full item list is given in appendix A.2. The DN10 flanges are used for the thermocouple feedthroughs and to connect vacuum ball valves (Vacom, Germany) to the vessels. The adsorbers are connected to the condenser using DN16 flanges and to the evaporator using DN25 flanges. Electro-pneumatic valves are assembled between the connections between the vessels as seen in Fig. 5.2b. The valves are very durable and have large orifices (DN16 and DN25) for the vapour to flow between the vessels. Evaporator and condenser each have DN40 viewports (Pfeiffer, Germany), which are connected to the vessel by the DN40 flanges. The assembled test rig sits on an aluminium frame to be accessed from all sides (Fig. 5.2b).

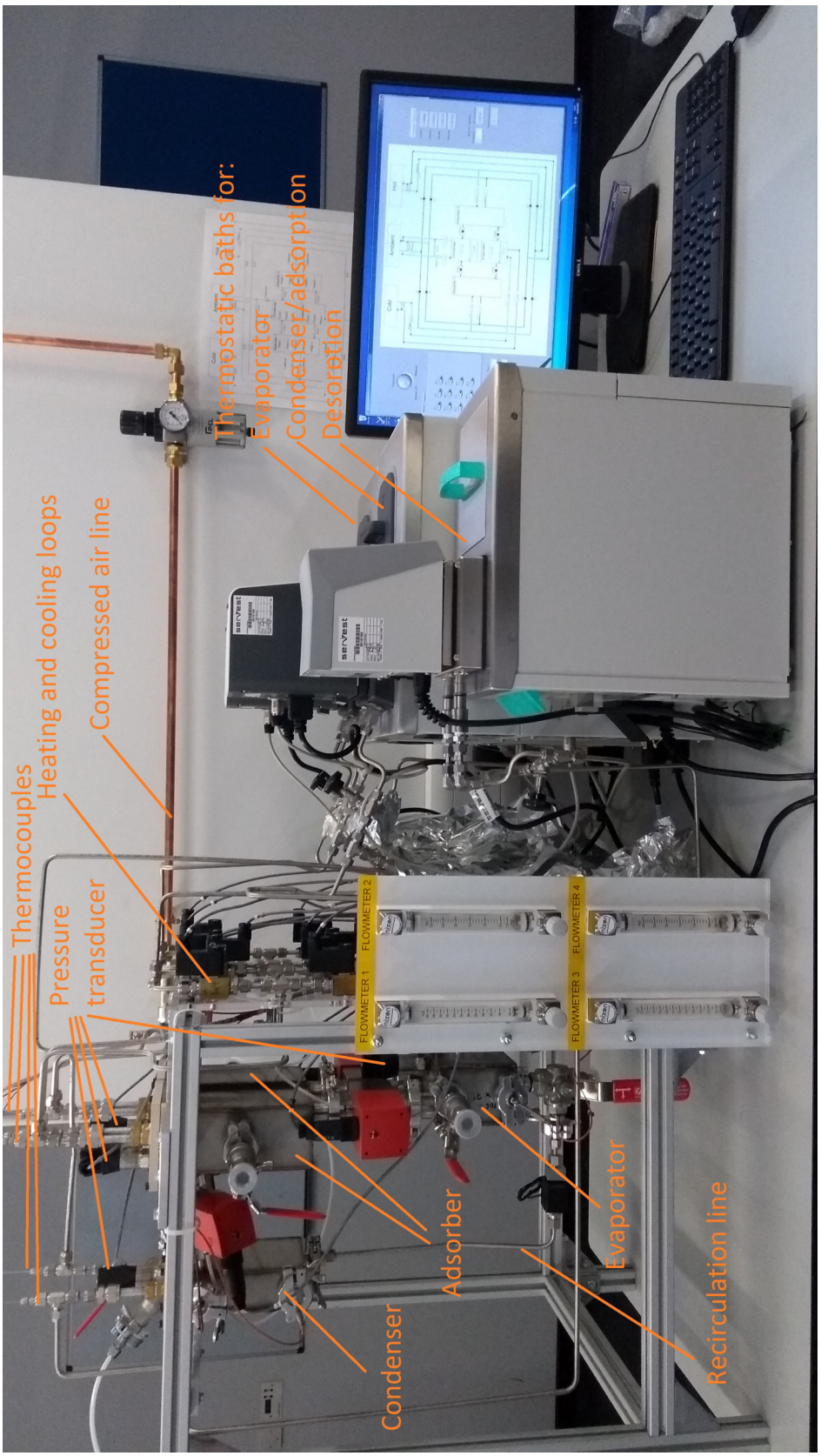


Figure 5.1: The adsorption test rig from left to right: The four adsorber vessels, the heating/cooling cycle, the thermostatic baths and the control PC.

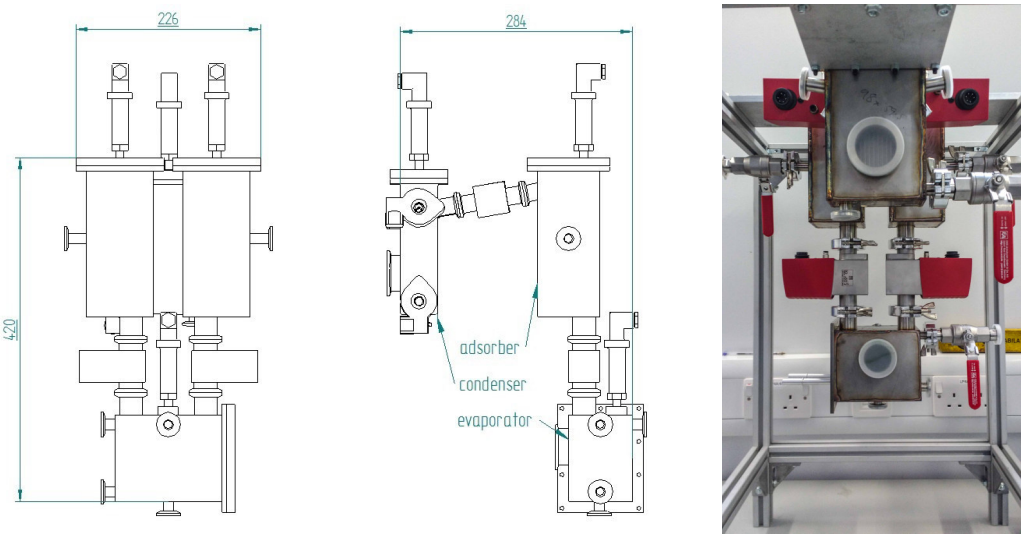


(a) (b)

Figure 5.2: (a) Computer-aided design front and side view of test rig.
(b) The assembled vessels mounted on their aluminium frame for the first time.

### 5.1.3 Process design

Two water loops simplify the piping of the system [132] and supply water from the thermostatic baths to the heat exchangers. The thermostatic baths provide heating or cooling water at three different temperature levels: cold, ambient and hot (Fig. 5.3a). Much larger heat sources are usually required to supply the beds of adsorption desalinators. By contrast, regular thermostatic baths are sufficient to heat and cool the 0.2 kg of silica gel inside each bed. The pipework, the heating and cooling loops and the rotameters can be seen in Fig. 5.3b.
The system features a recirculation line (Fig. 5.3c) and heat recovery (Fig. 5.3d). A heat recovery system improves the energy efficiency of the system by connecting the two adsorbers (Fig. 5.3a). No additional pumps are required for the heat recovery, because the pumps of the thermostatic baths are sufficient to pump water through the two adsorber heat exchangers in series. The heat recovery system uses two stainless steel solenoid valves (Type Ja, Connexion, UK/China) allowing to flow cold water through the hot adsorber bed after the end of a half cycle. The cold water is heated and flows through the cold bed afterwards transferring the heat to the cold bed. The recirculation line features a vacuum solenoid valve (Pfeiffer Vacuum, Germany) that connects condenser and evaporator.

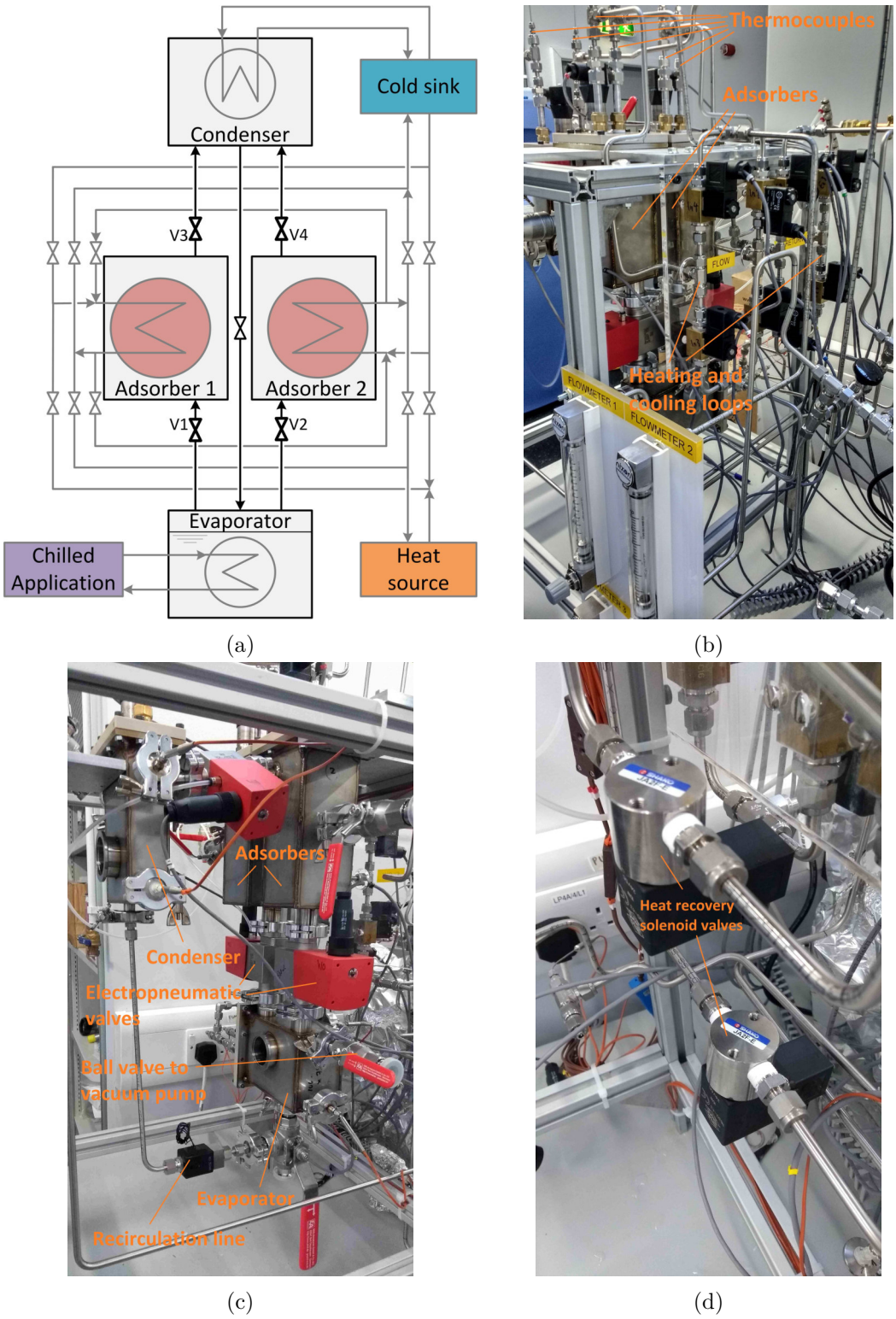


Figure 5.3: (a) The flow diagram of the adsorption test rig. (b) Photograph of the pipework supplying the test rig with heating and cooling water. (c) Recirculation line connecting condenser and evaporator. (d) Heat recovery solenoid valves.

### 5.1.4 Heat exchanger design

The heat exchangers inside the vacuum vessels are some of the most important components of the system. Therefore, it is important to select and design them carefully. However, the heat exchanger size required by the small-scale adsorption test rig is generally difficult to obtain as commercial heat exchangers are usually much bigger. Hence, custom-made heat exchangers were obtained.

This work investigated two different heat exchanger designs and materials to allow a better understanding on their impact on the system performance. Each one of the two different heat exchanger sets was made of a different material and a different geometry within the constraints given by the vessels. The materials were evaluated on the basis of their thermal diffusivity.

#### The geometrical design of the heat exchangers

The geometries of the two heat exchanger designs are shown in figure 5.4. The aluminium heat exchangers were manufactured by RC Racing (Cellole, Italy), while the copper heat exchangers were manufactured by Coolex Heat Transfer Ltd (Nottingham, UK). The geometrical design was influenced by the requirement of the process as well as the experiences of the manufacturers. The first heat exchangers have a finned design with channels to hold the silica gel beads. The water flow channels have baffles to increase the turbulence and thereby improve the heat transfer.

The second heat exchanger is inspired by a design which was popular from the 1920's to the 1950's, which was then superseded by the packed construction core. The packed construction core was adapted for the evaporator (Fig. 5.5). The design of the copper heat exchangers seemed ideal for the adsorption process, because it allows water vapour to access the material from all directions. Moreover, the new design requires less material than the aluminium design, which also resulted in the lower weight of the copper heat exchangers (500 g) compared to the aluminium heat exchangers (600 g). The lower weight is an important feature and could be achieved by reduced wall thickness, because the density of copper is three times higher than aluminium. Therefore, the improved thermal conductivity and heat capacity were expected to reduce the energy input required to heat/cool the material as well as improve the heat transfer. The open design also allowed to load more silica gel into the heat exchangers by increasing the capacity from 200 g to 250 g. The increased weight of silica gel and the reduced weight of copper resulted in an improved heat exchanger to silica gel mass ratio of 2:1 from 3:1. Copper has another advantage, as brass fittings are readily available to avoid corrosion, while aluminium fittings are rare.

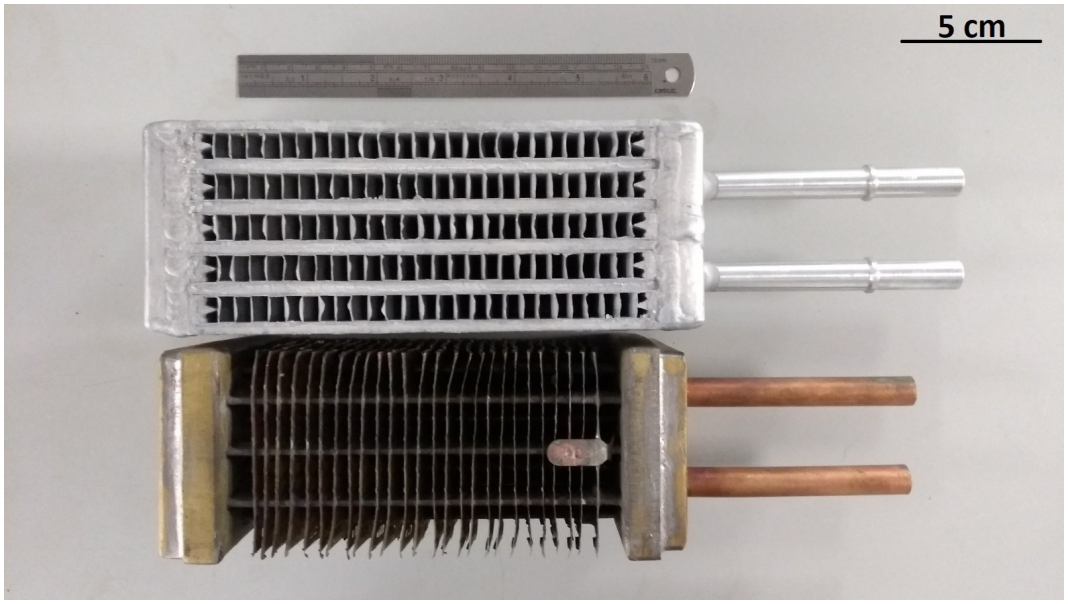


Figure 5.4: The adsorber heat exchangers: (top) aluminium, (bottom) copper.

The aluminium heat exchangers of the evaporator and condenser are shown in Fig. 5.5 with a mass of 150 g and 415 g respectively. The evaporator heat exchanger is placed flat, horizontally, and fully submerged in the liquid phase, while the condenser heat exchanger is operated vertically in the vapour phase. The finned design of the condenser heat exchanger allows condensed water droplets to flow down the heat exchanger towards the bottom of the condenser vessel.

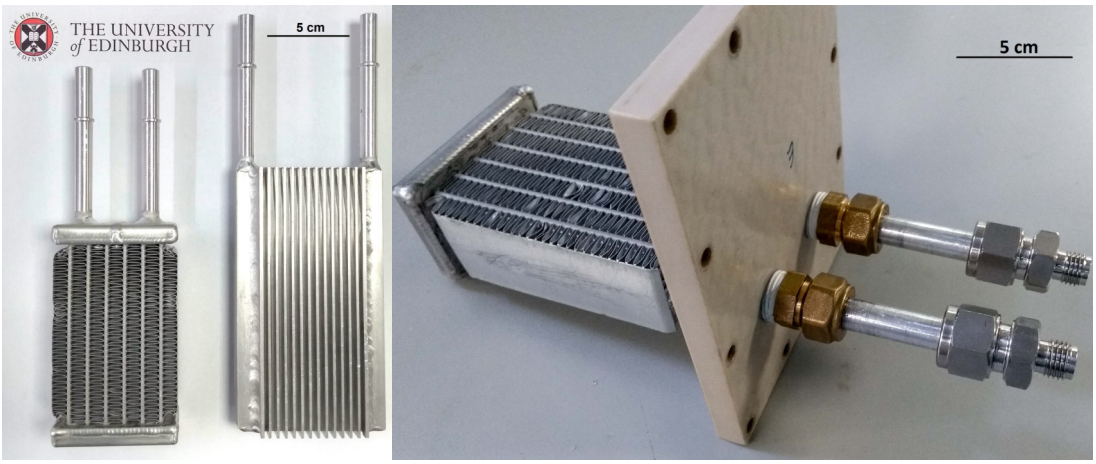


(a) (b)

Figure 5.5: (a) The aluminium heat exchangers of evaporator (left) and condenser (right). (b) The evaporator heat exchanger with PEEK plates and brass fittings.

### 5.1.5 Packing the heat exchangers with adsorbent

The aluminium heat exchangers were packed with 210 g of silica gel each (Siogel 0.5-2 mm, Oker Chemie GmbH, Germany). The silica gel beads were secured with

a polymer mesh (290 µm, open area 50 %, Plastok meshes and filtration, UK), which was glued to the heat exchanger using Loctite 454 adhesive. Fig. 5.6 shows both aluminium heat exchangers packed with silica gel.

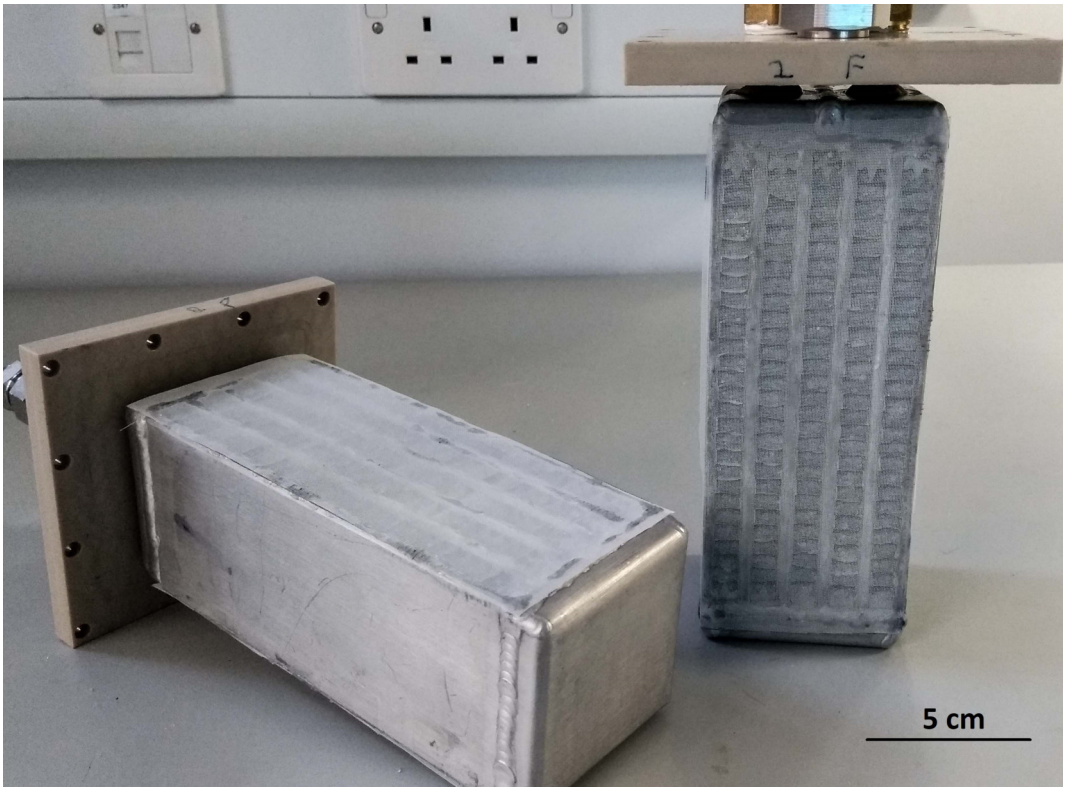


Figure 5.6: The two aluminium adsorber heat exchangers packed with silica gel before starting the experiments.

The open design of the copper heat exchanger did not allow the use of the polymer mesh from Fig. 5.6. Thus, a softer polyamide mesh (Sainsbury's, UK) was used to secure the beads. However, the polyamide itself became bulky as it is not strong enough to retain the beads inside the heat exchanger. Thus, perforated aluminium plates (6 mm hole, 0.7 mm thickness, 78 % open area, RS Components Ltd., UK) were adhered to the heat exchanger to avoid the bulky expansion of the polyamide mesh towards the vessel walls. The assembled heat exchanger with polyamide mesh, perforated plates and packed with 250 g of Siogel can be seen in Fig. 5.7a.
Ionogel (silica supported ionic liquid) was tested using the aluminium heat exchangers (Fig 5.7b). Twenty channels of the heat exchanger were filled with Ionogel in monoliths. The remaining channels were filled with polyethylene beads to reduce the void volume inside the vessel as void volume has a negative impact on the performance. The heat exchanger filled with Ionogel and polyethylene beads is displayed in Fig. 5.7b.

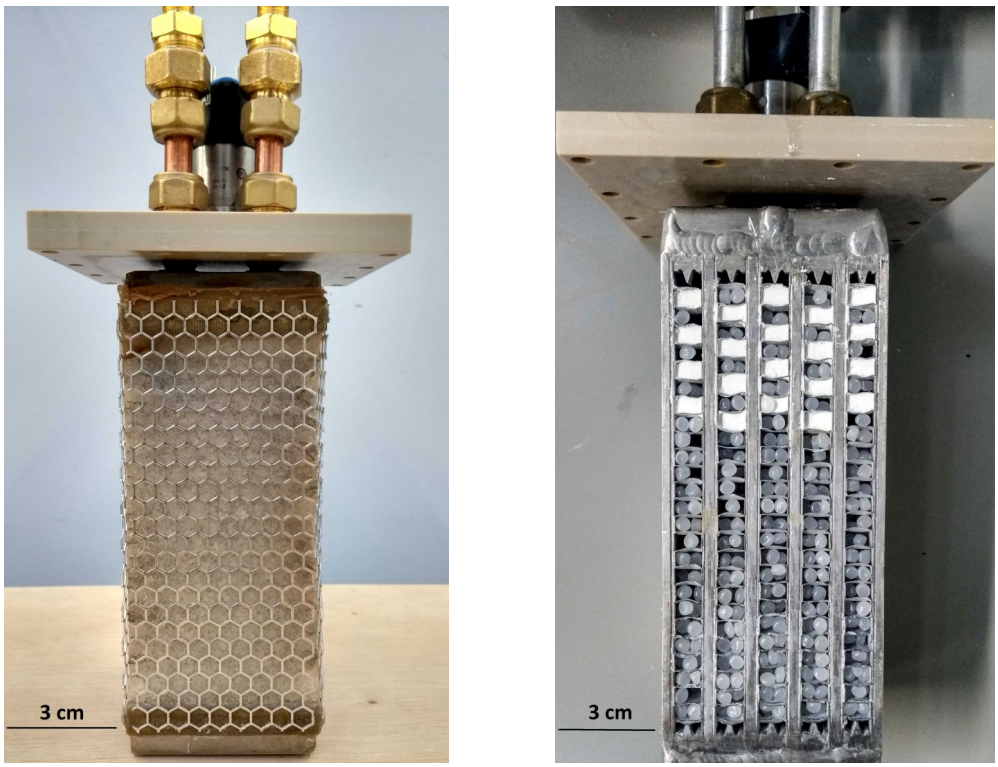


(a) (b)

Figure 5.7: (a) The copper heat exchanger packed with silica gel, which is secured by a polyamide mesh and perforated aluminium plates.
(b) The aluminium heat exchanger filled with Ionogel monoliths and polyethylene beads.

### 5.1.6 Data acquisition and control

The data acquisition and control of the test rig was accomplished using an Advantech ADAM 5000 board with input modules for the thermocouples and pressure transducers and output modules to control the solenoid valves. The ADAM board and the wire connections were set up by the technical support at the School of Engineering of the University as well as the Modbus connection. However, the implementation of the control sequence, the data acquisition and the user interface were implemented in National Instruments Labview 2016 as part of this work.

The user interface shown in figure 5.8 features a simplistic, intuitive design with the P&ID at its core. Within the P&ID the solenoid valves are represented by Boolean lights and the temperatures are displayed at their measuring point. The pressures are displayed on the side to avoid overloading of the P&ID. In addition to the input signals of the thermocouples and pressure transducers, the readings from the flow meters have to be entered manually. All the readings can be saved to a text file by turning the switch “Start DAQ” in the left bottom corner of the user interface. The time and the state of the sequence as seen in table 5.1 are saved in the text file along with the

temperatures [°C], pressures [bar] and volumetric flow rates [ml/min]. The readings are saved to the file once per second.

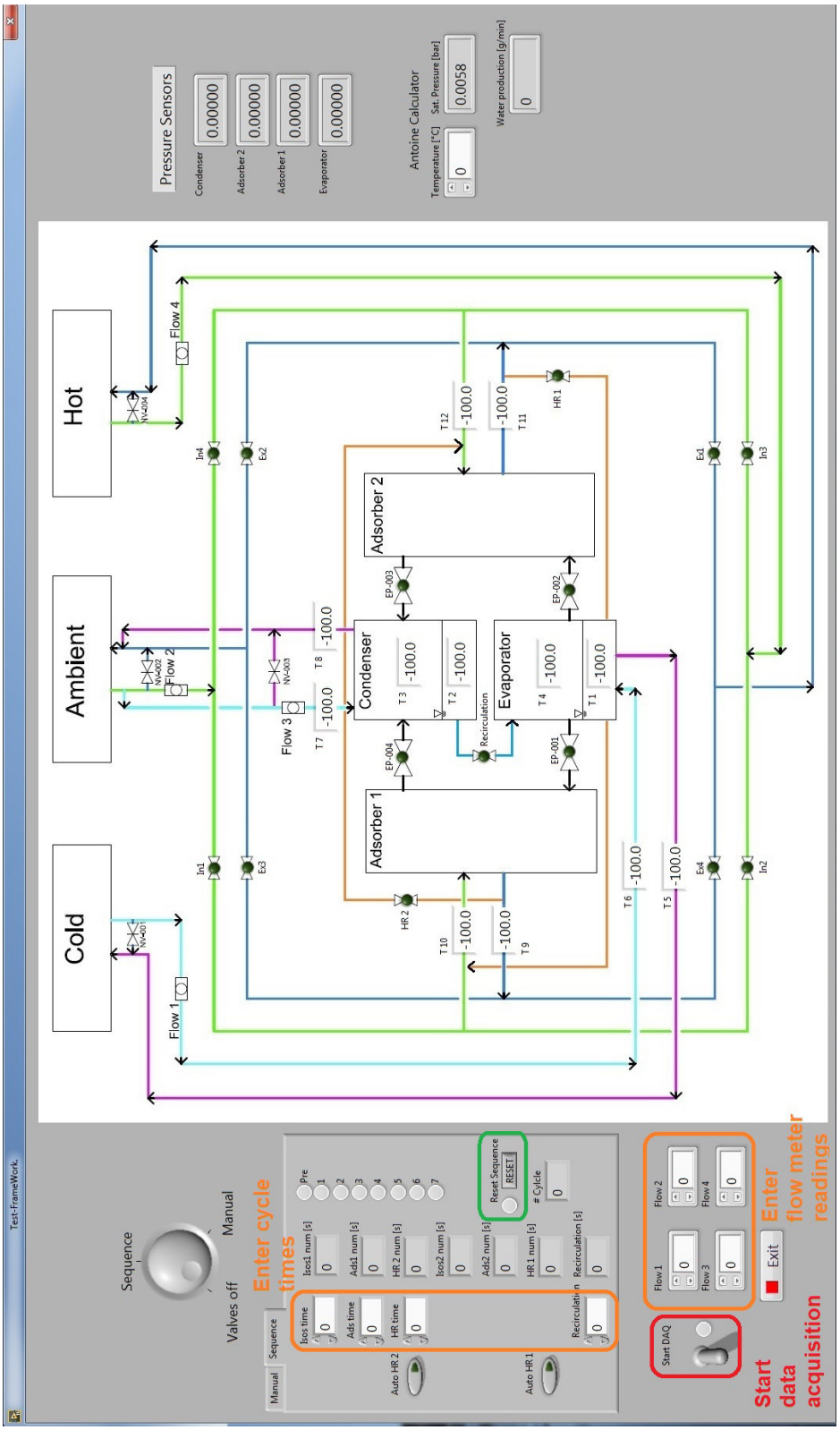


Figure 5.8: The software interface of the Labview control code.

The sequence implemented for the operation of the test rig is shown in table 5.1. Each one of the sequence steps is time controlled, where the time has to be entered manually. A step can be skipped by setting the time to zero, which for example, allows to skip the heat recovery mode or recirculation mode to run the system in its most basic set-up. In addition, all valves can be actuated manually by turning the control wheel on the top left to "manual". The wheel setting "Sequence" starts the sequence, but only if the sequence times of isosteric heating/cooling and adsorption/desorption are greater than zero. If they equal zero, the system is set in a safety mode, where all valves are closed. This prevents them from entering an endless loop of rapidly opening and closing the valves. The safety mode can be left by inserting values for the times and pressing the "reset" button afterwards.

Table 5.1: The sequence of the valves in Fig. 5.8. All states refer to adsorber 1, while adsorber 2 is in the opposite state: 1: Isosteric Cooling, 2: Adsorption, 3: Heat Recovery, 4: Isosteric Heating, 5: Desorption, 6: Heat Recovery, 7: Recirculation.
E = electropneumatic valve. SV-In/Ex = solenoid valves of heating and cooling loops. HR = solenoid valves of heat recovery. Re. = solenoid valve of recirculation line.
X = closed. O = open.

| States | 1 | 2 | 3 | 4 | 5 | 6 | 7 |
|---|---|---|---|---|---|---|---|
| E1 | X | X | X | X | O | X | X |
| E2 | X | O | X | X | X | X | X |
| E3 | X | X | X | X | O | X | X |
| E4 | X | O | X | X | X | X | X |
| SVEx1 | X | X | X | O | O | X | X |
| SVEx2 | O | O | O | X | X | X | X |
| SVEx3 | X | X | X | O | O | O | X |
| SVEx4 | O | O | X | X | X | X | X |
| SVIn1 | X | X | O | O | O | X | X |
| SVIn2 | O | O | X | X | X | X | X |
| SVIn3 | X | X | X | O | O | X | X |
| SVIn4 | O | O | X | X | X | O | X |
| HR1 | X | X | X | X | X | O | X |
| HR2 | X | X | O | X | X | X | X |
| Recirc | X | X | X | X | X | X | O |

### 5.1.7 Experimental procedure

Before each experiment the evaporator was filled with 500-600 ml of deionised water. Ng et al. have investigated the impact of the salinity on the performance [17]. They showed that the performance ratio does not change with the salinity and the SDWP is reduced by less than 10 % by using seawater instead of deionised water [17]. Deionised water reduces the risk of galvanic corrosion of the aluminium heat exchangers inside the stainless steel vessels. Thus, it was chosen for the experiments.
After the evaporator was filled, the evaporator was briefly connected to the vacuum

pump to lower the pressure to about 2-5 kPa to degas the water. A coldtrap was used to protect the vacuum pump from water vapour. The evaporator was usually left under vacuum overnight to degas the water. The high vacuum tightness of the system (about $1 \cdot 10^{-6}$ Pa/($m^3$s)) allows to run the vacuum pump only before the start of each experiment to pull a vacuum. During the experiment the vacuum pump can be switched off.

To start the experiment, the vacuum is pulled from each vessel down to the saturation pressure of water at the vessel temperature (≈1-4 kPa). Moreover, the thermostatic baths need to be switched on and set to the target temperatures of the experiment for evaporator, condenser+adsorption and desorption. The valve of the compressed air line needs to be opened and the pressure regulator set to 4 bar. Then, the cycle times is entered into the Labview control software and data acquisition needs to be started by switching the toggle in Fig. 5.8. In addition, the flow rates need to be read from the rotameters and manually entered into the respective fields in Labview.

The system runs fully automated until the operator decides to end the experiment by switching all valves off and stopping the data acquisition. The thermostatic baths also need to be turned off. The system can then remain under vacuum for a few days until a new experiment is conducted. In this case, the water is already degassed and a new experiment can be started again right away. In case no additional experiments are planned in the near future, the vacuum ball valves need to be opened and the water from the evaporator needs to be drained to allow the system to dry.

### 5.1.8 Data evaluation

The water production $\dot{m}_w$ is determined through an energy balance for the condenser:

$$\dot{m}_w = \frac{\dot{m}_{cond,in}\ c_{p,w}\ (T_{cond,in} - T_{cond,out})}{L} \tag{5.1}$$

where $\dot{m}_{cond,in}$ [kg/s] is the mass flow of cooling water supplied to the condenser heat exchanger, $c_{p,w}$ [kJ/(kgK)] is the specific heat of water, L [kJ/kg] is the latent heat, and $T_{cond,in/out}$ [K] the temperature differences between the inlet and outlet of the heat exchangers.

The energy balances to determine the heat input to each vessel [kJ/s] are:

$$\dot{Q}_{des} = \dot{m}_{hot}\ c_{p,w}\ (T_{des,in} - T_{des,out}) \tag{5.2}$$

$$\dot{Q}_{evap} = \dot{m}_{evap}\ c_{p,w}\ (T_{evap,in} - T_{evap,out}) \tag{5.3}$$

$$\dot{Q}_{cond} = \dot{m}_{cond}\ c_{p,w}\ (T_{cond,in} - T_{cond,out}) \tag{5.4}$$

Where ṁ is the mass flow rate of water from the thermostatic bath [kg/s], $c_{p,w}$ is the specific heat of water [kJ/(kgK)] and the temperature difference between the inlet $T_{in}$ and outlet $T_{out}$ to the heat exchanger [K].

The energy balances and water production are required to calculate the performance indicators in adsorption desalinaton and cooling: SDWP, PR, COP and SCC, which are described in eq. (2.2-2.5) in section 2.2.1. The reduced temperature $T_{red}$ is a useful tool to compare different experimental results and it is also introduced in section 2.2.1 eq. (2.1).

### Heat losses

Heat losses have been neglected, because the evaporator and condenser both operate at ambient temperature in adsorption desalination. The adsorber heat exchangers operate above ambient temperature during desorption. However, they are in a vacuum vessel, where the vacuum insulates the heat exchangers from the vessel walls. Moreover, the inlet and outlet tubes are thermally decoupled from the vessel by the PEEK plates, which further reduces heat losses. However, experimental heat losses were measured for the adsorber vessels, where the biggest heat losses occur, because the beds are heated to a maximum of 85 °C during desorption. For this, a baseline test was conducted where the empty aluminium heat exchangers were heated to 60 °C, 70 °C, and 80 °C. The results are shown in table 5.2 and in appendix D.3 in detail. They highlight that even at 80 °C the heat losses are only 20 W, while the peak heat input to the system is 900 W without heat recovery and 500 W with heat recovery [129]. Therefore, the heat losses are small for the adsorbers.

Table 5.2: Experimentally obtained heat losses.

| $T_{laboratory}$ [°C] | $T_{hot,in}$ [°C] | Heat loss [W] |
|---|---|---|
| 15 | 30 | 5 |
| 25 | 60 | 14 |
| 25 | 70 | 17 |
| 25 | 80 | 20 |

## 5.2 Results overview

The experiments in the test rig are split in three parts according to table 5.3. The first part presents a comprehensive analysis of silica gel in a performance analysis including a literature comparison. The system is then characterised beyond the established performance indicators in an adsorption cycle analysis and a novel thermal response experiment.
The second part presents the novel work on silica supported ionic liquids. Ionogels have never been tested in adsorption desalination. A preliminary screening of commercial ionic liquids identified the most promising possibilities for the experimental investigation. The experimental analysis presents a full characterisation of an Ionogel for different regeneration temperatures and times.
The third part of the experimental investigation is shown for silica gel in combination with the copper heat exchangers. The copper heat exchangers were lighter with a more open design, but the tests were not successful due to a malfunction of the heat exchanger, which is described in appendix D.4.

Table 5.3: Experimental testing split in three parts. The first two parts were performed with aluminium heat exchangers.

| |
|---|
| **Part I: Silica gel** |
| • Comparison with literature |
| • Performance analysis |
| • Adsorption cycle analysis |
| • Cycle time analysis |
| • Impact of heat recovery |
| • Characterisation of the adsorber |
| • Thermal Response Experiment |
| • Low temperature regeneration ≥ 40 °C |
| **Part II: Ionogel** |
| • Ionic liquids screening |
| • Ionogel possibilities and challenges |
| • Preparation of Ionogel for test rig |
| • Low temperature regeneration ≥ 25 °C |
| • Cycle time analysis |
| **Part III: Copper heat exchangers** |
| In appendix D.4. |
| The copper heat exchanger did not function as intended. |

## 5.3 Results part I: Silica gel

### 5.3.1 Comparison with literature

The SDWP is the key performance indicator in adsorption desalination as it describes the efficiency of the adsorption material and system. The SDWP can be maximised by fast cycle times in combination with a large working capacity, which is a result of little heat and mass transfer limitations, well designed heat exchangers, and a minimised void volume within the system. In addition, the SDWP is very sensitive to the system operating parameters and is largest in desalination when evaporator and condenser operate at the same pressure as this maximises the working capacity. Cooling requires a low evaporator temperature and pressure, which reduces the working capacity of the adsorption material.
Silica gel is an inexpensive, commercially available adsorption material. Thus, silica gel is commonly used as benchmark material in adsorption desalination and it is ideal for the comparison of different system designs. Fig. 5.9 compares different systems using silica gel at similar conditions.

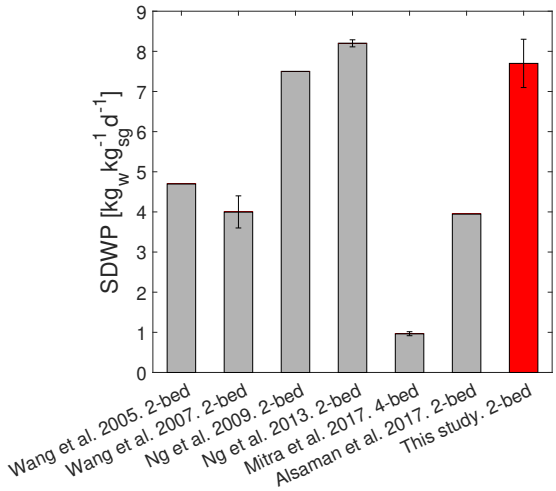


Figure 5.9: The systems performance in comparison to the best experimental results reported in the literature for silica gel [17, 46, 47, 53, 55, 133]. The highest SDWP in this study was achieved at $T_{evap,in} = T_{cond,in} = 30$ °C, $T_{hot,in} = 80$ °C and a half cycle time of 600 s.

Ng et al. [17] have reported the performance of their system in several configurations, where they have achieved the best results for silica gel. The best performance was achieved with the four beds configuration and heat integration between condenser and evaporator. The heat integration lifts the evaporator inlet temperature above the condenser inlet temperature, which leads to $P_{evap} \approx P_{cond}$ and improves the working capacity. In this configuration their large scale prototype with 144 kg of silica gel achieved a SDWP = 14.2 $kg_w/(kg_{sg}d)$ at $T_{hot,in} = 85$ °C. The experiments of the four

bed system [52, 134] were not compared to the two bed system presented here.
Ng et al. also reported the performance of the four bed system operated in two bed mode and without heat integration between their evaporator and condenser [17]. In this configuration, their prototype achieved SDWP = 8.2 $kg_w/(kg_{sg}d)$ at $T_{hot,in}$ = 80 °C, $T_{evap,in}$ = $T_{cond,in}$ = 30 °C, and a half cycle time of 600 s as displayed in Fig. 5.9 for comparison. At the same conditions, the adsorption desalinator introduced in this study reached SDWP = 7.7 $kg_w/(kg_{sg}d)$, which is 6 % lower. All other desalinators reported in the literature and utilising silica gel have much lower performances [53, 55]. Ng et al. have proposed the largest system with a total of 72 kg of silica gel in two beds mode, while the desalinator of this study is the smallest system design with a total of only 0.4 kg of silica gel. Hence, the smallest and the largest systems achieve the best performances in the literature highlighting that for properly designed systems the system size is irrelevant to the performance.

### 5.3.2 Performance analysis

The performance of the system varies depending on the cycle time and the temperature of the heating and cooling water supplied to the vessels. Both, the SDWP and SCC collapse on a single curve respectively when plotted over $T_{red}$. The reduced temperature is a dimensionless quantity, which considers the three system temperatures from eq. (2.1) allowing the comparison of different temperature lifts and heat source temperatures in a single graph.

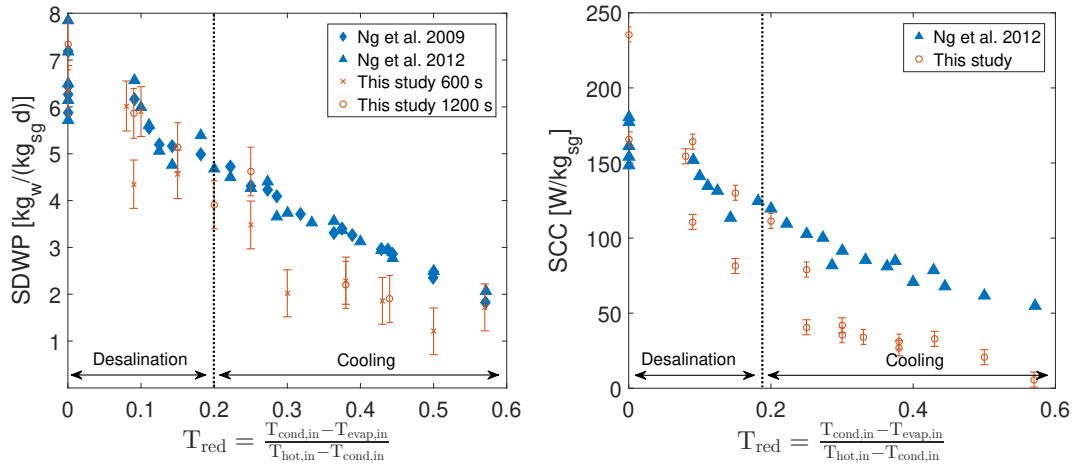


(a) (b)

Figure 5.10: (a) The SDWP plotted over $T_{red}$ based on inlet temperatures in comparison to the literature [47, 49]. The half cycle times are 600 and 1200 s, while $T_{hot,in}$ = 60-85 °C.
(b) The Specific Cooling Capacity plotted over $T_{red}$ in relation to the literature [49]. The half cycle times are 600 and 1200 s while $T_{hot,in}$ = 60-85 °C.

In Fig. 5.10, $T_{red}$ is based on the inlet temperatures to the heat exchangers of the ves-

sels. This allows the comparison of this study to the best performing reference system in the literature presented by Ng et al., because their results are based on the inlet temperatures as well [47, 49]. Desalination applications require $T_{red} < 0.2$, where the two systems show an almost identical performance in Fig. 5.10. The SDWP is highest at $T_{red} < 0.2$ in Fig 5.10a as the working capacity increases the closer the pressures in evaporator and condenser are to each other.
The SCC of the reference system is even exceeded at $T_{red} = 0$. For cooling applications $T_{red} > 0.2$, the performance achieved in this study is below the reference system, which is due to limitations of the evaporator. The performance can be improved by a larger evaporator heat exchanger surface area and spray nozzles, which increase the water surface area and the evaporation rate as in the reference system [49]. Both measures improve the relative humidity (RH) in the evaporator during adsorption, which is the ratio of the vapour pressure in the evaporator and the saturation pressure at the adsorption bed temperature: $RH_{ads} = P_{evap}/P_{sat}(T_{sg})$. The relative humidity for cooling applications is $RH_{ads} < 50$ %, while in desalination it is up to 99 %. The evaporator vapour temperature $T_{evap,vap}$ is as much as 10 °C below $T_{evap,in}$, because of the cooling effect of the evaporating water, which reduces the relative humidity, the evaporation rate and the adsorption uptake.

The experiments in Fig. 5.10 show that at $T_{evap,in} \approx T_{cond,in}$ the vapour temperature in the evaporator is below the condenser vapour temperature $T_{evap,vap} < T_{cond,vap}$, which reduces the relative humidity, working capacity, and performance. For a maximum working capacity and performance, the vapour temperatures need to be $T_{evap,vap} \approx T_{cond,vap}$ for $P_{evap} \approx P_{cond}$ as shown in Fig. 2.2b. Therefore, in Fig. 5.11a the inlet temperature supplied to the evaporator $T_{evap,in}$ was slightly increased over ambient temperature to improve the system performance. This measure compensates for the cooling effect caused by the evaporating water vapour and leads to $T_{evap,vap} \approx T_{cond,vap}$ for a maximum performance. In Fig. 5.11a, the reduced temperature is based on the vapour temperatures $T_{red,vap}$ to account for this. The results show that the SDWP increases by 41 % from 7.7 to 10.9 $kg_w/(kg_{sg}d)$ when the system is operated at $T_{evap,vap} \approx T_{cond,vap}$ (Fig. 5.11a). The result was achieved with the inlet temperatures $T_{hot,in} = 80$ °C, $T_{cond,in} = 25$ °C, $T_{evap,in} = 35$ °C and a half cycle time of 1200 s.
The optimised operational strategy found in this study increases the performance of the adsorption material by maximising the working capacity. Thu et al. used a similar strategy to achieve an SDWP of 9.96 $kg_w/(kg_{sg}d)$ at $T_{hot} = 70$ °C by implementing an internal heat recovery between evaporator and condenser to their 4-bed adsorption desalinator [52]. The latent heat of the condensing water increases the cooling water outlet temperature, which is then sent to the evaporator to achieve $T_{evap,in} > T_{cond,in}$ leading towards $P_{evap} \approx P_{cond}$. By contrast, the system presented in this study has a simpler set-up with only two adsorber beds.
The combination of chilling and desalination has recently gained a lot of attention

[47, 49, 56, 60, 135, 136]. Most studies employ silica gel-water as working pair, which is has a good performance for desalination as shown in Fig. 5.11a at $T_{red} < 0.1$. A change of $T_{red} > 0.1$ in Fig. 5.11 provides cooling in addition to potable water. However, cooling as well as the water production decrease at higher $T_{red}$. The system performance is reduced by more than 60 %, when the evaporator is operated below 10 °C, where the COP is reduced from 0.9 to less than 0.3 (Fig. 5.11b) and SDWP from 10.9 $kg_w/(kg_{sg}d)$ to less than 4.5 $kg_w/(kg_{sg}d)$ (Fig. 5.11a).

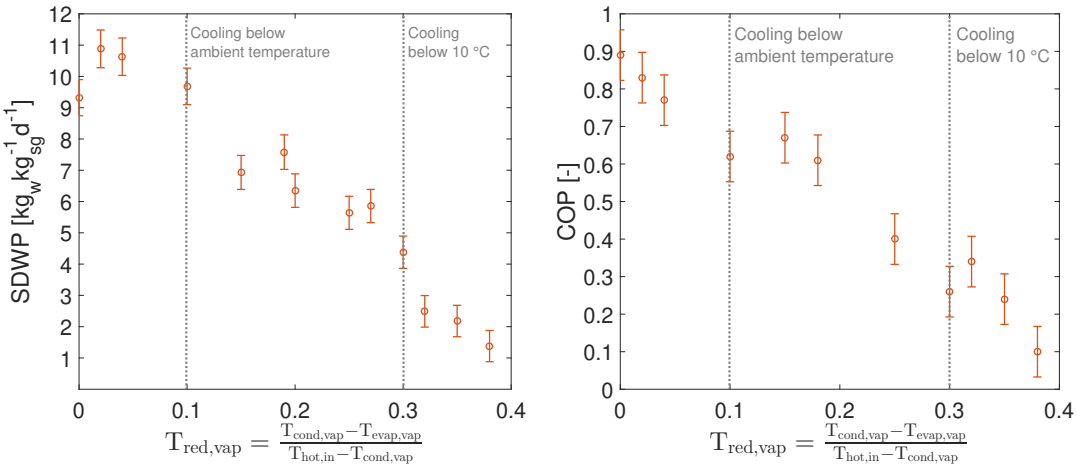


(a) (b)

Figure 5.11: (a) The SDWP investigation extended to cases where $T_{evap,vap} \approx T_{cond,vap}$. Thus, $T_{red,vap}$ is based on the vapour temperatures here. The half cycle times are 600 and 1200 s. 85 °C ≥ $T_{hot,in}$ ≥ 60 °C.
(b) The COP for different $T_{red,vap}$. The half cycle times are 600 - 1200 s including 90 s heat recovery time, ambient temperature 25-30 °C, and $T_{hot} \leq 85$ °C.

### 5.3.3 Adsorption cycle analysis

Theoretical analyses of adsorption desalination often focus on the theoretical performance by studying the thermodynamic cycle [62]. This approach neglects the heat and mass transfer limitations of real systems. Fig. 5.12a complements the theoretical analysis by showing the experimental adsorption cycle at two different cycle times against the thermodynamic cycle. The system follows the cycle in a clockwise direction 1→2→3→4→1 in Fig. 5.12a. The plot can be used to compare the deviation from ideal behaviour and reveals performance limitations at the same time.

In Fig. 5.12a from 2→3, the pressure inside the condenser is higher than the ideal condensing pressure. This lowers the system performance, as the condenser does not operate at ideal conditions. The pressure build-up can be reduced by increasing the condenser surface area [137]. At insufficient condenser area, water vapour desorbs from the material, but cannot condense at the same rate. The limited surface area is not an issue to reach equilibrium, but it increases the cycle time.

The ideal working capacity assessed through the thermodynamic cycle in Fig. 5.12a is 0.2 $kg_w/kg_{sg}$. The uptake is reduced to 0.13 $kg_w/kg_{sg}$ at the long cycle time and at the shorter cycle time to 0.08 $kg_w/kg_{sg}$.
The shorter cycle time affects both isosteres and shifts them closer together on both sides in Fig 5.12a. Thus, at the shorter cycle time neither the adsorption nor desorption capacity of the material are sufficiently used. By contrast, a longer cycle time allows the material to adsorb water sufficiently as the experimental isostere and the thermodynamic isostere 1→2 in Fig. 5.12a are almost overlapping. The isosteric heating and cooling time was selected based on the time required to increase the pressure to the condenser pressure. The two times of the system are equal to simplify the control sequence in table 6.6.
As a result, the cooling time is slightly longer than necessary, which can be seen from the curve of the longer cycle time. The pressure inside the adsorber bed goes below the pressure in the evaporator. Once the isosteric cooling time is elapsed, the valve between evaporator and condenser is opened and the pressure inside the adsorber vessel rises to the evaporator pressure. Flash evaporation takes place in the evaporator and the pressure immediately increases (Fig. 5.12a). The slightly increased isosteric cooling time does not have a negative impact on the performance since the isosteric cooling time is only a fraction of the total cycle time. In addition, the flash evaporation compensates for it.

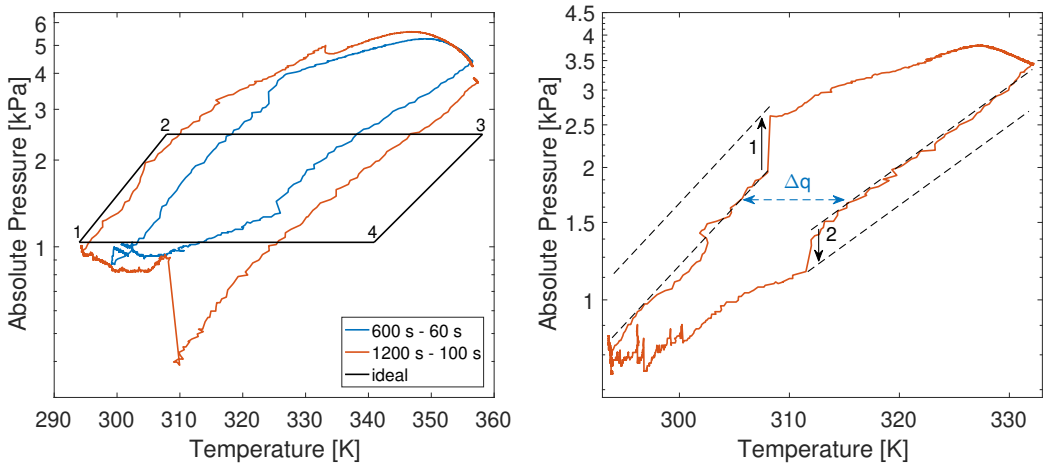


(a) (b)

Figure 5.12: (a) The influence of the cycle time on the adsorption cycle in comparison to the ideal, thermodynamic adsorption cycle. $T_{hot}$ = 85 °C, $T_{cond}$ = 20 °C and $T_{evap}$ = 10 °C.
(b) The effect of an insufficient cooling time on the adsorption cycle. $T_{hot}$ = 60 °C, $T_{cond}$ = 20 °C and $T_{evap}$ = 10 °C with $t_{ads/des}$=1200 s and $t_{isos}$ = 60 s.

Fig. 5.12b illustrates how insufficient isosteric heating and cooling times affect the adsorption cycle. During isosteric heating the pressure of the adsorber vessels is still

below the condenser pressure. When the valve between the two is opened, a flash evaporation occurs again with water evaporating from the condenser and adsorbing onto the adsorption material. This can be seen in Fig. 5.12b as the material shifts to a more saturated isostere.
The same effect occurs during isosteric cooling. The valve is opened before the adsorber vessel reaches the lower evaporator pressure and water desorbs from the material into the evaporator, while the material shifts to a drier isostere on the right. Therefore, the material desorbs while it should adsorb. The isosteres in Fig. 5.12b move further apart from one another, but the useful working capacity $\Delta$q remains the same. Thus, more energy is needed to reverse the additional and adversely occurring adsorption/desorption, which reduces the performance of the system. Therefore, it is imperative to operate at optimal isosteric heating and cooling time to reach $P_{ads} \geq P_{cond}$ before connection adsorber to condenser.

### 5.3.4 Impact of heat recovery

The first set of experiments were conducted with the basic system set-up without heat recovery or recirculation line. The PR without heat integration was 0.48 at long cycles times as shown in Fig. 5.13a. The heat recovery has the largest impact on the PR at very short half cycle times, where it improves the PR by a factor of three from 0.10 to 0.33 at 200 s. This half cycle time leads to a high frequency of heating and cooling the adsorber beds. The working capacity of the silica gel is reduced at short cycle times, while the aluminium heat exchangers have to be heated and cooled from ambient temperature to 80 °C during each cycle regardless of the cycle time requiring a fixed amount of energy to heat the metal mass $Q_{alu}$. At short cycle times, the material adsorbs little water during each cycle, while the metal mass needs to be heated and cooled at high frequency leading to a low PR. At long cycle times the working capacity of the material increases towards equilibrium, while the impact of $Q_{alu}$ on the PR becomes less dominant. Therefore, the impact of the heat recovery on the PR decreases, but the PR remains 25 % higher even at long cycle times with a maximum PR of 0.6.

At half cycle times longer than 600 s the SDWP is essentially independent of the heat recovery (Fig. 5.13b). By contrast, the heat recovery has a large impact on the SDWP at half cycle times below 600 s, which is unexpected as the SDWP in eq. (2.3) is independent of the heat input to the adsorbers. The heat recovery reduces the external heat input into the adsorbers, but does not affect the condenser. Thus, the impact of heat recovery should improve the PR, but not the SDWP. The sharp drop in PR and SDWP below 400 s can be explained by looking at the condenser inlet temperature. The inlet temperature is set to 30 °C in all cases of Fig. 5.13 and the thermostatic baths can provide this inlet temperature except for two cases: 200 s and 400 s without heat recovery. Here, the frequency of the cycles and heat input are too high for the bath to cool the

returning ambient water to the set temperature leading to $T_{cond,in}$ = 36 °C instead of 30 °C, which reduces the working capacity. The heat recovery overcomes this system limitation by reducing the peak energy input. Therefore, less cooling power needs to be provided and the overall system can cope with the fast cycles in virtue of the heat recovery system.

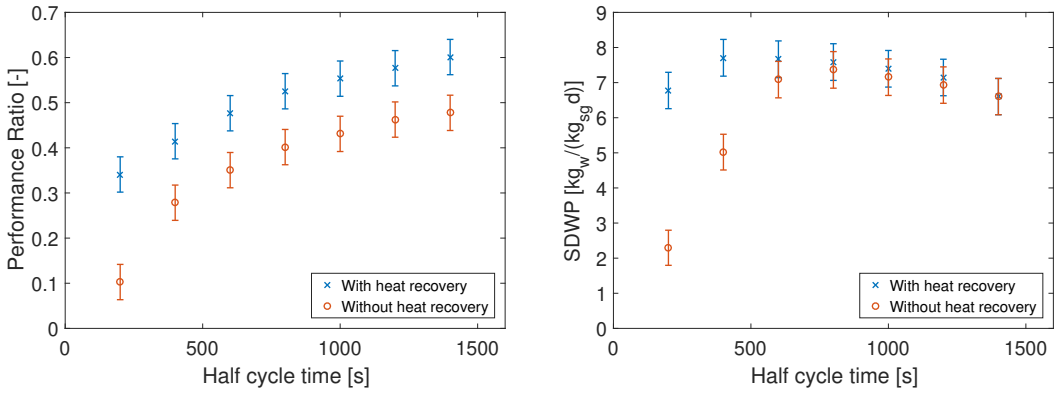


(a) (b)

Figure 5.13: (a) The impact of the heat recovery on the Performance Ratio for varying cycles times of the experiments at $T_{evap,in} = T_{cond,in}$ = 30 °C, $T_{hot,in}$ = 80 °C.
(b) The comparison of the Specific Daily Water Production with and without heat recovery under the same conditions as in (a).

Wang et al. [133] investigated the impact of heat recovery on their two bed adsorption system for full cycle times of 250 s to 600 s with $T_{hot}$ = 85 °C, $T_{cond}$ = 29.4 °C, and $T_{evap}$ = 12 °C. They reported an improvement of the PR by 30 % at short cycle times and 16 % at long cycle times on a two beds adsorption system. Hence, their results are comparable to this study with the exception of the very short half cycles in Fig. 5.13a. In addition, they implemented a mass recovery step equilibrating the pressure of the two adsorber beds by opening a valve between them, when switching the cycle from adsorption to desorption. Implementation of mass recovery in combination with heat recovery increased the PR of their system by 43 %.
Mass recovery is most effective at large pressure differences between evaporator and condenser as it is the case in their study [133]. The large pressure difference between $P_{evap}$ and $P_{cond}$ is present in cooling applications, where the mass recovery shortens the isosteric cooling time and increases the working capacity. However, in desalination applications mass recovery is not beneficial, because the evaporator and condenser operate at $P_{evap} \approx P_{cond}$ leading to one constant pressure throughout the entire system. Therefore, opening a valve between the two beds at the end of a cycle does not lead to any vapour flow, because no pressure gradient is present within the system. As a result, the performance of an adsorption desalinator cannot be significantly improved with a mass recovery.

### 5.3.5 Characterisation of the adsorber

The performance ratio is an indicator of the energy efficiency, but does not provide information on how the energy input is used in the system. The energy input during desorption contributes to heating of the aluminium heat exchangers, the adsorption material as well as the heat of desorption. The experimental procedure was altered to assess the energy required for each part of the process. In normal operation, the beds with the silica gel are pre-heated for less than a minute to an intermediate temperature, which increases the bed pressure. Afterwards, the adsorber is connected to the condenser and vapour desorbs from the material, while the bed is further heated up to the regeneration temperature.

The results of the experiments shown in Fig. 5.14 allow to separate the energy required to heat the beds from the heat of desorption. At first, the energy input of the blank heat exchanger without silica gel was measured by cycling the empty heat exchanger in temperature swings. This first step determines the sensible heat of the metal mass of the heat exchanger. Afterwards, the beds were packed with silica gel to repeat the temperature swings, but the preheating time was extended from 1 min to 20 min as opposed to a normal experiment. During the pre-heating phase, the beds are completely heated up to the regeneration temperature, while only limited desorption takes place. Hence, almost all the energy input can be associated with heating the aluminium heat exchangers and the silica gel beads. After 20 min of pre-heating, the valve between the adsorber and condenser is opened to desorb water for another 20 min. Moreover, on the basis of the blank experiment it is possible to quantify the sensible heat of the metal mass and the sensible heat of the silica gel. These experiments allow the sensible heat of the metal mass and silica gel to be separated from the heat of desorption.

The peak of the heat input between t = 0-5 min in Fig. 5.14 can be attributed to heating the heat exchangers, silica gel and the adsorbed water from ambient temperature up to the regeneration temperature. Here, the experiment with the blank heat exchanger without silica gel shows the highest and shortest peak. This experiment depicts the energy required to heat the aluminium alone that comes to (103 ± 5) kJ, which is 40 % of the entire energy input to the system.

The result of the blank experiment was subtracted from the original experiment of the heat exchanger containing material. The resulting curve of the difference shown in Fig. 5.14a represents the energy input ascribed to the silica gel alone neglecting the aluminium heat exchanger (sg alone). The energy required to heat the silica gel amounts to (153 ± 21) kJ and includes the sensible heat of the silica gel and partial water desorption. Some of the adsorbed water desorbs during the pre-heating phase, because the extensive heating to the regeneration temperature causes the material to leave the isostere. The partial desorption can be derived from the second peak of the heat input, which represents the heat of desorption.

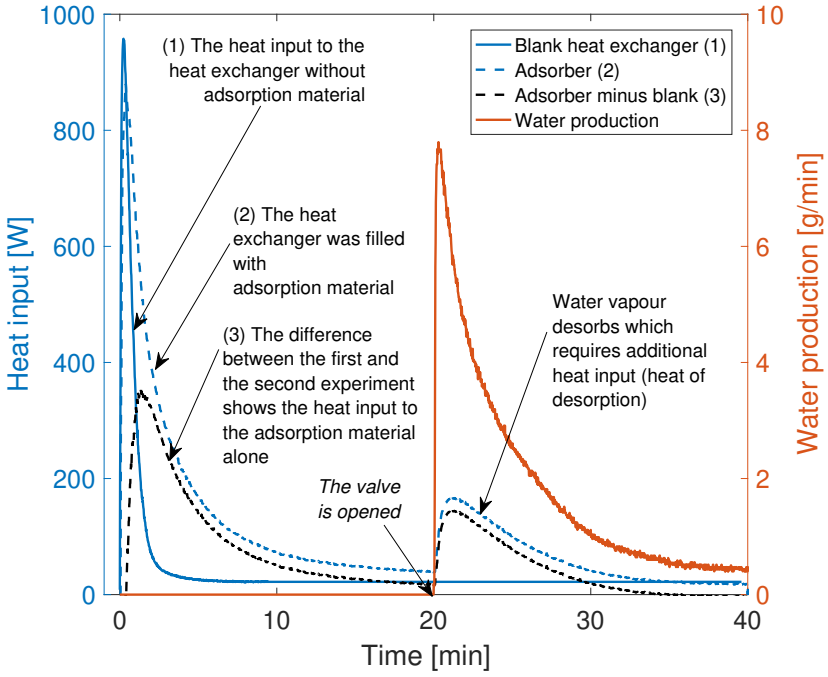


(a)

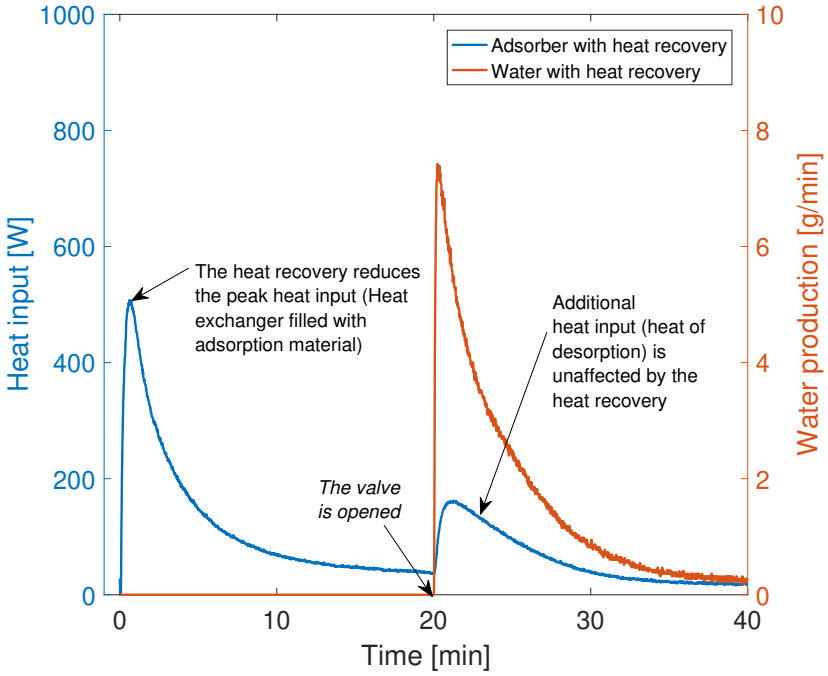


(b)

Figure 5.14: Thermal response experiment to evaluate partition of energy input in terms of sensible heat and heat of desorption. The adsorber heat exchangers are preheated to 80 °C for 20 min. Afterwards, the valve to the condenser is opened and water desorbs. (a) Without heat recovery. (b) With heat recovery.

A total of (40.6 ± 0.6) g of water was produced during desorption as shown in Fig. 5.14a between 20 to 40 min. The ratio of the heat input of the second peak to the amount of desorbed water is (1850 ± 100) kJ/$kg_w$ and can be ascribed to the heat of desorption. However, Sapienza et al. reported that Siogel-water has a heat of desorption of about 2800 kJ/kg [138]. Therefore, a part of the water desorbs during the long pre-heating phase with water vapour filling the void volume in the adsorbers. The ratio of the energy input without the aluminium heat exchanger to the produced water results in the Specific Energy Consumption leading to an experimental $SEC_{exp}$ = (3770 ± 520) kJ/$kg_w$. In comparison, the thermodynamic SEC calculated with eq. (6.21) predicts SEC = 3400 kJ/$kg_w$. Thus, $SEC_{exp}$ deviates by 10 % from the thermodynamic SEC. The small deviation is due to the very long half cycle time of 40 min reducing heat and mass transfer limitations significantly.
A third experiment was conducted with the heat recovery to assess the energy savings using heat recovery (Fig. 5.14b). The energy input with heat recovery amounts to (216 ± 18) kJ, which is 16 % less than the energy input without heat recovery. The energy savings of 16 % confirm the results of the PR analysis in Fig. 5.13a. Water production is not affected by heat recovery, which is why the reduction of the energy input by 16 % also reduces the PR. In addition, the peak power input is almost halved from 850 W to 500 W due to heat recovery. Hence, heat recovery allows the system to be connected to a smaller heat source to meet the peak demand.

### 5.3.6 Low temperature regeneration

Low temperature regeneration below 50 °C has a vast potential for adsorption desalination as no other thermal desalination technology can efficiently operate at such conditions despite the vast availability of heat. Fig. 5.15a extends the investigation below $T_{hot}$ = 60 °C down to 40 °C. The experiments were performed at $T_{evap,vap} \approx T_{evap,vap}$ like in Fig. 5.11a. The SDWP in Fig. 5.15a decreases by 70 % from 9.3 to 2.8 $kg_w/(kg_{sg}d)$, when the temperature is reduced from 60 °C to 40 °C. In case of $T_{hot,in}$ = 40 °C, the inlet temperatures to evaporator and condenser were $T_{evap,in}$ = 28 °C and $T_{cond,in}$ = 25 °C. The energy consumption of the system does not change with the low regeneration temperature of 40 °C. The PR is 0.68 when the slight heating of the evaporator by 3 °C is neglected and it is reduced to PR = 0.38 including the evaporator heating. These values are almost identical for $T_{hot,in}$ = 60 °C as well. Hence, silica gel adsorption desalination is possible at 40 °C, but three times more silica gel is needed to produce the same amount of water. The additional adsorption material increases the size of the adsorption desalination plant, but not the specific energy consumption. The PR is excellent considering that more than 700 MW are available from a single steam power plant as heat source at this temperature [139]. Moreover, Fig. 5.15b highlights that the system stably operates at 40 °C with smooth water production peaks. The peak heat input is reduced to 200 W in Fig. 5.15b, which is less than halved compared

to high regeneration temperatures $T_{hot,in} > 60$ °C, because less heat is required to heat the metal mass of the heat exchanger from ambient temperature to 40 °C.

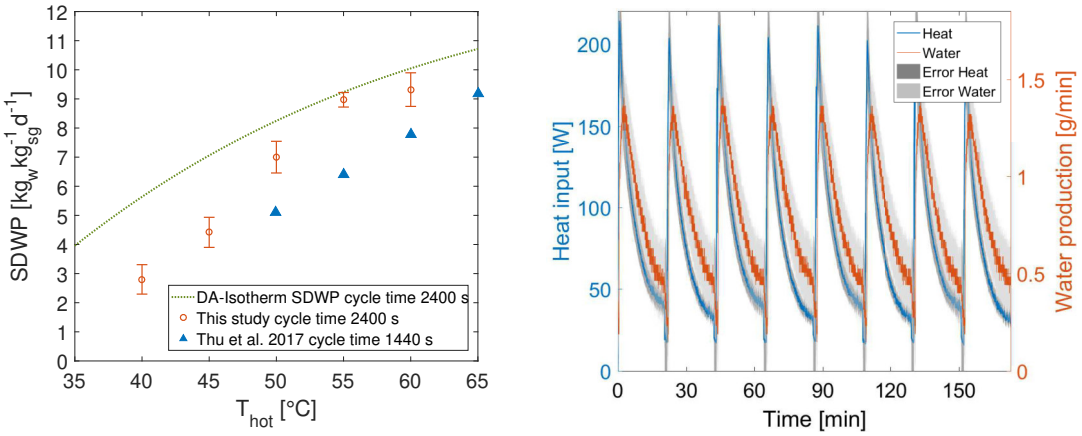


(a) (b)

Figure 5.15: (a) The SDWP at low temperature regeneration in comparison to the 4-bed system of Thu et al. [52] and a theoretical SDWP derived from the iostherm assuming equilibirum can be achieved within 2400 s of cycle time.
(b) The water production and heat input at 40 °C heat source highlighting the feasibility.

In comparison to the literature, the small-scale test rig has a 37 % higher SDWP at 50 °C than Thu et al. in Fig. 5.15a [52]. Moreover, at 50 °C the SDWP is still relatively high at 7.0 $kg_w/(kg_{sg}d)$ and utilises almost the full available working capacity of the material at $SDWP_{DA} = N \cdot \Delta q$ where $N = 86400 \frac{s}{day} / t_{cycle}$ and $\Delta q$ is the working capacity from the DA-equation eg. (4.32). For temperatures below 50 °C the results compared to $SDWP_{DA}$ in Fig. 5.15a show that the possible working capacity of the silica gel derived from the isotherms was not entirely utilised. A slight increase in $T_{evap,in}$ could have improved the SDWP further. However, the relative humidity was very high during the experiment and reached 98 %. $T_{evap,in}$ was not further increased to ensure RH < 100 % to avoid condensation.

## 5.4 Results part II: Ionogel

### 5.4.1 Ionic liquids screening

The advantage of ionic liquids in adsorption desalination is their large working capacity compared to competing adsorption materials like silica gel. Siogel silica gel has a saturation uptake of 0.38 g/g, but the working capacities achieved in the desalinator are 0.2 g/g and a full cycle time of 40 min. A large working capacity reduces the footprint of the system, which is correlated with the SDWP performance indicator. A large number of ionic liquids is available commercially and for some of them the VLE data is available in the Detherm database [140–148]. The available vapour liquid equilibria have been used to screen them for the best working capacities, which can be achieved under the conditions in an adsorption desalinator: $T_{evap}$ = 22-25 °C, $T_{cond}$ = 25 °C and $T_{hot}$ = 45-50 °C.

An ionic liquid screening evaluates the working capacities $\Delta q$ in two steps. Firstly, the VLE data from Detherm [149] is provided in mole-fractions and was converted to the water uptake $q$ [$g_w/g_{il}$]. Secondly, q was plotted over the adsorption potential $A$. The adsorption potential is given by $A = -RTln(\frac{P}{P_{sat}})$, where $R$ is the real gas constant [kJ/(molK)], $P$ the pressure [kPa] and $T$ the temperature [K]. The uptakes at different temperatures and pressures often collapse on a single, characteristic curve when they are plotted over the adsorption potential [122] as seen in the example in Fig. 5.16. The ratio of pressure to saturation pressure is also referred to as relative humidity $RH = \frac{P}{P_{sat}}$. The investigated temperatures for each vessel are $T_{evap}$ = 22-25 °C, $T_{cond}$ = 25 °C and $T_{hot}$ = 45-50 °C. The adsorption potential is calculated for adsorption (0.1-0.5 kJ/mol) and desorption conditions (2-3.5 kJ/mol). For each A at adsorption and desorption, the corresponding water uptake is interpolated from the experimental data. The difference in water uptake between adsorption and desorption equals the working capacity presented in Fig. 5.16.

The ideal ionic liquid should have a large working capacity over a wide range of relative humidities. However, most ionic liquids have a type III adsorption isotherm with water showing an exponential increase at low adsorption potentials. Less distinct exponential slopes are favourable for the process as they allow a large uptake for a wider range of relative humidities during adsorption.
This can also be seen from table 5.4. For example, BMIM Br has high working capacities at 94 % relative humidity, but a reduction of the relative humidity from 94 % to 83 % or $T_{evap}$ by 3 °C has a substantial impact on the uptake. This small temperature change diminishes the working capacity from 2.92 g/g to 0.58 $g_w/g_{il}$, where 0.58 $g_w/g_{il}$ is comparable to the working capacity of silica gel. EMIM Acetate was selected as first Ionogel to be tested as it maintains a high working capacity even at lower relative humidities in table 5.4. In addition, it is a non-toxic, non-corrosive Imidazolium salt.

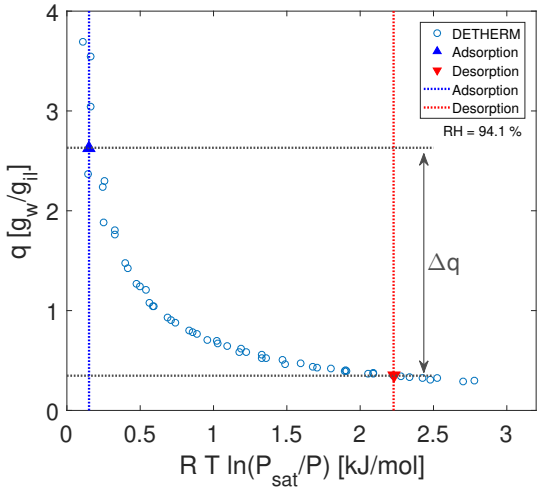


Figure 5.16: Example evaluation of Δq for 1-Butyl-3-methylimidazolium acetate from Passos et al. [140] at $T_{evap}$ = 24 °C, $T_{cond}$ = 25 °C and $T_{hot}$ = 40 °C

Table 5.4: Working capacities of pure ionic liquids for different relative humidities at different $T_{evap,in}$, but constant $T_{cond,in}$ = 25 °C and $T_{hot,in}$ = 50 °C.
EMIM = 1-Ethyl-3-methylimidaz. BMIM = 1-Butyl-3-methylimidaz. MMIM = 1,3-Dimethylimidaz. DEP = Diethyl phosphate. DMP = Dimethyl phosphate. SCN = Thiocyanate. TOS = Tosylate. Ac = Acetate. $BF_4$ = Tetrafluoroborate. $ESO_4$ = Ethyl sulfate.

| **RH** [%] | 83 | 86 | 88 | 91 | 94 |
|---|---|---|---|---|---|
| **IL name** | **Δq** $[g_w/g_{il}]$ | **Δq** $[g_w/g_{il}]$ | **Δq** $[g_w/g_{il}]$ | **Δq** $[g_w/g_{il}]$ | **Δq** $[g_w/g_{il}]$ |
| EMIM Ac [150] | 1.11 | 1.11 | 1.62 | 1.89 | 1.95 |
| EMIM $BF_4$ [143] | 0.51 | 0.63 | 0.86 | 1.28 | 2.30 |
| EMIM $ESO_4$ [144] | 0.88 | 1.05 | 1.32 | 1.45 | 2.50 |
| EMIM DEP [147] | 1.23 | 1.38 | 1.65 | 2.07 | 2.70 |
| BMIM Br [140] | 0.58 | 0.75 | 1.00 | 1.51 | 2.92 |
| BMIM Cl [141] | 1.27 | 1.46 | 1.74 | 2.05 | 3.71 |
| BMIM TOS [140] | 0.43 | 0.61 | 0.74 | 1.07 | 2.18 |
| BMIM Ac [140] | 0.95 | 1.20 | 1.58 | 2.18 | 2.28 |
| BMIM $CH_3SO_3$ [140] | 0.96 | 1.15 | 1.42 | 2.13 | 3.22 |
| BMIM $CF_3CO_2$ [140] | 0.68 | 0.79 | 1.18 | 1.81 | 3.30 |
| BMIM SCN [140] | 0.65 | 0.76 | 1.04 | 1.55 | 1.75 |
| BMIM CCN [146] | 0.43 | 0.69 | 0.80 | 1.25 | 2.51 |
| HMIM Cl [141] | 0.86 | 1.13 | 1.53 | 2.04 | 3.46 |
| MMIM DMP [148] | 1.12 | 1.33 | 1.61 | 2.05 | 2.74 |
| Choline Glycolate [142] | 2.08 | 2.31 | 2.53 | 2.62 | 2.62 |

Choline Glycolate is among the 4 only ionic liquids, which is non toxic and does not require any preventive efforts to protect health and environment. The results of those 4 non-toxic ionic liquids are shown in Fig. 5.17, where it is evident that Choline Glycolate

has the most promising working capacity. In Fig. 5.17, the working capacities of the pure ionic liquids in table 5.4 have been halved to account for a 50 wt% impregnation of silica gel as support material. Tests have shown that the ionic liquid starts leaking from the support structure at impregnations above 50 wt%. The impregnation level can be further increased up to 60 wt% with negligible leakage to push the material performance as the equilibrium uptake increases with the impregnation level [34, 151]. Adsorption heat pumps require supported ionic liquids instead of pure ionic liquids, because the adsorber beds need to be filled with a solid material. Unfortunately, Choline Glycolate can only be custom manufactured, but EMIM Acetate is commercially available. Thus, silica supported EMIM Acetate was selected for testing in the adsorption test rig for the first time. As shown from Fig. 5.17, EMIM Ac does not feature a strong exponential increase at very high relative humidities, but it has the second highest uptake at lower relative humidities.

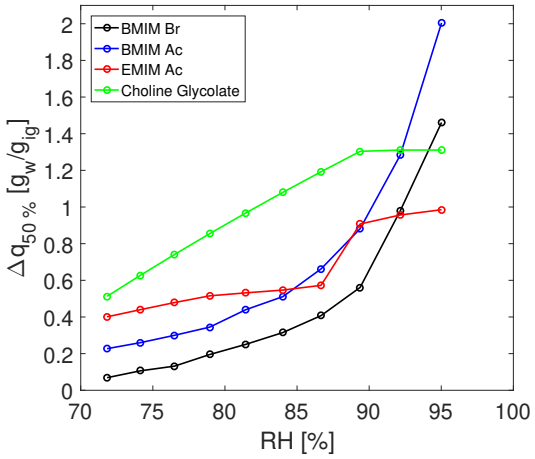


Figure 5.17: The uptake of the best, non-toxic ionic liquids at different relative humidities using experimental data from [140, 142, 150].

### Possibilities and challenges

The measured isotherms of Syloid 72P impregnated with 57 wt% of EMIM Ac were refitted (table 5.5) to match the Dubinin Astakhov equations [131]. A gravimetric sorption analyser (Surface Measurement System DVS Adventure, UK) was used to measure the isotherm of the ionogel at 25 °C. The DA parameters of for different adsorption materials are given in table 5.5.

The working capacities for four materials at heat source temperature differences $\Delta$T 2-70 °C were investigated for two different scenarios: $T_{evap}$ = 28 °C (dashed) and $T_{evap}$ = 29 °C (solid), while $T_{cond}$ = 30 °C. The results are shown in Fig. 5.18a. The Ionogel has the best working capacity of up to 1.4 $g_w/g_{ad}$, but even at very low temperature differences $\Delta T \approx 5$ °C the working capacity is $> 0.5$ $g_w/g_{ad}$. By contrast, achieve much lower working capacities except for SWS-1L, which has a lower capacity

than Ionogel, but exceeds the threshold of 1 $g_w/g_{ad}$. The working capacities of Siogel and CPO27Ni remain below 0.4 $g_w/g_{ad}$ for all hot temperatures in Fig. 5.18a. Thus, the equilibrium working capacities of Ionogel and SWS-1L are exceptionally interesting for the application in desalination applications.

Table 5.5: Fitting parameters for DA-isotherms of four materials shown in Fig. 5.18a. (1)SWS-1L: $E$ and $n$ are functions of the adsorption potential $A$.

| | Type | $q_0$ [$g_w/g_{ad}$] | E [J/mol] | n [-] | Ref. |
|---|---|---|---|---|---|
| CPO-27Ni | MOF | 0.46 | 10014 | 4 | [152] |
| Siogel | Silica gel | 0.38 | 3960 | 1.1 | [138] |
| SWS-1L | $CaCl_2$+silica gel | 1.9 | *612-8334* (1) | *0.4-4.7* (1) | [153] |
| Ionogel | EMIM Ac+silica gel | 7.98 | 19.86 | 0.275 | this study |

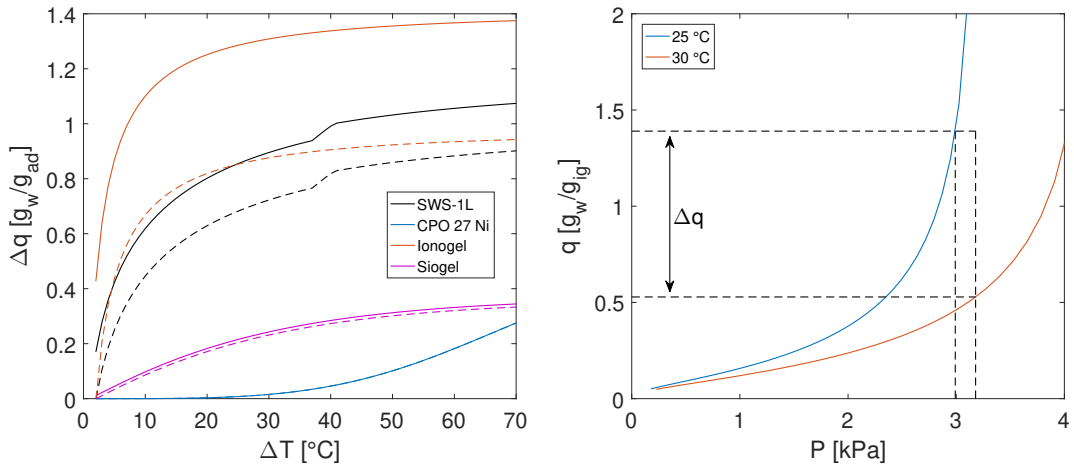


(a) (b)

Figure 5.18: (a) Comparison of the working capacities of three different materials from DA-isotherms [138, 152, 153] with experimental data for Siogel for different $\Delta T = T_{hot} - T_{cond}$ and $T_{cond} = 30$ °C. Dashed lines: $T_{evap} = 28$ °C. Solid lines: $T_{evap} = 29$ °C
(b) Low temperature regeneration of Ionogel indicates a high working capacity from the experimental isotherms. $T_{evap} = 24$ °C, $T_{cond} = 25$ °C, $T_{evap} = 30$ °C leading to $\Delta T = 5$ °C.

The main drawback of both materials is their sensitivity of the water uptake towards the evaporator temperature . The reduction of the evaporator temperature by 1 °C in Fig. 5.18a decreases the working capacity of Ionogel by a third and SWS-1L by a fifth. Siogel and CPO27Ni are not as temperature dependent as the solid and dashed lines in Fig. 5.18a.
CPO27Ni needs a temperature difference $\Delta T$ of at least 30 °C to regenerate any water, which is why the metal organic framework is not applicable in low temperature regeneration applications. By contrast, Ionogel needs only a very small temperature

difference for regeneration making it a very interesting material.
Fig. 5.18b shows how the working capacity is derived from the isotherms and highlights the potential of low temperature regeneration. Regeneration temperature differences as low as 5 °C have never been presented in the literature. Such low regeneration temperatures would enable the use of a large number of new heat sources that could be used to power the system as well as a remarkable variety of system applications, e.g. desalination, heat storage or heat transformation. Therefore, it is important to provide experimental evidence that low temperature regeneration is feasible on a system level.

### Preparation of Ionogel

Ionogel was prepared by impregnating 43 wt% of Syloid 72FP (W.R. Grace, USA) with 57 wt% of EMIM Ac (97 % purity, Sigma Aldrich, USA). Afterwards, the heat exchanger was prepared and weighed after each step: dry the heat exchanger, fill it with Ionogel, dry Ionogel inside the heat exchanger at 80 °C.
The Ionogel inside the heat exchanger was aged to minimise the leakage of ionic liquid inside the test rig [151]. The ageing process includes adsorbing water for 40 h at high humidity and ambient conditions and to desorb water from the Ionogel inside the heat exchanger at 80 °C. The heat exchanger was filled with 25.09 g of Ionogel with an EMIM Ac content of 57 wt% for the experiments in the test rig.

The Ionogel results are compared to silica gel (Siogel, microporous beads 0.5-2 mm Oker Chemie GmbH, Germany) using the same aluminium heat exchangers in both cases[129]. The silica gel experiments were conducted using 210 g per adsorber in two-bed mode and are reported in previous studies[128–130]. During the silica gel experiments, it was observed that large amounts of water evaporated causing temperature differences up to 10 °C within the evaporator due to the latent heat of evaporation. Thus, the amount of Ionogel was reduced to 25 g to limit the total amount of water evaporating during a cycle to achieve a more homogenous temperature distribution in the evaporator. The isotherms indicate high evaporator temperature sensitivity and the need for high relative humidities during adsorption (Fig. 5.16).

## 5.4.2 Results and discussion

### Material analysis

Scanning electron microscope images (ZEISS Crossbeam 550 Cryo FIB/SEM) were taken before testing the ionogel in the adsorption desalinator and are presented in Fig. 5.19. Syloid 72FP has an average particle size of 4.6-5.8 µm [154], while the average pore diameter of Syloid 72FP silica gel is 10-15 nm [155, 156], which is shown in Fig. 5.19a. The particles have a large size distribution forming agglomerates without regular structure. The silica gel particles are supporting the ionogel with the ionic liquid coating the surface, partially filling the pores and acting as binder at the same time. The ionic

liquid fills the pores as well as coats the external surface of the silica gel particles in Fig. 5.19b. Focus ion beam *FIB* etching was applied to view inside an ionogel particle in Fig 5.20, where the particle maintains some pores below a few hundred nanometre thick coating of EMIM Ac.

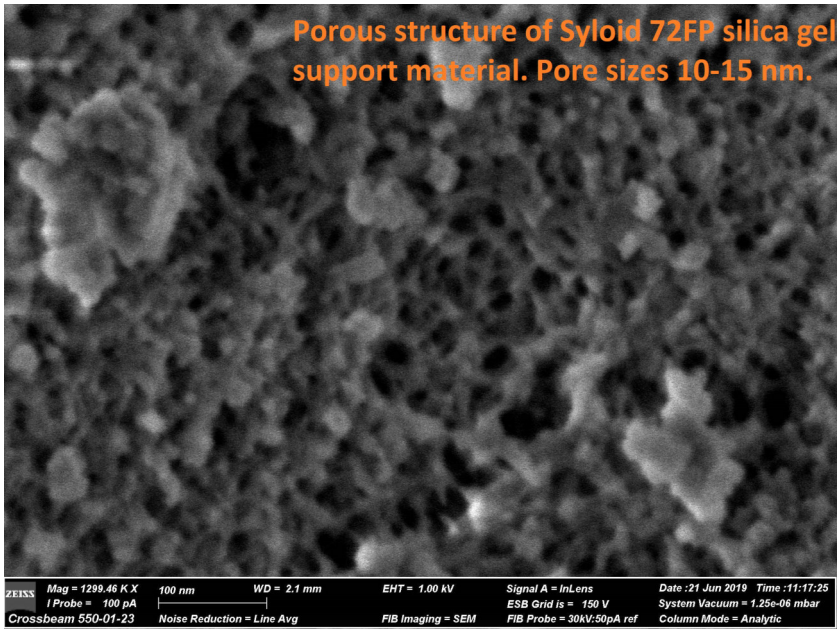


(a)

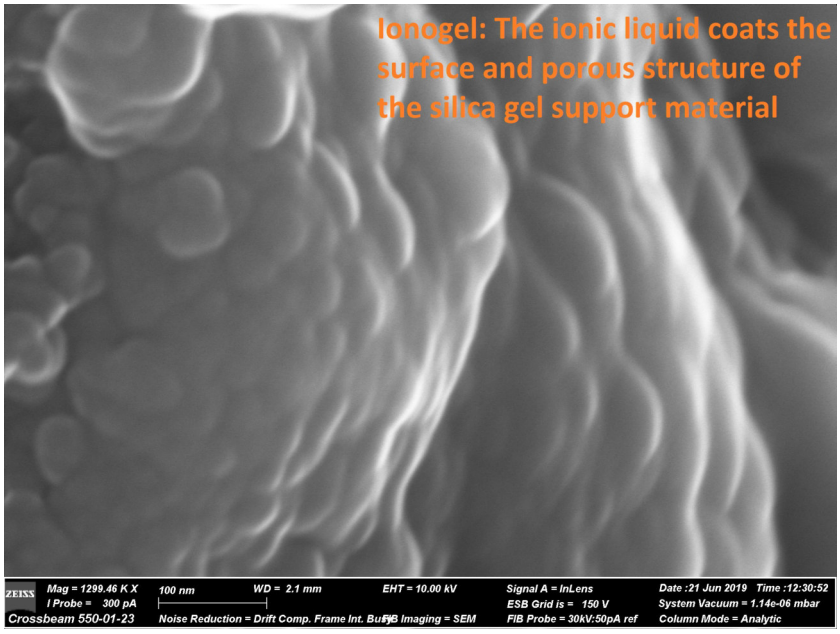


(b)

Figure 5.19: SEM images for comparison of the silica gel support material to the ionogel. (a) Pure Syloid 72FP silica gel. (b) Ionogel: EMIM Ac coats the surface of Syloid 72FP silica gel (cycled).

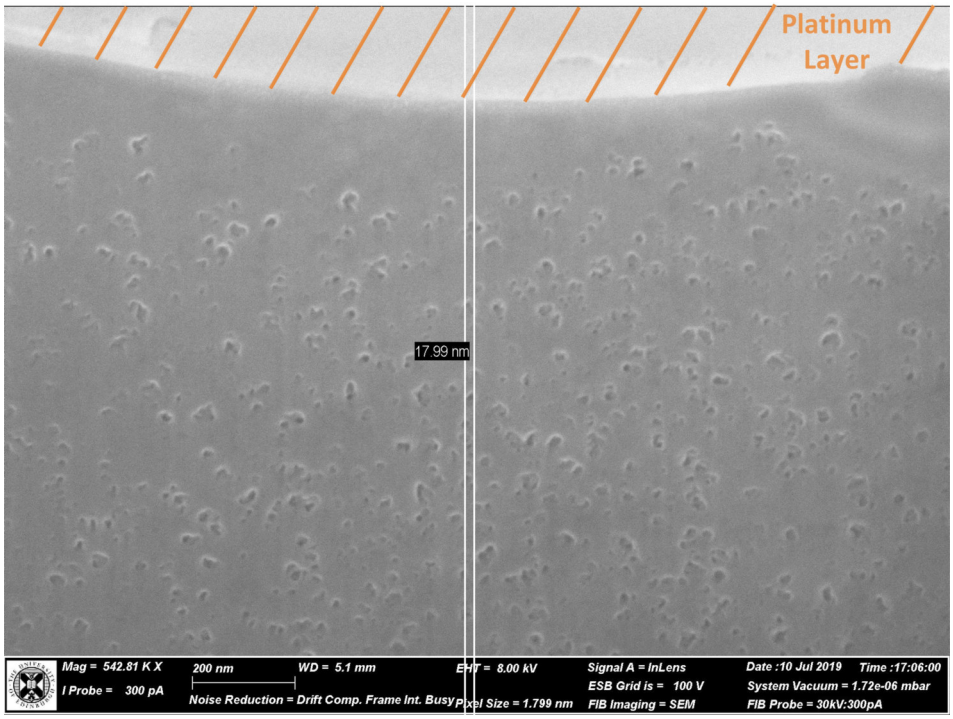


(a)

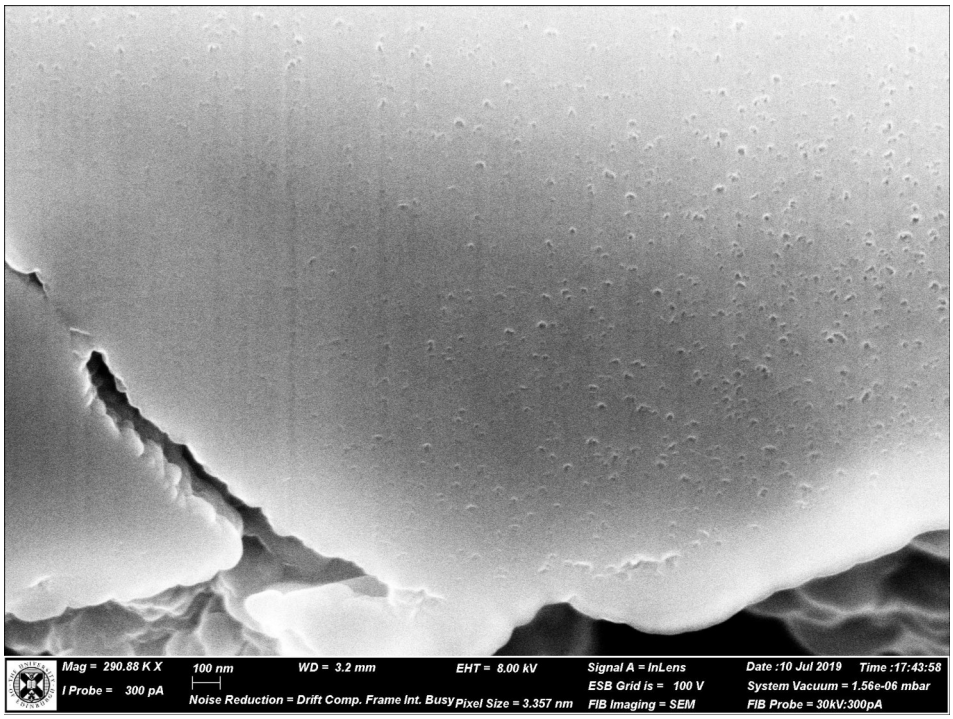


(b)

Figure 5.20: Cycled ionogel: (a) The particle was coated with Platinum for beam protection. Pores of 15 nm are visible. (b) Images of FIB etched particle shows that the porous structure is partially filled below the coated surface.

This is confirmed by Energy Dispersive Spectroscopy *EDS* of a FIB etched particle in Fig. 5.21. An SEM image of the same FIB etched particle is shown in Fig. 1f, SI. The EDS analysis focused on Carbon for EMIM Ac ($C_8H_{14}N_2O_2$) and Silicon for silica gel ($SiO_2$), which are only present in each one of the components. The ionic liquid mainly appears on the particle surface and directly below the surface, whereas the carbon distribution is low in the core of the particle.

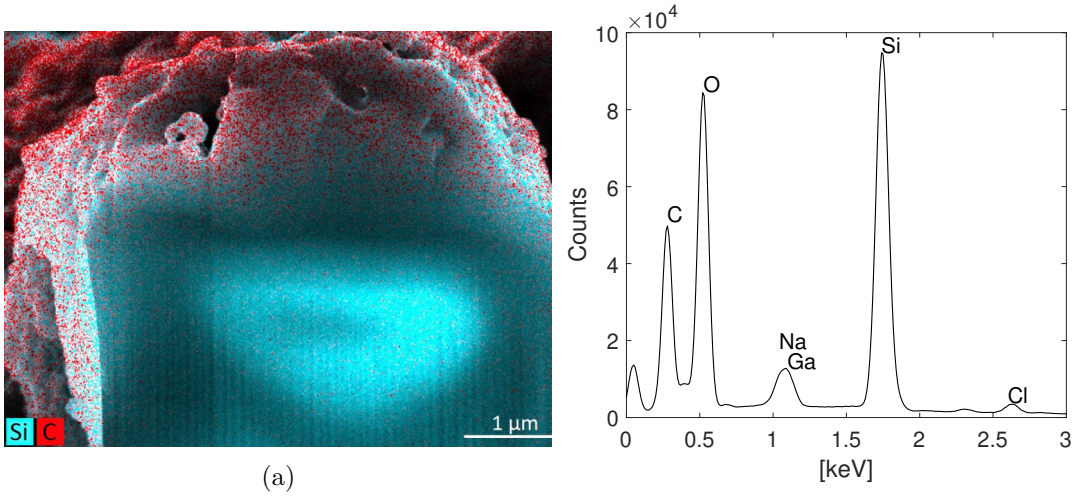


(a) (b)

Figure 5.21: EDS image (a) of FIB etched Ionogel particle. Silicon represents silica gel and Carbon for EMIM Ac. The spectral data is provided in (b).

### Desalination performance

A full characterisation of the novel Ionogel material was conducted inside the adsorption desalinator aiming at identifying the minimum regeneration temperature and optimal cycle time. The test rig was operated in one bed. One bed mode requires less adsorption material as only one heat exchanger needs to be filled, while still allowing to fully characterise the material in terms of SDWP. However, it does not allow the use of the heat recovery and characterisation in respect of the performance ratio, which is not expected to change by more than 10-20 %, because the heat of adsorption of ionogel [131] changes only by 10-20 % compared to siogel [138]. The material was adsorbing at 20 °C and the regenerating at different temperatures from 25 °C to 55 °C increased in increments of 5 °C for each experiment. The evaporator inlet temperature $T_{evap,in}$ was adjusted that $T_{evap,vap} < T_{ads,in}$ and $T_{evap} \approx T_{cond} \approx 20$ °C for all Ionogel experiments. This condition assures that the water vapour during adsorption is colder than the heat exchanger surface to prevent condensation.

Fig. 5.22a shows the temperature swings of the unprecedented $T_{hot,in} = 25$ °C experiment, where the process is operated within $\Delta T \approx 5$ °C. The driving temperature difference powering the process is described by $\Delta T = T_{hot} - T_{cond}$.

No other adsorption material can be regenerated at such low temperature differences.

It can be seen that $T_{evap,vap} < T_{ads,in}$ at all times to avoid condensation. The water production in Fig. 5.22b reaches a peak value of 0.4 g/min, which decreases at the end of desorption to less than 0.1 g/min. Seven different hot temperatures have been investigated in the same way to assess the SDWP of the material as given in Fig. 5.22.

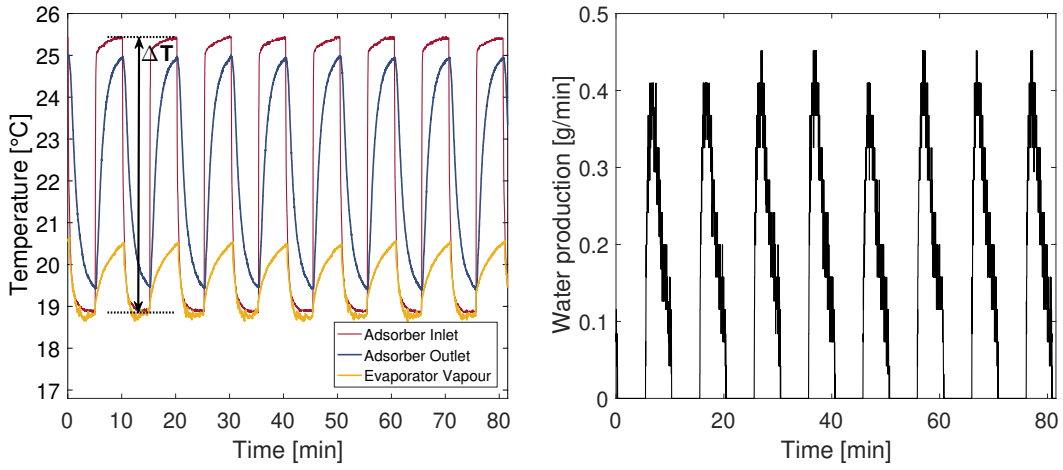


(a) (b)

Figure 5.22: (a) Temperature curves obtained from $\Delta T \approx 5$ °C experiment 280 s half cycle time.
(b) Water production from the same experiment.

The analysis in Fig 5.23a focuses on the optimal half cycle time to achieve the highest SDWP, which is an important preliminary step for the study on the heat source temperature in Fig. 5.23b.

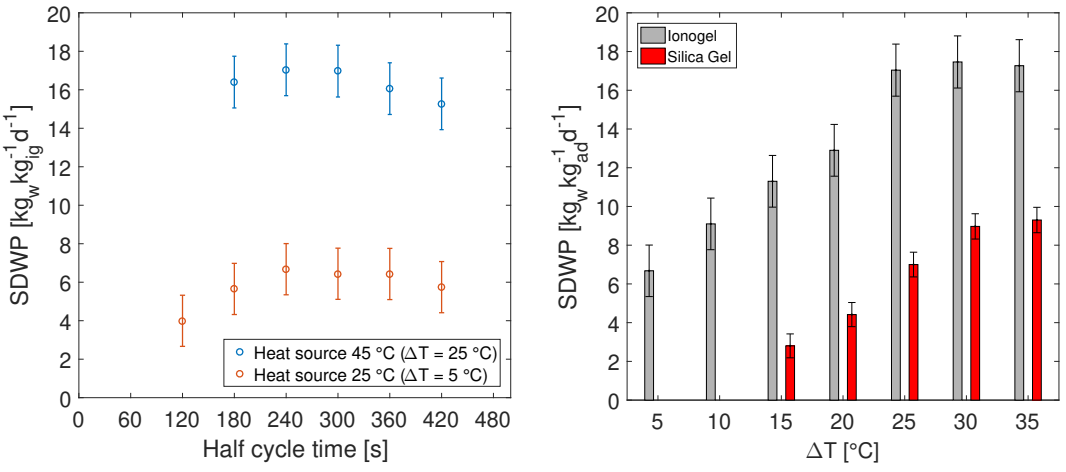


(a) (b)

Figure 5.23: (a) Experimental cycle time analysis for Ionogel at $T_{cond} = 20$ °C.
(b) Experimental SDWP comparison of silica gel and ionogel for different $\Delta T = T_{hot} - T_{cond}$. Ionogel: $T_{cond} = 20$ °C half cycle time 240 s. Silica gel: $T_{cond} = 25$ °C half cycle time 1200 s.

The SDWP is highest for half cycle times of 180 s to 300 s. Hence, half cycle times of 240 s were chosen for the experiments at different low temperatures. Silica gel requires much longer half cycles of 600 s to 1200 s. The heat transfer of the Ionogel monoliths is improved as they share a larger surface area with the aluminium heat exchanger than the silica gel beads. Ionogel has higher adsorption rates, where it reaches the same working capacity as silica gel in a quarter of the time. However, the working capacities of Ionogel in this set of experiment remained well below the working capacities suggested by the isotherms. In the test rig, the working capacities were around 0.2 $g_w/g_{ig}$, while the isotherms predict $\Delta q > 1$ $g_w/g_{ig}$. The deviation of the two $\Delta q$ correspond to Cao et al. [32], who reported fast sorption kinetics at first, which slow down at higher water uptakes. However, Fig. 5.24 shows that the system has not reached the slow down in kinetics yet as the slope of the experimental working capacity remains essentially linear for the tested cycle times. The working capacity in itself is not a performance indicator in adsorption desalination, while the SDWP as main performance indicator is a function of the working capacity as well as the number of cycles per day. The number of cycles per day decreases exponentially with longer cycle times as shown in Fig. 5.24. Hence, short cycle times are favourable for adsorption desalination. To reach equilibrium, the cycle times would have to be very long with the system resulting in very few cycles per day and poor performances in regard of the SDWP.

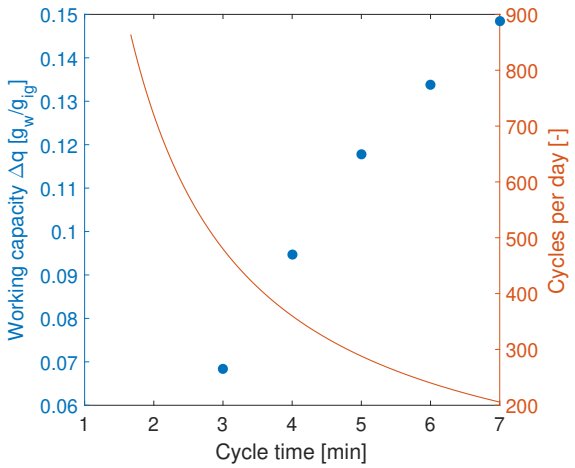


Figure 5.24: The two key contributors to the SDWP: The experimental working capacity increases almost linearly for the tested cycle times at heat source temperature 45 °C, but the calculated cycles per day decrease exponentially.

The isotherms illustrate the water uptake at equilibrium, while in the test rig the material cannot reach equilibrium within useful half cycles times. The high SDWP of Ionogel are a result of the fast kinetics and improved heat and mass transfer compared to silica gel, but not due to the large $\Delta q$ at equilibrium.
Fig. 5.23b shows the resulting SDWP for each hot temperature and compares them to experimental results of silica gel measured in the same test rig at $T_{cond,in} = 25$ °C

[128–130], while the Ionogel experiments were conducted at $T_{cond,in}$ = 20 °C. Therefore, the results are plotted over ΔT to allow a comparison.
Both materials show an almost linear increase of the SDWP at low temperatures until they reach a plateau, which begins at ΔT ≈ 25 °C for Ionogel and ΔT ≈ 30 °C for silica gel. The maximum SDWP of Ionogel is 17.5 $kg_w/(kg_{sg}d)$, which is almost double the SDWP of silica gel at 10.9 $kg_w/(kg_{sg}d)$. However, Ionogel does not have a minimum regeneration temperature, because even at ΔT = 5 °C it achieves SDWP = 6.7 $kg_w/(kg_{sg}d)$, which is comparable to the best silica gel results. By contrast, silica gel needs a temperature difference of at least 15 °C for SDWP = 2.8 $kg_w/(kg_{sg}d)$, where Ionogel is 4 times better at SDWP = 11.3 $kg_w/(kg_{sg}d)$.
The experimental results are compared to recent studies in adsorption desalination in Fig. 5.25 [52, 53, 55, 56].

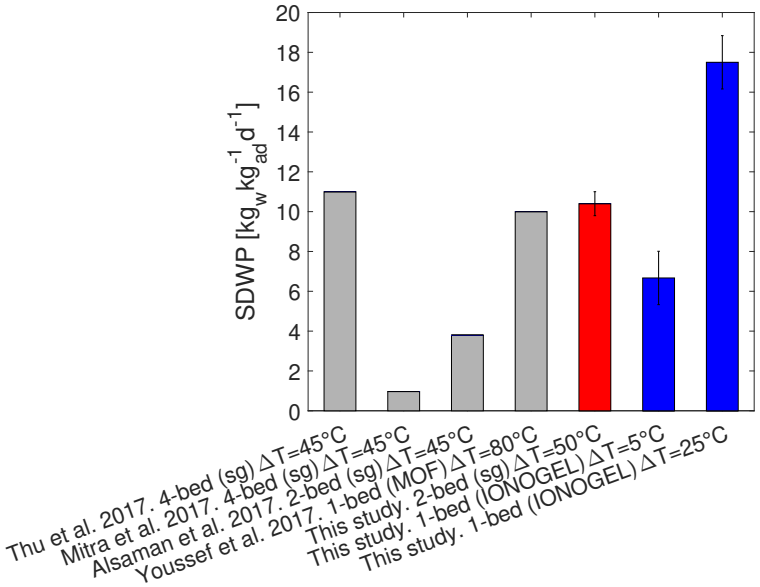


Figure 5.25: Comparison of Ionogel to other studies and materials [52, 53, 55, 56]

The results highlight the competitive advantage of Ionogels compared to materials tested in other systems. Thu et al. have presented a 4 bed system with silica gel, which is currently the largest system and best performing system using silica gel [52]. In a study from 2011 they reported the highest SDWP using the same 4 bed system and silica gel achieving 14.2 $kg_w/(kg_{sg}d)$ with ΔT = 55 °C [134]. The highest SDWP in their y is SDWP = 11 $kg_w/(kg_{sg}d)$ at ΔT = 45 °C [52]. Youssef et al. investigated the application of CPO27Ni MOF-material, which achieves high performances similar to Ionogel [56]. However, the regeneration temperatures are at least 95 °C or ΔT = 80 °C, while Ionogel achieves a higher SDWP at ΔT = 25 °C. Fig. 5.25 also shows the highest SDWP achieved with the experimental apparatus and silica gel within this study. Even at ΔT = 50 °C silica gel can only reach SDWP = 10.9 $kg_w/(kg_{sg}d)$, which is less than Ionogel at ΔT = 15 °C in Fig. 5.23b.

Fig. 5.26a displays the material after exposing it to several hundred temperature swings, which causes material ageing. Before the experiments, Ionogel is a white, dull, brittle substance that turns into a gray, glossy gel over time (Fig. 5.26a). Measurements of the isotherms of the cycled and freshly prepared materials showed that the water uptake did not change highlighting the material stability.

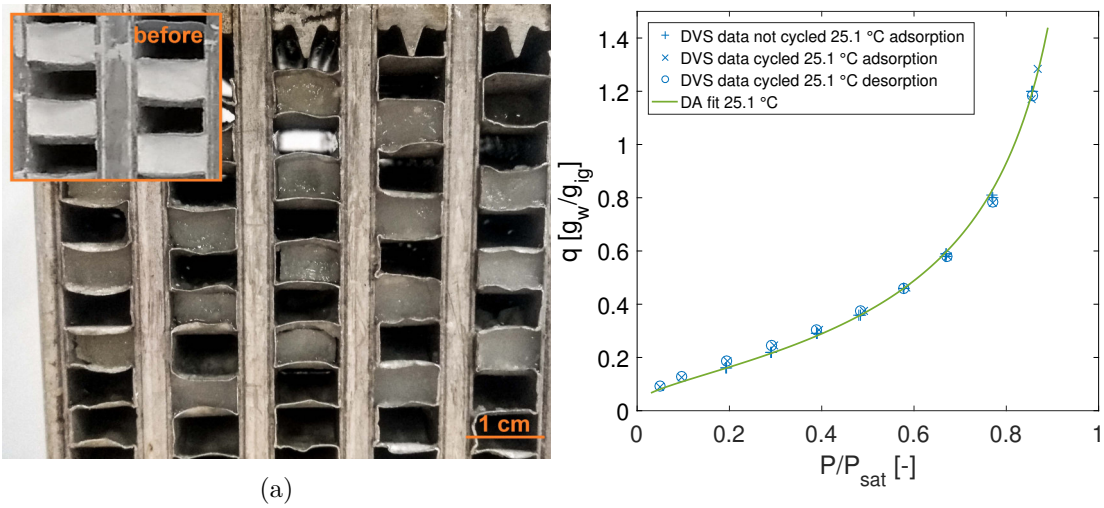


(a) (b)

Figure 5.26: (a) The fresh material is a white, brittle, powdery substance, whereas cycling turns it grey and shimmering.
(b) Measured isotherm of the cycled material fitted to the Dubinin-Astakhov isotherm equations and compared to the DA fit of the fresh, not-cycled material.

## 5.5 Conclusions

A novel, small-scale adsorption desalination prototype was designed, assembled and operated. The test rig is currently the world's smallest, reported design. The small-scale design allows an increased flexibility in testing new materials and system components compared to larger system designs.

The first part of the experimental investigation assessed the performance of Siogel silica gel packed inside aluminium heat exchangers. This starting point established a reference case, which is compared to the literature. The system achieved a Specific Daily Water Production of up to 7.7 $kg_w/(kg_{sg}d)$ at $T_{hot,in}$ = 80 °C and $T_{evap,in}$ = $T_{cond,in}$ = 30 °C. A change of the evaporator and condenser inlet temperatures to achieve $T_{evap,vap} \approx T_{cond,vap}$ increase the Specific Daily Water Production to 10.9 $kg_w/(kg_{sg}d)$ at $T_{hot,in}$ = 80 °C, $T_{evap,in}$ = 35 °C and $T_{cond,in}$ = 25 °C, which is among the highest results reported for silica gel. Hence, the small scale is not detrimental to the performance and a full analysis of novel adsorption materials is possible with this small-scale system in the future. Moreover, the impact of heat recovery between the adsorber beds on the system performance was investigated in two steps by focusing on the performance

indicators and by a thermal response experiment. The heat recovery increased the performance ratio by 25 % to 0.6. The system is further characterised by a thermal response experiment informing on the partition of energy, which shows that the peak heat input is 900 W without heat recovery. The heat recovery system reduces the peak energy input to 500 W, which would allow the application of smaller heat sources.
Copper heat exchangers were packed with silica gel, but the results (Appendix D.4) showed that their fins did not heat up properly. Hence, they could not be used for cyclic heating and cooling of the adsorption material and were discarded.
Ionogels were tested in adsorption desalination for the first time to replace silica gel as adsorption material. A screening of ionic liquids identified BMIM Br, BMIM Ac, EMIM Ac and Choline Glycolate as most promising, non toxic options for the desalination application. An Ionogel was prepared combining 43 wt% of Syloid 72FP silica gel with 57 wt% of EMIM Ac. The Ionogel was tested in the small-scale adsorption test rig leading to compelling SDWP results. The material achieves SDWP = 17.5 $kg_w/(kg_{ig}d)$ at regeneration temperatures as low as 45 °C. This is the highest result ever achieved in experimental adsorption desalinator in the literature with by far the lowest regeneration temperature. The tests showed that Ionogels can even be regenerated with a temperature difference of 5 °C accomplishing SDWP = 6.7 $kg_w/(kg_{ig}d)$, which is still comparable to the best silica gel results, but with an astonishingly low temperature difference. Thus, Ionogels represent a striking new class of materials for adsorption desalination.

# Chapter 6

# Adsorption reverse electrodialysis

This chapter proposes the integration of adsorption desalination into the RED Heat to Power process. The previous chapter has shown that adsorption desalination shows some extraordinary features like regeneration as low as 25 °C for Ionogels or 40 °C for silica gel.
Adsorption desalination may have a high thermal energy consumption compared to MED or ABVC, but it requires a minimum of internal electricity for pumps and moving parts maximising the net electricity output. Firstly, this chapter presents adsorption reverse electrodialysis (ADRED) in thermodynamic simulations to identify the performance, when all system limitations are neglected. In addition, a switch of solvent from water to liquid ammonia is considered, because ammonia has a lower latent heat of evaporation than water, which would improve the thermal efficiency of the regeneration. Secondly, a dynamic model is implemented taking system limitations into account as every modelling component is individually, experimentally validated.
The results of the first section of this chapter have been published in Applied Energy [119] and a publication presenting the second section is in preparation.

## 6.1 Thermodynamic model for the best salt and material

The proposed system converts low grade heat to electricity. [6]. For ADRED, low-grade heat temperatures below 70 °C are of particular interest. Papapetrou et al. identify the main industries emitting waste heat below 100 °C as the food industry and the paper industry [6]. For example, the exhaust air from the drying section of a mid-sized paper machine has a temperature of 70 °C with a heat output of 6 MW [157]. Another possible heat source could be provided by a solar collector [11, 132]. The system could also utilise waste heat from power plants, which is available in very large quantities below 100 °C [5].
The flow scheme of the ADRED system can be seen in Fig. 6.1. The two main components of the ADRED system are the Reverse Electrodialysis membrane and the adsorption desalinator. The outlet of the high salinity solution is connected to the

evaporator of the adsorption regeneration, where the solution is regenerated to its initial salt concentration. A part of the water is evaporated from the brine and the pure water vapour is adsorbed on the adsorption material. Low-grade waste heat is required to desorb the vapour from the material. Each adsorber undergoes a temperature swing adsorption cycle. The adsorption cycle includes a heating phase, when the adsorbate desorbs from the surface of the adsorbent material. Afterwards the material is cooled to ambient temperature to adsorb new adsorbate onto its surface. Therefore, one adsorption bed would only allow an intermittent process, since one bed can only either adsorb or desorb at a given time. Whereas, the addition of a second bed enables a semi-continuous operation. In this case one bed can adsorb water from the evaporator, while the other bed desorbs water vapour. The desorbing vapour is condensed and mixed with the low salinity outlet solution coming from the membrane.

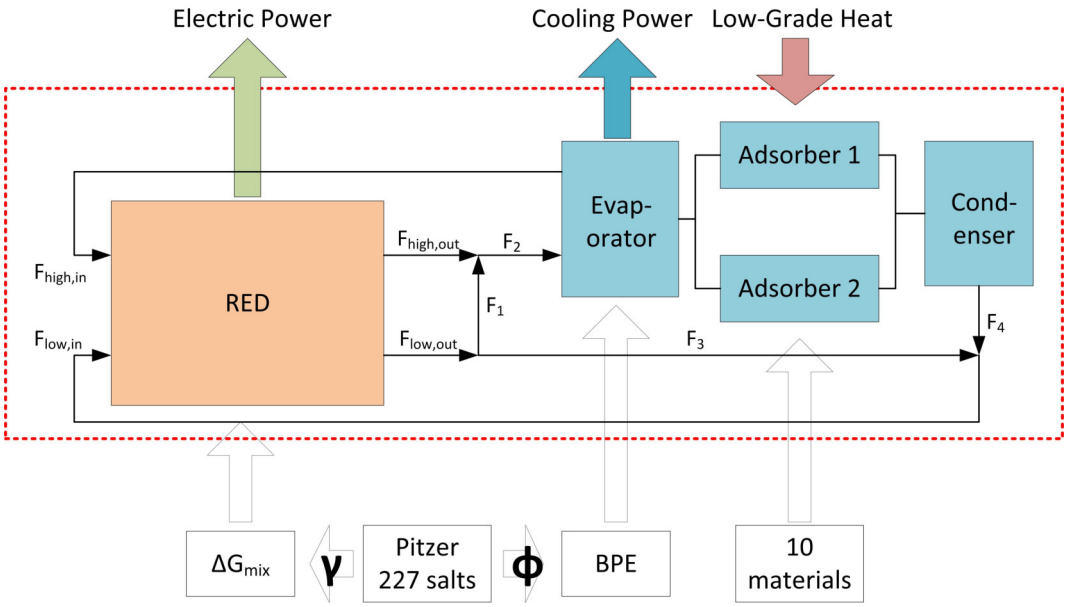


Figure 6.1: ADRED model illustrated in a simplified way

The entire system operates at the saturation pressures of the working fluid inside. Water vapour condensed at 30 °C necessitates an absolute condenser pressure of 0.04 bar [39]. However, the low pressure has no negative impact on the electricity generation, because RED is an electrochemical process driven by salinity gradients and not by pressure differences. In theory, the system could also be operated with different fluids and salt solutions. For example, the utilisation of solutions of pure liquid ammonia and salts would allow the operation of the system pressurised at an absolute pressure of 11.7 bar and a condenser temperature of 30 °C [39]. In addition, ammonia has a very low latent heat, which would increase evaporation and the efficiency of the regeneration. However, the mean activity coefficients of salt solutions with ammonia as solvent are low [158], which reduces $\Delta G_{mix}$. Furthermore, RED membranes are designed for aqueous salt solutions, but not for ammonia or other solvents. Thus, water is the most feasible and

environmentally friendly choice as fluid.

### 6.1.1 Thermodynamic model

The following assumptions were made for the model:

- Only salt ions pass through the RED membrane, but no water. This simplification is necessary to assess the electricity output by $\Delta G_{mix}$. A salt specific membrane model would be required to evaluate the water transport through the membrane itself, which cannot be prevented in a real system. However, this investigation addresses the ideal case for a large number of salts. Hence, the water transport through the membrane has been neglected.
- The electricity produced by the RED membrane is equal to the Gibbs free energy of mixing.
- The relationship between the activity of water and the saturation pressure is ideal.
- In most cases the specific heat capacity of the adsorption material $c_{p,AD}$ was not specified in the literature, so $c_{p,AD} \approx 1$ kJ/(kgK) was assumed from [159].
- The mass of the heat exchangers was neglected for the analysis of the SEC as they already represent a system limitation and this analysis focuses on the ideal case.
- All the salt remains in the evaporator and only pure water vapour reaches the adsorption material.
- The cooling power is neglected as system output, because it would reduce the desalination capacity of the material. Cooling power and electricity production are a trade-off, where the negligence of cooling maximises the working capacity of the adsorption material and with it, the electricity production of the system.
- The study neglects the change of latent heat caused by the salt. The latent heat of the salt solution would affect the cooling power of the system, but the SEC is independent of the latent heat in the evaporator. The salt remains in the evaporator and affects the latent heat of the salt solution in the evaporator alone. This changes the cooling power output of the evaporator, which is neglected by the investigation. Only pure water vapour is assumed to reach the adsorption material, which is why the latent heat of pure water applies to adsorption and desorption of the pure water vapour. Thus, the enthalpy difference of the salt solution can be neglected, because it does not affect the adsorption material.
- The internal electricity consumption of the system was neglected to assess the maximum thermodynamic efficiency achievable with the system. However, this

assumption is challenged with additional considerations following the main investigation to assess the impact on a real system application.

- For simplification the low and high salinity feed solutions to the RED stack have the same flow rate [116]

### Model equations for the ADRED flow scheme

Fig. 6.1 also presents the set-up of the ADRED model. The description in greyscale illustrates the base of the model with the Pitzer equations and the Dubinin Astakhov data for the adsorption materials, which are all required to assess the main part of the model highlighted by the dashed line. The Pitzer correlations provide the osmotic coefficient $\Phi$ and the activity coefficient $\gamma$ for each of the 227 salts [104] at the desired concentration. The coefficient $\gamma$ is needed to calculate $\Delta G_{mix}$ and thereby the electricity output of the RED membrane. The osmotic coefficient $\Phi$ is used to determine the boiling point elevation (BPE) of the high salinity solution. The high salinity solution is regenerated in the evaporator and its BPE influences the evaporator pressure $P_{sat}(T_{evap})$. The Dubinin Astakhov (DA) isotherm data for 10 adsorption materials was obtained from the literature [23, 24, 123, 160–163]. The isotherms are needed to assess the energy required to regenerate the salt solutions. Salt balances based on the flow scheme in Fig. 6.1 determine the amount of condensate needed to restore the salt gradient.

The mass and salt balances for the flow scheme in Fig. 6.1 are listed below.
Mass balances:

$$F_{High,in} = F_{Low,in} \tag{6.1}$$

$$F_1 = F_4 \tag{6.2}$$

$$F_{High,out} + F_1 = F_2 \tag{6.3}$$

$$F_{Low,out} - F_1 = F_3 \tag{6.4}$$

Salt balances:

$$F_{Low,out}C_{Low,out} + F_{High,out}C_{High,out} = F_{Low,in}C_{Low,in} + F_{High,in}C_{High,in} \tag{6.5}$$

$$F_2C_2 = F_{High,out}C_{High,out} + F_1C_1 \tag{6.6}$$

$$F_3C_{Low,out} = F_{low,in}C_{low,in} \tag{6.7}$$

$$C_{High,out} - C_{Low,out} = (1 - X)\ (C_{High,in} - C_{Low,in}) \tag{6.8}$$

$F_i$ [kg/s] represents the flow rates and $C_i$ [mol/kg] the salt concentrations. The conversion factor X determines the change of the salt concentrations after passing through the RED membrane. $F_1$ compensates for the amount of distillate $F_4$ to restore the initial salt concentrations $C_{high,in}$ and $C_{low,in}$.

### Parameters calculated using Pitzer equations

Part of the Pitzer model was already described in the previous section 3.1.3, where it was used to fit the Pitzer virial coefficients $\beta_{MX}{}^{(0)}$, $\beta_{MX}{}^{(1)}$ and $C_{MX}{}^{\Phi}$ to the osmotic coefficients $\Phi$ calculated from experimental data. In this chapter the Pitzer model from chapter 3 is used to calculate activity coefficients $\gamma$, which were not needed for the analysis in chapter 3.

The activity coefficient $\gamma$ can be obtained from the Pitzer correlations [104]:

$$ln(\gamma) = |z_M z_X| f^{\gamma} + m\left(\frac{2v_X v_M}{v}\right) B^{\gamma}_{MX} + m^2\left(\frac{2(v_M v_X)^{3/2}}{v}\right) C^{\gamma}_{MX} \tag{6.9}$$

$$f^{\gamma} = -A_{\Phi}\left[\frac{I^{1/2}}{1+bI^{1/2}} + \frac{2}{b} ln(1+bI^{1/2})\right] \tag{6.10}$$

$$B^{\gamma}_{MX} = 2\beta^{(0)}_{MX} + \frac{2\beta^{(0)}_{MX}}{\alpha^2 I}\left[1 - e^{-\alpha I^{1/2}}(1+\alpha I^{1/2} - (1/2)\alpha^2 I)\right] \tag{6.11}$$

$$C^{\gamma}_{MX} = \frac{3}{2} C^{\Phi}_{MX} \tag{6.12}$$

$$I = \frac{1}{2}\sum m_i z_i^2 \tag{6.13}$$

The coefficients b and $\alpha$ are constants with the values of 1.2 and 2 for all solutes [104]. The ionic strength is represented by I [mol/kg] in the equations above, $z_M$ and $z_X$ are the charges of the ions [-], while $v_M$ and $v_X$ are the number of ions [-]. The molality is given by m [mol/kg]. The Debye Hückel coefficient $A_{\Phi}$ for water is given by [104, 105] and is reported in eq. 3.11 in section 3.1.3. In addition, the vapour pressure of a solution can also be assessed through the Pitzer model using eq. (3.4) and (3.5) from section 3.1.3.

The Gibbs free energy of mixing represents a theoretical maximum value of the energy released due to the mixing of two solutions in a reversible process. In reality, the mixing of solutions is an irreversible process, which increases the entropy of the solution. The useable energy is therefore lower than the Gibbs free energy of mixing [164], whereas the model evaluates the ideal case.

The Gibbs free energy of mixing per mole of mixture is defined as [164]:

$$-\Delta G_{mix} = RT\left\{\left[\sum x_i ln(\gamma_i x_i)\right]_M - \Lambda_A\left[\sum x_i ln(\gamma_i x_i)\right]_A - \Lambda_B\left[\sum x_i ln(\gamma_i x_i)\right]_B\right\} \quad (6.14)$$

where $x_i$ are the mole fractions and $\Lambda_A$, $\Lambda_B$ are the ratios of total moles of each solution based on the entire system $\Lambda_A + \Lambda_B = 1$. The Gibbs free energy of mixing can be simplified for an aqueous solution of strong electrolytes and low salt concentrations [164]. At low concentrations, the mole fraction of water is approximately one and the activity coefficient of water is one as well making the contribution of water in eq. (6.14) negligible, which is why $\Delta G_{mix}$ can be approximated to [164]:

$$-\frac{\Delta G_{mix}}{vRT} \approx c_M\ ln(\gamma_{s,M} c_M) - \Psi c_{low}\ ln(\gamma_{s,low} c_{low}) - (1-\Psi) c_{high}\ ln(\gamma_{s,high} c_{high}) \quad (6.15)$$

where v represents the total number of ions dissociated into the solution from each electrolyte and $\Psi \approx V_{low}/(V_{low}+V_{high})$. Fig. 6.1 shows the case of two inlet streams and two outlet streams from the membrane. For the case presented in Fig. 6.1 the Gibbs free energy of mixing is:

$$\begin{aligned}-\frac{\Delta G_{mix}}{vRT} \approx \Psi\ c_{low,out}\ ln(\gamma_{s,low,out} c_{low,out}) + (1-\Psi) c_{high,out}\ ln(\gamma_{s,high,out} c_{high,out}) \\ -\Psi\ c_{low,in}\ ln(\gamma_{s,low,in} c_{low,in}) - (1-\Psi) c_{high,in}\ ln(\gamma_{s,high,in} c_{high,in})\end{aligned} \quad (6.16)$$

### Energy and exergy performance based on an adsorption cycle analysis

During the regeneration the adsorber beds are heated and cooled as shown in the adsorption cycle in Fig. 6.2.

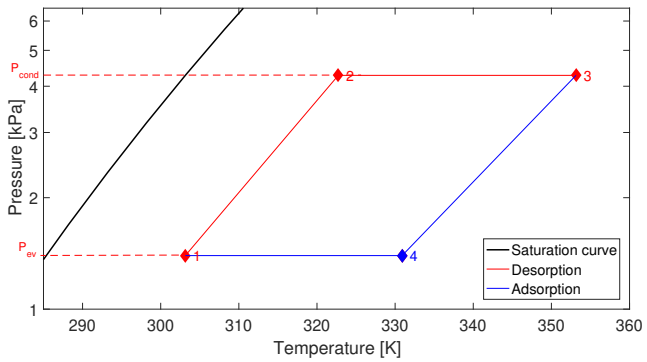


Figure 6.2: The adsorption cycle is split into desorption 1→3 and adsorption 3→1.

The specific energy consumption is a performance parameter, which predicts the amount of energy required per kilogram of pure water desorbed [120]:

$$SEC = \frac{Q_{1\to2} + Q_{2\to3}}{M_{water}} \quad (6.17)$$

The SEC represents the energy $Q_{1\to2\to3}$ required for the desorption process, where the adsorption beds are heated by the low-grade heat source. The first contributor $Q_{1\to2}$ is the energy required for isosteric heating to increase the pressure from the saturation pressure of the evaporator to the saturation pressure of the condenser. Thus, the beds are heated from ambient temperature $T_1$ to the intermediate temperature $T_2$. During this the two valves connecting the adsorber to evaporator and condenser are closed to increase the pressure without any adsorption or desorption occurring during this step.

$$Q_{1\to2} = m_{AD}(q_1 C_{p,H_2O} + C_{p,AD}) \cdot (T_2 - T_1) \tag{6.18}$$

As soon as the pressure of the adsorber beds equals the pressure of the condenser, desorption begins. The valve between the adsorber and condenser is opened. As a result, water vapour desorbs from the material while the bed continues to be heated from the intermediate temperature $T_2$ to the temperature of the low-grade heat source $T_3$, which is both accounted for by $Q_{2\to3}$:

$$Q_{2\to3} = m_{AD}\left((T_2 - T_1) + \left[C_{p,AD} + \frac{q_2 + q_3}{2} C_{p,H_2O}\right] \cdot (T_3 - T_2) + (q_2 - q_3)\Delta h\right) \tag{6.19}$$

$$M_{water} = m_{AD}(q_2 - q_3) \tag{6.20}$$

$$SEC = \frac{(q_1 C_{p,H_2O} + C_{p,AD})(T_2 - T_1) + \left[C_{p,AD} + \frac{q_2+q_3}{2} C_{p,H_2O}\right](T_3 - T_2) + (q_2 - q_3)\Delta h}{q_2 - q_3} \tag{6.21}$$

The SEC [$kJ/kg_{H_2O}$] is assessed through the analysis of the thermodynamic cycles. This analysis provides the parameters required in eq. (6.21), which are the temperatures at each state of the adsorption cycle $i$ $T_i$ [K], the uptake of the adsorption material $q_i$ [kg/kg] and the operating pressures $P_i$ [bar]. The mass of the adsorption material $m_{AD}$ cancels out in the SEC equations and therefore does not need to be defined.

While the SEC is required for the energy analysis, it must be extended by the Carnot factor to perform an exergy analysis of the process. The Carnot factor in eq. (6.28) describes the theoretically highest possible efficiency between the boundaries of the ambient temperature $T_{cond}$ and regeneration temperature $T_{hot}$ [78].

$$\eta_c = 1 - \frac{T_{cond}}{T_{hot}} \tag{6.22}$$

At low temperatures only a small fraction of the energy provided to the system can be used by the process (exergy), which in this case is the energy content available between ambient temperature and the heat source temperature. The analysis of the

exergy efficiency can be more useful than the energy efficiency alone, because it provides information on how well the available exergy is used by the process [78, 165].

$$\eta_{ex} = \frac{\eta}{\eta_c} \tag{6.23}$$

The exergetic SEC is defined in eq. (6.24):

$$SEC_{ex} = SEC\ \eta_c = \frac{(Q_{1\to2} + Q_{2\to3})\left(1 - \frac{T_a}{T_{hot}}\right)}{M_{water}} \tag{6.24}$$

In this study, the thermodynamic cycle was assessed by the use of the Dubinin-Astakhov isotherm (DA) [122].

$$q = q_0\ exp\left[-\left(\frac{A}{E}\right)^n\right] \tag{6.25}$$

$$A = -RT\ ln\left(\frac{P}{P_s}\right) \tag{6.26}$$

Where $q_0$ [kg/kg], $E$ [kJ/kg] and $n$ [-] are the Dubinin Astakhov parameters given in table 6.1. The isosteric heat of adsorption $\Delta$h was obtained from the following equation [124]:

$$\Delta h = L + E\ ln\left(\frac{q_0}{q}\right)^{1/n} + \frac{E\beta T}{n}\left(\frac{q_0}{q}\right)^{-(n-1)/n} \tag{6.27}$$

Where $\beta$ is the coefficient of thermal expansion [1/K].

Table 6.1: Dubinin-Astakhov parameters for different materials with water. In the cases of 1*: $c_{p,AD}$ was not specified and $c_{p,AD}$ = 1 kJ/(kgK) was taken from [159].

| Material | Type | $q_0$ [kg/kg] | E [kJ/kg] | n [-] | $c_{p,AD}$ [kJ/(kgK)] | Ref. |
|---|---|---|---|---|---|---|
| Siogel | Silica Gel | 0.38 | 220.0 | 1.10 | 0.8 | [123] |
| Grace 127 B | Silica Gel | 0.31 | 152.4 | 0.90 | 1* | [160] |
| Type-A5BW | Silica Gel | 0.45 | 199.2 | 1.25 | 1* | [24] |
| Type-RD 2560 | Silica Gel | 0.33 | 243.6 | 1.35 | 1* | [24] |
| Type-A++ | Silica Gel | 0.49 | 211.3 | 1.35 | 1* | [24] |
| CPO-27(Ni) | MOF | 0.46 | 556.3 | 4.00 | 1* | [161] |
| AQSOA Z01 | Zeolite | 0.21 | 222.2 | 5.00 | 1* | [23] |
| AQSOA Z02 | Zeolite | 0.31 | 388.9 | 3.00 | 1* | [23] |
| Köstrolith 13XBFK | Zeolite(13X) | 0.34 | 1192.3 | 1.55 | 0.88 | [162] |
| ZEOX OII | Zeolite(13X) | 0.23 | 1266.7 | 1.20 | 1* | [163] |

### Integrating the SEC into the ADRED flow scheme

The $SEC_{ex}$ expresses the exergy required to produce one kilogram of pure water. Thus, it needs to be integrated into the salt balances. In the model, both streams entering the RED membrane each have a mass flow of 1 kg/s and are mixed to a certain degree

depending on the conversion factor X. The salt balances determine the amount of distillate $F_4$ that needs to be regenerated. Multiplying the $SEC_{ex}$ with $F_4$ assesses the exergy needed to restore the salt concentrations in the model. The ratio of the key parameters indicates the exergy efficiency of the ADRED system.

$$\eta_{ex} = \frac{\Delta G_{mix}}{SEC\ \eta_c\ F_4} \tag{6.28}$$

### 6.1.2 Results and discussion

The ADRED model has eight degrees of freedom listed in table 6.2. In a preliminary investigation, the degrees of freedom were lowered to five to reduce the number of possible input scenarios from 20 million by two orders of magnitude. The aim was to calculate the exergetic performance for each combination of input scenarios and find the optimum combination of salt, material and system parameters.

Table 6.2: The degrees of freedom of the ADRED model

| **Parameter** | | **Unit** | **Range** | **No. of steps** |
|---|---|---|---|---|
| Evaporator Temperature | $T_{evap}$ | [°C] | 10-30 | 5 |
| Condenser Temperature | $T_{cond}$ | [°C] | 20-30 | 3 |
| Regeneration Temperature | $T_{hot}$ | [°C] | 60-100 | 5 |
| Inlet concentration low | $C_{low,in}$ | [mol/kg] | 0-$C_{max}$ | 5 |
| Inlet concentration high | $C_{high,in}$ | [mol/kg] | $C_{max}$ | 1 |
| Conversion factor | X | - | 0.2-1 | 5 |
| Salts | - | - | 227 | 227 |
| Adsorption materials | - | - | 10 | 10 |

The preliminary investigation showed that the ratio of $\Delta G_{mix}$ to $SEC_{ex}$ was highest at the maximum inlet concentration $C_{high,in}$ for all salts. The Pitzer tables [104] provide the maximum value of $C_{high,in}$=$C_{max}$ for each salt and it was used for the analysis. Furthermore, an analysis of the SEC for the regeneration side was performed to choose the best temperatures for the evaporator and condenser $T_{evap}$ and $T_{cond}$.

#### Temperature impact of the adsorption regeneration on the SEC

Twelve different, temperature combinations were identified to find the best temperature combination of $T_{evap}$ and $T_{cond}$ for the lowest SEC. For each combination, the exergetic $SEC_{ex}$ was calculated for an aqueous 5 mol/kg NaCl solution in the evaporator, the ten adsorption materials and five different regeneration temperatures between 60-100 °C. Afterwards an $SEC_{ex}$ was formed averaging all results for the regeneration temperatures taking all combinations of $T_{evap}$ and $T_{cond}$ into account as shown by the red bars in Fig. 6.3. The analysis of the total value for the $SEC_{ex}$ ensures that the chosen temperature combination provides the best overall results for all the materials. In desalination $T_{evap}$ and $T_{cond}$ are usually equal [120]. The result in Fig. 6.3 is in accordance with

the literature and $T_{evap}$=$T_{cond}$= 30 °C was selected as temperatures for the ADRED system simulation.

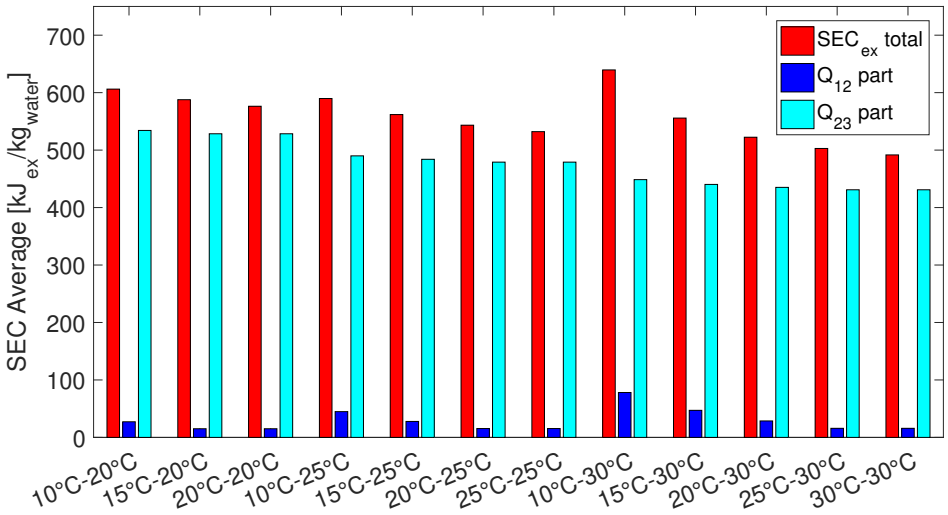


Figure 6.3: Desorption $Q_{23}$ has a higher contribution to the predicted SEC than the isosteric heating $Q_{12}$ (example shown with 5 m NaCl).

In addition, the $SEC_{ex}$ in Fig. 6.3 is split into the two parts $Q_{1\to2}$ and $Q_{2\to3}$ as shown in eq. (6.29).

$$SEC_{ex} = \frac{(Q_{1\to2})\left(1-\frac{T_{cond}}{T_{hot}}\right)}{M_{water}} + \frac{(Q_{2\to3})\left(1-\frac{T_{cond}}{T_{hot}}\right)}{M_{water}} \tag{6.29}$$

In Fig. 6.3, the difference of $SEC_{ex}$ between the least and the most efficient temperature combination is almost 30 %, which is caused by the contribution of the isosteric heating $Q_{1\to2}$. The larger the pressure difference between evaporator and condenser, the more energy is needed to increase the pressure of the adsorption bed from the evaporator pressure to the condenser pressure. The first part of eq. (6.29) accounts for this, which can be seen in Fig. 6.3. The second part of eq. (6.29) remains constant in Fig. 6.3 for each $T_{cond}$, even though the energy $Q_{2\to3}$ decreases at large temperature difference between $T_{evap}$ and $T_{cond}$ as it can be seen in Fig. 6.4. The amount of pure water $M_{water}$ produced in each cycle decreases with the temperature difference as well. The two effects cancel each other out, which is why the second part of eq. (6.29) remains essentially constant in Fig. 6.3.

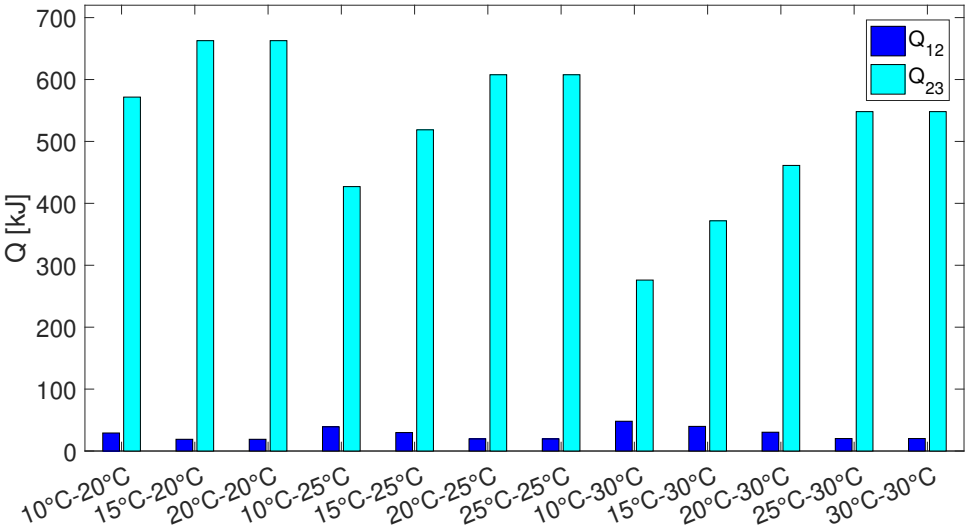


Figure 6.4: The predicted, average energy contribution of $Q_{12}$ and $Q_{23}$ for each combination of $T_{evap}$ to $T_{cond}$. The concentration of NaCl in the evaporator is 5 mol/kg in this example

### Influence of the boiling point elevation (BPE) on the adsorption cycle

Wu et al. [120] investigated the impact of the three temperature levels $T_{evap}$, $T_{cond}$ and $T_{hot}$ on the thermodynamic cycle in desalination, where they described the three possible cases $T_{evap} < T_{cond}$, $T_{evap} = T_{cond}$ and $T_{evap} > T_{cond}$. The results showed that the SEC for the case $T_{evap} \geq T_{cond}$ is generally the best. However, Wu et al. neglected the presence of salt in the evaporator. The salt-free case they assumed for $T_{evap} = T_{cond}$ is shown in Fig. 6.5. In this case the thermodynamic cycle is reduced to a straight line, where the condenser and evaporator operate at the same pressure $P_{evap} = P_{cond}$. Hence, the uptake $q_1 = q_{sat}$ is maximal and the process has the highest working capacity $\Delta q$ possible. By contrast, the second cycle shown in Fig. 6.5 illustrates the thermodynamic cycle of a 5 mol/kg $MgI_2$ solution considering the boiling point elevation, which reduces the pressure in the evaporator.
The BPE is defined as:

$$BPE = T_{sat,sol}(P_{sol}) - T_{sat,H_2O}(P_{sol}) \tag{6.30}$$

The effect of the BPE on the thermodynamic cycle in Fig. 6.5 is significant. The evaporator temperature in both cases in Fig. 6.5 remains the same $T_{evap} = 30$ °C. However, the BPE of 17 °C in the case of the $MgI_2$ solution lowers the pressure in the evaporator from 4.3 kPa to 1.4 kPa. As a result, the thermodynamic adsorption cycle of the aqueous $MgI_2$ solution in Fig. 6.5 has the same shape a pure water cycle would have of a pure water cycle at $T_{evap} = 13$ °C, $T_{cond} = 30$ °C and $T_{hot} = 80$ °C, even though the evaporator and condenser are actually operating at the same temperature

$T_{evap} = T_{cond} = 30$ °C. This has significant impact on the water uptake of the material during adsorption $\Delta q$, which is 19 % below the uptake in the salt-free case and leads to a decreased water production per cycle by the same factor. Despite the reduced working capacity, the increase of the SEC by 4 % in the example is rather low, because a reduced working capacity requires a reduced amount of heat for desorption.

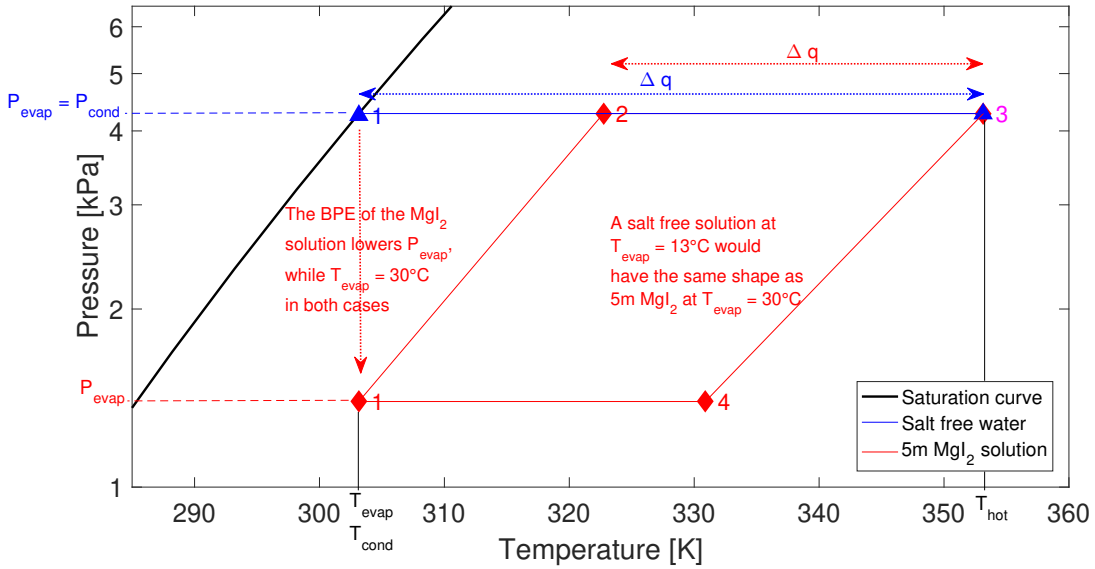


Figure 6.5: The 17 °C boiling point elevation of $MgI_2$ alters the adsorption cycle and reduces the working capacity of AQSOA Z01 compared to salt free water.

Fig. 6.6 shows the change of the energetic SEC for two different example salts. Sodium chloride is an example of a monovalent salt while magnesium iodide represents a divalent salt. The influence of the concentration of NaCl on the SEC is 0.3 % in the range between 0-5 mol/kg, while the increase of the SEC of aqueous $MgI_2$ solutions is less than 4 % within the same concentration range as mentioned above. Hence, the influence of salt, concentration and BPE on the SEC are almost negligible.
The independence between the salt concentration and the SEC is a very important aspect of the ADRED system. It allows the RED membrane to operate at optimal conditions without restrictions from the regeneration side. Thus, even saturation concentrations can be utilised in the ADRED system without lowering the specific performance of the adsorption regeneration.

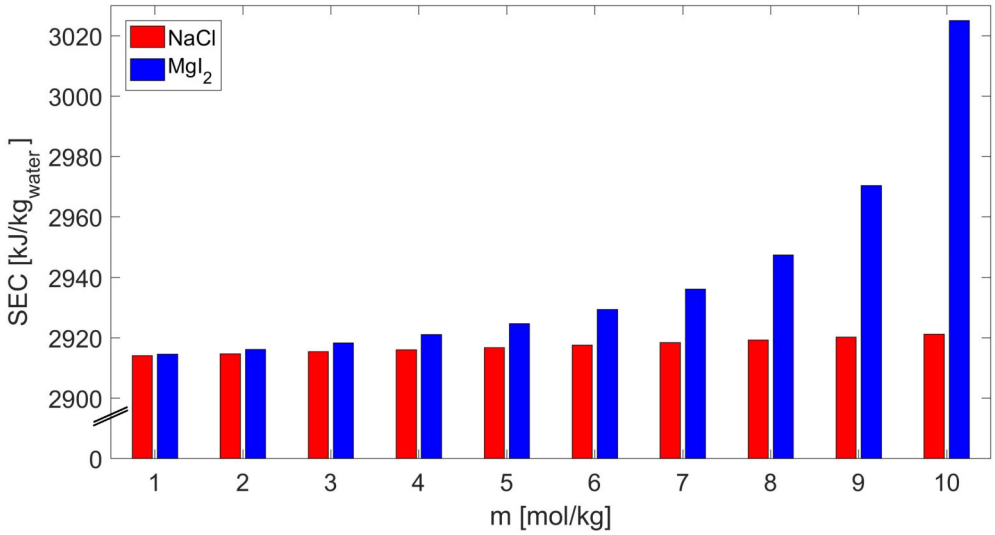


Figure 6.6: The influence of salts and their concentration are almost negligible for the energetic SEC of the adsorption regeneration

### Performance of the ADRED system

Fig. 6.7 shows the 15 best results of the ADRED system in terms of exergy and energy efficiencies and the corresponding input parameters. The results show that there is a possible range of low inlet concentrations $C_{low,in}$ between 0-2 mol/kg, which achieve a high performance. One could assume that a maximum salt gradient between the two inlet solutions would lead to the highest $\Delta G_{mix}$. Nonetheless, the activity coefficients of the salts often have a minimum between zero and the maximum concentration. Hence, a smaller salt gradient between the two inlet streams does not necessarily lead to a smaller $\Delta G_{mix}$. In case of $MgI_2$ this minimum implies that the best efficiencies can be achieved at $C_{low,in}$=2 mol/kg.

Looking at the conversion factor X in Fig. 6.7, the efficiency seems relatively independent of this parameter. A smaller value for X results in a smaller change of the salt gradient between the high and low salinity solutions after flowing through the membrane. As a result, less distillate needs to be produced during the regeneration to restore the initial salt gradient, therefore less energy is required for the regeneration. Conversely, less electricity is produced in the RED membrane because of the lower degree of mixing imposed by the conversion factor X. Both effects compensate for each other resulting in similar exergy efficiencies.

The best combination of salt and material is magnesium iodide and AQSOA Z01.

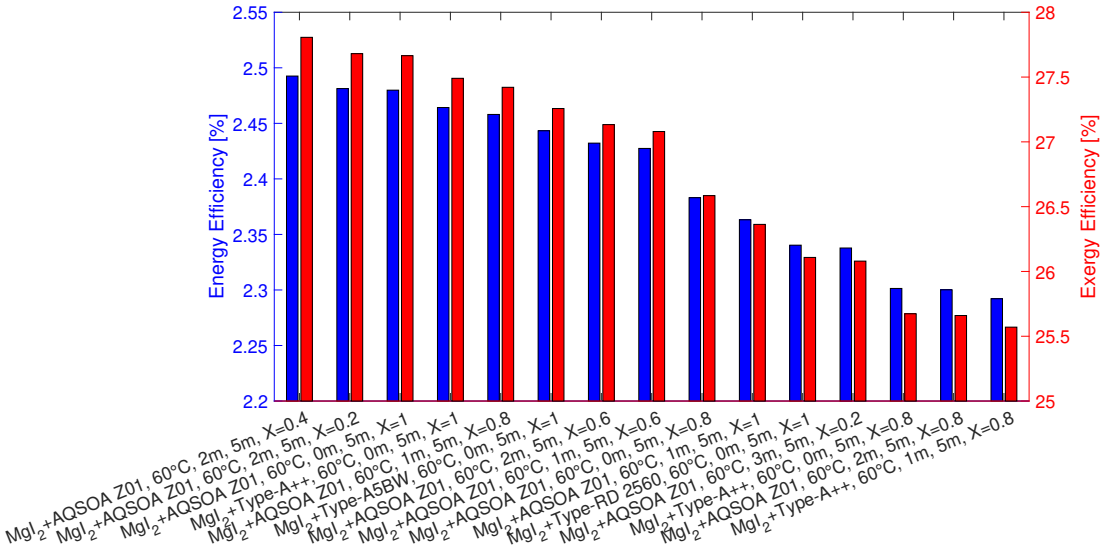


Figure 6.7: The 15 best results out of all 300,000 input scenarios. The blue bars represent the predicted energy efficiencies and the red bars the predicted exergy efficiencies

The isotherms of AQSOA Z01 and Siogel silica gel are shown in Fig. 6.8. $T_{evap}$ and $T_{cond}$ are both 30 °C, which is why the pressures of evaporator and condenser should be equal. However, the presence of salt in the evaporator reduces the pressure due to the BPE. An exemple BPE of 10 °C is shown in Fig. 6.8.

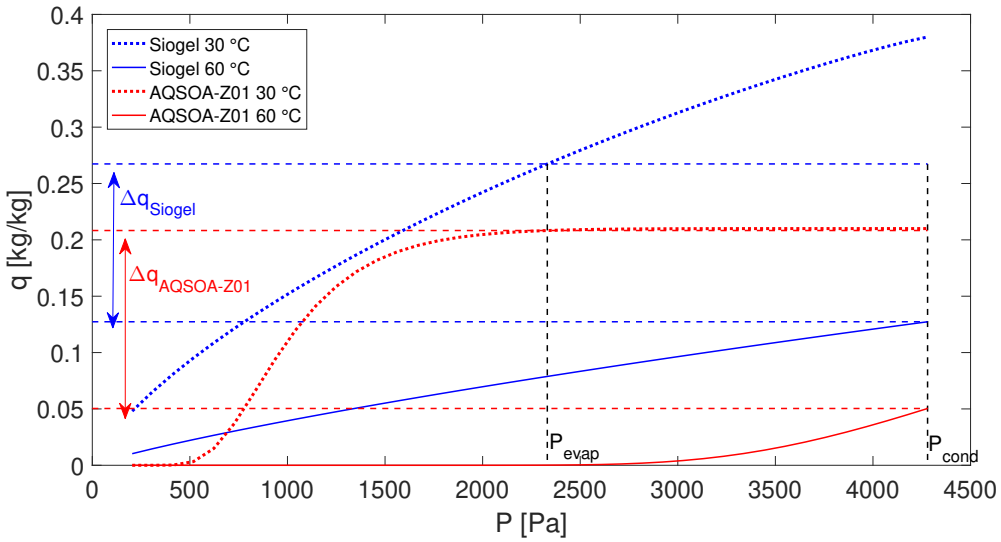


Figure 6.8: The working capacities Δq resulting from the isotherms of an exemplary silica gel (Siogel) and AQSOA Z01 at $T_{evap} = T_{cond} = 30$ °C and a regeneration temperature of 60 °C. $P_{evap} \neq P_{cond}$ because BPE = 10 °C.

It can be seen that the uptake of the silica gel is reduced due to the BPE. However, the working capacity of AQSOA Z01 is less sensitive to a reduced $P_{evap}$ due to its Type IV/V isotherm. Whereas, the working capacity of the silica gel decreases with increas-

ing salt concentrations. Apart from the working capacity, the heat of adsorption $\Delta h$ is a function of the uptake as well, but $\Delta h$ of the two material types is very similar [22].

The overall performance of the silica gel is similar to the performance of AQSOA Z01. In addition to their good performance, silica gels are much cheaper than AQSOA Z01. Therefore, the combination of low-cost and performance makes silica gels very attractive materials for the application in the ADRED process.

Fig. 6.9 presents the best exergy efficiency achievable with each one of the materials. Two cases were analysed, one was for all salts and the other only for the monovalent salts. Magnesium iodide showed the best result of all salts, but it is a divalent salt. Existing RED membranes are not designed for divalent salts and do not work very well with them [166]. Magnesium iodide gave the best results considering all materials and lithium chloride was the best monovalent salt. The high inlet concentrations for both salts were 5 mol/kg in the analysis. On average, the results for the monovalent LiCl were lower by a factor of 2.8 compared to the divalent $MgI_2$. LiCl is a monovalent salt, which is why it works with existing membranes. At 5 mol/kg it can achieve an exergy efficiency of almost 10 % in an ADRED system.

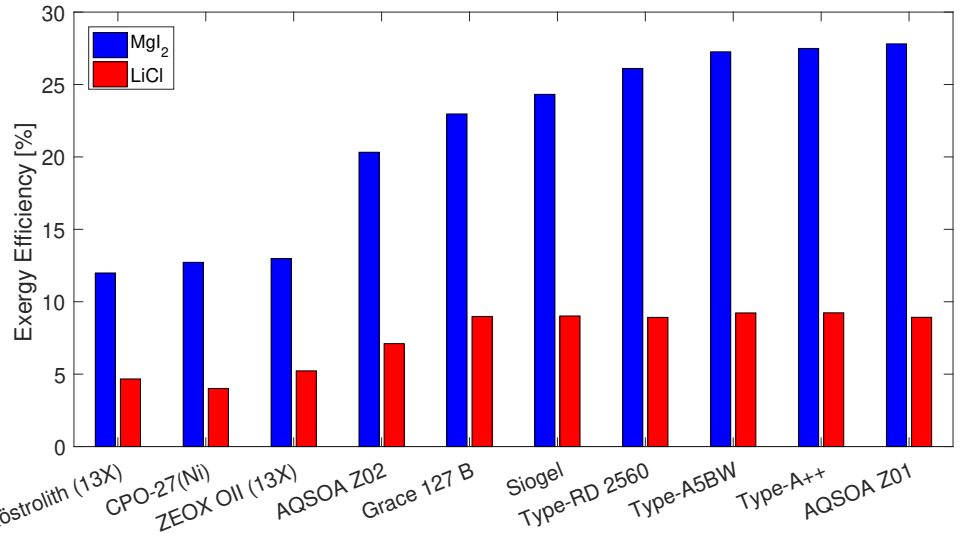


Figure 6.9: The best predicted exergy performance scenarios for each material. $MgI_2$ is the best overall salt, whereas LiCl is the best performing monovalent salt. The parameters used to achieve each result are listed in table 6.3.

The materials in Fig. 6.9 can be separated into two categories those that regenerate well at low temperatures and those that do not. The silica gels and AQSOA Z01 from the first category can be considered for the application in the ADRED system. By contrast, zeolite 13X, the metal organic framework and AQSOA Z02 require higher regeneration temperatures than considered in this study and therefore yield lower efficiencies.

Table 6.3: The overview of the parameters required to achieve the results shown in Fig. 6.9.

| **Material** | **Type** | **Salt** | $\mathbf{T_{hot}}$ [°C] | $\mathbf{C_{low,in}}$ [mol/kg] | $\mathbf{C_{high,in}}$ [mol/kg] | **X** [-] |
|---|---|---|---|---|---|---|
| Siogel | Silica Gel | $MgI_2$ | 60 | 2 | 5 | 0.4 |
| Grace 127 B | Silica Gel | $MgI_2$ | 60 | 2 | 5 | 0.4 |
| Type-A5BW | Silica Gel | $MgI_2$ | 60 | 0 | 5 | 1 |
| Type-RD 2560 | Silica Gel | $MgI_2$ | 60 | 0 | 5 | 1 |
| Type-A++ | Silica Gel | $MgI_2$ | 60 | 0 | 5 | 1 |
| CPO-27(Ni) | MOF | $MgI_2$ | 80 | 2 | 5 | 0.4 |
| AQSOA Z01 | Zeolite | $MgI_2$ | 60 | 2 | 5 | 0.4 |
| AQSOA Z02 | Zeolite | $MgI_2$ | 60 | 2 | 5 | 0.4 |
| Köstrolith (13X) | Zeolite | $MgI_2$ | 60 | 0 | 5 | 1 |
| ZEOX OII (13X) | Zeolite | $MgI_2$ | 60 | 0 | 5 | 1 |
| all (excl. MOF) | | LiCl | 60 | 0 | 6 | 1 |
| CPO-27(Ni) | MOF | LiCl | 80 | 0 | 6 | 1 |

### Impact of the process parameters on the exergy efficiency

Each of the key parameters $T_{hot}$, $C_{high,in}$, $C_{low,in}$ and the conversion factor X has a different leverage effect on the exergy efficiency. Fig. 6.10 shows the effect of each of the parameters on the exergy efficiency of the ADRED model. For this analysis AQSOA Z01 was chosen as material and $MgI_2$ as best performing salt. The interactions of two variables were studied for four different cases as shown in Fig. 6.10, where the regeneration temperature $T_{hot}$ and the inlet concentration of the low salinity solution $C_{low,in}$ are varied, while X=0.4 and $C_{high,in}$ = 5 mol/kg remain constant. The exergy efficiency decreases at higher regeneration temperatures proportionally to the Carnot factor. The Carnot factor at $T_{hot}$ = 100 °C is two times bigger than it is at $T_{hot}$ = 60 °C. Therefore, the specific exergy consumption $SEC_{ex}$ doubles from $T_{hot}$ = 60 °C to $T_{hot}$ = 100 °C. The increase of $SEC_{ex}$ leads to a proportional decrease of the exergy efficiency of the entire closed-loop system. As the exergy efficiency in Fig. 6.10 is most significantly dependent on the Carnot factor, it can be concluded that the adsorption material is sufficiently regenerated at 60 °C. Thus, a further increase of the regeneration temperature does not have significant advantages in terms of desorption. Furthermore, the inlet concentration of the low salinity solution peaks at $C_{low,in}$ = 2 mol/kg. The peak is caused by the conversion factor of X=0.4. Fig. 6.10 also shows an analysis where both, the conversion factor and $C_{low,in}$, were changed. The surface plot has a ridge starting at $C_{low,in}$ = 2 mol/kg for low conversion factors and ending at $C_{low,in}$ = 0 mol/kg at complete mixing X = 1 of the two inlet solutions. Therefore, it is important to choose the combination of $C_{low,in}$ and the conversion factor X carefully, because it has a large impact on the performance. Finally, the exergy efficiency has a maximum at the highest $C_{high,in}$, but it is also important to keep the concentration at $C_{low,in}$ = 2 mol/kg in this example, because of X = 0.4. The increase

of the salt gradient at the conversion factor X=0.4 would lower the exergy efficiency. It appears that $C_{high,in}$ has the highest impact on the exergy efficiency followed by $C_{low,in}$, $T_{hot}$ and X and have the lowest impact. $C_{low,in}$ and X are however correlated and need to be selected with care. The regeneration side has a lower impact on the exergy efficiency than the membrane side, because the impact of $T_{hot}$ is lower than the impact of the concentrations. This confirms that the $SEC_{ex}$ is relatively independent of the salt and its concentration as indicated in Fig 6.6. Therefore, increasing the salt concentration $C_{high,in}$ is the most straightforward approach to maximise performance.

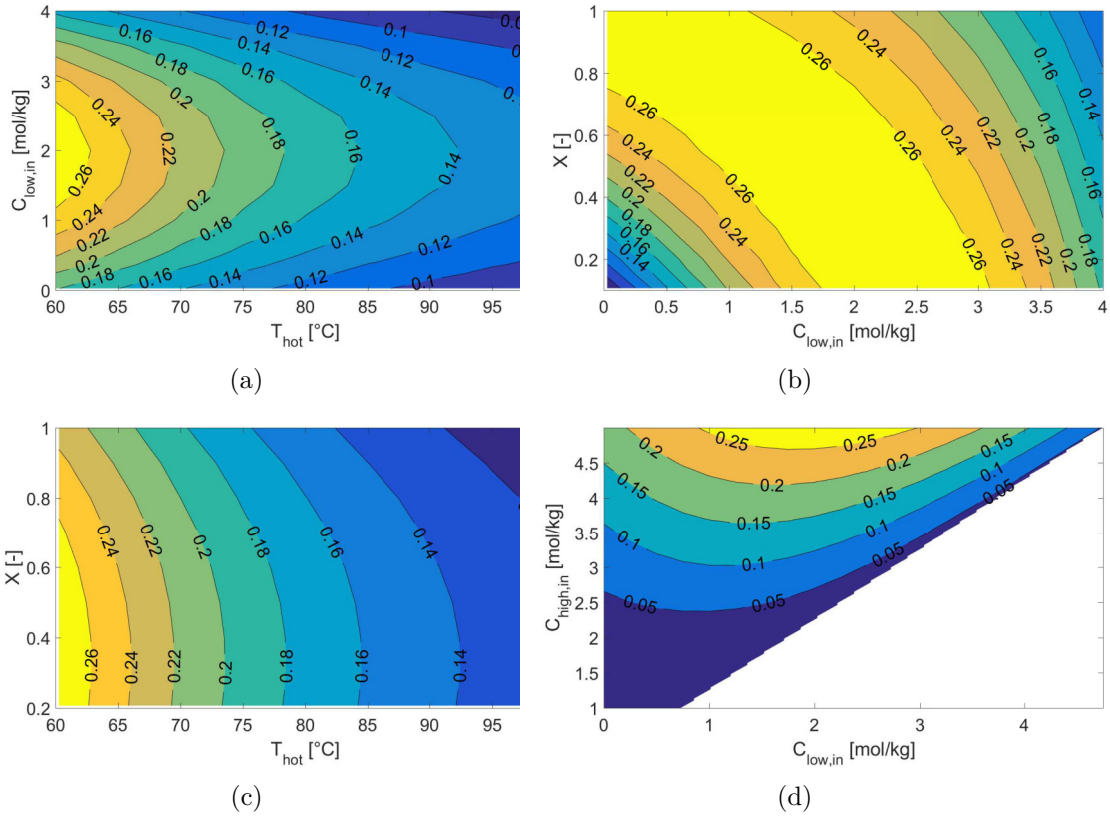


Figure 6.10: The exergy efficiencies on the contour lines are presented in absolute values.
(a) Exergy efficiency ($MgI_2$+AQSOA-Z01), where $T_{hot}$ and $C_{low,in}$ are varied and X=0.4 and $C_{high,in}$=5 mol/kg remain constant.
(b) Exergy efficiency ($MgI_2$+AQSOA-Z01), where and $C_{low,in}$ and X are varied and $T_{hot}$=60 °C and $C_{high,in}$=5 mol/kg remain constant.
(c) Exergy efficiency ($MgI_2$+AQSOA-Z01), where $T_{hot}$ and X are varied and $C_{low,in}$=2 mol/kg and $C_{high,in}$=5 mol/kg remain constant.
(d) Exergy efficiency ($MgI_2$+AQSOA-Z01), where and $C_{low,in}$ and $C_{high,in}$ are varied and $T_{hot}$=60 °C and X=0.4 remain constant.

### Maximising the performance with a saturated aqueous LiCl solution

The maximum concentration provided by the Pitzer tables is one of the advantages and limitations for this work at the same time. The Pitzer tables provide information on a large number of salts, which allows them to be all considered for the system. In addition, for many salts the maximum concentrations provided by Pitzer match their maximum solubility. For example, the tables provide a concentration limit for $MgI_2$ of 5 mol/kg, which is consistent with the maximum solubility of 5.3 mol/kg at ambient temperature [167]. However, some salts have much higher solubilities than the Pitzer tables suggest and a higher concentration leads to a higher $\Delta G_{mix}$. Lithium chloride was previously identified as the best monovalent salt at a concentration of 5 mol/kg. LiCl has an aqueous solubility of 20 mol/kg at ambient temperature [77]. Therefore, an additional simulation was performed to assess the system's performance for a saturated LiCl solution at 20 mol/kg.

Robinson published experimentally obtained activity coefficients, osmotic coefficients and water activities of LiCl solutions at 25 °C up to 20 mol/kg [127]. The previously described ADRED model was changed to use Robinson's data instead of the Pitzer correlations. Furthermore, the equation of $\Delta G_{mix}$ had to be altered from eq. (6.15) to eq. (6.14), because the assumption of relatively low concentrations does not apply to the saturated LiCl solution. On the adsorption side, a preheater for the evaporator was added to the process, because of the very high BPE(20 mol/kg, 30°C) = 33 °C. Without the preheater the pressure in the evaporator would be too low, which reduces the performance. Hence, the evaporator temperature was increased to the regeneration temperature $T_{ev} = T_{hot} = 60$ °C. The condenser continues to operate at ambient temperature $T_{cond} = 30$ °C in the simulation.

The results of the investigation are shown in table 6.4. The exergy performance of the system is 45 % and energy efficiency is 4 %, which is a significant increase compared to the results at low concentrations. The higher concentration of the LiCl solution from 5 mol/kg to 20 mol/kg increases the SEC of the adsorption regeneration only by 6.5 %, while the Gibbs free energy of mixing increases by a factor of seven. Hence, ADRED has great potential at very high salt concentrations. In addition, the performance of the much cheaper Siogel silica gel is almost the same as the performance achieved with AQSOA Z01.

Table 6.4: The performance of the ADRED system at very high concentrations of LiCl with a zeolite (AQSOA Z01) and silica gel (Siogel) as material

| Material | $T_{evap}$ [°C] | $T_{cond}$ [°C] | $T_{hot}$ [°C] | m [mol/kg] | $\eta$[%] | $\eta_{ex}$ [%] |
|---|---|---|---|---|---|---|
| AQSOA Z01 | 60 | 30 | 60 | 20 | 4.0 | 44.6 |
| Siogel | 60 | 30 | 60 | 20 | 3.9 | 43.2 |

### From thermodynamic considerations to a real system application

The 45 % exergy efficiency achieved with highly concentrated LiCl solutions represents an ideal value, which cannot be achieved due to real system limitations. The main investigation solely considered the thermal power input, but the real system would require electrical input for the operation as well. The pumps of an ADRED system would consume most of the electric power supplied to the system. Thus, the following considerations have been applied to quantifying the efficiency losses due to pumping power. Ng et al. estimated the electricity consumption of an AD desalination plant at 1.38 kWh/m$^3$ (≈ 5 kJ/kg) taking into account the valves and three water pumps, which are needed to supply the heat exchangers of evaporator, condenser and adsorbers with heating/cooling water [17]. Several studies have investigated the pumping power consumption of RED plants, the results vary depending on the membrane design. Post et al. approximated the pumping energy losses at 5 % for spacer-free membranes [168, 169]. Tamburini et al. reported the pumping losses here at 3-25 % [8], while spacer-filled channels lead to a power loss of 10-20 % [8]. In comparison to the RED plants presented in the literature, the pumping energy within the ADRED process would be slightly higher at high salt concentrations because of the viscosity increase. For example, the dynamic viscosity of a LiCl solution at 17 mol/kg is 10 mPa·s and at 12 mol/kg it is 5 mPa·s, both at 25 °C [170].

In Fig. 6.11, the analysis was extended to incorporate pumping losses for the best results, which are LiCl at 5 mol/kg and 20 mol/kg, as well as $MgI_2$ at 5 mol/kg.

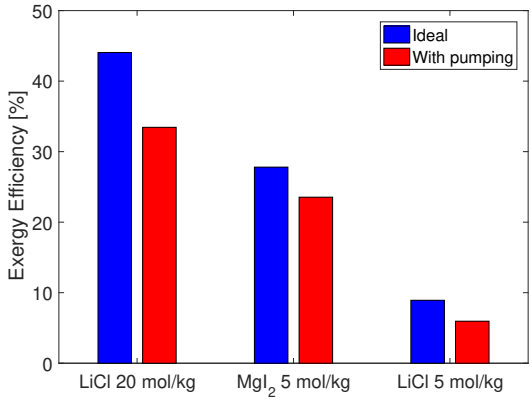


Figure 6.11: The predicted results of the best performing salts with AQSOA Z01 with and without pumping losses

The electricity consumption of the RED side of the system was estimated at 10 % for the salt solutions of 5 mol/kg and 20 % for the 20 mol/kg solution of LiCl, because of the increased viscosity. In addition, 5 kJ/kg of electricity were deducted from $\Delta G_{mix}$ to account for the electricity demands of the adsorption desalination side of the system. The results in Fig. 6.11 show that pumping losses reduce the exergy efficiency to

33 % for LiCl at 20 mol/kg, 6 % for LiCl at 5 mol/kg and 24 % for $MgI_2$. The results highlight the system's feasibility even after considering the pumping losses, which are relatively low because there are few moving parts within the system. In theory, the system could be operated with as little as 5 pumps in total: The 3 supply pumps to the adsorption desalinator and a pump for each of the high and low salinity solutions. Heat integration by connecting the cooling water of the condenser to the evaporator would reduce the number of required pumps down to 4.

The main challenge for the implementation of the system remains on the membrane side. Permselectivity of existing RED membranes is reduced at high LiCl concentrations. The reduced permselectivity causes a reduced membrane performance. Therefore, the exergy efficiency of 33 % including pumping losses still represents an ideal value, which demands improved membranes to be achievable.
This study demonstrates that $\Delta G_{mix}$ is large for Li-salts at very high concentrations, which can be processed in an AD desalinator. So far no other desalination technology connected in the closed-loop system to a RED membrane is able to supply such a high salinity solution to the RED stack. Thus, there was no incentive to develop such membranes. However, the energy requirements of the adsorption desalinator are independent of the salt concentration, which opens an entirely new field for the application of RED membranes in the future. A system operating at such high salt concentrations would face corrosion issues, where system components could be replaced by polymers to prevent corrosion and lower the costs.
The size of the system is another contributor to the costs of the system. Currently, AD desalinators produce water at a Specific Daily Water Production of 10 $m^3$ per tonne of adsorption material per day [17]. This performance indicator multiplied by $\Delta G_{mix}$ $\approx$ 93 kJ/kg for LiCl at 20 mol/kg and subtracting pumping losses, results in a power output of 10.7 kW per tonne of adsorption material. Post et al. showed that a 200 kW RED plant could be mounted on a 40 ft sea container frame [168]. The electric output of 200 kW corresponds to the afore-mentioned paper plant emitting 6 MW of waste heat into the environment. The 200 kW RED plant would require 20 tonnes of silica gel, which corresponds to bed sizes of 7 $m^3$ each, if it is split among 4 adsorber beds. Thus, the adsorption plant would be small enough to be built inside another 40 ft sea container frame resulting in a footprint of 30 $m^2$ for the entire ADRED system.

## 6.2 Non-aqueous ammonia solutions with low latent heat

The use of aqueous solutions has several advantages for the generation of electricity in a closed loop RED system. Water is non-toxic, environmentally friendly and is a very good solvent for electrolytes. In addition, seawater desalination is a well established field of research and the results can easily be applied to the regeneration side of the system. This is also true for the RED side of the system as well. RED membranes have been designed, developed and tested for aqueous solutions for years. Choosing a different solvent than water would require more fundamental research on both, the regeneration side and the membrane side of the system.

Many solvents have a lower latent heat than water, but the solubility of electrolytes is significantly reduced. Thus, the efficiency of the regeneration side of the system would improve, as less energy is needed to evaporate and regenerate the same amount of solution. However, the lower solubility of electrolytes leads to a reduced performance of the membrane. Assuming the membrane would be compatible with the nonaqueous solvent in the first place.

Liquid ammonia is a promising solvent as it is one of the few nonaqueous solvents with a high salt solubility which makes it an interesting alternative to water for ADRED. Ammonia has the advantage of a low latent heat of 1150 kJ/kg [39], a similar molar mass as water of 17 g/mol and a high dipole moment [171]. In addition, the application of ammonia would require the use of pressure equipment, which tends to be cheaper than the vacuum equipment needed for an ADRED system using water. Ammonia also has a high solubility of salts as it can be seen in table 6.5. Table 6.5 also compares the solubility of selected salts in water to their solubility in liquid ammonia. It can be seen that some salts like lithium chloride have low solubility in ammonia. Whereas, other salts like the ammonium halides or sodium nitrate have a much higher solubility in ammonia than in water.

Table 6.5: Solubility of salts in liquid ammonia compared to their solubility in water

| Salt | $NH_3$ [mol/kg] | $H_2O$ [mol/kg] | Ref. |
|---|---|---|---|
| Sodium Chloride | 2.2 | 6.1 | [171] |
| Sodium Bromide | 6.2 | 7.7 | [171] |
| Sodium Iodide | 8.8 | 10.7 | [171] |
| Sodium Nitrate | 15.0 | 8.6 | [171] |
| Lithium Chloride | 0.3 | 20.1 | [172, 173] |
| Ammonium Chloride | 23.2 | 7.4 | [174, 175] |
| Ammonium Bromide | 27.9 | 8.1 | [176, 177] |
| Ammonium Iodide | 33.9 | 12.3 | [176, 178] |
| Ammonium Nitrate | 60.4 | 24.4 | [179, 180] |

The solubility of ionic substances in a solvent depends on the properties like the dielectric constant or polarity [171]. The ion-dipole interactions between ionic substances and water are stronger compared to ammonia, because of the weaker dipole moment of ammonia [171]. This can be seen by the solubilities of the sodium salts in table 6.5. However, ammonium halide salts have a very high solubility in ammonia suggesting that they can be used in the closed-loop system to achieve a high Gibbs free energy of mixing.

Little research has been done on the application of liquid ammonia as a solvent of electrolytes. Notably, in 1934 Larsen and Hunt investigated the properties of liquid ammonia and determined the relative activity coefficients of Ammonium - Nitrate, Bromide, Iodide and Chloride [181] as shown in figure 6.12a. Larsen and Hunt determined the activity coefficients through VLE measurements and derived them using a graphical method. However, as the study was conducted in 1934 their equipment was not accurate enough to determine a pressure difference of an ammonium salt solution and pure ammonia at very low concentrations. Therefore, they had to assess the relative activity coefficient in relation to an arbitrarily chosen reference point at 1 molal. The relative mean activity coefficient can be used for the calculation of $\Delta G_{mix}$, because $\Delta G_{mix}$ assesses the differences between two states. Calculating the difference between two points with the same reference point still allows to obtain the correct result.

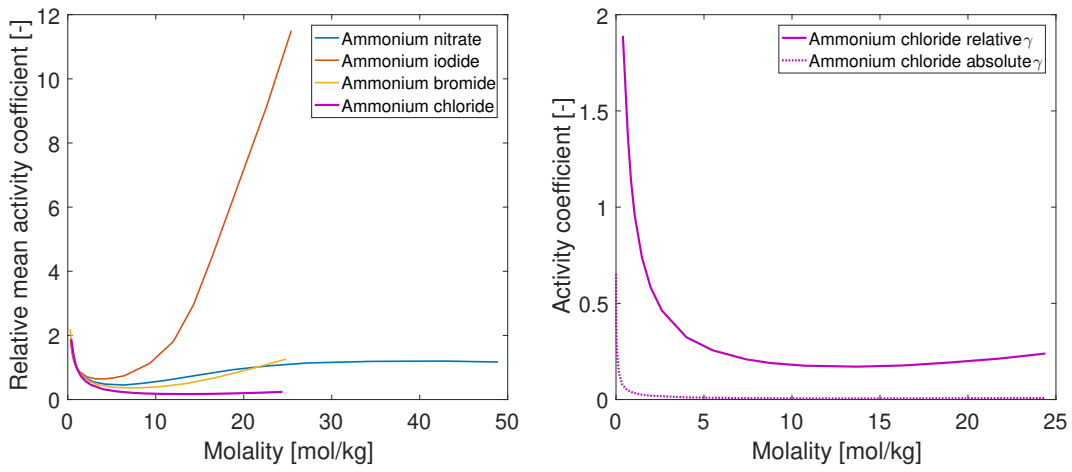


(a) (b)

Figure 6.12: (a) Experimental relative mean activity coefficients of the ammonium halides [158].
(b) Comparison of experimental data of the absolute γ [181] and relative γ [158] of liquid ammonia with ammonium chloride.

The absolute activity coefficients have been published for the solution of ammonia and ammonium chloride [181]. The comparison of the absolute and relative activity coefficient is shown in figure 6.12b. It can be seen that the curve of the relative activity

coefficients is simply shifted upwards. To confirm this $\Delta G_{mix}$ was calculated using both activity coefficients by reading them from the graph. Two solutions of 24 molal solution and 0.4 molal were mixed. The absolute activity coefficients lead to a $\Delta G_{mix}$ = 65 kJ/kg$_{mix}$, while the relative activity coefficients lead to $\Delta G_{mix}$ = 53 kJ/kg$_{mix}$. The deviation of the two values is less than 20 %, which can probably be attributed to the graphical method applied by Larsen and Hunt (1934) to determine the relative mean activity coefficient. However, $\Delta G_{mix}$ for the ammonia solution is quite low compared to lithium chloride in water. The mixing of aqueous lithium chloride solutions at similar concentrations releases $\Delta G_{mix}$ = 123 kJ/kg$_{mix}$, which is twice as much. The low $\Delta G_{mix}$ is due to the low activity coefficients of ammonia solutions despite their high concentrations.

On the regeneration side, two activated carbon materials were evaluated for the use in the adsorption regeneration system. The isosteric heat of adsorption was assessed using the Dubinin Astakhov parameters from [37]. The result of the analysis is shown in figure 6.13 in relation to the latent heat of ammonia.

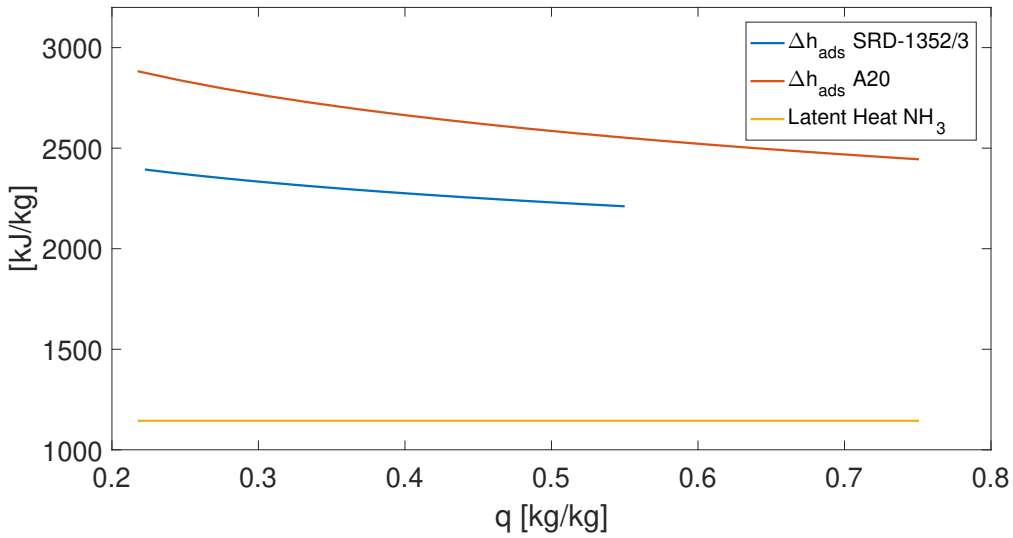


Figure 6.13: The heat of adsorption of two activated carbons in comparison to the latent heat of pure ammonia [37, 39]

The heat of adsorption for the ammonia/AC working pair is almost twice as high as the latent heat and similar to water and silica gel of 2800 kJ/kg. Given the relatively low $\Delta G_{mix}$ and the surprisingly high heat of adsorption of the ammonia-AC working pair, the overall system performance is not expected to exceed the performance of water and lithium chloride significantly.

Figure 6.14a shows the results of the performance analysis of the ADRED system

using non-aqueous solutions of ammonia and ammonium halide salts. For each one of the salts, the maximum and minimum concentrations shown in figure 6.12a were used to assess the efficiency under the same assumptions as for the rest of the ADRED investigation. The regeneration temperature was 60 °C and the ambient temperature was 30 °C. The benchmark case for comparing the two solvents is the saturated aqueous lithium chloride solution given in table 6.4. Ammonium iodide dissolved in liquid ammonia achieves even slightly better results in an ADRED system, while the other ammonium halides achieve lower performances. Ammonium nitrate has the lowest performance inside the ADRED system despite its very high concentration of $C_{high,in} = 50$ mol/kg. The activity coefficients of ammonium nitrate remain relatively constant over the large concentration span in figure 6.12a, which is why $\Delta G_{mix}$ remains low. Ammonium iodide has the highest activity coefficients of all ammonium halides. Therefore, it achieves a reasonable $\Delta G_{mix}$. $\Delta G_{mix}$ of ammonium iodide is still slightly lower compared to the aqueous lithium chloride solution, but the SEC of the AC/ammonia working pair is lower than the SEC of the zeolite/water working pair by 20 %. Hence, the overall efficiency is slightly better, but not high enough to justify the development of entirely new RED membranes optimised for ammonia.

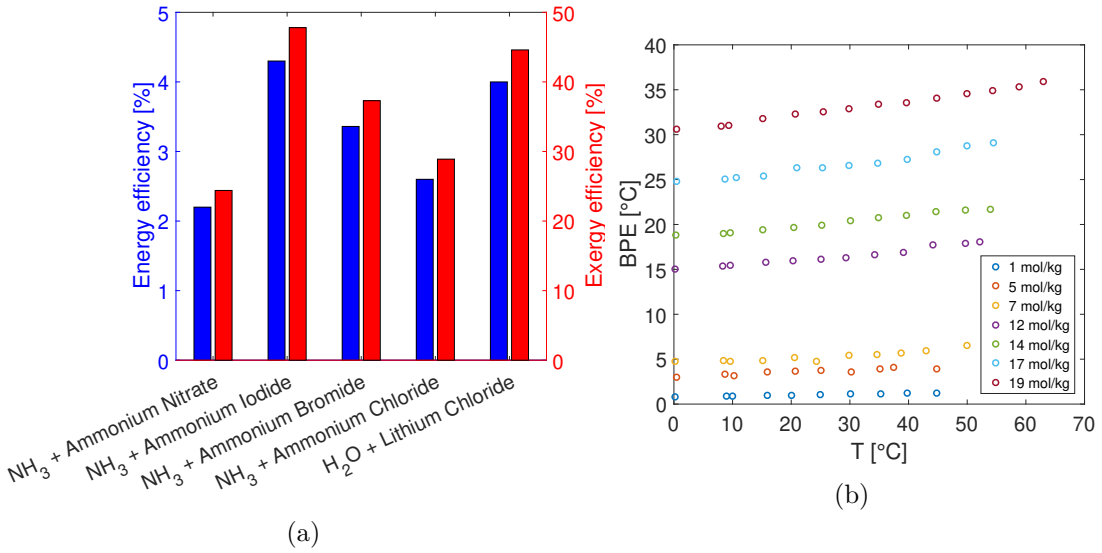


(a) (b)

Figure 6.14: (a) The predicted energetic and exergetic efficiencies of an ADRED system using a non-aqueous ammonia solution. For comparison, the results of the aqueous solution of lithium chloride is also shown in this graph. $T_{hot} = 60$ °C.
(b) The boiling point elevation of ammonium bromide in ammonia calculated from experimental VLE data given by [182].

The performance of the ADRED system is limited by the high heats of adsorption needed for the regeneration of the activated carbon. The working pair activated carbon/ammonia has not gained as much attention as silica gel/water in temperature swing adsorption systems and no commercial application has been established yet. Hence,

the materials have not been optimised as much and the heat of adsorption is twice as high as the latent heat of ammonia. By contrast, the latent heat of water and the heat of adsorption of silica gel/water are very close.

Other thermal regeneration systems like MED only have to overcome the latent heat and not the heat of adsorption. Therefore, MED systems would benefit more from the low latent heat of ammonia. However, the main limitation of MED systems is the boiling point elevation, because a large BPE limits the maximum number of MED-effects. Thus, the BPE of ammonia and ammonium bromide was assessed from VLE data published by Hunt and Larsen [182] and the results are shown in figure 6.14b.
At the highest molality of 19 mol/kg, the BPE is between 30 and 40 °C. Such a high BPE does not allow more than one evaporation effect in the same temperature window of $T_{hot}$ = 60 °C and $T_{ambient}$ = 30 °C, which is why MED is not a real alternative at high salt concentrations. Furthermore, the reduction of the concentration reduces the BPE, but also $\Delta G_{mix}$. Therefore, it is a trade-off between the number of effects and $\Delta G_{mix}$. The switch from water to ammonia would also not improve the efficiency of a MEDRED system significantly enough to justify the development of new membranes, because ammonia solutions can also have high boiling point elevations like aqueous solutions.

## 6.3 Dynamic model for increased power plant efficiency

### 6.3.1 Integrating adsorption reverse electrodialysis into the Rankine cycle

Fig. 6.15 shows the application of adsorption reverse electrodialysis *ADRED* [119] to a power plant for conversion of waste heat to power.

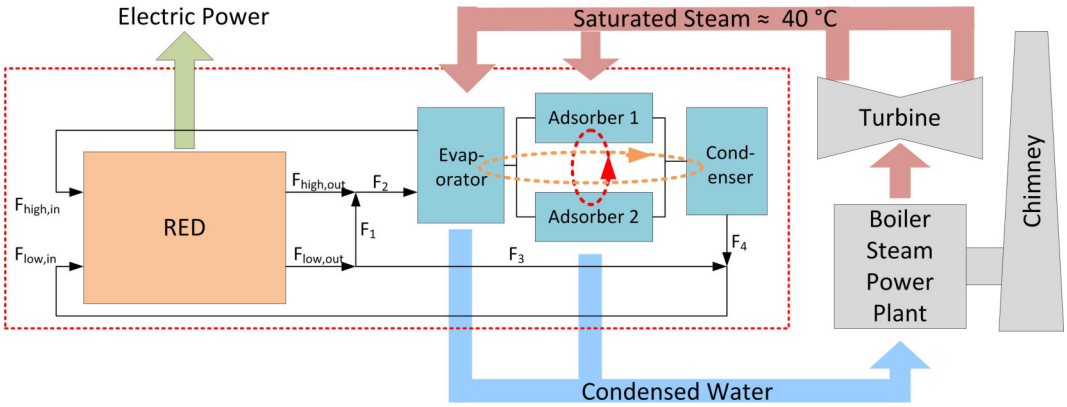


Figure 6.15: The ADRED system utilises the latent heat of the turbine steam to regenerate the adsorption beds. The produced distillate $F_4$ is used to restore the salt gradient between two saline solutions. A reverse electrodialysis generates electricity from this salt gradient.

ADRED circulates a high and a low salinity solution between the RED stack and the AD regeneration. The two solutions $F_{high,in}$ and $F_{low,in}$ enter RED, where electricity is generated through the salt gradient. Afterwards, the salinity gradient needs to be restored in the adsorption desalinator by partially evaporating water from the inlet flow $F_2$ in the AD evaporator. This water vapour is adsorbed by the silica gel in the adsorbers. For desorption, the low-pressure steam from the turbine powers the ADRED system by transferring the latent heat into the adsorber bed in a heat exchanger. The silica gel bed cools and condenses the low-pressure steam by desorbing water vapour. The desorbed water vapour is condensed in the AD condenser, which can either be cooled by an external heat sink or by heat integration with the AD evaporator [52]. The application of an external heat sink allows the evaporator to be heated by a part of the saturated turbine steam, which improves the performance of the silica gel material [130]. By contrast, the heat integration between evaporator and condenser allows ADRED to operate as a closed-loop cooling system and as an alternative to a cooling tower with the advantage of producing electricity.
Heat integration is also possible between the two adsorber beds increasing the energy efficiency and cycle time as a trade-off, because the specific distillate production of the adsorption material decreases with the cycle time.

### Modelling assumptions

The model is used to investigate different heat integration scenarios to identify the best compromise achieving the best efficiency and the highest power density of the material. Moreover, the model is moved from a thermodynamic to a dynamic, validated and more accurate representation compared to the previous analysis [119]. The RED model has been validated for aqueous sodium chloride solutions [8], which is why sodium chloride is the only salt investigated here. The model assumes:

- Homogeneous temperatures in all vessels and adsorption beds;
- Only pure water evaporates, while all salt remains in the evaporator [119];
- The salt concentration in the solution supplied from the evaporator to the membrane varies, because of the changing evaporation rate [17]. The adsorption desalination model takes the change of concentration into account, but the membrane model is steady-state and to save computation time the average salt concentration is used in each cycle;
- All components of the system are adiabatic;
- Ambient temperature $T_{cond,in}$ is 25 °C, unless otherwise specified;
- Average conditions for solutions and cell pair variables between inlet and outlet of the RED membrane as the model is independent of x-y-z-dimensions;
- Solvent flow and polarisation phenomena in the RED membrane are neglected [8];
- Ideal current distribution in RED membrane [8];
- The adsorbent mass of the adsorption desalinator is kept constant, while the membrane area is variable. This allows RED to cope with different distillate flow rates achieved under different conditions.

### Mass balances

The mass balances for the flow rates $F_i$ [$kg_{sol}/s$] and the corresponding salt mass fractions $w_i$ [$kg_{salt}/kg_{sol}$] based on the scheme in Fig. 6.15 are listed below:

$$F_{high,in} + F_{low,in} = F_{high,out} + F_{low,out} \tag{6.31}$$

$$F_{high,in} = F_{low,in} \tag{6.32}$$

$$F_{high,in}\ w_{high,in} + F_{low,in}\ w_{low,in} = F_{high,out}\ w_{high,out} + F_{low,out}\ w_{low,out} \tag{6.33}$$

$$F_3 \; w_{low,out} = F_{low,in} \; w_{low,in} \tag{6.34}$$

$$F_{high,out} \; w_{high,out} + F_1 \; w_{low,out} = F_2 \; w_2 \tag{6.35}$$

$$F_{high,out} + F_1 = F_2 \tag{6.36}$$

$$F_4 + F_3 = F_{low,in} \tag{6.37}$$

$$F_{high,in} + F_4 = F_2 \tag{6.38}$$

### RED model

Tamburini et al. presented a validated RED model, which was adapted for this study including all the membrane specific parameters [8]. Moreover, they optimised the membrane operational variables and the result achieving the highest efficiency were used for this study as well.
The volumetric flow rate $\dot{V}$ through the RED membrane [$m^3$] is defined as:

$$\dot{V} = \varepsilon_{sp} \; N_{cell} \; \delta_{low} \; l \; v \tag{6.39}$$

where $\varepsilon_{sp} = 0.6$ is the spacer porosity (-), $\delta_{low/high} = 270 \cdot 10^{-6} \; m$ is the high and low compartment thicknesses, $N_{cell} = 50$ number of cell pairs, $v = 0.01$ m/s is the fluid velocity in the membrane and $l = 0.01 \; m$ is the length of the membrane [8].
The Nernst equation is required to determine the cell voltage $E_{cell}$ [V]:

$$E_{cell} = (\alpha_{CEM} + \alpha_{AEM}) \frac{RT}{F} ln \left( \frac{\gamma_{high} m_{high}}{\gamma_{low} m_{low}} \right) \tag{6.40}$$

where $F = 96485.3 \; C/mol$ is the Faraday constant, $\alpha_{CEM/AEM}$ is the permselectivity of the cation and anion exchange membranes ($CEM$ and $AEM$) respectively, $m_{high/low}$ is the molality [mol/kg] of the solutions, $\gamma$ the activity coefficients of electrolytes from the Pitzer model in section 6.1.1, and the equivalent conductivity $\Lambda$ [S $m^2$/mol] is obtained through the Jones and Dole equation [183]:

$$\Lambda = \Lambda_0 - \frac{A_\Lambda C^{1/2}}{1 + B_\Lambda C^{1/2}} - C_\Lambda C \tag{6.41}$$

where $C$ is the molarity [mol/L], $\Lambda_0 = 0.01265 \; Sm^2/mol$ [184] and the other parameters were fitted on the experimental results of Chambers et al. [185] by this study: $A_\Lambda = -9.3 \cdot 10^{-3}$, $B_\Lambda = 1.756$, $C_\Lambda = 6.965$.
The electrical resistances $R_{low/high}$ [$\Omega m^2$] of the low and high salinity solutions are

given by:

$$R_{low} = s_f \frac{\delta_{low}}{\Lambda_{low} C_{low}} \tag{6.42}$$

$$R_{high} = s_f \frac{\delta_{high}}{\Lambda_{high} C_{high}} \tag{6.43}$$

where $s_f$ is the spacer shadow factor [-]. The concentrations $C_{low} = 2\ mol/L$ and $C_{high} = 5\ mol/L$ lead to the highest membrane efficiency [8]. The cell resistance $R_{cell}$ is composed of the resistances of the solutions and the AEM and CEM membrane resistances $R_{AEM} = 2.96 \cdot 10^{-4}\ \Omega m^2$ and $R_{AEM} = 1.55 \cdot 10^{-4}\ \Omega m^2$ [8].

$$R_{cell} = R_{low} + R_{high} + R_{AEM} + R_{CEM} \tag{6.44}$$

The stack resistance $R_{stack}$:

$$R_{stack} = N\ R_{cell} + R_{blank} \tag{6.45}$$

The Open Circuit Voltage $OCV$

$$OCV = N\ E_{cell} \tag{6.46}$$

The electrical current density j [A/m$^2$], where the stack resistance is approximately equal to the load resistance $R_{stack} = R_{ext}$ [8].

$$j = \frac{E_{stack}}{R_{ext}} = \frac{OCV}{2\ R_{stack}} \tag{6.47}$$

The power per cell pair area $P_d$ [W/m$^2$] is defined as:

$$P_d = \frac{j^2 R_{ext}}{N} \tag{6.48}$$

The salt flux through the membrane [mol/(m$^2$s)]:

$$J_{salt} = \frac{j}{F} + \frac{2\ D_{salt}\ (C_{high} - C_{low})}{\delta_m} \tag{6.49}$$

The outlet concentrations [mol/L] from the membrane can be calculated by the following equation:

$$C_{high,out} = C_{high,in} - \frac{J_{salt}\ A_{cell}}{\dot{V}} \tag{6.50}$$

$$C_{high,out} = C_{low,in} + \frac{J_{salt}\ A_{cell}}{\dot{V}} \tag{6.51}$$

The density of sodium chloride solutions [kg/m$^3$] was measured by Kiepe et al. [186]

and fitted to the following equation by this study:

$$\rho_{sol} = 1133.12 - 0.44\ T + 41.30\ m - 0.024\ m\ T \tag{6.52}$$

The flow rate specific power output $P_{d,s}$ [W s/kg] is required to assess the overall efficiency of the system and defined by:

$$P_{d,s} = \frac{P_d\ A_{cell}\ N}{\dot{V}\rho_{sol}} \tag{6.53}$$

### 6.3.2 Mathematical model for high performance adsorption desalination

El-Dessouky and Ettouney presented a fully heat integrated adsorption vapour compression $ADVC$ system in a simplified mathematical model [187] achieving high performances due to heat integration. Their heat integration between the adsorbers does not require additional vessels. After adsorption (point 1 in Fig. 6.16) and desorption (point 4), water is circulated between the hot, dry bed and the cold saturated bed until they are at equal temperatures in point 3 and 6 in Fig. 6.16. During internal circulation the water cycle is cooled by the heat of desorption 2→3, while it is heated by the heat of adsorption 5→6 of the other bed. This facilitates the process until both beds are almost at equal temperatures $T_3 \leq T_6$ The internal circulation scheme is ideal for adsorption desalination as seen in Fig. 6.16.

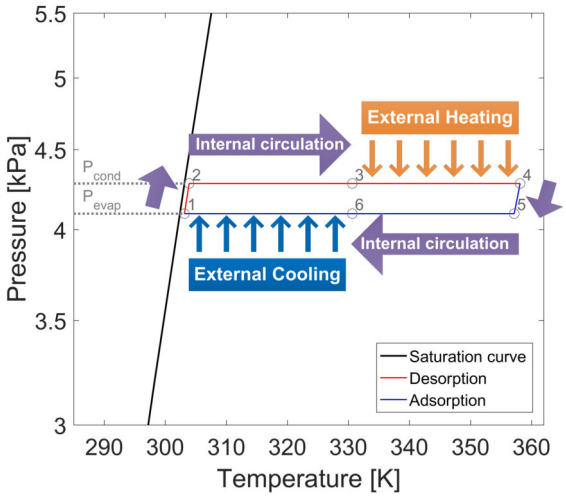


Figure 6.16: The internal recovery scheme as proposed by El-Dessouky and Ettouney [187] halves the energy input for desalination as the system can desorb about half the water from 2→3 without external energy input.

The heat integration is simple, straightforward and has been known for almost 20 years, but has never been tested in a dynamic model let alone in an experimental system, because the process is less advantageous for heat pumps than desalinators. Heat

integrations in experimental systems usually flow cold water through the hot bed first to preheat the cold bed during isosteric heating, but do not use the heat for desorption (Fig. 6.16).

A lumped parameter, dynamic model [132, 188] was adapted for the interpretation of the experimental adsorption desalinator and updated with the heat integration scheme of El-Dessouky. Table 6.6 shows the two additional phases II and IV required for internal circulation. Table 6.7 shows sequence parameters used to adjust the modelling equations according to the phases in table 6.6. All parameters used in the model are given in table 6.8.

Table 6.6: The six phases of the adsorption desalination cycle in Fig. 6.16

| **Phase** | **Cycle 1** | **Bed 1** | **Cycle 2** | **Bed 2** | **Heat source** |
|---|---|---|---|---|---|
| I | 1 → 2 | Isosteric Heating | 4 → 5 | Isosteric Cooling | Internal circ. |
| II | 2 → 3 | Desorption | 5 → 6 | Adsorption | Internal circ. |
| III | 3 → 4 | Desorption | 6 → 1 | Adsorption | External |
| IV | 4 → 5 | Isosteric Cooling | 1 → 2 | Isosteric Heating | Internal circ. |
| V | 5 → 6 | Adsorption | 2 → 3 | Desorption | Internal circ. |
| VI | 6 → 1 | Adsorption | 3 → 4 | Desorption | External |

Table 6.7: Model sequence parameters for each adsorption cycle phase in table 6.6

| **Phase** | **I** | **II** | **III** | **IV** | **V** | **VI** |
|---|---|---|---|---|---|---|
| $\tau_1$ | 0 | 1 | 1 | 0 | 0 | 0 |
| $\tau_2$ | 0 | 0 | 0 | 0 | 1 | 1 |
| $\omega$ | 0 | 1 | 1 | 0 | 1 | 1 |
| $\xi$ | 0 | 0 | 1 | 0 | 0 | 1 |

The water uptake of the Siogel silica gel (Oker Chemie, Germany) is assessed by Dubinin Astakhov (DA) isotherms [37, 122]

$$q^* = q_0 \; exp\left(-\left[\frac{RT}{E} ln\left(\frac{p_{sat}}{p}\right)\right]^n\right) \tag{6.54}$$

The adsorption kinetics are analysed by the linear driving force (LDF) equation:

$$\frac{dq_{1/2}}{dt} = \omega_{1/2} \; \frac{15 D_{S0} \; exp(\frac{-E_a}{RT})}{R_p^2} \; (q^* - q) \tag{6.55}$$

The mass balances of the condenser and evaporator are shown below:

$$\frac{dM_{evap}}{dt} = -M_{sg}\left(\tau_1 \frac{dq_1}{dt} + \tau_2 \frac{dq_2}{dt}\right) + F_2 - F_{high,in} \tag{6.56}$$

$$\frac{dM_{cond}}{dt} = M_{sg}\left(\tau_2\frac{dq_1}{dt} + \tau_1\frac{dq_2}{dt}\right) - F_4 \tag{6.57}$$

The salt mass fraction $w_{evap}$ in the evaporator changes according to:

$$\frac{w_{evap}}{dt} = \frac{-w_{evap}}{M_{evap}}\ \frac{dM_{evap}}{dt} + F_2\ w_2 - F_{high,in}\ w_{high,in} \tag{6.58}$$

The energy balance for the evaporator is:

$$(M_{hxev}c_{p,hx} + M_{evap}c_{p,sol,evap})\frac{dT_{evap}}{dt} =$$
$$\left(\tau_1\frac{dq_1}{dt} + \tau_2\frac{dq_2}{dt}\right)M_{sg}L + \dot{m}_{evap}c_{p,w}(T_{evap,in} - T_{evap,out}) \tag{6.59}$$

Where $M_{hxev}$ is the mass of the heat exchanger [kg], the latent heat L [kJ/kg], $c_{p,hx}$ is the specific heat of the aluminium heat exchanger [kJ/(kgK)], $c_{p,w}$ is the specific heat of the cooling water [kJ/(kgK)] and $c_{p,sol,w}$ is the specific heat of the solution inside the evaporator, which is about 3.3 kJ/(kgK) for concentrated NaCl solutions at ambient temperature [189]. It should be noted that the specific heat energies of the liquid phases inside the vessels in eq. (6.59-6.63) are related to the internal energy of the system. However, the difference between $c_p$ and $c_v$ is minimal for liquids and $c_p$ was used in the dynamic energy balances.
The energy balance of the condenser is:

$$(M_{hxco}c_{p,hx} + M_{cond}c_{p,w,cond})\frac{dT_{cond}}{dt} =$$
$$\left(\tau_2\frac{dq_1}{dt} + \tau_1\frac{dq_2}{dt}\right)M_{sg}L + \dot{m}_{cond}c_{p,w}(T_{cond,in} - T_{cond,out}) \tag{6.60}$$

The energy balance for the adsorbers are:

$$(M_{sg}c_{p,sg} + M_{hx,ads}c_{p,hx,ads} + M_{w,ads}c_{p,w,ads})\frac{dT_{ads1}}{dt} = \Delta h_{ads}M_{sg}\frac{dq_1}{dt} +$$
$$+\dot{m}_{ads}c_{p,w}[\xi\ (T_{ads2,out} - T_{ads1,out}) + (1-\xi)(T_{ads,in} - T_{ads1,out})] \tag{6.61}$$

$$(M_{sg}c_{p,sg} + M_{hx,ads}c_{p,hx,ads} + M_{w,ads}c_{p,w,ads})\frac{dT_{ads2}}{dt} = \Delta h_{ads}M_{sg}\frac{dq_2}{dt} +$$
$$+\dot{m}_{ads}c_{p,w}[\xi\ (T_{ads1,out} - T_{ads2,out}) + (1-\xi)(T_{ads,in} - T_{ads2,out})] \tag{6.62}$$

All outlet temperatures $T_{i,out}$ [K] are determined by the logarithmic mean temperature difference:

$$T_{out} = T_{vessel} + (T_{in} - T_{vessel})\ exp\left(\frac{-UA}{\dot{m}\ c_p}\right) \tag{6.63}$$

Where U is the overall heat transfer coefficient [W/(m$^2$K)], A is the surface area of the heat exchanger [m$^2$] and $\dot{m}$ is the flow rate of water supplied to the heat exchanger [kg/s]. The heat of adsorption $\Delta h_{ads}$ [kJ/kg] is derived from Clausius-Clapeyron and

the DA isotherm [124], where $\Theta = q_1/q_0$:

$$\Delta h_{ads} = L + E\ ln\left(\frac{1}{\Theta}\right)^{1/n} + \frac{E\alpha T}{n}\left(\frac{1}{\Theta}\right)^{-(n-1)/n} \tag{6.64}$$

The two main performance indicators in adsorption desalination are the Specific Daily Water Production $SDWP$ [$kg_w/(kg_{sg}d)$] and Performance Ratio $PR$ [-], which are given by eq. (2.3) and eq. (2.2) in chapter 2.2.1.

The relative humidity $RH$ [%] is defined as:

$$RH = 100\ \frac{P_{evap,vap}}{P_{bed,ads}} \tag{6.65}$$

where $p_{bed,ads}$ is the saturation pressure at the temperature of the adsorption bed.

The adsorption model and the reverse electrodialysis model are the two main building blocks of the model linked by the mass balances as third block. First, the adsorption desalination block runs for 10 cycles to achieve cyclic steady state, then the model is connected to the other two system blocks. The average evaporator mass fraction $w_{high,in}$ is passed on to the RED model, which calculates the power production of the membrane and outlet concentrations. These are passed on to the mass balances, which require the distillate production $F_4$ and the concentrations to calculate the return feed from the membranes to the evaporator.
The output values of the model are SDWP and PR as the two performance indicators of the regeneration side. In addition, the energy efficiency $\eta_{en}$, exergy efficiency $\eta_{ex}$ and power density of silica gel $P_{d,ADRED}$ [$W/kg_{sg}$] are assessed for the overall system and defined by:

$$\eta_{en} = \frac{P_{d,s}\ H_{high,in}\ t_{sim}}{Q_{evap} + Q_{des}} \tag{6.66}$$

$$\eta_{ex} = \frac{P_{d,s}\ H_{high,in}\ t_{sim}}{Q_{evap}\left(1 - \frac{T_{cond,in}}{T_{evap,in}}\right) + Q_{des}\left(1 - \frac{T_{cond,in}}{T_{ads,in}}\right)} \tag{6.67}$$

$$P_{d,ADRED} = \frac{P_{d,s}\ F_{high,in}}{M_{sg}} \tag{6.68}$$

The electric power output $P_{el,ADRED}$ [MW] is a function of $\eta_{en}$ and the energy of the saturated steam from the power plant $\dot{Q}_{steam}$ [MW]:

$$P_{el,ADRED} = \eta_{en}\ \dot{Q}_{steam} \tag{6.69}$$

Table 6.8: Simulation parameters for the small-scale adsorption desalinator [128] and Siogel silica gel.

| Property | Unit | Value | Reference |
|---|---|---|---|
| $\dot{m}_{evap}$ | L/min | 0.4 | - |
| $\dot{m}_{cond}$ | L/min | 0.8 | - |
| $\dot{m}_{ads/des}$ | L/min | 0.4 | - |
| $M_{hxev}c_{p,hx}$ | kJ/K | 0.137 | - |
| $M_{hxco}c_{p,hx}$ | kJ/K | 0.378 | - |
| $M_{hxads}c_{p,hx,ads}$ | kJ/K | 0.546 | - |
| $UA_{ads}$ | W/K | 14 | - |
| $UA_{cond}$ | W/K | 7 | - |
| $UA_{evap}$ | W/K | 40 | - |
| $t_{cycle}$ | s | 1200-4000 | - |
| $R_p$ | m | 0.002 | - |
| $M_{sg}$ | kg | 0.21 | [128] |
| $c_{p,sg}$ | kJ/(kgK) | 0.65 | [190] |
| $D_{sO}$ | $m^2/s$ | $2.5 \cdot 10^{-4}$ | [17] |
| $E_a$ | J/mol | $4.2 \cdot 10^{-4}$ | [17] |
| $q_0$ | kg/kg | 0.38 | [123] |
| $E$ | kJ/kg | 220 | [123] |
| $n$ | - | 1.1 | [123] |
| $R$ | J/(molK) | 8.314 | [39] |

### 6.3.3 Adsorption model validation for low temperature regeneration

The lumped parameter, dynamic model was validated with experimental data obtained from the small scale adsorption test rig described in section 5.1.1 and [129]. The model in table 6.6 was adapted to represent the physical system by skipping the internal circulation phases. Three low temperature experiments [130] were used to fit the model on the parameter $UA$ [W/K] of each vessel. The experiments were conducted by slightly heating the evaporator to achieve $P_{evap} \approx P_{cond}$ [120] with $T_{cond,in} = 25$ °C, while $T_{evap,in} > T_{cond,in}$ and $t_{cycle} = 2400$ s [130]. The best fitting parameters representing the experiments are $UA_{ads} = 14\ W/K$, $UA_{cond} = 7\ W/K$ and $UA_{evap} = 40\ W/K$.

The model was fitted on the system performance in terms of PR and SDWP as shown in Fig. 6.17. In Fig. 6.17a the PR for the lowest regeneration temperature is in very good agreement with the model, while for the two higher temperatures it slightly overpredicting them within the experimental error. The SDWP in Fig. 6.17b is overpredicted for the lowest regeneration temperature, while the two higher temperatures are in line with the experimental results. However, fitting the model on all experimentally obtained temperatures, pressures and time combinations with a single set of UA can lead to deviations of more than 100 % in some of the results. One of the main limitations of the lumped parameter, dynamic model lies in the assumption homogeneous temperatures throughout the units, whereas real systems are characterised by

temperature distributions (e.g. up to 10 °C measured in the evaporator). By contrast, several authors have reported excellent agreement between the model and the experimental results [17, 55], which cannot be confirmed by this study. Based on this study, it can be concluded that the model is appropriate for system design, when no exact representation of the experimental apparatus is required.

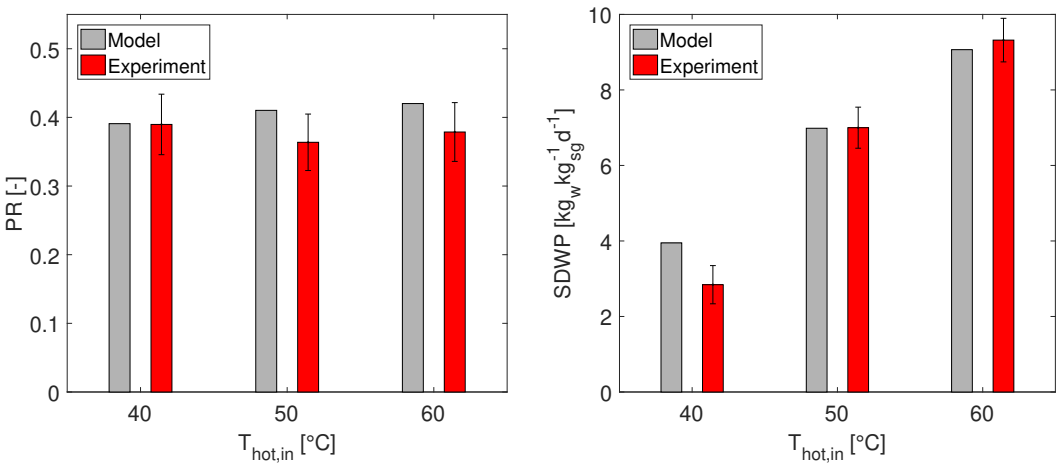


(a) (b)

Figure 6.17: (a) The model predicts the PR within the experimental uncertainty for low temperature regeneration.
(b) The SDWP is over-predicted by the model for very low regeneration temperatures.

### Improved performance model with internal circulation scheme

The PR of eq. (2.2) quantifies the energy efficiency of the adsorption desalination system. Large thermal desalination systems like multi effect distillation can achieve PR ≈ 10 [72], which means they generate ten times more water per unit of energy than simple distillation. However, these systems are very large. Adsorption desalinators are much more compact, have lower investment costs [17], but achieve PR < 1, where Ng. et al. have reported up to PR = 0.75 in an experimental study [17]. The performance ratio of experimental systems was addressed in early studies [133]. Much recent work focused on maximising the SDWP through material design, while the PR of even the most advanced systems remained constant around 0.6 [129] to 0.75 [17]. However, for commercial applications it is essential to develop the technology beyond PR > 1, which requires an optimised process design with favourable heat exchanger to adsorption material weight ratios [191] as well as a more advanced heat integration within the system.

Fig. 6.18 highlights the potential of adsorption desalination with internal circulation for different internal circulation times. The internal circulation times of phase II and V in table 6.6 were varied from 0-1400 s, while phases III + VI were kept constant at 600 s each and phases I + IV at 30 s. Moreover, the inlet temperatures in Fig. 6.18

are $T_{evap,in} = T_{cond,in} = 30$ °C and $T_{hot,in} = 80$ °C.

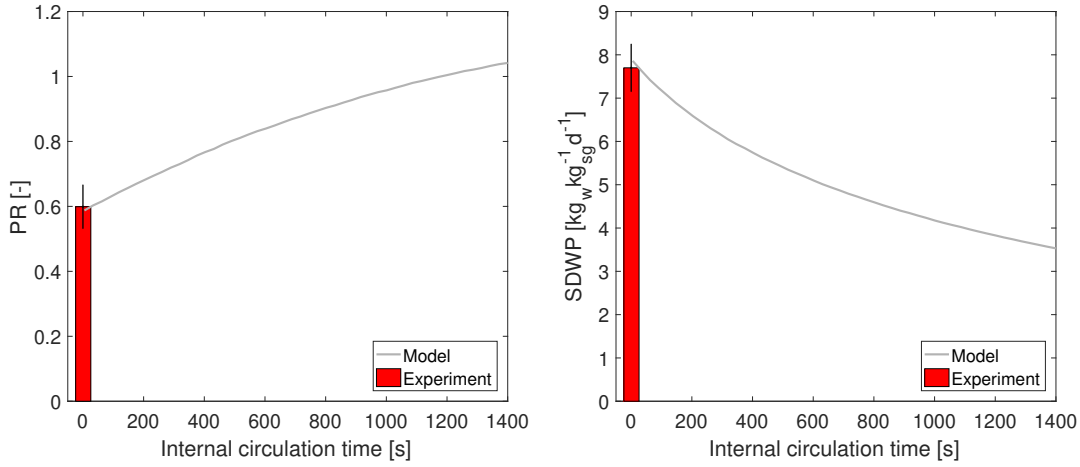


(a) (b)

Figure 6.18: The model predicts that increasing internal circulation times can boost the PR above the threshold of PR=1 (a), while sacrificing the SDWP (b). The experiment is conducted without internal circulation with $T_{hot,in} = 80$ °C, $T_{evap,in} = T_{cond,in} = 30$ °C, 600 s half cycle time and is used to validate the model.

The starting point of the investigation in Fig. 6.18 is zero internal circulation time, which resembles the experimental system [129] without the proposed internal circulation and only a simple heat recovery described in [129]. For $t_{ads,int} = 0$ s, the model and the experimental result are in agreement (Fig. 6.18). When, $t_{ads,int}$ is increased up to 1400 s., the PR increases from PR = 0.60 up to 1.04 (Fig. 6.18a), which is an improvement of 75 % compared to the experimental result. This indicates that adsorption desalinators can exceed the threshold of PR ≥ 1, which is imperative for the commercial success of adsorption desalination. However, the SDWP decreases with increasing $t_{ads,int}$ as the total cycle time increases with $t_{ads,int}$. Therefore, the optimal performance is a trade-off between the two indicators. An increased PR indicates increased energy efficiency, while a decreased SDWP implies a greater amount of silica gel and larger system footprint. The generally low SDWP of 4-8 $kg_w/(kg_{sg}d)$ is silica gel specific and a move to newly developed adsorption materials could significantly increase the SDWP and decrease the footprint with it. For example, Askalany et al. presented novel Ionogels, where experimentally obtained SDWP ≈ 25 $kg_w/(kg_{ig}d)$ was reported [131]. Moreover, improved heat exchanger designs with larger UA-parameters would reduce the cycle time and increase the SDWP as well. Modelling the ADRED system with ionogels would require further experiments with two fully packed heat exchangers and heat recovery to assess the PR of ionogels in addition to the SDWP. Moreover, kinetic measurements would be required for the LDF equation.

The experiment in Fig. 6.18 was conducted with salt free water in the evaporator, while

the salinity in the model was 35 g/kg (≈ 0.6 mol/kg) for seawater [95]. The presence of salt has an effect on the system performance through the boiling point elevation which decreases the pressure in the evaporator as described in [17, 119]. However, the boiling point elevation for seawater is small BPE = 0.3 °C reducing the pressure by 0.06 kPa or the relative humidity from 100 % to 98 % at $T_{evap} = T_{cond}$. In the ADRED process the salinity in the evaporator is 5 $mol_{NaCl}/kg$ causing BPE = 3-4 °C and lowering the pressure by 0.6 kPa or RH from 100 % to 81 % at $T_{evap} = T_{cond}$, which impairs the working capacity. The reduced RH due to the high BPE can be compensated by heating the evaporator.

### 6.3.4 Results for validated, small-scale Adsorption Reverse Electrodialysis model

The model assesses the energy efficiency $\eta_{en}$ and exergy efficiency $\eta_{ex}$ of the ADRED process depending on the heat source temperature for each case. Moreover, it determines the SDWP and PR for the adsorption side of the system. $P_{d,ADRED}$ is calculated from eq. (6.68) and $P_{el,ADRED}$ from eq. (6.69) with $\dot{Q}_{steam} = 700$ MW leading to the mass of silica gel $M_{sg} = P_{el,ADRED}/P_{d,ADRED}$. The results are compared for 6 different degrees of heat integration shown in table 6.9 to find the best configuration for each case. The first scenarios 1xyz in table 6.9 describe the system with no heat integration between evaporator and condenser, but increasing degrees of internal circulation as described in section 6.3.2 above. The other scenarios 2xyz feature heat integration between evaporator and condenser, which lets water always circulate between the two. The evaporator cools the water flow, while the condenser heats it up due to the latent heat of water. Hence, no external heat sink is required for the condenser in 2xyz. In addition, increasing degrees of internal circulation are also investigated in scenarios 2yz.

Table 6.9: Different scenarios and input parameters for the ADRED model. Below, "c-e int." stands for heat integration between AD condenser and AD evaporator and "circ." for circulation. For all cases $t_{ads} = 600$ s and $t_{isos} = 30$ s.

| **Scenario** | **Description** | $\mathbf{T_{evap,in}}$ **[°C]** | $\mathbf{t_{ads,int}}$ **[s]** |
|---|---|---|---|
| 1x | No heat integration | 30 | 1 |
| 1y | Short internal circulation | 30 | 600 |
| 1z | Long internal circulation | 30 | 1200 |
| 2x | No internal circ. + c-e int. | - | 1 |
| 2y | Short internal circ. + c-e int. | - | 600 |
| 2z | Long internal circ. + c-e int. | - | 1200 |

The input conditions of the steam power plant ($T_{ads,in} = 40$ °C) are used by the validated small-scale model to assess the process performance. The first three scenarios in table 6.9 consider external evaporator heating, while the last three feature heat in-

tegration between evaporator and condenser. Within each category, the subscenarios xyz test the suitability of the internal circulation for this application.
Fig. 6.19a shows that the PR of the AD side increases with the degree of heat integration. Overall, the PR is less than 1 because the working capacity of silica gel is reduced at 40 °C compared to 80 °C in Fig. 6.19a. However, the fully heat integrated system (scenario 2z) achieves PR = 0.63, which is 64 % higher than the PR with no heat intergation in scenario 1x. The energy efficiency of scenarios 1xyz is below 2xyz in Fig. 6.19c, because the evaporator heating in cases 1xyz requires additional heat input, which is accounted for in the energy efficiency. The silica gel power density in Fig. 6.19b is highest for the system with no heat integration 1x, because it achieves the highest SDWP. In 1xyz as well as in 2xyz the SDWP decreases with the cycle time from x to z as less cycles can be performed within one day at long cycle times.

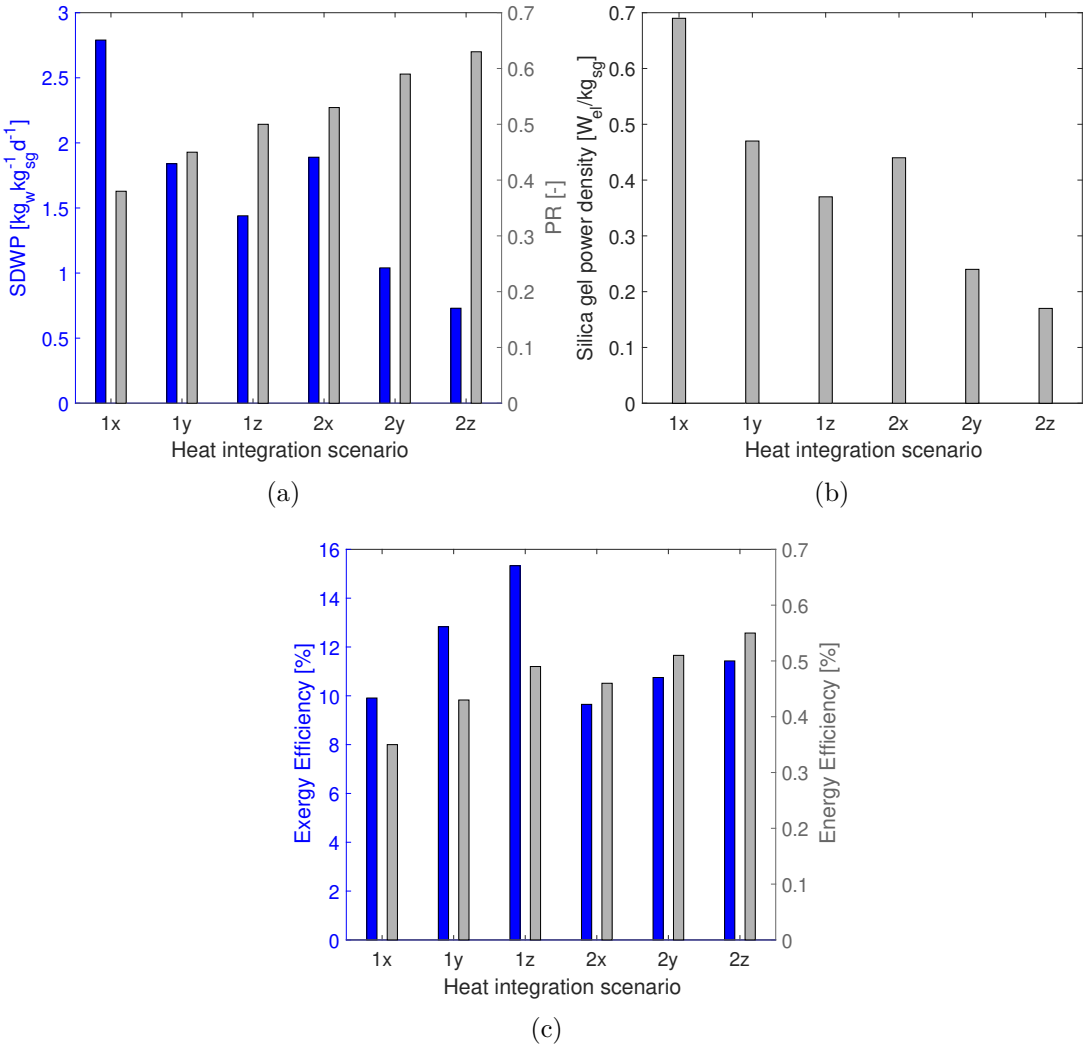


Figure 6.19: Predicted performance of the small scale ADRED system. Input conditions are given in table 6.9:
(a) PR and SDWP of the adsorption desalination system for different heat integrations.
(b) The electric power output per kg of silica gel for the overall system.
(c) The energy and exergy efficiency of the overall ADRED system.

The exergy efficiency in Fig. 6.19c is highest at 15.3 % for scenario 1z, where the evaporator is heated externally and the internal circulation time is maximised. The Carnot factor ($= 1 - T_{cond,in}/T_{evap/hot,in}$) in eq. (6.67) is used to convert the energy efficiency to the exergy efficiency. Heat with lower heat source temperature contains less exergy, because the Carnot factor is lower. Here, it is is 2.9 times lower for $T_{evap,in} = 30$ °C than it is for $T_{hot,in} = 40$ °C at $T_{cond,in} = 25$ °C. Thus, heating the evaporator does not impair the exergy efficiency, because of the lower Carnot factor at 30 °C. Instead, the higher working capacity of the silica gel increases the exergy efficiency of 1xyz above 2xyz for each respective scenario. The working capacity of the material increases with evaporator heating, which is represented by the higher SDWP in 1xyz compared to 2xyz in Fig. 6.19a.

The overall system performance could be further improved by novel adsorption materials with higher SDWP and working capacities, future developments in heat integration and the development of improved RED membranes. The thermodynamic analysis in the preceding publication showed that highly concentrated LiCl solutions (20 mol/kg) could improve the exergy efficiency to more than 40 % [119], but this is impossible to achieve with current membranes, which are optimised for sodium chloride solutions.

### 6.3.5 Application to 700 MW of waste heat from a power plant

A steam power plant with 700 MW condenser power at 40 °C was assumed as waste heat source [139]. Fig. 6.20 scales the specific results of Fig. 6.19 up to the absolute sizes of the adsorber beds and the electricity output of the large scale power plant. The smallest system in Fig. 6.20a with the highest power density scenario (1x), which requires an external heat sink like the sea. The fully heat integrated system in 2z produces 56 % more electricity but requires 6 times more silica gel.
The best trade-off between size, electricity output and without external heat sink is scenario 2x, which does not feature the internal circulation. Therefore, the cycle times can be shorter leading to an improved distillate production.

The volume of 7300 tons silica gel in 2x can be split between 4 cylindrical adsorber beds of 30 m height and a diameter of 14 m. The silica gel volume was doubled to account for heat exchangers inside the adsorbers and to estimate their sizes in Fig. 6.20b. New adsorption materials with working capacities $> 1$ $g_w/g_{ig}$ at 40 °C can reduce the footprint of the adsorbers significantly [131]. However, the energy efficiency of the system with an improved working capacity is unlikely to change as $\Delta h_{ads}$ is always at least $L_w$.
Fig. 6.20b compares the size of the proposed ADRED system to the size of a 122 m high natural air flow cooling tower of a similar cooling capacity [192], which is replaced by the ADRED system. The size of the RED plant was extrapolated from the results of Post et al. [168], where a 100 kW RED plant was estimated to fit inside a 40 ft container.

The ADRED system utilises most of the heat supplied by the power plant, but would still require a small external heat sink for the last step of the adsorption cycle as shown in Fig. 6.16. However, the discharged heat flow of ADRED is significantly smaller than the waste heat flow of the power plant and discharged at ambient temperature instead of 40 °C. Therefore, the power plant does no longer require the large cooling tower in presence of ADRED.
The system generates 3.2 MW of electricity. About 5 $kJ_{el}/kg_w$ are estimated to be lost due to pumping in an AD plant [17, 128] and the distillate flow rate from the large scale ADRED plant is $SDWP \cdot M_{sg}$ = 160 $kg_w/s$ resulting in pumping losses of 0.8 MW for the AD side of the system. An additional 5 % of the electricity are lost to pumping

in the RED plant [8, 168]. Thus, the ADRED system generates 2.3 MW net electricity at an energy efficiency of 0.33 % and the exergy efficiency of 7.1 %.

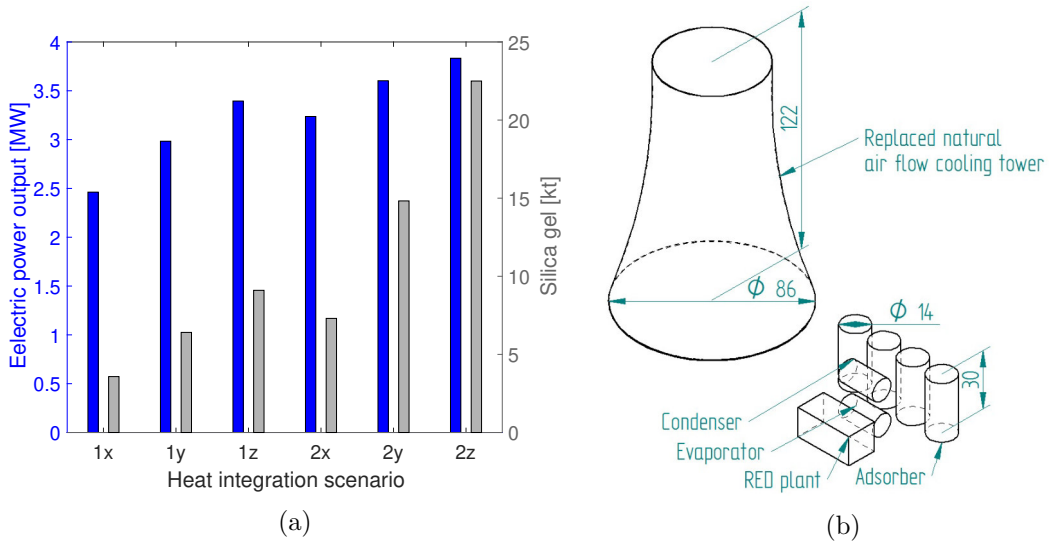


(a) (b)

Figure 6.20: (a) The electricity output and mass of silica in kilotons for each heat integration configuration.
(b) Size comparison [m]: ADRED system based on the modelling results of heat integration scenario 2.1 (front) to natural air flow cooling tower (back).

### Adsorption Reverse Electrodialysis using Ionogels

Ionogels achieve high SDWP at low regeneration temperatures. Thus, they are ideal for the application in the closed loop system. In scenario 1, Ionogels achieve SDWP of 11 $kg_w/(kg_{ig}d)$ based on the experiments in the previous chapter. This result is about four times higher than the SDWP of silica gel. Thus, the adsorber beds of scenario 1x in case 1 would be reduced to about 800 tons leading to a much smaller system. However, the ADRED system using Ionogel cannot be modelled yet for two reasons. Firstly, kinetic properties of water adsorption on Ionogels are not available yet, but are a requirement for the LDF model. Secondly, more Ionogel experiments are necessary with higher loadings of Ionogel on the heat exchanger. The dynamic model needs to validate on the PR as well as the SDWP, where the SDWP is an adsorbent mass specific performance indicator, which is why it is independent of the mass of Ionogel inside the heat exchanger. By contrast, the PR takes the energy supplied to the heat exchanger as well as the Ionogel into account. The heat exchanger has a mass of 600 g, while only 25-60 g of Ionogel were packed inside the heat exchangers, which is enough to assess the SDWP, but insufficient for the PR as contribution of the aluminium mass to the PR is too significant. Thus, the impact of Ionogels on the energy performance could only be made based on qualitative considerations.
The PR will improve slightly by less than 10 % by switching from Siogel silica gel to Ionogel. The heat requirements of the heat exchanger mass will remain constant, but

the heat of desorption improves by about 15 % for Ionogel. The heat of adsorption of Siogel is about 2800 kJ/kg$_w$ [123], while Ionogel has a slightly reduced $\Delta h_{ads}$ of 2400 kJ/kg$_w$ [131]. Thus, the energy efficiency of the process will remain at 0.3-0.6 %, but the exergy efficiency will improve at low regeneration temperatures of 25 °C due to the Carnot factor. An energy efficiency of 0.5 % at $T_{ambient}$ = 20 °C and $T_{hot}$ = 25 °C leads to an exergy efficiency of 30 %.

## 6.4 Cost analysis - levelized cost of electricity

A cost analysis of ADRED is performed to assess the levelized cost of electricity (LCOE) of the system and to compare it to other renewable energy technologies. The LCOE is defined as [193]:

$$LCOE = \frac{CapEx \cdot \sum_{t=1}^{n} \frac{OpEx_t + \cancel{Fuel_t + Carbon_t}}{(1+r)^t}}{\sum_{t=1}^{n} \frac{E_t}{(1+r)^t}} \tag{6.70}$$

In eq. (6.71) CapEx are the capital expenses, $OpEx_t$ the operational expenses, $Fuel_t$ the cost of fuel at purchase, $Carbon_t$ the carbon emission cost, $E_t$ the electricity production and r the discount rate at 5 %. The cost of fuel at purchase and the carbon emission costs are not considered in eq. (6.71), because the low-grade heat source is presumed to be free in the form of industrial waste heat. In addition, the system is a renewable process and no carbon is emitted through the application of the process.

The electricity produced each year is assessed by the following equation:

$$E_t = (PowerOutput) \cdot (Seconds\ per\ year) \cdot (Uptime) \tag{6.71}$$

The power output of the system is assumed to be 3200 kW taken from the dynamic simulation in the previous section. Furthermore, an uptime of 90 % of the plant was estimated allowing time for repairs and revision.

The calculation of the capital expenses was based on a publication by Daniildis et al. [169], who assessed the LCOE for a RED power plant. Hence, their assumptions were considered for the RED side of the closed-loop ADRED system. The capital expenses of the regeneration side of the ADRED system were based on a cost analysis performed by Ng et al. for an adsorption desalination plant [17]. The sum of the capital expenses can be split into five contributors: the construction cost $C_{constr}$, the equipment cost $C_{equip}$, the membrane cost $C_{membrane}$ and the cost of the AD plant $C_{AD}$ with the labour cost $C_{labour}$ being 20 % of the capital expenses.

$$CapEx = \sum [(C_{constr} + C_{equip} + C_{membrane} + C_{AD}) \cdot (1 + C_{labour})] \tag{6.72}$$

The construction cost of the building was assessed by Daniildis et al. [169]. The cost to build a high-tech factory building was assumed to be 1123 €/m$^2$. The factory building has an installation volume of 4 kW/m$^3$, where a construction height of 15 m was assumed. These considerations are incorporated into the following equation:

$$C_{constr} = \frac{(PowerOutput) \cdot (Hightech\ factory\ per\ m^2)}{(Installation\ Volume) \cdot (Construction\ height)} \tag{6.73}$$

The equipment cost are taken into account at $C_{pump}$ = 1600 €/kW, which leads to:

$$C_{equip} = C_{pump} \cdot (PowerOutput) \tag{6.74}$$

The cost of an adsorption desalination plant was analysed by Ng et al. [17]. Ng et al. did not provide many details in their publication, but they estimated the cost of a plant producing 12.5 m$^3$/day at USD 108k, which converts to $AD_{cost}$ = 606k EUR/(kg/s). The flow rate of distillate which needs to be provided by the adsorption plant can be estimated by the ratio of the plant output and $\Delta G_{mix}$. Aqueous sodium chloride solutions of 5 mol/kg can achieve $\Delta G_{mix} \approx$ 12 kJ/kg. In addition, an efficiency factor for the membrane of $\eta$= 0.8 was considered as no membrane can convert the entire $\Delta G_{mix}$ into electricity. The cost of the adsorption regeneration is summarised by the following equation:

$$C_{AD} = \frac{(PowerOutput) \cdot AD_{cost}}{\Delta G_{mix} \cdot \eta} \tag{6.75}$$

Daniildis et al. assumed that the operational expenses are 6% of the capital expenses [169]. For simplicity, the same was assumed for the adsorption plant, which roughly matches Ng's operational expenses [17].

$$OpEx_t = CapEx \cdot 0.06 \tag{6.76}$$

The LCOE was calculated for an ADRED system utilising a saturated aqueous lithium chloride solution as working fluid. All the considerations above lead to an LCOE of 1.56 €/kWh for a system with a lifetime of 25 years. Hence, the electricity generated by an ADRED system is about 10 times more expensive than photovoltaic and 20 times more expensive than coal/nuclear energy [193].

## 6.5 Conclusions

In this chapter an entirely new process to generate electricity from low-grade waste heat using an Adsorption - Reverse Electrodialysis (ADRED) system has been developed. The ADRED system aims to generate electricity from low and high salinity solutions in a closed-loop system by utilising low-grade heat between 60-100 °C. After flowing through the Reverse Electrodialysis membrane the two solutions are regenerated by an adsorption desalinator driven by the low-grade heat source. Compared to other desali-

nation methods, adsorption desalinators have a simpler system design, fewer moving parts, a lower electricity consumption and can utilise low-grade heat as low as 40 °C with current, commercially available materials. Future development of materials could reduce the regeneration temperature down to an unprecedented temperature of 25 °C.

A model for the prediction of exergy efficiencies for the ADRED system has been developed. The model has been used to screen 227 salts and ten different adsorption materials for their applicability in the ADRED system and calculate the exergy efficiency for each material, salt over a large number of possible system operating parameters. It was demonstrated that the specific exergy consumption is widely unaffected by the salt and its concentration. This is an important feature, because it allows the application of highly concentrated salt solutions and the optimisation of the Reverse Electrodialysis membrane without restrictions from the regeneration side. By contrast, other desalination methods impose constraints on the maximum salt concentration, because their thermal energy consumption increases with the salt concentration.

This investigation has focused on the performance of the ADRED system. A total number of 300,000 different combinations of salts, materials and system parameters have been analysed to identify the optimum combination. Firstly, the study analysed the best overall results considering all salts. Secondly, the list of salts was reduced to monovalent salts, because current Reverse Electrodialysis membranes are designed for them. In the first analysis AQSOA Z01 proved to be an excellent material for low temperature regeneration, where it had the best performance and it performed best in combination with $MgI_2$ yielding an exergy efficiency of 28 %. In case of the monovalent salts, LiCl showed the highest performance. However, the Pitzer correlations are only fitted for LiCl up to a maximum concentration of 5 mol/kg, whereas the actual saturation concentration of this salt is 20 mol/kg. Therefore, an additional investigation assessed the performance with a saturated LiCl solution, as LiCl is the best monovalent salt from the main investigation. The result revealed an outstanding exergy efficiency of 45 % and an energy efficiency of 4 % with AQSOA Z01 as well as Siogel silica gel.

Water has very high latent heat. Hence, a lot of energy is required to regenerate aqueous salt solutions. Other fluids have a much lower latent heat, while showing decent salt solubility at the same time. Liquid ammonia was considered as an alternative fluid to water, because it has a low latent heat of evaporation 1150 kJ/kg and some salts show very high solubility in liquid ammonia of up to 60 mol/kg. The combination of low latent and high salt solubility of liquid ammonia promised improved energy efficiency. Thus, the thermodynamic ADRED model was adjusted to use the working pair ammonia - activated carbon. However, literature data on liquid ammonia is scarce and only few papers from the 1930s report activity coefficients, which could be used for modelling. In addition, only few studies worked on adsorption of ammonia on acti-

vated carbons and the heat of adsorption reported is twice as high as the latent heat of ammonia. Thus, the results were comparable to the aqueous solutions of LiCl from the preceding investigation. Hence, the investigation indicated no clear advantage of switching the fluid from water to ammonia.

A promising application for ADRED is the conversion of waste heat emitted by power plants, amounting to 4000 TWh/year between 40-49 °C in the USA alone, which has a vast potential even at very low energy efficiencies. The only other thermal desalination method that can be operated at such low temperatures is membrane distillation, but the internal electricity demand would be too high for the RED heat engine.
A dynamic model was implemented to test the application of an ADRED system powered by steam coming from the low pressure turbine of a power plant at 40 °C as waste heat source for conversion into electricity.
An adsorption desalination unit is powered by the low pressure steam and condenses the steam in the heat exchanger of the adsorption beds. The analysis is conducted with in a simulation, where each component is experimentally validated. Moreover, the process scheme of the adsorption desalination model was enhanced increasing the performance ratio above 1. This was achieved through an innovative heat integration between the two adsorber beds. The validated reverse electrodialysis and adsorption desalination models were combined and analysed for the input conditions of the power plant. The investigation screened six different heat integration schemes achieving exergy efficiencies 10-15 % and energy efficiency of 0.35-0.55 % for silica gel. Therefore, the system can convert a waste heat source of 700 MW into a net electricity production of 2.3 MW, which increases the electrical output of the steam power plant by 0.5 %.

# Chapter 7

# Conclusions and future work

This work is motivated by the utilisation of industrial low-grade waste heat 40-100 °C, which is available in abundance, but is usually emitted into the environment leading to thermal pollution and economic losses. Instead, waste heat can be used for electricity generation by combining a thermal desalination system with a reverse electrodialysis membrane *RED* in a closed loop of two saline solutions. The RED membrane generates electricity from the salt gradient between the two solutions, while the thermal regeneration unit restores the salt gradient and is powered by the waste heat source.

In this work adsorption desalination as well as other thermal desalination methods were investigated for their application within the RED heat to power process. The thermodynamic properties of salt solutions are highly important for the process. Thus, the characteristics of salt solutions were investigated first. An experimental analysis was conducted using a Barker's cell to measure saturation pressures and temperatures of novel acetate salt solutions. The analysis extended the available data in the literature significantly. Caesium, lithium and potassium acetate salt solutions were each measured at concentrations up to 9 mol/kg and temperatures 10-90 °C. Pitzer model virial coefficients were fitted to the experimental data obtained for the novel acetate salt.

### Conclusions on desalination

Desalination modelling was conducted for multi-effect distillation *MED*, multi-effect distillation adsorption *MEDAD* and absorption vapour compression *ABVC* in different simulation platforms. A MED model was implemented in Honeywell UniSim Design R443 using OLI electrolytes package. The results show that the performance is very sensitive to the number of effects and the thermal energy consumption decreases from 150 kWh/$^3$ for 5 effects to 30 kWh/$^3$ for 27 effects. The combination of MED with adsorption was proposed by the group of Prof. Ng and investigated within this work as well. A thermodynamic, steady state model was implemented in Matlab, but the results show no significant improvement compared to MED alone. Another promising

novel desalination method proposed by El-Dessouky is ABVC, which was simulated in UniSim. The system has a much simpler set up than MED, but achieves 250 kWh/$^3$ regardless of salt type and concentration.

An experimental adsorption desalinator was designed, built and experimentally tested. Adsorption desalination features the simplest process design and lowest electricity consumption. Moreover, it can also be powered by the lowest regeneration temperatures, but has a comparably high thermal energy consumption of more than 850 kWh/m$^3$. The best performing adsorption desalinator in the scientific literature uses 144 kg of silica gel, whereas the design presented here requires only 0.025 kg to 0.4 kg, which is currently the world's smallest, reported design. The small scale minimises the lab space requirements and allows the testing of novel, non-commercial materials. Larger systems can only test established, commercial materials, but technology advances are more likely to arise from novel materials.
Silica gel is an inexpensive, commercial material that has been tested in almost all experimental adsorption desalinators and is commonly used for benchmarking. A comprehensive analysis was conducted using Siogel silica gel for different temperatures and cycle times. The system achieved a maximum Specific Daily Water Production *SDWP* of 10.9 $kg_w/(kg_{sg}d)$ and Performance Ratio of 0.6, both at 80 °C and full cycle times between 1200 s and 2400 s. Low temperature regeneration testing reduced the Specific Daily Water Production to 2.8 $kg_w/(kg_{sg}d)$ at 40 °C. A novel thermal response experiment and adsorption cycle analysis provided deeper insight into the process beyond the established performance indicators.
Ionogels are novel, non-commercial adsorption materials composed of a silica gel support structure impregnated with an ionic liquid. Ionic liquids are attracting widespread interest in fields such as fuel cells, batteries, heat storage or catalysis, while water sorption for supported ionic liquids is an entirely novel field. A preliminary screening of different ionic liquids identified the most promising candidates for temperature conditions present in adsorption desalination achieving high water uptakes at relative humidity $> 60$ %. The two most promising candidates were EMIM Ac (1-ethyl-3-methylimidazolium acetate) and choline glycolate (2-hydroxyethyl-trimethylammonium 2-hydroxyethanoate). EMIM Ac is readily commercially available, whereas choline glycolate needs to be custom manufactured. Thus, one heat exchanger was packed using monoliths of Syloid 72FP silica gel impregnated with 60 wt% EMIM Ac. A cycle time analysis revealed that the Ionogel monoliths feature improved heat and mass transfer compared to the Siogel silica gel beads, which reduced the full cycle time to 300-800 s. In addition, low temperature regeneration $< 50$ °C was conducted showing that Ionogel can be regenerated as low as 25 °C achieving SDWP = 6.8 $kg_w/(kg_{ig}d)$, which is similar to silica gel at 50 °C. An increase of the regeneration temperature to 45 °C improves the SDWP to 17.5 $kg_w/(kg_{ig}d)$, which is almost twice as high as silica gel at 80 °C. Therefore, Ionogels are proven to be an exciting new class of adsorption materials that

deserve further investigations.

### Conclusions on adsorption reverse electrodialysis

The integration of adsorption desalination into the RED heat to power process was proposed forming adsorption reverse electrodialysis *ADRED*. The ADRED concept is entirely novel and combines the outcomes of the previous chapters in two sections.

The first sections investigated ADRED's performance from an ideal, thermodynamic point of view neglecting the design limitations of a real system, e.g. heat and mass transfer limitations, membrane resistances and permselectivity. A thermodynamic model was created to assess the energy and exergy performances of the integrated system for 10 different adsorption materials and 227 different salts. The performance of the adsorption desalinator is calculated through the Specific Energy Consumption, an indicator neglecting all system heat and mass transfer limitations. For the RED electricity production, the Pitzer model was used to determine the Gibbs free energy of mixing at different concentrations for all 227 salts. Salt and mass balances combine the two model components with each other. The results show that the energy consumption of adsorption desalination is almost independent of the salt concentration, which is a standalone feature compared to other desalination methods and allows the RED membranes to operate at high concentrations for higher electricity production. Aqueous solutions of the divalent salt $MgI_2$ achieve the best exergy efficiencies up to 30 % at relatively low concentrations 5 mol/kg and regeneration at 60 °C. Monovalent salts require much higher salinities to achieve similarly high exergy efficiencies as 5 mol/kg of LiCl accomplishes up to 10 %. An increase of the LiCl salinity to 20 mol/kg improves ADRED's exergy efficiency to 45 % and energy efficiency of 4 %. In addition, the investigation was extended to solvents other than water. Water has a high latent heat of 2400 kJ/kg that decreases the efficiency of the thermal desalination system, whereas ammonia has a latent heat of 1200 kJ/kg with a similar molar mass and polarity as water leading to high salt solubility. However, the results show that the activity coefficients of salts dissolved in liquid ammonia are low compared to water. Therefore, the overall performance is similar, but not favourable in comparison to water.

A second step investigated the performances that can currently be achieved with state of the art adsorption desalinators and RED membranes. A dynamic adsorption desalination model was implemented and fitted to low temperature regeneration results ≤ 60 °C experimentally obtained from the adsorption test rig using silica gel. In addition, an advanced thermal heat integration process was integrated into a dynamic adsorption model for the first time. A validated RED model using NaCl ≤ 5 mol/kg was adapted from the literature taking resistances and permselectivity into account. Again, the two validated models were combined through salt and mass balances. The

results demonstrate that the advanced heat integration can enhance the Performance Ratio of adsorption desalination above 1, which is an important threshold for the progression of the technology. The overall model reveals that exergy efficiencies up to 15 % and energy efficiency up to 0.55 % are currently possible with ADRED. In a case study, ADRED was scaled up to be powered by 700 MW waste heat at 40 °C from a large steam power plant to mitigate the power plant's thermal pollution. Such a large waste heat source would require a very large ADRED system of 7300 $tons_{sg}$ that could generate 2.3 MW net electricity with a net exergy efficiency of 7.1 % and net energy efficiency of 0.3 %. Moreover, the system would alleviate the surrounding environment (e.g. air, rivers) from a large portion of the 700 MW waste heat.

### Future work

Future investigations are needed to explore and further develop adsorption desalination and ADRED.
An integrated experimental system should be tested with a small RED stack connected to evaporator and condenser of the present adsorption test rig. Some minor changes to the current system would be needed like replacing the evaporator aluminium heat exchanger with a stainless steel one to reduce corrosion. Although the electricity production from the small-scale ADRED would be so little that only a few LEDs could be powered by it, the system would be an essential proof of concept.

Apart from an experimental ADRED heat engine, novel adsorption materials need to be tested to improve the efficiency of adsorption desalination.
Ionogels represent a very promising type of adsorption materials and should be further investigated. Ionic liquids should be tested in the test rig to investigate their performance on a system level for the first time. In addition, experimental results are necessary for model validation. Apart from experiments on system level, the material properties should be assessed as well. Water sorption processes inside the Ionogel are not well understood yet, but are essential for a meaningful material design. The adsorption kinetic parameters need to be determined for system modelling as well. Once these parameters are available, Ionogels can also be applied to ADRED modelling. The energy efficiency should not improve much, but the system size could be reduced by up to one order of magnitude.
An interesting addition to ADRED would be the combined production of electricity and cooling for air-conditioning or refrigeration at the same time. The cooling energy output would save electricity needed for vapour-compression air-conditioning elsewhere in the plant, which can be significant. Thus, the overall efficiency would be increased substantially. SAPO-34 represents a material that can provide cooling without sacrificing any desalination capacity, but requires regeneration temperatures $> 80$ °C. By contrast, silica gel has a reduced water uptake in cooling applications due to the low rel-

ative humidity in the evaporator, which is why silica gel is not suitable for the combined application. The S-shaped isotherms of SAPO-34 allow the combination of cooling and desalination at constant SDWP making this an interesting commercial material.

An improvement to ADRED modelling could be the implementation of a multidimensional adsorption desalination model. The lumped parameter, dynamic model is useful tool for system design. However, the model has certain limitations as it has only three fitting parameters (overall heat transfer coefficients) and assumes homogeneous temperatures in each vessel and homogeneous water uptake throughout the adsorber bed. A multidimensional model could be developed to describe the experimental system in greater detail. It might be necessary to adjust the design of the adsorber beds and heat exchangers to facilitate the modelling activity. Temperature measurements inside the adsorber would be necessary to fit the model to non-homogeneous adsorber bed temperature distributions.

The performance of the adsorption desalinator could be enhanced through system upgrades, which are listed in Appendix E.

# Appendices

# Appendix A

# Items

## A.1 Barker's cell

Table A.1: The items used for the Barker's cell

| Item | Product |
|---|---|
| Pressure transducer | General Electric UNIK5000 |
| Thermostatic bath | Julabo Corio CD-300F |
| T-thermocouple | RS Pro Type T Thermocouple Copper probe 814-0153 |
| Vacuum pump | Edwards nXDS 6i |
| Magnetic stirring plate | Hanna Instruments HI 200M |
| Deionised water machine | Elga Centra R200 |
| Pressure display | London Electronics Ltd - INT2-P panel meter |
| T Reader | Digitron T202KC |
| Heater for tape | Electrothermal MC5 |
| Balance 1 | AND HR-300i |
| Balance 2 | Mettler Toledo XS205 DualRange |
| Sodium Acetate | Sigma Aldrich S2889-1KG |
| Potassium Acetate | Sigma Aldrich 791733-1KG |
| Lithium Acetate | Sigma Aldrich 517992-100G |
| Cesium Acetate | Sigma Aldrich 329827-100G |

## A.2 Adsorption test rig

Table A.2: Main items used for test rig

| Item | Material | Manufacturer | Product Number |
|---|---|---|---|
| Cold/Ambient Bath | - | JULABO USA Inc. | CD300F |
| Hot Bath | - | JULABO USA Inc. | F12-ED |
| Vacuum Pump | - | Edwards | nXDS 6i |
| DAQ | - | Advantech USA | ADAM-5000E-AE |
| DAQ | - | Advantech USA | ADAM-5018-A2E |
| DAQ | - | Advantech USA | ADAM-5017P-AE |
| DAQ | - | Advantech USA | ADAM-5069-AE |
| E-Pneumatic Valve | Stainless Steel | Pfeiffer Vacuum GmbH | PF D38 533 |
| E-Pneumatic Valve | Stainless Steel | Pfeiffer Vacuum GmbH | PF D48 533 |
| Recirculation Valve | Stainless Steel | Pfeiffer Vacuum GmbH | DVI 005 M n.c. |
| ISO-KF fittings | Stainless Steel | Pfeifer and Vacom | - |
| Solenoid valve | Brass | Connexion Develop. Ltd | PU22002A9VITON |
| Heat Recovery Valves | Stainless Steel | Connexion Develop. Ltd | JA1/4FE-24VDC |
| Flowmeter | Stainless Steel | Nixon Flowmeters Ltd | NFX-1/4”-B-V |
| Thermocouple | Stainless Steel | Omega | TMT316SS-IM150U-150 |
| Pressure Transducer | Stainless Steel | WIKA | S-20 |
| Mesh | Polyester | Plastok | 290 MICRON |
| O-Ring 112 mm | Nitrile | Polymax | 112X4N70 |
| O-Ring 90 mm | Nitrile | Polymax | 90X4N70 |
| O-Ring 96 mm | EPDM | Polymax | 96X4E70 |
| Deionised water | - | Elga | Centra R200 |
| Vacuum Grease | - | DOW CORNING | 976V |
| Glue | Ethyl cyanoacrylate | Henkel Loctite | 454 |
| Leak Sealant | Epoxy Resin | Kurt Lesker | TORR SEAL |
| Leak Sealant | Silicone Resin | AGAR SCIENTIFIC LTD | Vacseal |

# Appendix B

# Result tables vapour liquid equilibria

The results in tables B.4 and B.6 were measured as part of this thesis and are published as novel solutions by Giacalone et al. [101]. Lithium acetate in table B.5 is an entirely novel solution. The vapour pressures of pure water in table B.1 were compared to literature values from NIST refprop [103] to obtain a calibration curve and convert the temperature readings $T_{exp}$ to $T_{corr}$. In table B.2 an aqueous was measured.

## B.1 Validation

Table B.1: Saturation pressures and temperatures of deionised water from Elga Centra R200. The results are used for calibration and conversion of $T_{exp}$ to the corrected temperature $T_{corr}$

| **Salt** | $\mathbf{C_{exp}}$ **[mol/kg]** | $\mathbf{T_{exp}}$ **[°C]** | $\mathbf{T_{corr}}$ **[°C]** | $\mathbf{P_{exp}}$ **[bar]** | **BPE [°C]** | **Φ[-]** |
|---|---|---|---|---|---|---|
| - | 0 | 10.2 | - | 0.0130 | - | - |
| - | 0 | 20.1 | - | 0.0246 | - | - |
| - | 0 | 29.9 | - | 0.0437 | - | - |
| - | 0 | 39.8 | - | 0.0747 | - | - |
| - | 0 | 50.0 | - | 0.1233 | - | - |
| - | 0 | 60.1 | - | 0.1968 | - | - |
| - | 0 | 70.5 | - | 0.3050 | - | - |
| - | 0 | 80.9 | - | 0.4558 | - | - |
| - | 0 | 91.9 | - | 0.6756 | - | - |

Table B.2: Saturation pressures and temperatures sodium chloride were measured for validation and training purposes on the Barker's cell. The results are compared to OLI electrolytes in UniSim.

| **Salt** | **$C_{exp}$ [mol/kg]** | **$T_{exp}$ [°C]** | **$T_{corr}$ [°C]** | **$P_{exp}$ [bar]** | **$P_{OLI}$ [bar]** | **Error [%]** |
|---|---|---|---|---|---|---|
| NaCl | 4.006 | 10.0 | 9.9 | 0.0101 | 0.0104 | 2.8 |
| NaCl | 4.006 | 24.8 | 24.9 | 0.0270 | 0.0269 | -0.3 |
| NaCl | 4.006 | 29.6 | 29.7 | 0.0361 | 0.0357 | -1.2 |
| NaCl | 4.006 | 39.7 | 39.7 | 0.0626 | 0.0621 | -0.9 |
| NaCl | 4.006 | 49.8 | 49.6 | 0.1036 | 0.1031 | -0.5 |

## B.2 Potassium Acetate

Table B.3: The measured saturation pressures, temperatures and concentrations and the calculated BPE and Φ for potassium acetate: Part 1

| **Salt** | **$C_{exp}$ [mol/kg]** | **$T_{exp}$ [°C]** | **$T_{corr}$ [°C]** | **$P_{exp}$ [bar]** | **BPE [°C]** | **Φ[-]** |
|---|---|---|---|---|---|---|
| KAc | 2.006 | 10.3 | 10.9 | 0.0120 | 1.3 | 1.20 |
| KAc | 2.006 | 20.0 | 20.7 | 0.0226 | 1.3 | 1.08 |
| KAc | 2.006 | 30.0 | 30.6 | 0.0404 | 1.5 | 1.19 |
| KAc | 2.006 | 39.9 | 40.3 | 0.0692 | 1.5 | 1.14 |
| KAc | 2.006 | 50.0 | 50.1 | 0.1146 | 1.6 | 1.09 |
| KAc | 2.006 | 60.2 | 59.8 | 0.1830 | 1.6 | 1.05 |
| KAc | 2.006 | 70.6 | 69.5 | 0.2836 | 1.7 | 1.04 |
| KAc | 2.006 | 81.1 | 79.2 | 0.4264 | 1.8 | 1.04 |
| KAc | 2.006 | 91.9 | 89.1 | 0.6249 | 2.1 | 1.11 |
| KAc | 2.999 | 10.7 | 10.7 | 0.0114 | 1.83 | 1.14 |
| KAc | 2.999 | 19.9 | 19.9 | 0.0207 | 1.86 | 1.08 |
| KAc | 2.999 | 29.8 | 29.8 | 0.0372 | 2.09 | 1.12 |
| KAc | 2.999 | 39.5 | 39.5 | 0.0637 | 2.20 | 1.10 |
| KAc | 2.999 | 49.3 | 49.1 | 0.1053 | 2.26 | 1.05 |
| KAc | 2.999 | 58.4 | 57.9 | 0.1604 | 2.52 | 1.10 |
| KAc | 2.999 | 70.4 | 69.2 | 0.2694 | 2.60 | 1.06 |
| KAc | 2.999 | 81.5 | 79.5 | 0.4057 | 3.31 | 1.26 |
| KAc | 2.999 | 91.5 | 88.6 | 0.5809 | 3.48 | 1.25 |
| KAc | 4.999 | 10.4 | 10.4 | 0.0097 | 3.90 | 1.47 |
| KAc | 4.999 | 20.1 | 20.1 | 0.0183 | 4.01 | 1.40 |
| KAc | 4.999 | 30.1 | 30.1 | 0.0334 | 4.23 | 1.37 |
| KAc | 4.999 | 39.9 | 39.9 | 0.0575 | 4.47 | 1.35 |
| KAc | 4.999 | 50.1 | 49.9 | 0.0964 | 4.77 | 1.34 |
| KAc | 4.999 | 60.4 | 59.8 | 0.1561 | 5.00 | 1.31 |
| KAc | 4.999 | 70.6 | 69.4 | 0.2375 | 5.61 | 1.38 |
| KAc | 4.999 | 81.1 | 79.1 | 0.3562 | 6.05 | 1.39 |
| KAc | 4.999 | 91.0 | 88.1 | 0.5070 | 6.47 | 1.41 |

Table B.4: The measured saturation pressures, temperatures and concentrations and the calculated BPE and Φ for potassium acetate: Part 2

| **Salt** | $\mathbf{C_{exp}}$ **[mol/kg]** | $\mathbf{T_{exp}}$ **[°C]** | $\mathbf{T_{corr}}$ **[°C]** | $\mathbf{P_{exp}}$ **[bar]** | **BPE [°C]** | **Φ[-]** |
|---|---|---|---|---|---|---|
| KAc | 6.986 | 9.9 | 9.9 | 0.0082 | 5.82 | 1.59 |
| KAc | 6.986 | 19.6 | 19.6 | 0.0156 | 5.98 | 1.51 |
| KAc | 6.986 | 29.8 | 29.8 | 0.0290 | 6.29 | 1.47 |
| KAc | 6.986 | 40.2 | 40.1 | 0.0511 | 6.88 | 1.49 |
| KAc | 6.986 | 50.2 | 50.0 | 0.0857 | 7.14 | 1.44 |
| KAc | 6.986 | 60.5 | 59.9 | 0.1391 | 7.48 | 1.41 |
| KAc | 6.986 | 70.7 | 69.5 | 0.2148 | 7.91 | 1.40 |
| KAc | 6.986 | 80.9 | 79.0 | 0.3186 | 8.47 | 1.41 |
| KAc | 6.986 | 91.8 | 88.8 | 0.4762 | 8.74 | 1.37 |
| KAc | 8.977 | 19.9 | 19.9 | 0.0139 | 8.04 | 1.59 |
| KAc | 8.977 | 29.9 | 29.9 | 0.0253 | 8.67 | 1.59 |
| KAc | 8.977 | 40.3 | 40.2 | 0.0447 | 9.35 | 1.59 |
| KAc | 8.977 | 50.2 | 50.0 | 0.0746 | 9.78 | 1.56 |
| KAc | 8.977 | 60.4 | 59.8 | 0.1212 | 10.18 | 1.51 |
| KAc | 8.977 | 70.9 | 69.7 | 0.1891 | 10.86 | 1.51 |
| KAc | 8.977 | 81.5 | 79.5 | 0.2859 | 11.51 | 1.50 |
| KAc | 8.977 | 91.7 | 88.8 | 0.4106 | 12.27 | 1.51 |

## B.3 Lithium Acetate

Table B.5: The measured saturation pressures, temperatures and concentrations and the calculated BPE and Φ for lithium acetate

| **Salt** | $\mathbf{C_{exp}}$ **[mol/kg]** | $\mathbf{T_{exp}}$ **[°C]** | $\mathbf{T_{corr}}$ **[°C]** | $\mathbf{P_{exp}}$ **[bar]** | **BPE [°C]** | **Φ[-]** |
|---|---|---|---|---|---|---|
| LiAc | 2.004 | 10.2 | 10.8 | 0.0122 | 0.9 | 0.88 |
| LiAc | 2.004 | 20.1 | 20.8 | 0.0228 | 1.2 | 1.04 |
| LiAc | 2.004 | 29.9 | 30.5 | 0.0407 | 1.3 | 1.01 |
| LiAc | 2.004 | 39.9 | 40.3 | 0.0697 | 1.4 | 1.04 |
| LiAc | 2.004 | 50.1 | 50.2 | 0.1152 | 1.6 | 1.08 |
| LiAc | 2.004 | 60.2 | 59.8 | 0.1839 | 1.5 | 0.98 |
| LiAc | 2.004 | 70.7 | 69.6 | 0.2864 | 1.6 | 0.96 |
| LiAc | 2.004 | 81.2 | 79.3 | 0.4320 | 1.6 | 0.91 |
| LiAc | 2.004 | 92.0 | 89.2 | 0.6361 | 1.7 | 0.92 |
| LiAc | 4.066 | 10.3 | 10.9 | 0.0108 | 2.9 | 1.31 |
| LiAc | 4.066 | 20.1 | 20.8 | 0.0202 | 3.2 | 1.34 |
| LiAc | 4.066 | 30.0 | 30.6 | 0.0367 | 3.1 | 1.24 |
| LiAc | 4.066 | 40.0 | 40.4 | 0.0634 | 3.2 | 1.19 |
| LiAc | 4.066 | 50.1 | 50.2 | 0.1054 | 3.3 | 1.14 |
| LiAc | 4.066 | 60.4 | 60.0 | 0.1693 | 3.5 | 1.11 |
| LiAc | 4.066 | 70.7 | 69.6 | 0.2638 | 3.5 | 1.04 |
| LiAc | 4.066 | 81.3 | 79.4 | 0.3978 | 3.7 | 1.04 |
| LiAc | 4.066 | 92.1 | 89.2 | 0.5883 | 3.8 | 1.01 |
| LiAc | 6.050 | 30.0 | 30.6 | 0.0327 | 5.1 | 1.36 |
| LiAc | 6.050 | 40.0 | 40.4 | 0.0568 | 5.3 | 1.31 |
| LiAc | 6.050 | 50.0 | 50.1 | 0.0949 | 5.3 | 1.23 |
| LiAc | 6.050 | 60.2 | 59.8 | 0.1532 | 5.4 | 1.16 |
| LiAc | 6.050 | 70.7 | 69.6 | 0.2400 | 5.6 | 1.13 |
| LiAc | 6.050 | 81.3 | 79.4 | 0.3632 | 5.9 | 1.12 |
| LiAc | 6.050 | 92.1 | 89.2 | 0.5369 | 6.1 | 1.10 |
| LiAc | 8.027 | 40.0 | 40.4 | 0.0521 | 6.8 | 1.28 |
| LiAc | 8.027 | 50.1 | 50.2 | 0.0875 | 6.9 | 1.22 |
| LiAc | 8.027 | 60.3 | 59.9 | 0.1420 | 7.0 | 1.16 |
| LiAc | 8.027 | 70.6 | 69.5 | 0.2224 | 7.2 | 1.10 |
| LiAc | 8.027 | 81.2 | 79.3 | 0.3389 | 7.4 | 1.07 |
| LiAc | 8.027 | 92.0 | 89.2 | 0.5030 | 7.7 | 1.04 |

## B.4 Caesium Acetate

Table B.6: The measured saturation pressures, temperatures and concentrations and the calculated BPE and Φ for caesium acetate

| **Salt** | $\mathbf{C_{exp}}$ **[mol/kg]** | $\mathbf{T_{exp}}$ **[°C]** | $\mathbf{T_{corr}}$ **[°C]** | $\mathbf{P_{exp}}$ **[bar]** | **BPE [°C]** | **Φ[-]** |
|---|---|---|---|---|---|---|
| CsAc | 2.007 | 10.3 | 10.9 | 0.0120 | 1.3 | 1.20 |
| CsAc | 2.007 | 20.2 | 20.9 | 0.0226 | 1.4 | 1.21 |
| CsAc | 2.007 | 30.0 | 30.6 | 0.0402 | 1.6 | 1.26 |
| CsAc | 2.007 | 39.9 | 40.3 | 0.0690 | 1.6 | 1.17 |
| CsAc | 2.007 | 50.0 | 50.1 | 0.1142 | 1.6 | 1.13 |
| CsAc | 2.007 | 60.3 | 59.9 | 0.1824 | 1.8 | 1.16 |
| CsAc | 2.007 | 70.6 | 69.5 | 0.2826 | 1.8 | 1.09 |
| CsAc | 2.007 | 81.2 | 79.3 | 0.4289 | 1.8 | 1.01 |
| CsAc | 2.007 | 92.0 | 89.2 | 0.6268 | 2.1 | 1.12 |
| CsAc | 4.003 | 10.3 | 10.9 | 0.0109 | 2.7 | 1.27 |
| CsAc | 4.003 | 20.1 | 20.8 | 0.0202 | 3.2 | 1.36 |
| CsAc | 4.003 | 30.0 | 30.6 | 0.0362 | 3.4 | 1.36 |
| CsAc | 4.003 | 39.9 | 40.3 | 0.0619 | 3.6 | 1.34 |
| CsAc | 4.003 | 50.0 | 50.1 | 0.1029 | 3.7 | 1.29 |
| CsAc | 4.003 | 60.2 | 59.8 | 0.1644 | 3.9 | 1.27 |
| CsAc | 4.003 | 70.5 | 69.4 | 0.2546 | 4.1 | 1.24 |
| CsAc | 4.003 | 81.1 | 79.2 | 0.3850 | 4.3 | 1.23 |
| CsAc | 4.003 | 91.9 | 89.1 | 0.5664 | 4.6 | 1.24 |
| CsAc | 6.005 | 10.2 | 10.8 | 0.0092 | 5.1 | 1.60 |
| CsAc | 6.005 | 20.2 | 20.9 | 0.0176 | 5.4 | 1.57 |
| CsAc | 6.005 | 30.0 | 30.6 | 0.0314 | 5.8 | 1.56 |
| CsAc | 6.005 | 40.0 | 40.4 | 0.0540 | 6.2 | 1.55 |
| CsAc | 6.005 | 50.1 | 50.2 | 0.0900 | 6.4 | 1.50 |
| CsAc | 6.005 | 60.3 | 59.9 | 0.1446 | 6.7 | 1.46 |
| CsAc | 6.005 | 70.7 | 69.6 | 0.2253 | 7.0 | 1.43 |
| CsAc | 6.005 | 81.4 | 79.5 | 0.3409 | 7.5 | 1.43 |
| CsAc | 6.005 | 92.1 | 89.2 | 0.5069 | 7.6 | 1.37 |
| CsAc | 8.006 | 10.2 | 10.8 | 0.0083 | 6.6 | 1.55 |
| CsAc | 8.006 | 20.1 | 20.8 | 0.0148 | 8.0 | 1.76 |
| CsAc | 8.006 | 30.0 | 30.6 | 0.0270 | 8.3 | 1.69 |
| CsAc | 8.006 | 40.0 | 40.4 | 0.0470 | 8.6 | 1.64 |
| CsAc | 8.006 | 50.0 | 50.1 | 0.0783 | 9.0 | 1.59 |
| CsAc | 8.006 | 60.3 | 59.9 | 0.1261 | 9.5 | 1.57 |
| CsAc | 8.006 | 70.6 | 69.5 | 0.1966 | 9.8 | 1.53 |
| CsAc | 8.006 | 81.2 | 79.3 | 0.2981 | 10.4 | 1.51 |
| CsAc | 8.006 | 91.9 | 89.1 | 0.4375 | 11.0 | 1.51 |

## B.5 Salt mixture: NaCl + LiCl

Table B.7: Experimental results of T and P measurement of an aqueous mixed salts solution of 2.5 mol/kg LiCl + 2.5 mol/kg NaCl. BPE, $a_w$ and $\Phi$ are derived from the T-P measurements

| **Salts** | $\mathbf{T_{exp}}$ **[°C]** | $\mathbf{P_{exp}}$ **[kPa]** | **BPE [°C]** | $\mathbf{a_w}$ **[-]** | $\mathbf{\Phi}$**[-]** |
|---|---|---|---|---|---|
| NaCl + LiCl | 10.3 | 0.99 | 3.48 | 0.79 | 1.63 |
| NaCl + LiCl | 20.0 | 1.86 | 3.65 | 0.80 | 1.59 |
| NaCl + LiCl | 30.1 | 3.38 | 4.02 | 0.79 | 1.62 |
| NaCl + LiCl | 39.9 | 5.75 | 4.51 | 0.78 | 1.70 |
| NaCl + LiCl | 49.8 | 9.59 | 4.81 | 0.78 | 1.69 |
| NaCl + LiCl | 59.7 | 15.46 | 5.10 | 0.79 | 1.67 |
| NaCl + LiCl | 69.5 | 24.12 | 5.34 | 0.79 | 1.63 |
| NaCl + LiCl | 79.5 | 36.55 | 5.80 | 0.79 | 1.66 |
| NaCl + LiCl | 89.3 | 53.96 | 6.07 | 0.79 | 1.64 |

# Appendix C

# Continuing desalination modelling

## Absorption Desalination

During the RED Heat-to-Power Horizon 2020 project meeting in Tilburg in January 2017 it was proposed to use an absorption heat pump to regenerate the concentrated and diluted solutions coming from the RED membrane.
Absorption heat pumps are thermally driven, where the heat input is usually low temperature waste heat, which can come from industrial processes to provide cooling. Absorption heat pumps are also used in small scale applications where propane can be burned to power the refrigeration cycle.

An absorption heat pump has four main components: absorber, generator, condenser and evaporator. The system operates by using a binary solution of refrigerant and absorbent as working fluid, which circulates through the system [194]. It is important that the absorbent has a high affinity to the refrigerant. There are two common fluid pairs in use, which can either be LiBr and water or water and ammonia.
Two pressure levels are maintained throughout the system. The lower pressure is set at the saturation pressure of the absorber and it depends on the temperature of the cooling water and concentrations of the working fluid. The high pressure depends on the cooling water temperature as well and is set at the saturation temperature in the condenser.
The refrigerant evaporates in the evaporator by taking up heat from its environment, which provides cooling. The vapour travels to the absorber driven by the vapour pressure difference in the adsorber [195]. In the absorber, the refrigerant absorbs and therefore needs cooling to remove the heat of absorption. This is necessary to maintain the temperature and pressure level in the absorber. The working fluid is continuously pumped out of the absorber to the generator. The pump increases the pressure from the low pressure level to the higher pressure level. The generator is driven by low

grade heat and the refrigerant is desorbed from the solution. The refrigerant vapour is condensed and flows through an expansion valve back into the evaporator. The absorbent flow is recirculated through another expansion valve back to the absorber. [196]

### The design of the absorption regeneration unit

The proposed design is a simplified version of the absorption cycle as it is shown in figure C.1. It consists of an evaporator, which can be seen as a desorber and a condenser which functions as an absorber. The concentrated fluid from the membrane flows through a preheater and enters the evaporator, where low grade waste heat is applied. A part of the feed evaporates and leaves the evaporator at a higher LiBr concentration. The water vapour is condensed and mixed with the low concentration stream coming from the RED membrane to be further diluted. The simplified design aims to reduce the complexity of the design.

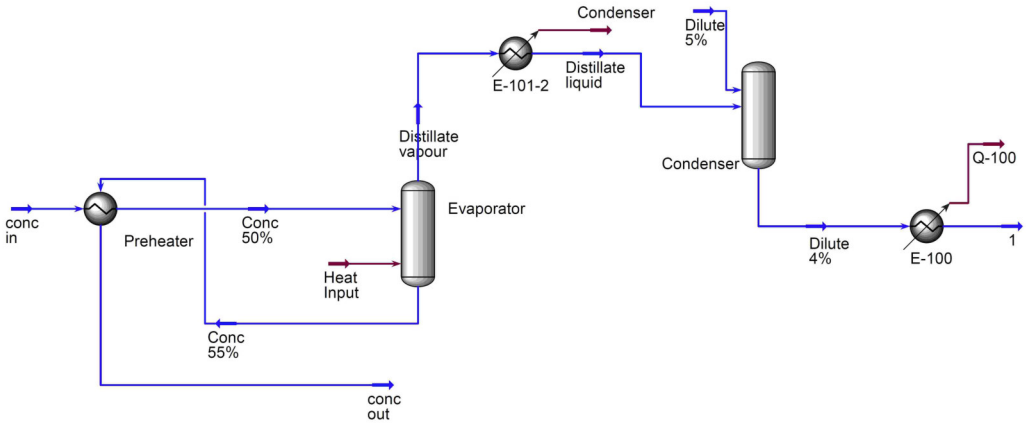


Figure C.1: UniSim model of simplified Absorption regeneration using highly concentrated aqueous LiBr solutions

### OLI thermodynamic properties for LiBr

At first the OLI properties needed to be verified. Therefore, the properties were compared with values given in the literature [21]. The accuracy of the vapour pressures calculated in UniSim by the OLI electrolytes package proved to be very accurate even for very high LiBr concentrations. The results of this investigation are shown in table C.1. Hence, the OLI electrolytes package can be used for an the simulations.

Table C.1: Comparison of vapour liquid equilibria of aqueous LiBr solutions between the literature [21] and data obtained from the OLI electrolytes package. $BPE_{lit}$ is derived from the vapour pressures of [21].

| T [°C] | C [m] | $P_{lit}$ [kPa] | Ref. | $BPE_{lit}$ [°C] | $P_{OLI}$ [kPa] | $BPE_{OLI}$ [°C] | Deviation BPE [%] |
|---|---|---|---|---|---|---|---|
| 20 | 9.4 | 0.87 | [21] | 14.6 | 0.84 | 15.1 | -3.8 |
| 35 | 15.3 | 0.87 | [21] | 29.6 | 0.79 | 30.9 | -4.7 |
| 40 | 17.3 | 0.87 | [21] | 34.6 | 0.75 | 36.5 | -5.7 |
| 70 | 15.3 | 5.62 | [21] | 35.2 | 5.56 | 35.4 | -0.5 |
| 75 | 23.4 | 2.34 | [21] | 54.9 | 2.07 | 56.9 | -3.5 |
| 100 | 18.8 | 12.3 | [21] | 50.4 | 13.07 | 49.1 | 2.4 |
| 105 | 24.5 | 7.38 | [21] | 65.3 | 7.40 | 65.2 | 0.1 |

### Modelling results

Nine input scenarios were simulated in which the concentrations of the concentrate mass flow remained at a constant molality of 15 mol/kg. All input and output streams had a constant temperature of 25 °C. The mass flows of the two streams at low and high concentrations coming from the membrane were set to 10 kg/h. The result of the investigation is shown in table C.2.

Table C.2: Results table for the performance investigation of the absorption regeneration. The result is shown in kWh per cubic meter of distillate as the specific thermal consumption.

| # | $C_{Conc.In}$ [m] | $C_{Dil.in}$ [m] | $\dot{M}_{Dist.}$ [kg/h] | $C_{Dil.out}$ [m] | $\varrho_{Conc.In}$ [kg/m$^3$] | Heat [kW] | **STC** [kWh/m$^3$] |
|---|---|---|---|---|---|---|---|
| 1 | 8 | 1 | 2.75 | 0.77 | 1400 | 1.78 | **643** |
| 2 | 8 | 4 | 2.75 | 2.92 | 1400 | 1.78 | **643** |
| 3 | 8 | 7 | 2.75 | 4.85 | 1400 | 1.78 | **643** |
| 4 | 11 | 1 | 1.36 | 0.87 | 1515 | 1.12 | **816** |
| 5 | 11 | 4 | 1.36 | 3.38 | 1515 | 1.12 | **816** |
| 6 | 11 | 7 | 1.36 | 5.74 | 1515 | 1.12 | **816** |
| 7 | 14 | 1 | 0.30 | 0.97 | 1614 | 0.34 | **1113** |
| 8 | 14 | 4 | 0.30 | 3.84 | 1614 | 0.34 | **1113** |
| 9 | 14 | 7 | 0.30 | 6.67 | 1614 | 0.34 | **1113** |

The absorption regeneration system has a relatively high energy consumption between 600 and 1100 kWh/m$^3$ depending on the input scenario.

## Three stage MED modelling results

Table C.3: Results for the 3 effects MED system shown in Fig. 4.7 from UniSim

| **Name** | **Seaw.** | **Brine** | **Dist.** | **1** | **2** | **3** | **4** | **5** | **6** |
|---|---|---|---|---|---|---|---|---|---|
| **Vapour fraction** | 0.00 | 0.00 | 0.00 | 0.00 | 0.04 | 1.00 | 0.00 | 1.00 | 0.00 |
| **Temperature [°C]** | 25.00 | 43.27 | 42.85 | 79.00 | 86.47 | 86.47 | 86.47 | 62.57 | 62.57 |
| **Pressure [kPa]** | 60.00 | 8.60 | 8.60 | 60.00 | 60.00 | 60.00 | 60.00 | 22.00 | 22.00 |
| **Mass flow [kg/h]** | 10.00 | 8.65 | 1.35 | 10.00 | 10.00 | 0.43 | 9.57 | 0.39 | 9.18 |
| **Mole fraction water** | 0.99 | 0.99 | 1.00 | 0.99 | 0.99 | 1.00 | 0.99 | 1.00 | 0.99 |
| **Mole fraction NaCl** | 0.01 | 0.01 | 0.00 | 0.01 | 0.01 | 0.00 | 0.01 | 0.00 | 0.01 |
| | **7** | **8** | **9** | **10** | **11** | **12** | **13** | **14** | **15** |
| **Vapour fraction** | 0.00 | 0.23 | 0.00 | 1.00 | 0.00 | 0.01 | 1.00 | 0.17 | 1.00 |
| **Temperature [°C]** | 60.00 | 85.98 | 40.00 | 62.58 | 62.58 | 62.58 | 62.72 | 42.85 | 62.12 |
| **Pressure [kPa]** | 60.00 | 60.00 | 60.00 | 22.00 | 22.00 | 22.00 | 22.00 | 8.60 | 22.00 |
| **Mass flow [kg/h]** | 10.00 | 0.43 | 10.00 | 0.09 | 9.08 | 9.18 | 0.49 | 1.35 | 0.15 |
| **Mole fraction water** | 0.99 | 1.00 | 0.99 | 1.00 | 0.99 | 0.99 | 1.00 | 1.00 | 1.00 |
| **Mole fraction NaCl** | 0.01 | 0.00 | 0.01 | 0.00 | 0.01 | 0.01 | 0.00 | 0.00 | 0.00 |
| | **16** | **17** | **18** | **19** | **20** | **21** | **22** | **23** | **24** |
| **Vapour fraction** | 1.00 | 0.00 | 0.00 | 0.02 | 1.00 | 1.00 | 0.46 | 0.00 | 1.00 |
| **Temperature [°C]** | 43.26 | 43.26 | 62.12 | 43.27 | 43.27 | 43.92 | 42.85 | 85.98 | 80.85 |
| **Pressure [kPa]** | 8.60 | 8.60 | 22.00 | 8.60 | 8.60 | 8.60 | 8.60 | 60.00 | 49.00 |
| **Mass flow [kg/h]** | 0.29 | 8.79 | 0.15 | 8.79 | 0.15 | 0.46 | 0.46 | 0.10 | 0.00 |
| **Mole fraction water** | 1.00 | 0.99 | 1.00 | 0.99 | 1.00 | 1.00 | 1.00 | 1.00 | 1.00 |
| **Mole fraction NaCl** | 0.00 | 0.01 | 0.00 | 0.01 | 0.00 | 0.00 | 0.00 | 0.00 | 0.00 |
| | **25** | **26** | **27** | **28** | **29** | **30** | **31** | **32** | **33** |
| **Vapour fraction** | 0.00 | 0.02 | 1.00 | 0.00 | 0.30 | 0.00 | 1.00 | 0.00 | 0.00 |
| **Temperature [°C]** | 80.85 | 62.12 | 57.78 | 57.78 | 62.12 | 62.12 | 85.98 | 85.98 | 85.98 |
| **Pressure [kPa]** | 49.00 | 22.00 | 18.00 | 18.00 | 22.00 | 22.00 | 60.00 | 60.00 | 60.00 |
| **Mass flow [kg/h]** | 0.43 | 0.92 | 0.02 | 0.89 | 0.49 | 0.34 | 0.10 | 0.33 | 0.43 |
| **Mole fraction water** | 1.00 | 1.00 | 1.00 | 1.00 | 1.00 | 1.00 | 1.00 | 1.00 | 1.00 |
| **Mole fraction NaCl** | 0.00 | 0.00 | 0.00 | 0.00 | 0.00 | 0.00 | 0.00 | 0.00 | 0.00 |
| | **Steam** | | | | | | | | |
| **Heat flow [kJ/h]** | 1290 | | | | | | | | |

## Multi effect distillation with adsorption results

Table C.4: STC comparison between MED and MEDAD for different concentrations of NaCl, Recovery ratios, numbers of effects.

| | | | **MED** | | | **MEDAD** | | |
|---|---|---|---|---|---|---|---|---|
| **#** | **$C_f$** [mol/kg] | **$T_s$** [°C] | **RR** [-] | **N** [-] | **STC** [kWh/m$^3$] | **RR** [-] | **N** [-] | **STC** [kWh/m$^3$] |
| 1 | 0.5 | 60 | 0.1 | 5 | 220 | 0.4 | 11 | 185 |
| 2 | 0.5 | 60 | 0.3 | 5 | 167 | 0.8 | 11 | 153 |
| 3 | 0.5 | 70 | 0.1 | 7 | 193 | 0.3 | 13 | 184 |
| 4 | 0.5 | 70 | 0.3 | 7 | 134 | 0.6 | 13 | 144 |
| 5 | 0.5 | 70 | 0.5 | 7 | 122 | 1.0 | 13 | 130 |
| 6 | 0.5 | 80 | 0.1 | 9 | 180 | 0.3 | 15 | 185 |
| 7 | 0.5 | 80 | 0.3 | 9 | 117 | 0.6 | 15 | 138 |
| 8 | 0.5 | 80 | 0.5 | 9 | 106 | 0.8 | 15 | 123 |
| 9 | 0.5 | 90 | 0.3 | 11 | 109 | 0.5 | 17 | 136 |
| 10 | 0.5 | 90 | 0.5 | 11 | 95 | 0.8 | 17 | 117 |
| 11 | 0.5 | 90 | 0.7 | 11 | 90 | 1.0 | 17 | 107 |
| 12 | 0.5 | 100 | 0.3 | 13 | 103 | 0.5 | 19 | 134 |
| 13 | 0.5 | 100 | 0.5 | 13 | 90 | 0.7 | 19 | 113 |
| 14 | 0.5 | 100 | 0.7 | 13 | 85 | 0.9 | 19 | 102 |
| 15 | 1 | 60 | 0.1 | 5 | 217 | 0.4 | 11 | 184 |
| 16 | 1 | 60 | 0.3 | 5 | 163 | 0.8 | 11 | 152 |
| 17 | 1 | 70 | 0.1 | 7 | 193 | 0.3 | 13 | 184 |
| 18 | 1 | 70 | 0.3 | 7 | 132 | 0.7 | 13 | 143 |
| 19 | 1 | 70 | 0.5 | 7 | 120 | 1.0 | 13 | 130 |
| 20 | 1 | 80 | 0.1 | 9 | 177 | 0.3 | 15 | 184 |
| 21 | 1 | 80 | 0.3 | 9 | 116 | 0.6 | 15 | 138 |
| 22 | 1 | 80 | 0.5 | 9 | 104 | 0.8 | 15 | 122 |
| 23 | 1 | 90 | 0.3 | 11 | 108 | 0.5 | 17 | 136 |
| 24 | 1 | 90 | 0.5 | 11 | 95 | 0.7 | 17 | 117 |
| 25 | 1 | 90 | 0.7 | 11 | 89 | 1.0 | 17 | 107 |
| 26 | 1 | 100 | 0.3 | 13 | 103 | 0.5 | 19 | 135 |
| 27 | 1 | 100 | 0.5 | 13 | 90 | 0.7 | 19 | 113 |
| 28 | 1 | 100 | 0.7 | 13 | 84 | 0.9 | 19 | 102 |

Table C.5: Continuation of table C.4

| | | | MED | | | MEDAD | | |
|---|---|---|---|---|---|---|---|---|
| # | $C_f$ [mol/kg] | $T_s$ [°C] | RR [-] | N [-] | STC [kWh/m$^3$] | RR [-] | N [-] | STC [kWh/m$^3$] |
| 29 | 1.5 | 60 | 0.1 | 5 | 215 | 0.4 | 11 | 183 |
| 30 | 1.5 | 60 | 0.3 | 5 | 161 | 0.8 | 11 | 151 |
| 31 | 1.5 | 70 | 0.1 | 7 | 192 | 0.3 | 13 | 185 |
| 32 | 1.5 | 70 | 0.3 | 7 | 131 | 0.7 | 13 | 144 |
| 33 | 1.5 | 70 | 0.5 | 7 | 118 | 1.0 | 13 | 129 |
| 34 | 1.5 | 80 | 0.1 | 9 | 177 | 0.3 | 15 | 185 |
| 35 | 1.5 | 80 | 0.3 | 9 | 116 | 0.6 | 15 | 139 |
| 36 | 1.5 | 80 | 0.5 | 9 | 102 | 0.8 | 15 | 121 |
| 37 | 1.5 | 90 | 0.3 | 11 | 106 | 0.5 | 17 | 136 |
| 38 | 1.5 | 90 | 0.5 | 11 | 93 | 0.7 | 17 | 117 |
| 39 | 1.5 | 90 | 0.7 | 11 | 88 | 1.0 | 17 | 118 |
| 40 | 1.5 | 100 | 0.3 | 13 | 102 | 0.5 | 19 | 135 |
| 41 | 1.5 | 100 | 0.5 | 13 | 89 | 0.7 | 19 | 113 |
| 42 | 1.5 | 100 | 0.7 | 13 | 84 | 0.9 | 19 | 102 |
| 43 | 2.5 | 60 | 0.1 | 5 | 214 | 0.4 | 11 | 184 |
| 44 | 2.5 | 60 | 0.3 | 5 | 154 | 0.8 | 11 | 149 |
| 45 | 2.5 | 70 | 0.1 | 7 | 191 | 0.4 | 13 | 185 |
| 46 | 2.5 | 70 | 0.3 | 7 | 127 | 0.7 | 13 | 143 |
| 47 | 2.5 | 70 | 0.5 | 7 | 114 | 1.0 | 13 | 128 |
| 48 | 2.5 | 80 | 0.3 | 9 | 112 | 0.6 | 15 | 139 |
| 49 | 2.5 | 80 | 0.5 | 9 | 99 | 0.9 | 15 | 122 |
| 50 | 2.5 | 90 | 0.3 | 11 | 105 | 0.5 | 17 | 138 |
| 51 | 2.5 | 90 | 0.5 | 11 | 91 | 0.8 | 17 | 118 |
| 52 | 2.5 | 100 | 0.3 | 13 | 102 | 0.5 | 19 | 138 |
| 53 | 2.5 | 100 | 0.5 | 13 | 88 | 0.7 | 19 | 115 |
| 54 | 3.5 | 60 | 0.1 | 5 | 208 | 0.4 | 11 | 183 |
| 55 | 3.5 | 60 | 0.3 | 5 | 148 | 0.8 | 11 | 150 |
| 56 | 3.5 | 70 | 0.1 | 7 | 192 | 0.4 | 13 | 187 |
| 57 | 3.5 | 70 | 0.3 | 7 | 122 | 0.7 | 13 | 143 |
| 58 | 3.5 | 80 | 0.3 | 9 | 111 | 0.6 | 15 | 141 |
| 59 | 3.5 | 90 | 0.3 | 11 | 105 | 0.5 | 17 | 141 |

# Appendix D

# Additional information on the adsorption test rig

## D.1 Two dimensional drawings of the test rig

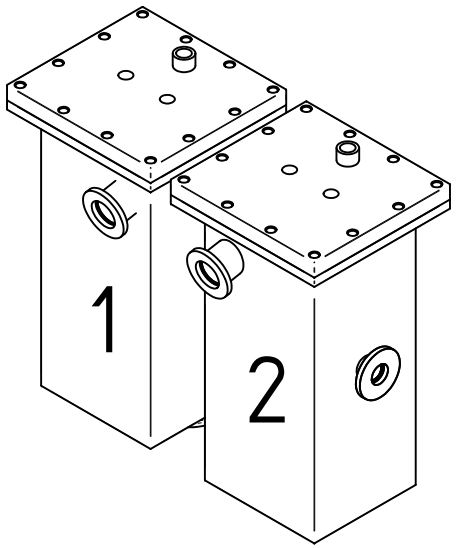


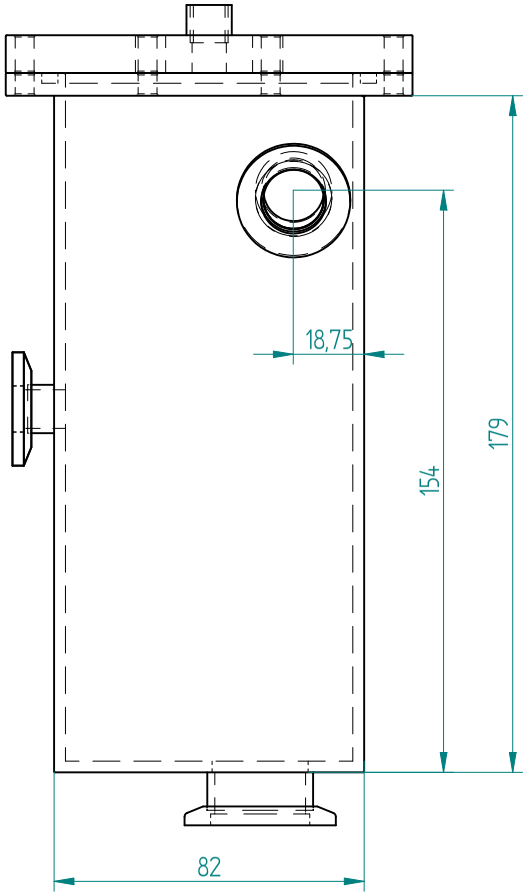


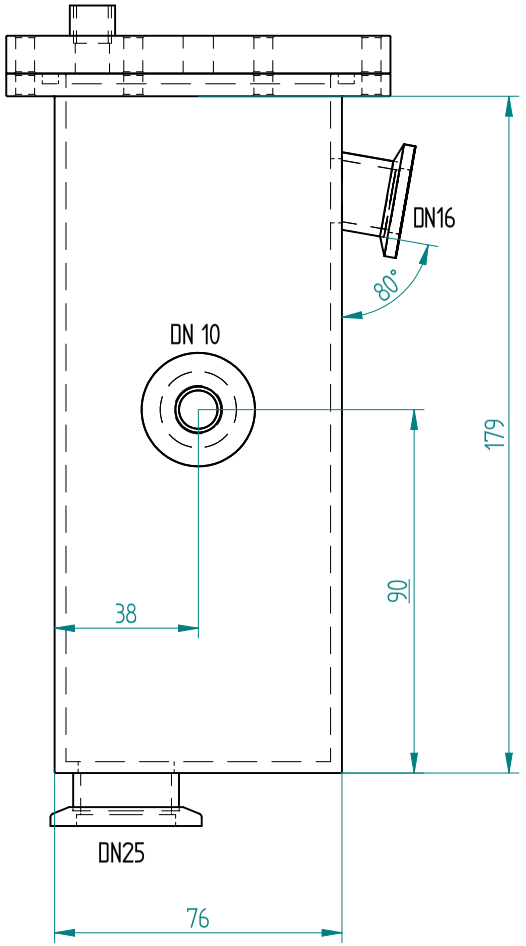


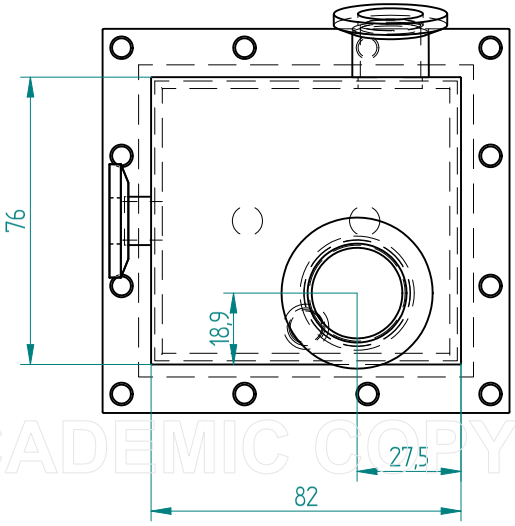




| | NAME | DATE |
|---|---|---|
| DRAWN | C Olkis | 19/05/2016 |
| CHECKED | | |
| ENG APPR | | |
| MGR APPR | | |

UNLESS OTHERWISE SPECIFIED
DIMENSIONS ARE IN MILLIMETERS
ANGLES ±X.X°
2 PL ±X.XX 3 PL ±X.XXX

University of Edinburgh

TITLE: Adsorber 1

SIZE A2 | DWG NO | REV

FILE NAME: Assembly Adsorber no1.dft

SCALE: | WEIGHT: | SHEET 1 OF 1

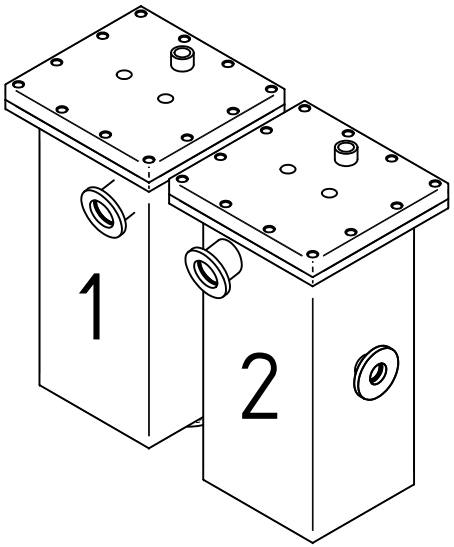


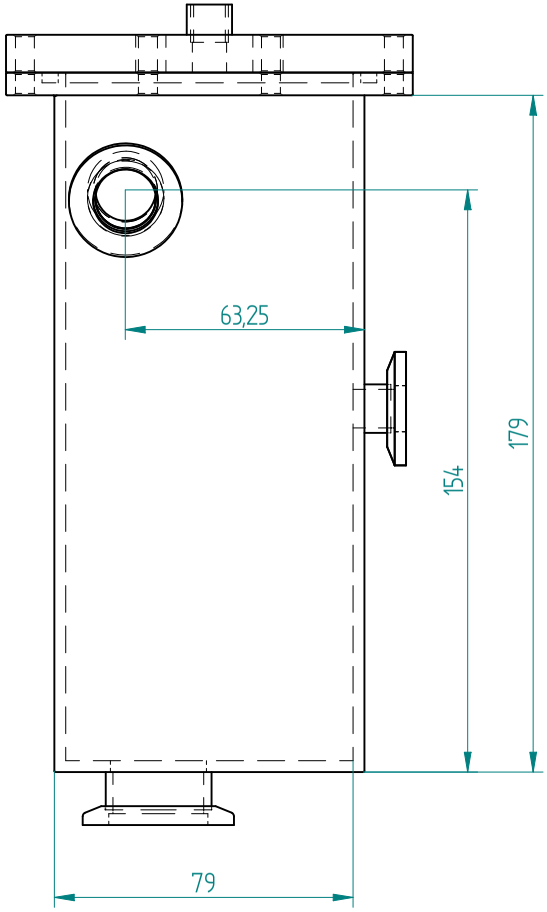


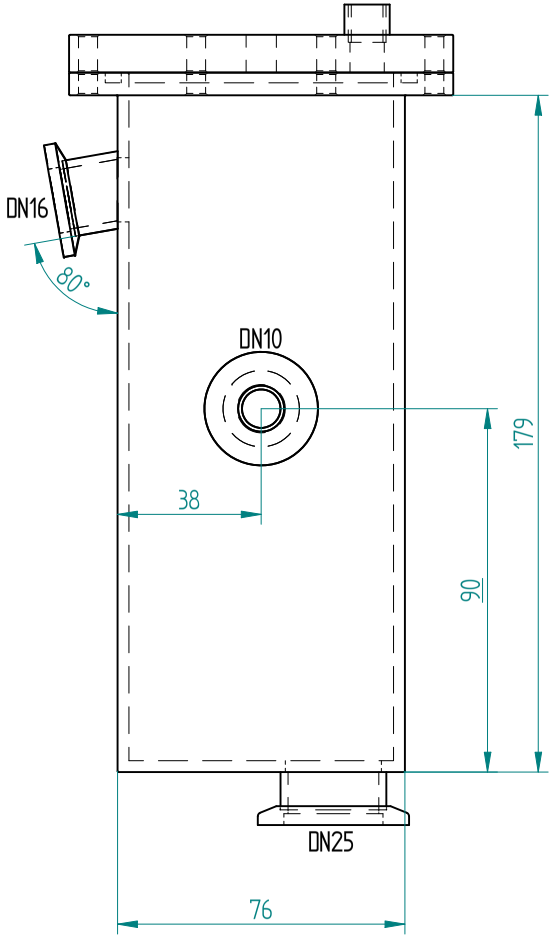


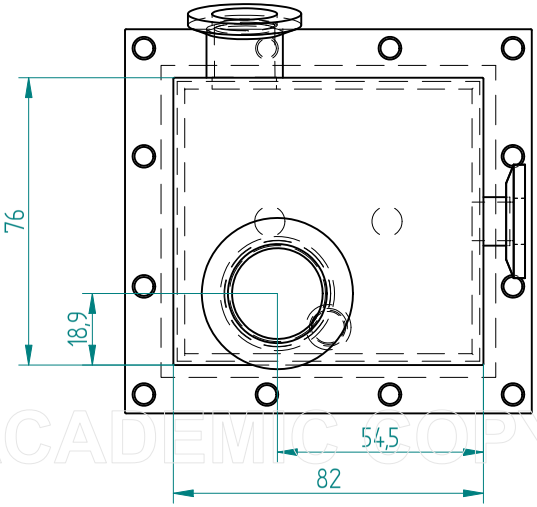




| | NAME | DATE |
|---|---|---|
| DRAWN | C Olkis | 19/05/2016 |
| CHECKED | | |
| ENG APPR | | |
| MGR APPR | | |

UNLESS OTHERWISE SPECIFIED
DIMENSIONS ARE IN MILLIMETERS
ANGLES ±X.X°
2 PL ±X.XX 3 PL ±X.XXX

University of Edinburgh

TITLE: Adsorber 2

SIZE A2 | DWG NO | REV

FILE NAME: Assembly Adsorber no2.dft

SCALE: | WEIGHT: | SHEET 1 OF 1

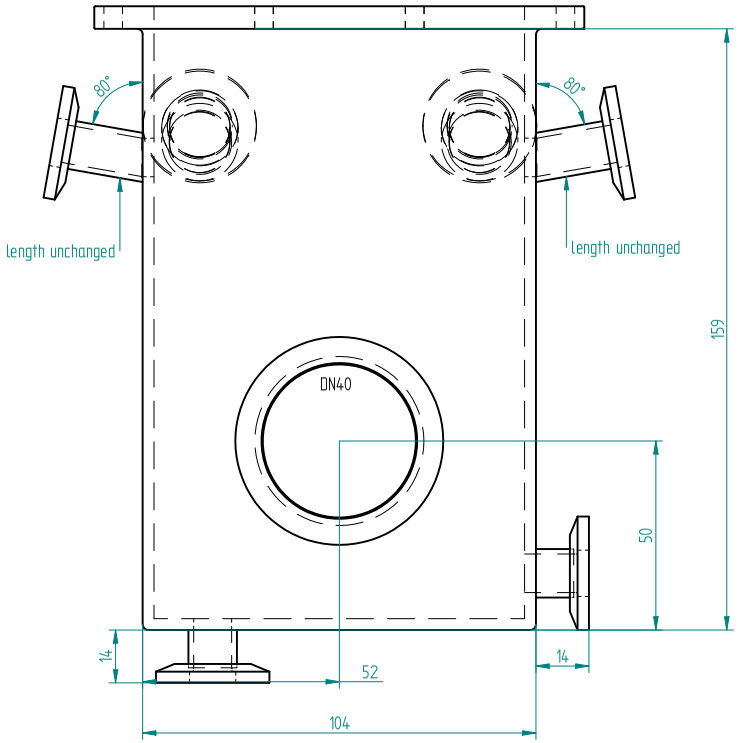


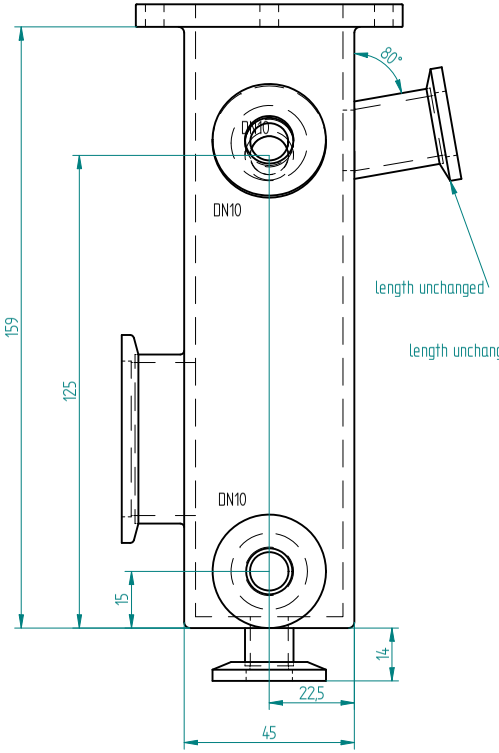


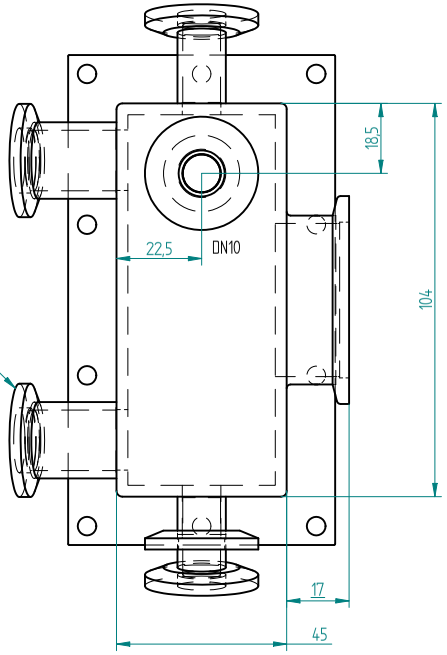


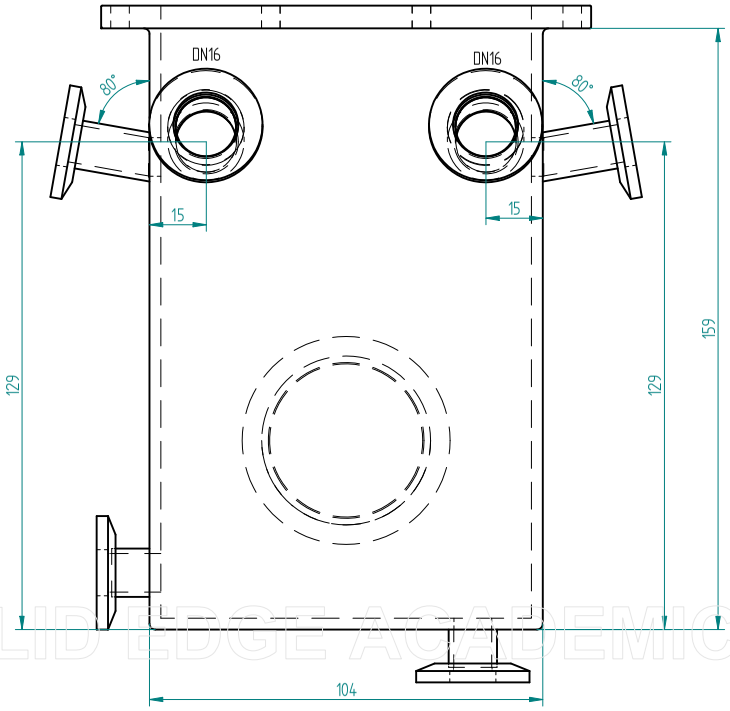


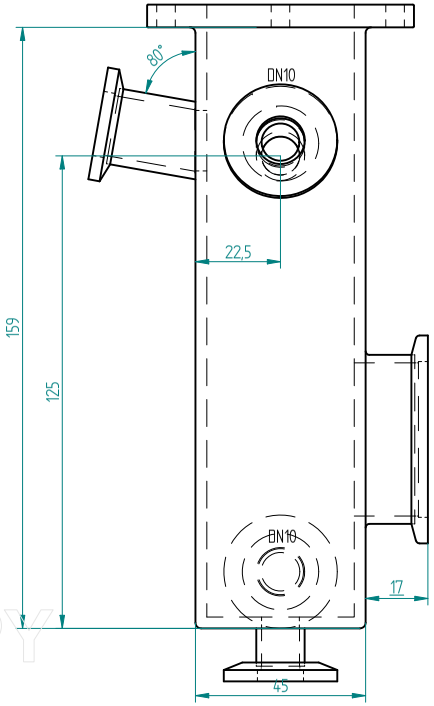


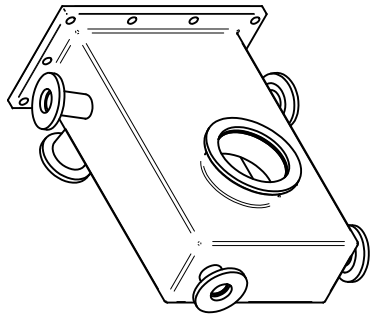

| | NAME | DATE |
|---|---|---|
| DRAWN | CJ Olkis | 17/05/2016 |
| CHECKED | | |
| ENG APPR | | |
| MGR APPR | | |

UNLESS OTHERWISE SPECIFIED
DIMENSIONS ARE IN MILLIMETERS
ANGLES ±X.X°
2 PL ±X.XX 3 PL ±X.XXX

University of Edinburgh

TITLE: Condenser

SIZE A2 | DWG NO | REV

FILE NAME: Draft Condenser.dft

SCALE: | WEIGHT: | SHEET 1 OF 1

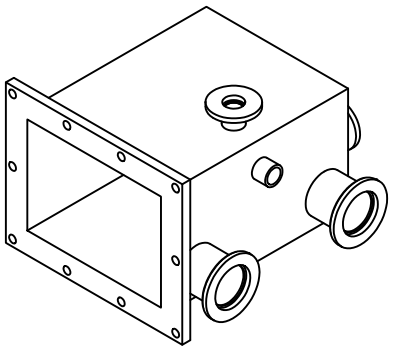

| | NAME | DATE |
|---|---|---|
| DRAWN | CJ Okkis | 17/05/2016 |
| CHECKED | | |
| ENG APPR | | |
| MGR APPR | | |

UNLESS OTHERWISE SPECIFIED
DIMENSIONS ARE IN MILLIMETERS
ANGLES ±X.X°
2 PL ±X.XX 3 PL ±X.XXX

University of Edinburgh

TITLE: Evaporator

SIZE: A2 | DWG NO | REV

FILE NAME: Draft Evaporatordft

SCALE: | WEIGHT: | SHEET 1 OF 1

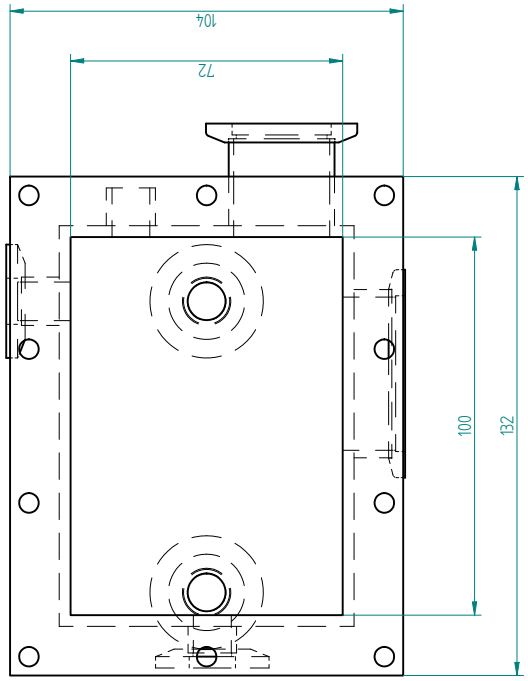


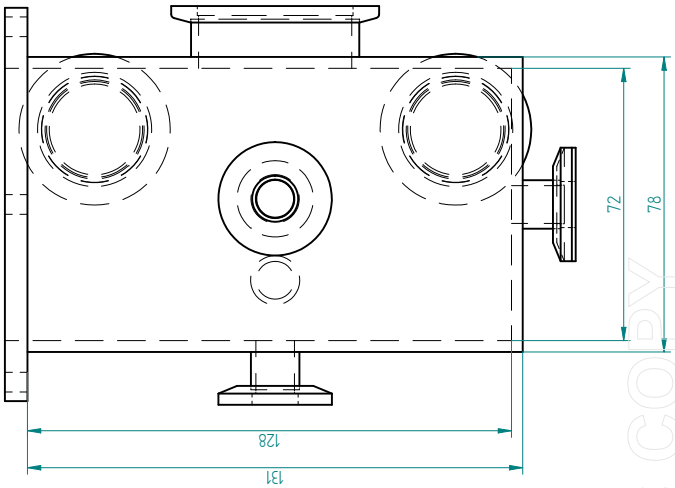


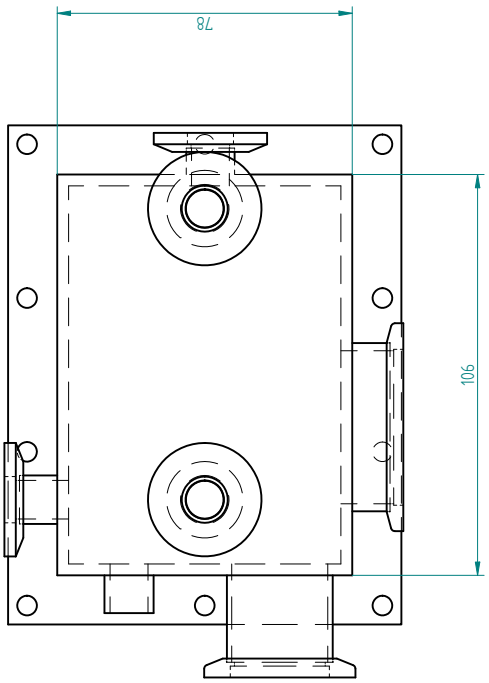


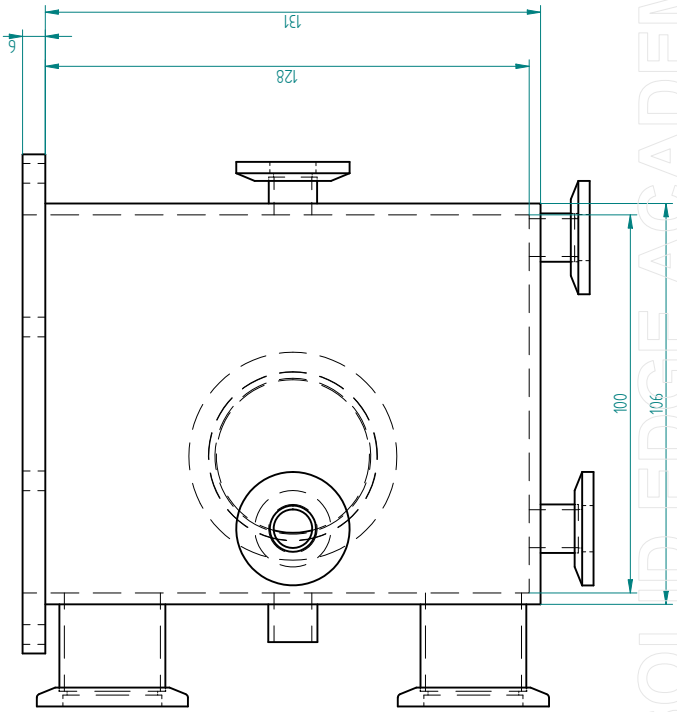

## D.2 Vacuum leak tests

## Background

The leak rate is defined as:

$$Q_L = \frac{\Delta p \cdot V}{\Delta t} \tag{D.1}$$

Where $Q_L$ is defined as the leak rate in [Pa $m^3$ $s^{-1}$], $\Delta$p represents the pressure change [Pa] of the Volume V [$m^3$] in the time period [s]. [197]

## Procedure of the leak tests

The first vacuum test revealed a very large leak rate for all vessels. All vessels returned to ambient pressure within one minute. The leak test revealed a leak rate of $1\text{-}2 \cdot 10^0$ Pa $m^3$ $s^{-1}$ for all four vessels. The next step aimed at localizing the leaks. For this a helium leak test was performed at the Scottish Microelectronics Centre (SMC). The helium leak test indicated large leaks around the main flanges of the vessels, but the leak rate was too high to localize them precisely.

### Sealing the evaporator

It was decided to focus all efforts on the evaporator in order to seal it first. The experiences gained from the evaporator would help sealing the other three vessels. The evaporator was equipped with an aluminium plate to replace the PEEK lid until the leaks on the main part of the vessel were fixed. This measure had to be taken to rule out leaks coming from the heat exchanger and the Giacomini brass compression fittings.

A simple test in a water bucket turned out to be the solution to localise the leaks. The evaporator was pressurized with compressed air to a pressure of 2-3 bar absolute pressure and submerged into the bucket, which was filled with water. The photograph in figure D.1 shows the bubbles formed around the edges below the flange of the evaporator.

Figure D.1: The bubble test of the pressurized evaporator revealed the location of the leaks

It was found that the vacuum tightness was compromised by the way the stainless steel sheets were welded together. All welds are on the outside except for the weld connecting the top flange to the main vessel. Hence, the air could travel through the gap and around the welds. The issue was solved by drilling a hole in every corner and connecting the outside welds with the inside welds by filling them with welding material to ensure vacuum tightness. Apart from that the O-rings were replaced with new ones, which have a larger cross section of 4 mm instead of 2.5 mm. Further tests were undertaken with and without lubrication of the O-rings with vacuum grease (DOW CORNING high vacuum grease), which can reduce the leak rate depending on the compression of the O-ring [198]. It was found that the vacuum grease reduced the leak rate by a factor of two.

**Sealing the vessels and heat exchangers of the adsorbers and the condenser**

All vessels, but the evaporator have the pressure transducer on the PEEK plate. The pressure transducer should not be fully submerged into the water bath, which is why a new aluminium lid was machined for each vessel to perform the bubble leak test. As expected the vessels were leaking around the flange of the lid as the evaporator did, because they were welded in the same way. Moreover, more leaks were found around the welds of the Pfeiffer ISO-KF flanges of the two adsorbers. Consequently, the welds were fixed in the workshop.

Afterwards attention was paid to the heat exchangers on the PEEK plates. All four were pressurised with compressed air and submerged in the bubble bath. It was found that the heat exchangers of evaporator and condenser were leaking from the inside. The heat exchangers were manufactured externally by RC Racing in Italy. The workshop fixed the leaking welds, which were identified by the bubble bath test. For this purpose aluminium weld points were put onto the leaking spots. This was challenging because the PEEK plates could not be detached from the heat exchangers any more. Later it was found that a small leak on the top heat exchanger of the condenser was missed. It

would have been impossible to repair this small leak by welding due to its closeness to the PEEK plate. The heat of the welding might have damaged the PEEK material.

The PEEK plates were mounted onto their vessels and another leak test was performed in the bubble bath. The adsorbers and the evaporator passed the test. However, it could be seen that bubbles were forming around the thread of the Giacomini brass fitting of the condenser.

Figure D.2: The leaking area on the condenser heat exchanger between the PEEK plate before resin was applied to the surface

Torr Seal does not bond well with certain plastic materials according to the data sheet and it is possible that Torr Seal does not adhere sufficiently on the smooth surface of the PEEK plate to ensure vacuum tightness. Though Torr Seal is a very strong material and it can only be removed by brute force, but not by a solvent. In addition to Torr Seal, another resin was identified as a commonly used vacuum sealant.
Vacseal (Vacseal Inc, USA) is a silicone resin, which can be used for permanent repairs of vacuum leaks as well, albeit its mechanical resistance is much lower. Vacseal is a single component resin with a low viscosity and can be applied to the surface with a simple brush. Vacseal silicone resin was applied on top of the Torr Seal layer since Torr Seal cannot be removed from surfaces. The leaking area was coated in Vacseal. This process included several steps due to the low viscosity the resin could only be spread on an even surface. Vacseal was applied to one side of the area and after a few hours the heat exchanger could be turned so Vacseal could be put onto the next part of the area. This was repeated until the leaking area was entirely coated with Vacseal. The following leak test showed that the coating of the area was successful and all vessel were at a sufficiently low leak rate around $1 \cdot 10^{-6}$ Pa $m^3$ $s^{-1}$.

## D.3 Characterisation of the system without adsorption material

Several tests at different temperatures were performed with the system before the heat exchangers were filled with adsorption material. The aim of the experiments was to determine the peak heating and cooling input and the thermal losses. The heat input was assessed through the thermocouples at the inlet and outlet pipes to the heat exchangers of the two adsorbers. The measurements were performed at hot water temperatures of 60 °C, 70 °C, 80 °C and 90 °C and a constant ambient water temperature of 25 °C for cooling. The time for each step of the cycle was set to 1000 s to ensure steady state was reached. The result of the 90 °C measurement can be seen in Fig. D.3.

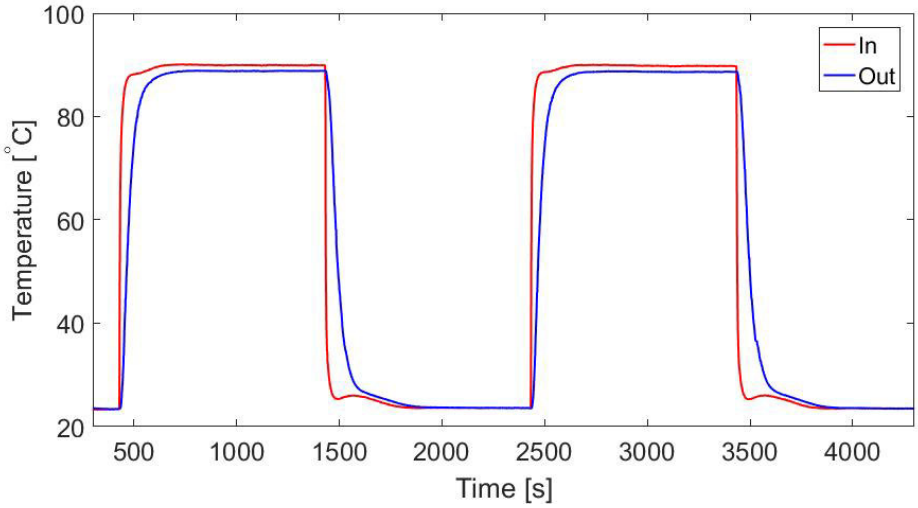


Figure D.3: Temperature curve measured at the inlet and outlet pipe of the empty adsorber heat exchanger

In the beginning of each heating and cooling period, a large $\Delta$T can be observed which is probably caused by the low flow rate of 0.3 L/min, which results in a relatively long residents time of the water inside the exchanger. Right before the target temperature is reached a kink can be seen in the curve. Apparently, the hot/cold water has gone through the cold/hot heat exchanger for the first time and reaches the water bath with a temperature changed by the large $\Delta$T. Hence the water bath has to start heating/cooling, which happens with a time delay and the cooling power of the water baths at 0.3 kW is below the cooling energy uptake of the heat exchanger. This can be seen in Fig. D.3, where the inlet temperature goes up by a few degrees during the cooling process.

Fig. D.4 shows the heating and cooling input into the system at four different temperatures. The energy input for heating and cooling is very similar and between 600 and 1100 W depending on the target temperature of the heat exchanger.

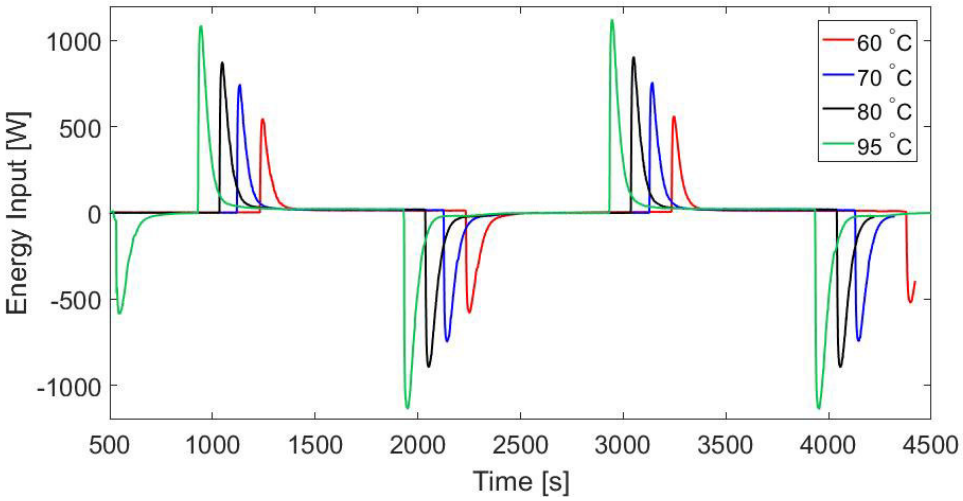


Figure D.4: Heat input into the system at 60 °C, 70 °C, 80 °C and 95 °C

Fig. D.5 presents the same plot as Fig. D.4, but focuses on the energy input at steady state conditions in detail. From this plot, the heat losses of the system without any kind of insulation can be estimated. The heat losses to the environment can be up to 25 W for a hot bath temperature of 95 °C.

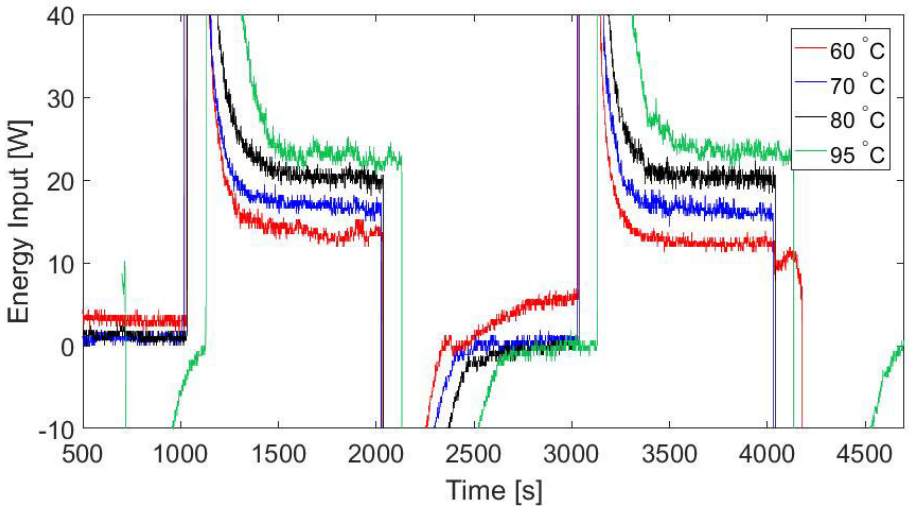


Figure D.5: Enlargement of figure D.4 to assess the heat losses when the system has reached steady state conditions at 60 °C, 70 °C, 80 °C and 95 °C

## D.4 Experimental results part III: copper heat exchangers and silica gel

### Heat exchanger material

The thermal diffusivity is an important parameter for the material selection. A high thermal diffusivity indicates a fast heat movement through the material. The thermal diffusivity [$m^2/s$] can be determined by the fraction of the thermal conductivity k [W/(m·K)], the density ρ [$kg/m^3$] and the specific heat capacity $c_p$ [J/(kg·K)] [21]:

$$\alpha = \frac{k}{\rho \cdot c_p} \tag{D.2}$$

Aluminium, copper and graphite were identified as potential heat exchanger materials as shown in Fig. D.1. Graphite has the highest thermal diffusivity due to its low density. Graphite is a novel material in heat exchanger applications, which is why it needs to be considered for the design [199]. No work has been done using graphite heat exchangers in adsorption desalination and refrigeration. Graphite can be used in chemically challenging environments like strong acids, but it can cause galvanic corrosion to metal components due to its high galvanic potential [200].
Copper has the highest thermal conductivity and specific heat capacity are best for copper. A low specific heat capacity is beneficial for a high performance ratio, because less energy is dissipated for heating and cooling the mass of the heat exchanger.
Aluminium is an inexpensive material with good thermal properties as it can be seen in table D.1. In comparison to other metals, aluminium has a very low density, a high thermal conductivity and an average specific heat capacity. The thermal conductivity of aluminium is even slightly better than graphite. Although aluminium is prone to galvanic corrosion as it is only noble to magnesium in the galvanic series [200], which is why care has to be taken when designing the system.
Aluminium and copper were chosen to be tested as heat exchanger materials material for the first two sets of heat exchangers. Aluminium represents a benchmark material as all other adsorption systems in the literature use it, which establishes a good basis for comparison. In addition, copper was chosen due to its low specific heat capacity to improve the performance ratio.

Table D.1: Thermal properties of copper, alumnium and graphite [21, 39].

| | | **Aluminium** [39] | **Copper** [39] | **Graphite** [21] |
|---|---|---|---|---|
| k | W/(mK) | 236 | 401 | 100 |
| ρ | $kg/m^3$ | 2700 | 8960 | 500 |
| $c_p$ | J(kgK) | 840 | 381 | 700 |
| α | $m^2/s$ | $1.04 \cdot 10^{-4}$ | $1.17 \cdot 10^{-4}$ | $2.85 \cdot 10^{-4}$ |

The copper heat exchangers were designed to achieve a higher performance than the

aluminium heat exchangers because of:

- Open design: all 4 sides of the heat exchangers are open, which should reduce mass transfer limitations.
- Weight: each copper heat exchanger weighs 500 g, which is 100 g less than the aluminium. Moreover, they can hold 250 g of silica gel that is an increase of 50 g compared to the aluminium heat exchangers. Thus, the weight ratio is improved from 3:1 to 2:1.
- Compact design: more space between the vessel walls and the heat exchanger designed to allow an improved water vapour flow.
- Sensible heat: copper has a $c_{p,Cu} = 381$ J/(kgK), whereas $c_{p,Al} = 840$ J/(kgK). Thus, it takes 55 % less energy to heat up copper.
- Thermal conductivity of copper is 40 % higher than aluminium improving heat transfer within the heat exchanger. However, the true heat transfer limitation is between the copper and the silica gel beads. Thus, heat transfer was not expected to be improved significantly.

Therefore, the heat exchangers were expected to increase the PR, because of the open, compact design and the advantageous thermal properties of copper. The design stage of the copper heat exchangers was before the implementation of the basic heat recovery. However, the heat recovery improved the PR of the aluminium heat exchangers from 0.4 to 0.6, while the SEC analysis showed that PR = 0.8 is the threshold, when the metal mass of the heat exchangers is neglected and no advanced heat integration (see section 6.3.2) is powering a part of desorption. Thus, the copper heat exchangers were expected to lead to a significant improvement compared to aluminium without heat recovery. With the heat recovery in place the copper heat exchangers were expected to achieve a $0.6 < PR < 0.8$.

### Upgrading the system

First tests of the copper heat exchangers revealed a high vacuum leak rate. It was found that epoxy resin (Torr seal, Kurt J. Lesker, UK) cannot be used with temperature swings as the expansion of the heat exchanger during heating breaks the resin and causes new vacuum leakage. The leaks on the copper heat exchangers were identified by leak test in a water bath similar to appendix D.2. Several leaks were found and repaired using additional soldering material.
Fig. D.6 shows the result of the final leak test, which included temperature swings. The pressure stabilised after a first increase and remained constant over a period of 3 h. Based on this result the adsorber was packed with silica gel to proceed with the performance analysis.

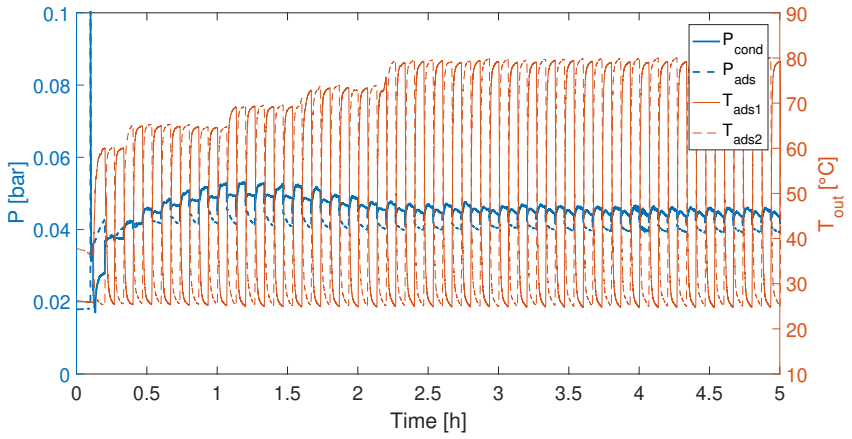


Figure D.6: A temperature swing leak test

### Performance analysis

An experiment in single bed mode was conducted with the copper heat exchanger filled with 250 g silica gel. The adsorber bed was heated to $T_{ads,in} = 80$ °C with $T_{cond,in} = 30$ °C and $T_{ads,in} = 30$ °C in Fig. D.7a. Despite heating with a heat source temperature of 80 °C and 20 min full cycle time, only 1.8 g of water were produced within 80 min leading to SDWP ≈ 0.07. (Fig. D.7b, which is well below the experimental uncertainty. Therefore, the performance analysis was discontinued to investigate the failed experiment.

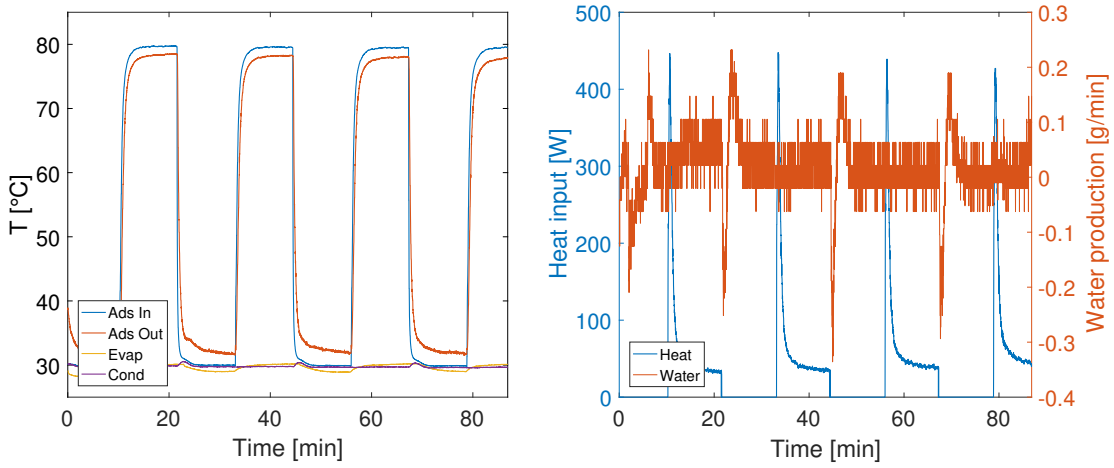


(a) (b)

Figure D.7: (a) Single bed experiment with copper heat exchanger. Inlet temperature of the adsorber and outlet temperature curves of adsorber, condenser and evaporator. $T_{hot,in} = 80$ °C, $T_{cond,in} = 30$ °C, $T_{evap,in} = 30$ °C and 600 s half cycle time.
(b) Water production and heat input of copper heat exchanger calculated from temperature curves and flow rates.

The aim of the investigation was to find out if the copper heat exchangers work properly.

A thermocouple was placed on the heat exchanger fins to measure the fin temperature at ambient pressure. The set up can be seen in Fig. D.8a for copper and in Fig. D.8b for aluminium. It was important that the thermocouple touched the fin, but not the water tubes inside the heat exchanger. In addition, the outlet temperature from the heat exchanger was measured as well. The heat exchanger was heated at 80 °C inlet temperature from the thermostatic bath. The result can be seen in Fig. D.8c. The fin temperature of the aluminium heat exchanger follows the outlet temperature very well and is 10 °C below the outlet temperature after 4 minutes, when the heat exchanger was cooled back to 30 °C, where the fin was cooled faster than the outlet. By contrast, the fin temperature of the copper heat exchangers did not exceed 40 °C, while the outlet temperature of the water was 75 °C. The copper heat exchangers malfunction as heat is not transferred from the water to the fins. If the fins stay cold, the silica gel remains cold as well, which is why water cannot desorb from the material (Fig. D.7). Heat transfer limitations between tubes and fins cause the fins to remain cold. The fins appear to be pushed onto the tubes with no sturdy solders or welds connecting them to the tubes, which would facilitate heat transfer (Fig. D.8d). There are 14 vertical tubes times 26 fins resulting in 364 connections and many of them are not easily accessible. Thus, a decision was made against trying to repair the heat exchangers.

The copper heat exchangers were simultaneously planned to the heat recovery lines. The performance ratio of the test rig without heat recovery was PR≈0.4. The heat recovery improved the PR to 0.6, while the maximum PR of the system in this configuration is $PR \approx L_w/\Delta h_{ads} \approx 0.8$, which leaves little room for improvement to the copper heat exchangers even if they were working properly. Therefore, the focus of phase IV was laid upon increasing the SDWP with novel adsorption materials.

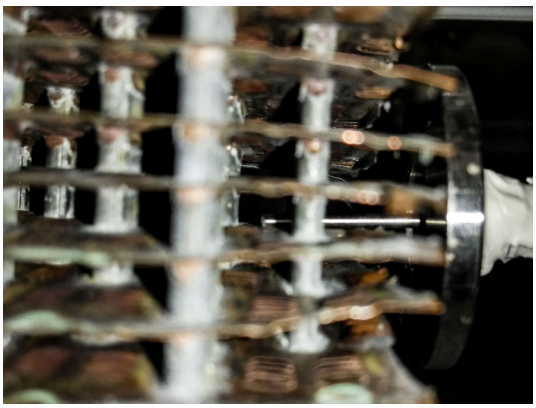

(a)

(b)

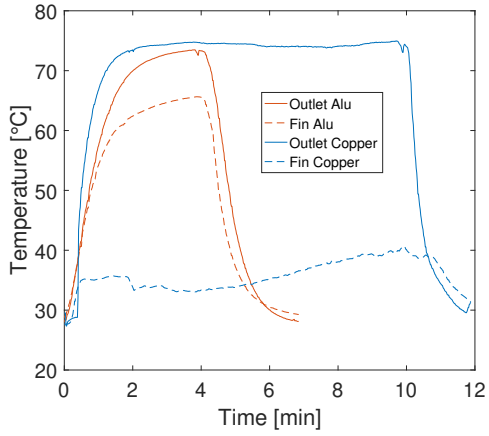


(c)

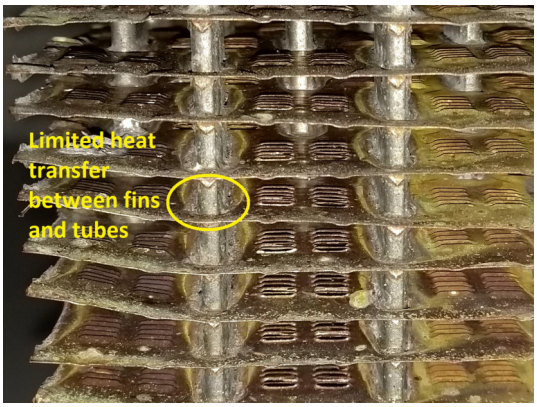


(d)

Figure D.8: (a) A thermocouple measuring the fin temperature of the copper heat exchanger.
(b) A thermocouple measuring the fin temperature of the aluminium heat exchanger
(c) Results from set up shown in Fig. D.8a and D.8b. Heat exchanger outlet and fin temperatures for the copper and aluminium heat exchangers.
(d) Limited heat transfer between tubes and fins causes malfunction.

# Appendix E

# Upgrades to the test rig

Additions to the test rig could include:

The heat integration between the two adsorber beds proposed in chapter 6 could be implemented and tested to experimentally proof that adsorption desalination can achieve performance ratios above 1. In addition, lighter and smaller adsorber heat exchangers would further improve the performance ratio. The cycle analysis revealed that the condenser and evaporator heat exchanger surface areas are both too small for the present adsorber beds. This issue could be addressed by down-scaling the adsorber beds and heat exchangers further. If the evaporator heat exchanger is replaced, the new heat exchanger should be made of stainless steel to be able to test salt solutions in the test rig.

Minor changes could include the replacement of the brass solenoid valves with stainless steel valves with larger orifices. The current solenoid valves have an orifice diameter of 2.3 mm, which limits the flow rate supplied to the adsorber beds to 0.3-0.4 L/min. The flow meters of the adsorber should also be replaced with the same type used for the condenser that have a scale of 0.1-1.2 L/min. This would reduce the experimental error, allow precise adjustments of the flow rate and test the impact of the flow rate on the system.

# Reference list


[1] Clemens Forman, Ibrahim Kolawole Muritala, Robert Pardemann, and Bernd Meyer. Estimating the global waste heat potential. *Renewable and Sustainable Energy Reviews*, 57:1568–1579, 2016.

[2] Mohammad Rahimi, Anthony P. Straub, Fang Zhang, Xiuping Zhu, Menachem Elimelech, Christopher A. Gorski, and Bruce E. Logan. Emerging electrochemical and membrane-based systems to convert low-grade heat to electricity. *Energy Environ. Sci.*, 11:276–285, 2018.

[3] Yasmine Ammar, Sharon Joyce, Rosemary Norman, Yaodong Wang, and Anthony P. Roskilly. Low grade thermal energy sources and uses from the process industry in the uk. *Applied Energy*, 89(1):3 – 20, 2012. Special issue on Thermal Energy Management in the Process Industries.

[4] Sarah Brückner, Selina Liu, Laia Miró, Michael Radspieler, Luisa F. Cabeza, and Eberhard Lävemann. Industrial waste heat recovery technologies: An economic analysis of heat transformation technologies. *Applied Energy*, 151:157 – 167, 2015.

[5] Alexander S. Rattner and Srinivas Garimella. Energy harvesting, reuse and upgrade to reduce primary energy usage in the usa. *Energy*, 36(10):6172 – 6183, 2011.

[6] Michael Papapetrou, George Kosmadakis, Andrea Cipollina, Umberto La Commare, and Giorgio Micale. Industrial waste heat: Estimation of the technically available resource in the eu per industrial sector, temperature level and country. *Applied Thermal Engineering*, 138:207 – 216, 2018.

[7] Zhang Shengjun, Wang Huaixin, and Guo Tao. Performance comparison and parametric optimization of subcritical organic rankine cycle (orc) and transcritical power cycle system for low-temperature geothermal power generation. *Applied Energy*, 88(8):2740 – 2754, 2011.

[8] A. Tamburini, M. Tedesco, A. Cipollina, G. Micale, M. Ciofalo, M. Papapetrou, W. Van Baak, and A. Piacentino. Reverse electrodialysis heat engine for sustainable power production. *Applied Energy*, 206:1334 – 1353, 2017.

[9] Shihong Lin, Ngai Yin Yip, Tzahi Y Cath, Chinedum O Osuji, and Menachem Elimelech. Hybrid pressure retarded osmosis–membrane distillation system for power generation from low-grade heat: Thermodynamic analysis and energy efficiency. *Environmental science & technology*, 48(9):5306–5313, 2014.

[10] Keith E Herold, Reinhard Radermacher, and Sanford A Klein. *Absorption chillers and heat pumps*. CRC press, 2016.

[11] Giulio Santori, Salvatore Santamaria, Alessio Sapienza, Stefano Brandani, and Angelo Freni. A stand-alone solar adsorption refrigerator for humanitarian aid. *Solar Energy*, 100:172 – 178, 2014.

[12] Patricia Palenzuela, Ashraf S. Hassan, Guillermo Zaragoza, and Diego-C. Alarcón-Padilla. Steady state model for multi-effect distillation case study: Plataforma solar de almería med pilot plant. *Desalination*, 337:31 – 42, 2014.

[13] Chasik Park, Hoseong Lee, Yunho Hwang, and Reinhard Radermacher. Recent advances in vapor compression cycle technologies. *International Journal of Refrigeration*, 60:118 – 134, 2015.

[14] Shihong Lin and Menachem Elimelech. Staged reverse osmosis operation: Configurations, energy efficiency, and application potential. *Desalination*, 366:9 – 14, 2015. Energy and Desalination.

[15] Menachem Elimelech and William A Phillip. The future of seawater desalination: energy, technology, and the environment. *Science*, 333(6043):712–717, 2011.

[16] Mesfin M Mekonnen and Arjen Y Hoekstra. Four billion people facing severe water scarcity. *Science advances*, 2(2):e1500323, 2016.

[17] Kim Choon Ng, Kyaw Thu, Youngdeuk Kim, Anutosh Chakraborty, and Gary Amy. Adsorption desalination: An emerging low-cost thermal desalination method. *Desalination*, 308:161 – 179, 2013. New Directions in Desalination.

[18] Sarah Brückner, Selina Liu, Laia Miró, Michael Radspieler, Luisa F. Cabeza, and Eberhard Lävemann. Industrial waste heat recovery technologies: An economic analysis of heat transformation technologies. *Applied Energy*, 151:157 – 167, 2015.

[19] Muhammad Wakil Shahzad, Kim Choon Ng, Kyaw Thu, Bidyut Baran Saha, and Won Gee Chun. Multi effect desalination and adsorption desalination (medad): A hybrid desalination method. *Applied Thermal Engineering*, 72(2):289 – 297, 2014. Special Issue: International Symposium on Innovative Materials for Processes in Energy Systems 2013 (IMPRES2013).

[20] Douglas M Ruthven. *Principles of adsorption and adsorption processes*. John Wiley & Sons, 1984.

[21] Robert H Perry and Don W Green. *Perry's chemical engineers' handbook*. McGraw-Hill Professional, 1999.

[22] M.J. Goldsworthy. Measurements of water vapour sorption isotherms for rd silica gel, aqsoa-z01, aqsoa-z02, aqsoa-z05 and ceca zeolite 3a. *Microporous and Mesoporous Materials*, 196:59 – 67, 2014.

[23] Sibnath Kayal, Sun Baichuan, and Bidyut Baran Saha. Adsorption characteristics of aqsoa zeolites and water for adsorption chillers. *International Journal of Heat and Mass Transfer*, 92:1120–1127, 2016.

[24] Kyaw Thu, Anutosh Chakraborty, Bidyut Baran Saha, and Kim Choon Ng. Thermo-physical properties of silica gel for adsorption desalination cycle. *Applied Thermal Engineering*, 50(2):1596–1602, 2013.

[25] Pia Küsgens, Marcus Rose, Irena Senkovska, Heidrun Fröde, Antje Henschel, Sven Siegle, and Stefan Kaskel. Characterization of metal-organic frameworks by water adsorption. *Microporous and Mesoporous Materials*, 120(3):325 – 330, 2009.

[26] Chenghong Wang, Xinlei Liu, Nilay Keser Demir, J Paul Chen, and Kang Li. Applications of water stable metal–organic frameworks. *Chemical Society Reviews*, 45(18):5107–5134, 2016.

[27] Marina V. Solovyeva, Yuri I. Aristov, and Larisa G. Gordeeva. Nh2-mil-125 as promising adsorbent for adsorptive cooling: Water adsorption dynamics. *Applied Thermal Engineering*, 116:541 – 548, 2017.

[28] Hong-Cai Zhou, Jeffrey R. Long, and Omar M. Yaghi. Introduction to metal–organic frameworks. *Chemical Reviews*, 112(2):673–674, 2012. PMID: 22280456.

[29] Larisa G. Gordeeva, Marina V. Solovyeva, and Yuri I. Aristov. Nh2-mil-125 as a promising material for adsorptive heat transformation and storage. *Energy*, 100:18 – 24, 2016.

[30] Jean Le Bideau, Lydie Viau, and André Vioux. Ionogels, ionic liquid based hybrid materials. *Chemical Society Reviews*, 40(2):907–925, 2011.

[31] Kenneth R Seddon, Annegret Stark, and María-José Torres. Influence of chloride, water, and organic solvents on the physical properties of ionic liquids. *Pure and Applied Chemistry*, 72(12):2275–2287, 2000.

[32] Yuanyuan Cao, Yu Chen, Xiaofu Sun, Zhongmin Zhang, and Tiancheng Mu. Water sorption in ionic liquids: kinetics, mechanisms and hydrophilicity. *Physical Chemistry Chemical Physics*, 14(35):12252–12262, 2012.

[33] S. Cuadrado-Prado, M. Domínguez-Pérez, E. Rilo, S. García-Garabal, L. Segade, C. Franjo, and O. Cabeza. Experimental measurement of the hygroscopic grade on eight imidazolium based ionic liquids. *Fluid Phase Equilibria*, 278(1):36 – 40, 2009.

[34] Ahmed A. Askalany, Angelo Freni, and Giulio Santori. Supported ionic liquid water sorbent for high throughput desalination and drying. *Desalination*, 452:258 – 264, 2019.

[35] Ariel I Horowitz and Matthew J Panzer. Poly (dimethylsiloxane)-supported ionogels with a high ionic liquid loading. *Angewandte Chemie International Edition*, 53(37):9780–9783, 2014.

[36] Ernest B Miller. Refrigeration, September 24 1929. US Patent 1,729,081.

[37] Giulio Santori and Chiara Di Santis. Optimal fluids for adsorptive cooling and heating. *Sustainable Materials and Technologies*, 12:52 – 61, 2017.

[38] I.I. El-Sharkawy, M. Hassan, B.B. Saha, S. Koyama, and M.M. Nasr. Study on adsorption of methanol onto carbon based adsorbents. *International Journal of Refrigeration*, 32(7):1579 – 1586, 2009.

[39] VDI-Gesellschaft Verfahrenstechnik und Chemieingenieurwesen (VDI-GVC). Wärmeatlas, vdi 10. auflage, 2006.

[40] A. Frazzica, V. Palomba, B. Dawoud, G. Gullì, V. Brancato, A. Sapienza, S. Vasta, A. Freni, F. Costa, and G. Restuccia. Design, realization and testing of an adsorption refrigerator based on activated carbon/ethanol working pair. *Applied Energy*, 174:15 – 24, 2016.

[41] Z Tamainot-Telto and RE Critoph. Adsorption refrigerator using monolithic carbon-ammonia pair. *International Journal of Refrigeration*, 20(2):146–155, 1997.

[42] Zacharie Tamainot-Telto, Steven John Metcalf, Robert E Critoph, Y Zhong, and Roger Thorpe. Carbon–ammonia pairs for adsorption refrigeration applications: ice making, air conditioning and heat pumping. *International Journal of Refrigeration*, 32(6):1212–1229, 2009.

[43] J Bauer, R Herrmann, W Mittelbach, and W Schwieger. Zeolite/aluminum composite adsorbents for application in adsorption refrigeration. *International Journal of Energy Research*, 33(13):1233–1249, 2009.

[44] Tomas Núñez, Walter Mittelbach, and Hans-Martin Henning. Development of an adsorption chiller and heat pump for domestic heating and air-conditioning applications. *Applied Thermal Engineering*, 27(13):2205 – 2212, 2007. Heat Powered Cycles – 04.

[45] Yu.I. Aristov, D.M. Chalaev, B. Dawoud, L.I. Heifets, O.S. Popel, and G. Restuccia. Simulation and design of a solar driven thermochemical refrigerator using new chemisorbents. *Chemical Engineering Journal*, 134(1):58 – 65, 2007. Proceedings of the XVII International Conference on Chemical Reactors CHEMREACTOR-17 and Post-Symposium "Catalytic Processing of Renewable Sources: Fuel, Energy, Chemicals".

[46] Xiaolin Wang and Kim Choon Ng. Experimental investigation of an adsorption desalination plant using low-temperature waste heat. *Applied Thermal Engineering*, 25(17):2780 – 2789, 2005.

[47] Kim Choon Ng, Kyaw Thu, Anutosh Chakraborty, Bidyut Baran Saha, and Won Gee Chun. Solar-assisted dual-effect adsorption cycle for the production of cooling effect and potable water. *International Journal of Low-Carbon Technologies*, 4(2):61–67, 2009.

[48] KC Ng, HT Chu, and X Wang. Prototype testing of a novel four-bed regenerative silica gel-water adsorption chiller. In *International Congress of Refrigeration*, pages 0–0, 2003.

[49] Kim Choon Ng, Kyaw Thu, Bidyut Baran Saha, and Anutosh Chakraborty. Study on a waste heat-driven adsorption cooling cum desalination cycle. *International Journal of Refrigeration*, 35(3):685 – 693, 2012. Refrigeration and Heat Pumping with Sorption Processes.

[50] Xiaolin Wang, Hui Tong Chua, and Kim Choon Ng. Experimental investigation of silica gel–water adsorption chillers with and without a passive heat recovery scheme. *International Journal of Refrigeration*, 28(5):756 – 765, 2005.

[51] Kyaw Thu, Bidyut Baran Saha, Anutosh Chakraborty, Won Gee Chun, and Kim Choon Ng. Study on an advanced adsorption desalination cycle with evaporator–condenser heat recovery circuit. *International Journal of Heat and Mass Transfer*, 54(1):43 – 51, 2011.

[52] Kyaw Thu, Hideharu Yanagi, Bidyut Baran Saha, and Kim Choon Ng. Performance investigation on a 4-bed adsorption desalination cycle with internal heat recovery scheme. *Desalination*, 402:88 – 96, 2017.

[53] Sourav Mitra, Kyaw Thu, Bidyut Baran Saha, and Pradip Dutta. Performance evaluation and determination of minimum desorption temperature of a two-stage air cooled silica gel/water adsorption system. *Applied Energy*, 206:507 – 518, 2017.

[54] Jun W. Wu, Mark J. Biggs, and Eric J. Hu. Dynamic model for the optimisation of adsorption-based desalination processes. *Applied Thermal Engineering*, 66(1):464 – 473, 2014.

[55] Ahmed S. Alsaman, Ahmed A. Askalany, K. Harby, and Mahmoud S. Ahmed. Performance evaluation of a solar-driven adsorption desalination-cooling system. *Energy*, 128:196 – 207, 2017.

[56] Peter G. Youssef, Hassan Dakkama, Saad M. Mahmoud, and Raya K. AL-Dadah. Experimental investigation of adsorption water desalination/cooling system using cpo-27ni mof. *Desalination*, 404:192 – 199, 2017.

[57] Eman Elsayed, Raya AL-Dadah, Saad Mahmoud, Paul.A. Anderson, Ahmed Elsayed, and Peter G. Youssef. Cpo-27(ni), aluminium fumarate and mil-101(cr) mof materials for adsorption water desalination. *Desalination*, 406:25 – 36, 2017. Desalination and the Environment.

[58] Peter G Youssef, Saad M Mahmoud, and Raya K Al-Dadah. Performance analysis of four bed adsorption water desalination/refrigeration system, comparison of aqsoa-z02 to silica-gel. *Desalination*, 375:100–107, 2015.

[59] Ehab S. Ali, Ahmed A. Askalany, K. Harby, Mohamed Refaat Diab, and Ahmed S. Alsaman. Adsorption desalination-cooling system employing copper sulfate driven by low grade heat sources. *Applied Thermal Engineering*, 136:169 – 176, 2018.

[60] Sourav Mitra, Pramod Kumar, Kandadai Srinivasan, and Pradip Dutta. Performance evaluation of a two-stage silica gel + water adsorption based cooling-cum-desalination system. *International Journal of Refrigeration*, 58:186 – 198, 2015.

[61] B.B Saha, A Akisawa, and T Kashiwagi. Solar/waste heat driven two-stage adsorption chiller: the prototype. *Renewable Energy*, 23(1):93 – 101, 2001.

[62] Jun W Wu, Mark J Biggs, Philip Pendleton, Alexander Badalyan, and Eric J Hu. Experimental implementation and validation of thermodynamic cycles of adsorption-based desalination. *Applied energy*, 98:190–197, 2012.

[63] K Thu. Adsorption desalination theory and experiment: National university of singapore. 2010.

[64] El-Dessouky and Ettouney. *Fundamentals of Salt Water Desalination*, volume 1. Elsevier Science, 2002.

[65] Edward Jones, Manzoor Qadir, Michelle T.H. van Vliet, Vladimir Smakhtin, and Seong mu Kang. The state of desalination and brine production: A global outlook. *Science of The Total Environment*, 657:1343 – 1356, 2019.

[66] Muhammad Wakil Shahzad, Muhammad Burhan, Li Ang, and Kim Choon Ng. Energy-water-environment nexus underpinning future desalination sustainability. *Desalination*, 413:52 – 64, 2017.

[67] G. Zaragoza, A. Ruiz-Aguirre, and E. Guillén-Burrieza. Efficiency in the use of solar thermal energy of small membrane desalination systems for decentralized water production. *Applied Energy*, 130:491 – 499, 2014.

[68] Noel Dow, Stephen Gray, Jun de Li, Jianhua Zhang, Eddy Ostarcevic, Audra Liubinas, Paul Atherton, Gareth Roeszler, Andrew Gibbs, and Mikel Duke. Pilot trial of membrane distillation driven by low grade waste heat: Membrane fouling and energy assessment. *Desalination*, 391:30 – 42, 2016. Advances in Membrane Des: Keynotes from MEMDES 2-Singapore.

[69] I.G. Wenten and Khoiruddin. Reverse osmosis applications: Prospect and challenges. *Desalination*, 391:112 – 125, 2016. Advances in Membrane Des: Keynotes from MEMDES 2-Singapore.

[70] M. Al-Shammiri and M. Safar. Multi-effect distillation plants: state of the art. *Desalination*, 126(1):45 – 59, 1999.

[71] Xiaolin Wang, Alexander Christ, Klaus Regenauer-Lieb, Kamel Hooman, and Hui Tong Chua. Low grade heat driven multi-effect distillation technology. *International Journal of Heat and Mass Transfer*, 54(25–26):5497 – 5503, 2011.

[72] Patricia Palenzuela, Ashraf S Hassan, Guillermo Zaragoza, and Diego-C Alarcón-Padilla. Steady state model for multi-effect distillation case study: Plataforma solar de almería med pilot plant. *Desalination*, 337:31–42, 2014.

[73] Hyuk Soo Son, Muhammad Wakil Shahzad, Noreddine Ghaffour, and Kim Choon Ng. Pilot studies on synergetic impacts of energy utilization in hybrid desalination system: Multi-effect distillation and adsorption cycle (med-ad). *Desalination*, 477:114266, 2020.

[74] Kim Choon Ng, Kyaw Thu, Seung Jin Oh, Li Ang, Muhammad Wakil Shahzad, and Azhar Bin Ismail. Recent developments in thermally-driven seawater desalination: Energy efficiency improvement by hybridization of the med and ad cycles. *Desalination*, 356:255 – 270, 2015. State-of-the-Art Reviews in Desalination.

[75] Abdullah Alkhudhiri, Naif Darwish, and Nidal Hilal. Membrane distillation: A comprehensive review. *Desalination*, 287:2 – 18, 2012. Special Issue in honour of Professor Takeshi Matsuura on his 75th Birthday.

[76] Hyung Won Chung, Jaichander Swaminathan, David M. Warsinger, and John H. Lienhard V. Multistage vacuum membrane distillation (msvmd) systems for high salinity applications. *Journal of Membrane Science*, 497:128 – 141, 2016.

[77] J.R. Rumble and J. Rumble. *CRC Handbook of Chemistry and Physics, 98th Edition*. CRC Handbook of Chemistry and Physics. CRC Press LLC, 2017.

[78] Peter Stephan, Karlheinz Schaber, Karl Stephan, and Franz Mayinger. *Thermodynamische Prozesse, Maschinen und Anlagen*, pages 319–397. Springer Berlin Heidelberg, Berlin, Heidelberg, 2013.

[79] O. Badr, S. Naik, P.W. O'Callaghan, and S.D. Probert. Expansion machine for a low power-output steam rankine-cycle engine. *Applied Energy*, 39(2):93 – 116, 1991.

[80] Karl Strauß. *Kraftwerkstechnik*. Springer, 2016.

[81] Techno-economic survey of organic rankine cycle (orc) systems. *Renewable and Sustainable Energy Reviews*, 22:168 – 186, 2013.

[82] DW Kirkley. Determination of the optimum configuration for a stirling engine. *Journal of Mechanical Engineering Science*, 4(3):204–212, 1962.

[83] E.D. Rogdakis, G.D. Antonakos, and I.P. Koronaki. Thermodynamic analysis and experimental investigation of a solo v161 stirling cogeneration unit. *Energy*, 45(1):503 – 511, 2012. The 24th International Conference on Efficiency, Cost, Optimization, Simulation and Environmental Impact of Energy, ECOS 2011.

[84] Francis J DiSalvo. Thermoelectric cooling and power generation. *Science*, 285(5428):703–706, 1999.

[85] Lon E Bell. Cooling, heating, generating power, and recovering waste heat with thermoelectric systems. *Science*, 321(5895):1457–1461, 2008.

[86] Wei He, Gan Zhang, Xingxing Zhang, Jie Ji, Guiqiang Li, and Xudong Zhao. Recent development and application of thermoelectric generator and cooler. *Applied Energy*, 143:1 – 25, 2015.

[87] Mohammad Rahimi, Anthony P. Straub, Fang Zhang, Xiuping Zhu, Menachem Elimelech, Christopher A. Gorski, and Bruce E. Logan. Emerging electrochemical and membrane-based systems to convert low-grade heat to electricity. *Energy Environ. Sci.*, 11:276–285, 2018.

[88] M. Micari, A. Cipollina, F. Giacalone, G. Kosmadakis, M. Papapetrou, G. Zaragoza, G. Micale, and A. Tamburini. Towards the first proof of the concept of a reverse electrodialysis - membrane distillation heat engine. *Desalination*, 453:77 – 88, 2019.

[89] Kerri L. Hickenbottom, Johan Vanneste, Leslie Miller-Robbie, Akshay Deshmukh, Menachem Elimelech, Michael B. Heeley, and Tzahi Y. Cath. Techno-economic assessment of a closed-loop osmotic heat engine. *Journal of Membrane Science*, 535:178 – 187, 2017.

[90] Seok Hun Kang. Design and experimental study of orc (organic rankine cycle) and radial turbine using r245fa working fluid. *Energy*, 41(1):514 – 524, 2012. 23rd International Conference on Efficiency, Cost, Optimization, Simulation and Environmental Impact of Energy Systems, ECOS 2010.

[91] Steven Lecompte, Henk Huisseune, Martijn van den Broek, Bruno Vanslambrouck, and Michel De Paepe. Review of organic rankine cycle (orc) architectures for waste heat recovery. *Renewable and Sustainable Energy Reviews*, 47:448 – 461, 2015.

[92] Bruce E Logan and Menachem Elimelech. Membrane-based processes for sustainable power generation using water. *Nature*, 488(7411):313, 2012.

[93] Sidney Loeb. Method and apparatus for generating power utilizing reverse electrodialysis, October 16 1979. US Patent 4,171,409.

[94] J. Veerman, M. Saakes, S.J. Metz, and G.J. Harmsen. Reverse electrodialysis: Performance of a stack with 50 cells on the mixing of sea and river water. *Journal of Membrane Science*, 327(1):136 – 144, 2009.

[95] Frank J. Millero, Rainer Feistel, Daniel G. Wright, and Trevor J. McDougall. The composition of standard seawater and the definition of the reference-composition salinity scale. *Deep Sea Research Part I: Oceanographic Research Papers*, 55(1):50 – 72, 2008.

[96] Jordi Moreno, Simon Grasman, Ronny van Engelen, and Kitty Nijmeijer. Upscaling reverse electrodialysis. *Environmental Science & Technology*, 52(18):10856–10863, 2018. PMID: 30102521.

[97] Sidney Loeb. Method and apparatus for generating power utilizing pressure-retarded-osmosis, September 16 1975. US Patent 3,906,250.

[98] Jan W. Post, Joost Veerman, Hubertus V.M. Hamelers, Gerrit J.W. Euverink, Sybrand J. Metz, Kitty Nymeijer, and Cees J.N. Buisman. Salinity-gradient power: Evaluation of pressure-retarded osmosis and reverse electrodialysis. *Journal of Membrane Science*, 288(1):218 – 230, 2007.

[99] Ngai Yin Yip and Menachem Elimelech. Comparison of energy efficiency and power density in pressure retarded osmosis and reverse electrodialysis. *Environmental Science & Technology*, 48(18):11002–11012, 2014. PMID: 25157687.

[100] K.L. Lee, R.W. Baker, and H.K. Lonsdale. Membranes for power generation by pressure-retarded osmosis. *Journal of Membrane Science*, 8(2):141 – 171, 1981.

[101] F. Giacalone, C. Olkis, G. Santori, A. Cipollina, S. Brandani, and G. Micale. Novel solutions for closed-loop reverse electrodialysis: Thermodynamic characterisation and perspective analysis. *Energy*, 166:674 – 689, 2019.

[102] Daniel R. Stull. Vapor pressure of pure substances. organic and inorganic compounds. *Industrial & Engineering Chemistry*, 39(4):517–540, 1947.

[103] Eric W. Lemmon, M. L. Huber, and M. O. McLinden. *NIST Standard Reference Database 23: Reference Fluid Thermodynamic and Transport Properties - REFPROP*. National Institute of Standards and Technology, Standard Reference Data Program, Gaithersburg, 9.0 edition, 2010.

[104] Kenneth S Pitzer and Guillermo Mayorga. Thermodynamics of electrolytes. ii. activity and osmotic coefficients for strong electrolytes with one or both ions univalent. *The Journal of Physical Chemistry*, 77(19):2300–2308, 1973.

[105] Leonard F Silvester and Kenneth S Pitzer. Thermodynamics of electrolytes. 8. high-temperature properties, including enthalpy and heat capacity, with application to sodium chloride. *The Journal of Physical Chemistry*, 81(19):1822–1828, 1977.

[106] Daniel J Bradley and Kenneth S Pitzer. Thermodynamics of electrolytes. 12. dielectric properties of water and debye-hueckel parameters to 350. degree. c and 1 kbar. *Journal of physical chemistry*, 83(12):1599–1603, 1979.

[107] J.R. Taylor. *Introduction To Error Analysis: The Study of Uncertainties in Physical Measurements*. A series of books in physics. University Science Books, 1997.

[108] Nevil Vincent Sidgwick and Joseph Alfred Hector Roberts Gentle. Ccxxi.—the solubilities of the alkali formates and acetates in water. *Journal of the Chemical Society, Transactions*, 121:1837–1843, 1922.

[109] Robert Anthony Robinson and Robert Harold Stokes. *Electrolyte solutions*. Courier Corporation, 1959.

[110] R. Beyer. *Characterization of binary and ternary electrolyte systems with anions of organic acids. Measurement of the water activity coefficient and thermodynamic modeling*. PhD thesis, University of Hamburg, 2001.

[111] R. A. Robinson and R. H. Stokes. Tables of osmotic and activity coefficients of electrolytes in aqueous solution at 25° c. *Trans. Faraday Soc.*, 45:612–624, 1949.

[112] Walter J Hamer and Yung-Chi Wu. Osmotic coefficients and mean activity coefficients of uni-univalent electrolytes in water at 25° c. *Journal of Physical and Chemical Reference Data*, 1(4):1047–1100, 1972.

[113] R.A. Robinson, R.H. Wood, and P.J. Reilly. Calculation of excess gibbs energies and activity coefficients from isopiestic measurements on mixtures of lithium and sodium salts. *The Journal of Chemical Thermodynamics*, 3(4):461 – 471, 1971.

[114] Stanley I Sandler. *Models for thermodynamic and phase equilibria calculations*. Dekker, 1994.

[115] Patricia Palenzuela, Marina Micari, Bartolomé Ortega-Delgado, Francesco Giacalone, Guillermo Zaragoza, Diego-César Alarcón-Padilla, Andrea Cipollina, Alessandro Tamburini, and Giorgio Micale. Performance analysis of a red-med salinity gradient heat engine. *Energies*, 11(12):3385, 2018.

[116] Michele Tedesco, Andrea Cipollina, Alessandro Tamburini, I. David L. Bogle, and Giorgio Micale. A simulation tool for analysis and design of reverse electrodialysis using concentrated brines. *Chemical Engineering Research and Design*, 93:441 – 456, 2015.

[117] Bartolome Ortega-Delgado, Lourdes Garcia-Rodriguez, and Diego-Cesar Alarcon-Padilla. Opportunities of improvement of the med seawater desalination process by pretreatments allowing high-temperature operation. *Desalin. Water Treat*, 97, 2017.

[118] R.Philip Hammond, David M. Eissenberg, Dieter K. Emmermann, John E. Jones, Hugo H. Sephton, Ferric C. Standiford, Ronald F. Scott, William J. Rider, and David W. Dean. Seawater desalination plant for southern california. *Desalination*, 99(2):483 – 508, 1994.

[119] C. Olkis, G. Santori, and S. Brandani. An adsorption reverse electrodialysis system for the generation of electricity from low-grade heat. *Applied Energy*, 231:222 – 234, 2018.

[120] Jun W Wu, Eric J Hu, and Mark J Biggs. Thermodynamic cycles of adsorption desalination system. *Applied energy*, 90(1):316–322, 2012.

[121] M.A. Darwish, Faisal Al-Juwayhel, and Hassan K. Abdulraheim. Multi-effect boiling systems from an energy viewpoint. *Desalination*, 194(1):22 – 39, 2006.

[122] M. M. Dubinin and V. A. Astakhov. Development of the concepts of volume filling of micropores in the adsorption of gases and vapors by microporous adsorbents. *Bulletin of the Academy of Sciences of the USSR, Division of chemical science*, 20(1):3–7, Jan 1971.

[123] Alessio Sapienza, Andreas Velte, Ilya Girnik, Andrea Frazzica, Gerrit Füldner, Lena Schnabel, and Yuri Aristov. "water - silica siogel" working pair for adsorption chillers: Adsorption equilibrium and dynamics. *Renewable Energy*, 110(Supplement C):40 – 46, 2017.

[124] Duong D Do. *Adsorption Analysis: Equilibria and Kinetics:(With CD Containing Computer Matlab Programs)*, volume 2. World Scientific, 1998.

[125] Muhammad W Shahzad and Kim C Ng. An improved multievaporator adsorption desalination cycle for gulf cooperation council countries. *Energy Technology*, 5(9):1663–1669, 2017.

[126] Kyaw Thu, Young-Deuk Kim, Gary Amy, Won Gee Chun, and Kim Choon Ng. A hybrid multi-effect distillation and adsorption cycle. *Applied Energy*, 104:810 – 821, 2013.

[127] RA Robinson. The water activities of lithium chloride solutions up to high concentrations at 25°. *Transactions of the Faraday Society*, 41:756–758, 1945.

[128] C. Olkis, S. Brandani, and G. Santori. A small-scale adsorption desalinator. *Energy Procedia*, 158:1425 – 1430, 2019. Innovative Solutions for Energy Transitions.

[129] Christopher Olkis, Stefano Brandani, and Giulio Santori. Design and experimental study of a small scale adsorption desalinator. *Applied Energy*, 253:113584, 2019.

[130] C Olkis, S Brandani, and G Santori. Cycle and performance analysis of a small-scale adsorption heat transformer for desalination and cooling applications. *Chemical Engineering Journal*, 378:122104, 2019.

[131] Ahmed Askalany, Christopher Olkis, Emilia Bramanti, Dmitry Lapshin, Luigi Calabrese, Edoardo Proverbio, Angelo Freni, and Giulio Santori. Silica-supported ionic liquids for heat-powered sorption desalination. *ACS Applied Materials & Interfaces*, 2020. PMID: 31512475.

[132] Giulio Santori, Alessio Sapienza, and Angelo Freni. A dynamic multi-level model for adsorptive solar cooling. *Renewable Energy*, 43(Supplement C):301 – 312, 2012.

[133] Xiaolin Wang, Kim Choon Ng, Anutosh Chakarborty, and Bidyut Baran Saha. How heat and mass recovery strategies impact the performance of adsorption desalination plant: Theory and experiments. *Heat Transfer Engineering*, 28(2):147–153, 2007.

[134] Kyaw Thu, Bidyut Baran Saha, Anutosh Chakraborty, Won Gee Chun, and Kim Choon Ng. Study on an advanced adsorption desalination cycle with evaporator–condenser heat recovery circuit. *International Journal of heat and mass transfer*, 54(1):43–51, 2011.

[135] Peter G Youssef, Saad M Mahmoud, and Raya K Al-Dadah. Numerical simulation of combined adsorption desalination and cooling cycles with integrated evaporator/condenser. *Desalination*, 392:14–24, 2016.

[136] Bidyut Baran Saha, Ibrahim I. El-Sharkawy, Muhammad Wakil Shahzad, Kyaw Thu, Li Ang, and Kim Choon Ng. Fundamental and application aspects of adsorption cooling and desalination. *Applied Thermal Engineering*, 97:68 – 76, 2016. Polygeneration processes, systems, technologies and applications.

[137] Nejib Douss, Francis E Meunier, and Lian Ming Sun. Predictive model and experimental results for a two-adsorber solid adsorption heat pump. *Industrial & engineering chemistry research*, 27(2):310–316, 1988.

[138] Alessio Sapienza, Andreas Velte, Ilya Girnik, Andrea Frazzica, Gerrit Füldner, Lena Schnabel, and Yuri Aristov. "water-silica siogel" working pair for adsorption chillers: Adsorption equilibrium and dynamics. *Renewable Energy*, 110:40–46, 2017.

[139] Marc A Rosen. Energy- and exergy-based comparison of coal-fired and nuclear steam power plants. *Exergy, An International Journal*, 1(3):180 – 192, 2001.

[140] Helena Passos, Imran Khan, Fabrice Mutelet, Mariana B Oliveira, Pedro J Carvalho, Luis MNBF Santos, Christoph Held, Gabriele Sadowski, Mara G Freire, and Joao AP Coutinho. Vapor–liquid equilibria of water+ alkylimidazolium-based ionic liquids: Measurements and perturbed-chain statistical associating fluid theory modeling. *Industrial & Engineering Chemistry Research*, 53(9):3737–3748, 2014.

[141] Pedro J Carvalho, Imran Khan, Antonio Morais, Jose FO Granjo, Nuno MC Oliveira, Luis MNBF Santos, and Joao AP Coutinho. A new microebulliometer for the measurement of the vapor–liquid equilibrium of ionic liquid systems. *Fluid Phase Equilibria*, 354:156–165, 2013.

[142] Dana Constantinescu, Karlheinz Schaber, Friederike Agel, Marco H Klingele, and Thomas JS Schubert. Viscosities, vapor pressures, and excess enthalpies of choline lactate+ water, choline glycolate+ water, and choline methanesulfonate+ water systems. *Journal of Chemical & Engineering Data*, 52(4):1280–1285, 2007.

[143] Carsten Jork, Matthias Seiler, York-Alexander Beste, and Wolfgang Arlt. Influence of ionic liquids on the phase behavior of aqueous azeotropic systems. *Journal of Chemical & Engineering Data*, 49(4):852–857, 2004.

[144] Noelia Calvar, Begoaa Gonzalez, Elena Gomez, and Angeles Dominguez. Vapor–liquid equilibria for the ternary system ethanol+ water+ 1-ethyl-3-methylimidazolium ethylsulfate and the corresponding binary systems containing the ionic liquid at 101.3 kpa. *Journal of Chemical & Engineering Data*, 53(3):820–825, 2008.

[145] Nina Merkel, Christina Weber, Matthias Faust, and Karlheinz Schaber. Influence of anion and cation on the vapor pressure of binary mixtures of water+ionic liquid and on the thermal stability of the ionic liquid. *Fluid Phase Equilibria*, 394:29 – 37, 2015.

[146] Ying Huang, Xiangping Zhang, Xin Zhang, Haifeng Dong, and Suojiang Zhang. Thermodynamic modeling and assessment of ionic liquid-based co2 capture processes. *Industrial & Engineering Chemistry Research*, 53(29):11805–11817, 2014.

[147] Yong Peng and Xiuyang Lu. Isobaric vapor–liquid equilibria for water + acetic acid + 1-ethyl-3-methylimidazolium diethylphosphate at 101.32 kpa. *Journal of Chemical & Engineering Data*, 59(2):250–256, 2014.

[148] Ryo Kato and Jürgen Gmehling. Measurement and correlation of vapor–liquid equilibria of binary systems containing the ionic liquids [emim][(cf 3 so 2) 2 n],[bmim][(cf 3 so 2) 2 n],[mmim][(ch 3) 2 po 4] and oxygenated organic compounds respectively water. *Fluid Phase Equilibria*, 231(1):38–43, 2005.

[149] U. Westhaus, T. Dröge, and R. Sass. Detherm®—a thermophysical property database. *Fluid Phase Equilibria*, 158-160:429 – 435, 1999.

[150] Christiane Roemich, Nina C Merkel, Alessandro Valbonesi, Karlheinz Schaber, Sven Sauer, and Thomas JS Schubert. Thermodynamic properties of binary mixtures of water and room-temperature ionic liquids: Vapor pressures, heat capacities, densities, and viscosities of water+ 1-ethyl-3-methylimidazolium acetate and water+ diethylmethylammonium methane sulfonate. *Journal of chemical & engineering data*, 57(8):2258–2264, 2012.

[151] Hongsheng Dong, Ahmed A. Askalany, Christopher Olkis, Jiafei Zhao, and Giulio Santori. Hydrothermal stability of water sorption ionogels. *Energy*, 189:116186, 2019.

[152] Eman Elsayed, AL-Dadah Raya, Saad Mahmoud, Paul A Anderson, Ahmed Elsayed, and Peter G Youssef. Cpo-27 (ni), aluminium fumarate and mil-101 (cr) mof materials for adsorption water desalination. *Desalination*, 406:25–36, 2017.

[153] Andrea Frazzica and Angelo Freni. Adsorbent working pairs for solar thermal energy storage in buildings. *Renewable Energy*, 110:87 – 94, 2017. Increasing the renewable share for heating and cooling by the means of sorption heat pumps and chillers.

[154] Talib Hussain, Laura J. Waters, Gareth M.B. Parkes, and Yasser Shahzad. Microwave processed solid dispersions for enhanced dissolution of gemfibrozil using non-ordered mesoporous silica. *Colloids and Surfaces A: Physicochemical and Engineering Aspects*, 520:428 – 435, 2017.

[155] David Hespeler, Jonas Kaltenbach, and Sung Min Pyo. Glabridin smartpearls – silica selection, production, amorphous stability and enhanced solubility. *International Journal of Pharmaceutics*, 561:228 – 235, 2019.

[156] Yotsanan Weerapol, Sontaya Limmatvapirat, Chaweewan Jansakul, Hirofumi Takeuchi, and Pornsak Sriamornsak. Enhanced dissolution and oral bioavailability of nifedipine by spontaneous emulsifying powders: Effect of solid carriers and dietary state. *European Journal of Pharmaceutics and Biopharmaceutics*, 91:25 – 34, 2015.

[157] Lingbo Kong, Lynn Price, Ali Hasanbeigi, Huanbin Liu, and Jigeng Li. Potential for reducing paper mill energy use and carbon dioxide emissions through plant-wide energy audits: A case study in china. *Applied Energy*, 102:1334 – 1342, 2013. Special Issue on Advances in sustainable biofuel production and use - XIX International Symposium on Alcohol Fuels - ISAF.

[158] WE Larsen and Herschel Hunt. Liquid ammonia as a solvent. iv. activities of ammonium nitrate, iodide, bromide, and chloride at 25° c. *The Journal of Physical Chemistry*, 39(6):877–884, 1935.

[159] Stefano Brandani, Celio Cavalcante, Anemir Guimarães, and Douglas Ruthven. Heat effects in zlc experiments. *Adsorption*, 4(3):275–285, Sep 1998.

[160] Douglas B Riffel, Ferdinand P Schmidt, Francisco A Belo, Antonio PF Leite, Farid B Cortés, Farid Chejne, and Felix Ziegler. Adsorption of water on grace silica gel 127b at low and high pressure. *Adsorption*, 17(6):977–984, 2011.

[161] Eman Elsayed, AL-Dadah Raya, Saad Mahmoud, Paul A Anderson, Ahmed Elsayed, and Peter G Youssef. Cpo-27 (ni), aluminium fumarate and mil-101 (cr) mof materials for adsorption water desalination. *Desalination*, 406:25–36, 2017.

[162] Barbara Mette, Henner Kerskes, Harald Drück, and Hans Müller-Steinhagen. Experimental and numerical investigations on the water vapor adsorption isotherms and kinetics of binderless zeolite 13x. *International Journal of Heat and Mass Transfer*, 71:555 – 561, 2014.

[163] Daniel Ferreira, Roberto Magalhaes, Pedro Taveira, and Adelio Mendes. Effective adsorption equilibrium isotherms and breakthroughs of water vapor and carbon dioxide on different adsorbents. *Industrial & Engineering Chemistry Research*, 50(17):10201–10210, 08 2011.

[164] Ngai Yin Yip and Menachem Elimelech. Thermodynamic and energy efficiency analysis of power generation from natural salinity gradients by pressure retarded osmosis. *Environmental science & technology*, 46(9):5230–5239, 2012.

[165] Ibrahim Dincer and Marc A Rosen. *Exergy: energy, environment and sustainable development*. Newnes, 2012.

[166] Ramato Ashu Tufa, Sylwin Pawlowski, Joost Veerman, Karel Bouzek, Enrica Fontananova, Gianluca di Profio, Svetlozar Velizarov, João Goulão Crespo, Kitty Nijmeijer, and Efrem Curcio. Progress and prospects in reverse electrodialysis for salinity gradient energy conversion and storage. *Applied Energy*, 225:290 – 331, 2018.

[167] Sanjay R. Chemburkar. *Magnesium Iodide. e-EROS Encyclopedia of Reagents for Organic Synthesis*. John Wiley & Sons, Ltd, 2001.

[168] J. W. Post, C. H. Goeting, J. Valk, S. Goinga, J. Veerman, H. V. M. Hamelers, and P. J. F. M. Hack. Towards implementation of reverse electrodialysis for power generation from salinity gradients. *Desalination and Water Treatment*, 16(1-3):182–193, 2010.

[169] Alexandros Daniilidis, Rien Herber, and David A. Vermaas. Upscale potential and financial feasibility of a reverse electrodialysis power plant. *Applied Energy*, 119:257 – 265, 2014.

[170] J Martin Wimby, Thore S Berntsson, et al. Viscosity and density of aqueous-solutions of libr, licl, znbr2, cacl2, and lino3. 1. single salt-solutions. *Journal of Chemical and Engineering Data*, 39(1):68–72, 1994.

[171] JJ Lagowski. Solution phenomena in liquid ammonia. *Pure and Applied Chemistry*, 25(2):429–456, 1971.

[172] Linhard M. and Stephan M. *Z. Phys. Chem.*, 167:143–155, 1934.

[173] Gustav F Hüttig and Fritz Reuscher. Studien zur chemie des lithiums. i. über die hydrate des lithiumchlorids und lithiumbromids. *Zeitschrift für anorganische und allgemeine Chemie*, 137(1):155–180, 1924.

[174] P. R. Marshall and Herschel Hunt. Solubility measurements on the systems ammonium, sodium, and potassium perchlorate and ammonium, sodium, and potassium chloride. *Journal of Chemical & Engineering Data*, 4(3):217–222, 1959.

[175] J. N. Pearce and G. G. Pumplin. The apparent and partial molal volumes of ammonium chloride and of cupric sulfate in aqueous solution at 25°1. *Journal of the American Chemical Society*, 59(7):1221–1222, 1937.

[176] Hideki Yamamoto and Junji Tokunaga. Densities and viscosities of ammonium bromide-ammonia and ammonium iodide-ammonia. *Journal of Chemical and Engineering Data*, 36(3):277–280, 1991.

[177] Jack Allen Campbell and Frederick L. Marsh. The system magnesium bromide, ammonium bromide and water at 25°. *The Journal of Physical Chemistry*, 63(2):316–317, 1959.

[178] Alexander Apelblat and Eli Korin. Vapour pressures of saturated aqueous solutions of ammonium iodide, potassium iodide, potassium nitrate, strontium chloride, lithium sulphate, sodium thiosulphate, magnesium nitrate, and uranyl nitrate fromt=(278 to 323) k. *The Journal of Chemical Thermodynamics*, 30(4):459 – 471, 1998.

[179] H. W. Foote and S. R. Brinkley. Equilibrium in the system ammonia: Ammonium nitrate: Ammonium thiocyanate. *Journal of the American Chemical Society*, 43(5):1018–1031, 1921.

[180] Cohen E. and Bredee H.L. The virtual heats of solution of enantiotropic modifications in the transformation point. *Z. Phys. Chem. Leipzig*, 117:143–155, 1925.

[181] Harold W Ritchey and Herschel Hunt. Activity coefficients of ammonium chloride in liquid ammonia at 25° c. *Journal of Physical Chemistry*, 43(4):407–416, 1939.

[182] Herschel Hunt and W. E. Larsen. Liquid ammonia as a solvent. ii. vapor pressures of solutions at 25°c. *The Journal of Physical Chemistry*, 38(6):801–807, 1933.

[183] Grinnell Jones and Malcolm Dole. The electrical conductance of aqueous solutions of barium chloride as a function of the concentration. *Journal of the American Chemical Society*, 52(6):2245–2256, 1930.

[184] SS Islam, RL Gupta, and K Ismail. Extension of the falkenhagen-leist-kelbg equation to the electrical conductance of concentrated aqueous electrolytes. *Journal of chemical and engineering data*, 36(1):102–104, 1991.

[185] J. F. Chambers, Jean M. Stokes, and R. H. Stokes. Conductances of concentrated aqueous sodium and potassium chloride solutions at 25°. *The Journal of Physical Chemistry*, 60(7):985–986, 1956.

[186] Jörn Kiepe, Anne Karine de Araújo Rodrigues, Sven Horstmann, and Jürgen Gmehling. Experimental determination and correlation of liquid density data of electrolyte mixtures containing water or methanol. *Industrial & Engineering Chemistry Research*, 42(9):2022–2029, 2003.

[187] Hisham T El-Dessouky and Hisham Mohamed Ettouney. *Fundamentals of salt water desalination*. Elsevier, 2002.

[188] Kyaw Thu, Kim Choon Ng, Bidyut B Saha, Anutosh Chakraborty, and Shigeru Koyama. Operational strategy of adsorption desalination systems. *International Journal of Heat and Mass Transfer*, 52(7):1811–1816, 2009.

[189] Donald G Archer and Richard W Carter. Thermodynamic properties of the nacl+ h2o system. 4. heat capacities of h2o and nacl (aq) in cold-stable and supercooled states. *The Journal of Physical Chemistry B*, 104(35):8563–8584, 2000.

[190] G. Santori, A. Frazzica, A. Freni, M. Galieni, L. Bonaccorsi, F. Polonara, and G. Restuccia. Optimization and testing on an adsorption dishwasher. *Energy*, 50:170 – 176, 2013.

[191] Phillip Bendix, Gerrit Füldner, Marc Möllers, Harry Kummer, Lena Schnabel, Stefan Henninger, and Hans-Martin Henning. Optimization of power density and metal-to-adsorbent weight ratio in coated adsorbers for adsorptive heat transformation applications. *Applied Thermal Engineering*, 124:83 – 90, 2017.

[192] Phillip L Gould and Wilfried B Krätzig. Cooling tower structures. *Handbook of structural engineering. Boca Raton, FL: CRC Press Inc*, pages 473–504, 1998.

[193] Christoph Kost et al. Studie stromgestehungskosten erneuerbare energien. mai 2012. *Freiburg: Fraunhofer-Institut für Solare Energiesysteme ISE*, 2012.

[194] Pongsid Srikhirin, Satha Aphornratana, and Supachart Chungpaibulpatana. A review of absorption refrigeration technologies. *Renewable and sustainable energy reviews*, 5(4):343–372, 2001.

[195] Roy J Dossat and Thomas J Horan. *Principles of refrigeration*. Prentice-Hall, 2002.

[196] C Somers, A Mortazavi, Y Hwang, R Radermacher, P Rodgers, and S Al-Hashimi. Modeling water/lithium bromide absorption chillers in aspen plus. *Applied Energy*, 88(11):4197–4205, 2011.

[197] Pfeiffer Vacuum GmbH. *The Vacuum Technology Know-how book*. Pfeiffer Vacuum GmbH, 2013.

[198] Parker Hannifin Corporation. *Parker O-Ring Handbook 50th Edition*. Parker Hannifin Corporation, 2016.

[199] Wamei Lin, Jinliang Yuan, and Bengt Sundén. Review on graphite foam as thermal material for heat exchangers. In *World Renewable Energy Congress-Sweden; 8-13 May; 2011; Linköping; Sweden*, number 57, pages 748–755. Linköping University Electronic Press, 2011.

[200] Harvey P Hack. *Galvanic corrosion*, volume 978. ASTM International, 1988.